TECHNISCHE
UNIVERSITÄT
DARMSTADT

Collective Excitations in Nuclei with *ab initio* Methods

Vom Fachbereich Physik
der Technischen Universität Darmstadt

zur Erlangung des Grades
eines Doktors der Naturwissenschaften (Dr. rer. nat.)

genehmigte Dissertation von
Laura Mertes

Referent: Prof. Dr. Robert Roth
Korreferent: Prof. Dr. Jens Braun

Darmstadt 2024

Collective Excitations in Nuclei with *ab initio* Methods
Kollektive Kernanregungen mit *ab initio* Methoden

Genehmigte Dissertation von Laura Mertes
Darmstadt, Technische Universität Darmstadt

Tag der Prüfung: 24.06.2024

Jahr der Veröffentlichung auf TUprints: 2025
URN: urn:nbn:de:tuda-tuprints-298000
URL: https://tuprints.ulb.tu-darmstadt.de/id/eprint/29800

Die Veröffentlichung steht unter folgender Creative Commons Lizenz:
Namensnennung – Nicht kommerziell – Keine Bearbeitungen 4.0 International
https://creativecommons.org/licenses/by-nc-nd/4.0/

Abstract

Collective excitations offer a unique perspective of the structure of nuclei and give crucial insights into their properties. An elegant standard observable to probe collective excitations are transition strengths. They depend on the detailed form of the wave function, are accessible in experiments and, thus, allow for a verification of the applied theory and the underlying interactions.

Two different approaches for the investigation of collective excitations from low-lying excitations to the giant-resonance regime are employed throughout this thesis. The random-phase approximation (RPA), which was developed in the 1950s in quantum chemistry, has been established as a standard tool for the description of transitions strengths. The RPA is based on the particle-hole (ph) formalism, which allow for the construction of excited states via ph and hp excitations of the ground state in terms of excitation creation operators. The aforementioned operators serve as starting point for the derivation of conditional equations by utilization of the variational principle and the equations-of-motion method. An extension of the RPA, the so-called second-order RPA (SRPA), includes additional 2p2h (de-)excitations besides the ph (de-)excitations. Beyond the RPA, we address a second access to collective excitations, which combines the importance-truncated no-core shell model (IT-NCSM) with the Lanczos strength-function method by Whitehead. Within this framework, an eigenstate of a previous IT-NCSM calculation and the Hamiltonian serve as starting point. With the help of the simple Lanczos algorithm, a tridiagonal matrix is produced. Standard techniques are then utilized in order to diagonalize this matrix. Based on the obtained eigenvalues and states in the Lanczos basis, the strength distributions can be calculated.

In this thesis, we focus on the extension of the (S)RPA to different input single-particle bases and to the inclusion of ground-state correlations from the in-medium similarity renormalization group. We present the electric monopole, dipole, and quadrupole transition strengths of selected oxygen and calcium isotopes and examine the model space convergence for several truncation parameters for different single-particle bases. The second-order RPA shows the pathological behavior of an artificial energy shift to lower energies compared to first-order RPA, independently of the underlying single-particle basis. Moreover, the transition strengths from first- and second-order RPA with matrix elements from the in-medium similarity renormalization group lie at higher energies compared to RPA using standard single-particle bases, which causes the instabilities to disappear. Furthermore, the electric monopole and quadrupole responses of different oxygen and helium isotopes are explored with the Lanczos strength function method comparing different interactions from chiral effective field theory. Due to the sensitivity of strength distributions to the details of the wave function, those observables provide a testing ground for state-of-the-art chiral interactions. Both approaches are compared with regard to fragmentation, fine structure, and their limitations.

In recent years, the uncertainty estimation of theoretical observables has received close attention in order to achieve a better comparability to experimental data. Thus, we present an uncertainty estimation for the running sum of discrete electric monopole, dipole, and quadrupole strengths based on the chiral expansion of the interaction and rooted in Bayesian statistics.

Zusammenfassung

Kollektive Anregungen bieten einen einzigartigen Blickwinkel auf die Kernstruktur und geben entscheidenden Aufschluss über Eigenschaften von Kernen. Übergangsstärken gelten als elegante Observablen zur Untersuchung kollektiver Anregungen. Diese hängen von der exakten Form der Wellenfunktion ab, können in Experimenten gemessen werden und ermöglichen somit eine Überprüfung der angewandten Theorie und der zugrundeliegenden Wechselwirkung.

In dieser Arbeit werden zwei verschiedene Methoden zur Untersuchung kollektiver Anregungen im Energiebereich von niedrig liegenden angeregten Zuständen bis hin zu Riesenresonanzen verwendet. Die Random-Phase-Approximation (RPA), die in der Quantenchemie in den 1950er Jahren entwickelt wurde, hat sich als Standardmethode für die Beschreibung von Übergangsstärken etabliert. Die RPA basiert auf dem Teilchen-Loch-Formalismus, der die Konstruktion von angeregten Zuständen als Teilchen-Loch- und Loch-Teilchen-Anregungen des Grundzustands in Form von Anregungsoperatoren ermöglicht. Diese Operatoren fungieren als Startpunkt für die Herleitung von Bestimmungsgleichungen unter Verwendung des Variationsprinzips und der Bewegungsgleichungsmethode. Eine Erweiterung der RPA zur zweiten Ordnung, die sogenannte second-order RPA (SRPA), umfasst neben den Ein-Teilchen-Ein-Loch-Anregungen bzw. -Abregungen zusätzlich Zwei-Teilchen-Zwei-Loch-Anregungen bzw. -Abregungen. Darüber hinaus beschäftigen wir uns mit einem zweiten Zugang zu kollektiven Anregungen, der das Importance-trunkierte No-Core Schalenmodell (IT-NCSM) mit der Lanczos-Stärkefunktionenmethode von Whitehead kombiniert. Ein Eigenzustand aus einer zuerst durchgeführten IT-NCSM Rechnung sowie die Hamiltonmatrix sind der Startpunkt in diesem Modell. Mithilfe des einfachen Lanczos-Algorithmus wird eine tridiagonale Matrix erzeugt. Diese Matrix wird anschließend unter Verwendung von Standardtechniken diagonalisiert. Die auf diese Weise erhaltenen Eigenwerte und Eigenzustände in der Lanczos-Basis werden herangezogen, um die Stärkeverteilungen zu berechnen.

In der vorliegenden Dissertation befassen wir uns mit der Erweiterung der RPA auf verschiedene Einteilchenbasen und der Einbeziehung von Grundzustandskorrelationen der In-Medium Similarity Renormalization Group. Wir präsentieren elektrische Monopol-, Dipol- und Quadrupolübergangsstärken für ausgewählte Sauerstoff- und Calciumisotope und untersuchen die Modellraumkonvergenz für unterschiedliche Trunkierungsparameter der verschiedenen Einteilchenbasen. Die RPA zweiter Ordnung weist im Vergleich zur RPA erster Ordnung ein pathologisches Verhalten einer Energieverschiebung zu niedrigeren Energien auf, unabhängig von der zugrundeliegenden Einteilchenbasis. Des Weiteren befinden sich die Übergangsstärken aus RPA erster und zweiter Ordnung für Matrixelemente aus der In-Medium Similarity Renormalization Group bei höheren Energien verglichen mit der RPA für üblicherweise verwendete Einteilchenbasen, was zum Verschwinden der zuvor erwähnten Instabilitäten führt. Außerdem werden die elektrischen Monopol- und Quadrupolübergänge verschiedener Sauerstoff- und Heliumisotope mit der Lanczos-Stärkefunktionenmethode untersucht und es werden die Ergebnisse für verschiedene Wechselwirkungen der chiralen effektiven Feldtheorie verglichen. Da die Stärkeverteilungen sensitiv auf Details der Wellefunktionen reagieren, bieten diese Observablen ein Versuchsfeld für moderne chirale Wechselwirkungen. Des Weiteren werden beide Methoden im Hinblick auf Fragmentierung, Feinstruktur und deren Anwendungsgrenzen verglichen.

In den letzten Jahren erfuhr die Unsicherheitsabschätzung theoretischer Observablen ein besonderes Augenmerk, um eine bessere Vergleichbarkeit mit experimentellen Daten zu erzielen.

Daher stellen wir eine Unsicherheitsabschätzung für die aufsummierten diskreten Übergangsstärken der elektrischen Monopol-, Dipol- und Quadrupolübergänge vor, die auf der chiralen Entwicklung der Wechselwirkung sowie der Bayes'schen Statistik beruht.

Contents

Acronyms and Abbreviations

χEFT	chiral effective field theory
CC	coupled cluster
CE	centroid energy
CGC	Clebsch-Gordan coefficient
ECO	excitation creation operator
EFT	effective field theory
EOM	equations of motion
EWSR	energy-weighted sum rule
HF	Hartree-Fock
hp	hole-particle
HO	harmonic oscillator
IT-NCSM	importance-truncated no-core shell model
IM-SRG	in-medium similarity renormalization group
IM-(S)RPA	in-medium (second-order) random-phase approximation
ISM	isoscalar monopole
ISQ	isoscalar quadrupole
IVD	isovector dipole
LEC	low-energy constant
LIT	Lorentz-integral transform
LO	leading order (of chiral effective field theory)
LV	Lanczos vectors
NAT	natural orbitals
NCSM	no-core shell model
NEWSR	non energy-weighted sum rule
NLO	next-to-leading order (of chiral effective field theory)
N^{2}LO	next-to-next-to-leading order (of chiral effective field theory)
N^{3}LO	next-to-next-to-next-to-leading order (of chiral effective field theory)
NN	nucleon-nucleon
NO2B	normal-ordered two-body
pdf	probability distribution function
ph	particle-hole
QCD	quantum chromodynamics
SD	Slater determinant
SRG	similarity renormalization group
(S)RPA	(second-order) random-phase approximation
(S)TDA	(second-order) Tamm-Dancoff approximation

1

Introduction

The aim of *ab initio* nuclear structure theory is the description of nuclear properties, which allows conclusions to be drawn about their structure. This involves not only the description of experimentally measured observables but also the prediction of unknown properties of nuclei, e.g. of exotic nuclei. Those properties include various observables, from ground-state energies and radii to electromagnetic observables, such as magnetic moments and transition strengths. The latter provide access to the investigation of collective excitations and can easily and directly be targeted in experiments. Due to their dependence on the detailed form of the wave function, transition strengths are suitable for testing the applied theory and underlying interactions. The importance of collective excitations is reflected in past and current experiments, targeting giant electric monopole, dipole, and quadrupole resonances [92] as well as the so-called pygmy dipole resonance, the fragmentation and fine structure of giant resonances.

The nuclear Hamiltonian serves as starting point in nuclear structure calculations, as shown in Fig. 1.1. Besides the kinetic energy, the Hamiltonian contains the interaction among nucleons, the constituents of nuclei. There are different possibilities to choose the interaction. Traditional potentials in this field of application were phenomenological for many decades, e.g. the Argonne V18 [21] or the CD-Bonn [26] potentials, and continue to be part of current research with the Daejeon16 interaction [79, 90]. Since phenomenological interactions contain fits to experimental data of nuclei close to the valley of stability, the description of more exotic nuclei breaks down. An almost opposite approach [56, 61] starts with the fundamental constituents of nuclei, quarks, and gluons, and constructs the interaction based on those as degrees of freedom within the framework of quantum chromodynamics (QCD). An established compromise is the utilization of nucleons and pions as degrees of freedom while keeping the chiral symmetry, which is the fundamental symmetry of QCD. This leads to the chiral effective field theory (EFT), which was developed by Weinberg [13] in 1979. Within the framework of chiral EFT [37, 42, 47, 53], two- and many-nucleon interactions as well as electromagnetic current operators [35, 58, 76, 88] are deduced consistently. Those operators are used to determine observables, such as magnetic moments [87].

Besides the interaction, a single-particle basis is set. Typical choices are the harmonic oscillator (HO) basis, the Hartree-Fock (HF) basis or natural orbitals (NAT) [81]. Current research deals among others with the development of new basis sets, as for instance scaled natural orbitals (SNATs) [96].

The demand on nuclear structure theory is in particular the *ab initio* aspect, which comprises controllable approximations only, allowing for a systematical improvement, and the possibility to quantify uncertainties. Various methods have been established in order to solve the many-body eigenvalue problem and to treat ground-state observables. Common approaches, whose range of application across the nuclear chart has benefited from the accompanied further development of computational resources, are for instance the no-core shell model

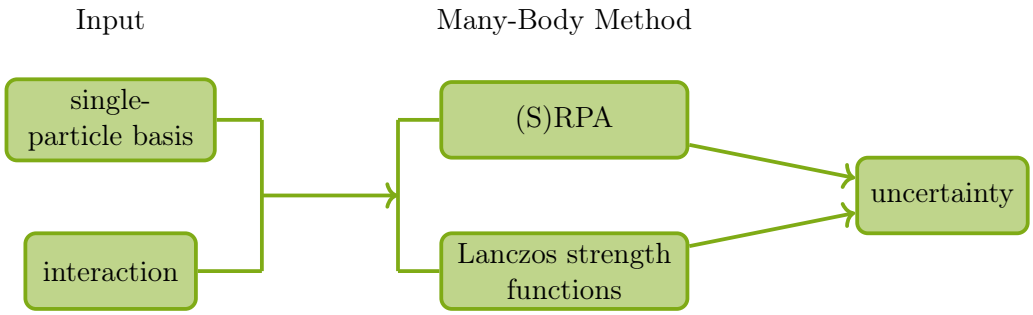

Figure 1.1: Workflow for the determination of collective excitations. Starting with an interaction, a single-particle basis is chosen as input which is followed by the method itself, namely the (S)RPA or the Lanczos strength functions. Completing the investigation, an uncertainty estimation can be done.

(NCSM) [38, 55, 57] for light nuclei up to p-shell and its extension in terms of the importance-truncated NCSM (IT-NCSM) [40], the in-medium similarity renormalization group (IM-SRG) for medium mass nuclei [68] and the combination of the latter two, known as in-medium NCSM (IM-NCSM) [74], the coupled cluster (CC) method and the Green's function Monte Carlo method.

The theoretical access to collective excitations, which was influenced by phenomenological models in the past [32, 51, 62], has shifted towards *ab initio* methods. This has been achieved both by employing interactions from chiral EFT as input [70] and combining existing approaches with *ab initio* methods, for instance the Lorentz-integral transform (LIT) method combined with the CC method [54, 60, 69, 72, 91]. In this thesis, we concentrate on two different approaches, the random-phase approximation (RPA) and extensions thereof as well as a model which applies the Lanczos strength function method together with the IT-NCSM. The RPA was developed by Bohm and Pines [7, 8, 9] in quantum chemistry in the early 1950s. They introduced the RPA for electron gases, attempting the description of interacting electrons and their collective behavior as an example of quantum many-body systems. In the current version, the RPA addresses closed-subshell nuclei across the nuclear chart, especially excited collective states and their transitions [29]. In the past, phenomenological three-body interactions or density-functional theories and, more recently, three-body interactions from chiral EFT were utilized in the RPA framework. The RPA is built on the particle-hole (ph) formalism. Excitation creation operators (ECOs) are constructed in order to describe excited states as $np n$h (de-)excitations of the correlated ground state, which itself contains ph excitations and is, thus, not equal to a single Slater determinant. Taking only 1p1h (de-)excitations in the ECOs into account leads to the first-order RPA, whereas the inclusion of additional 2p2h (de-)excitations defines the second-order RPA (SRPA) [43], which emerges as a natural extension of the RPA. The RPA equations, which are solved in order to obtain the transition strengths, are derived via the equations-of-motion method. They comprise two and four submatrices, respectively, in the case of first- and second-order RPA. These matrices are explicitly determined for a generic single-particle basis. Typically, collective excitations are investigated with RPA regarding Hartree-Fock (HF) basis states [49, 70], labeled as HF-(S)RPA. The IM-(S)RPA, where the (S)RPA is supplemented by IM-SRG transformed matrix elements, includes ground-state correlations in contrast to HF-(S)RPA. A consistent description of collective excitations within this framework is part of current research [98]. The purpose of this thesis is the extension of the (S)RPA framework to natural orbitals, referred to as NAT-(S)RPA, as well as the inclusion of ground-state correlations in the form of IM-SRG transformed matrix elements. The peculiarities of the different RPA-type methods are demonstrated.

The second model, which provides an *ab initio* access to collective excitations, combines the Lanczos strength function method by Whitehead [15] with the IT-NCSM. The state, which enters the Lanczos algorithm [5] as initial state, is a modified ground-state eigenvector obtained from a previous IT-NCSM calculation. The modification consists of the application of the electromagnetic transition operator on that ground-state. In addition to the initial state, also known as pivot state, the Lanczos algorithm requires an input matrix, which is the Hamiltonian in our case. With these ingredients, the Lanczos algorithm produces a tridiagonal matrix, which can be diagonalized with the aid of standard techniques. This procedure yields the eigenvalues and eigenstates in the Lanczos basis. The transition matrix elements, which are required for the transition strengths, are contained therein. The Lanczos strength function method [77, 78] is restricted to light nuclei as it is based on the IT-NCSM.

An uncertainty estimation is advantageous for a complete investigation of observables in order to achieve a meaningful and better comparability with experimental data. Chiral EFT does not only provide interactions and consistent electromagnetic operators, but also the possibility of such an uncertainty estimation in the same framework, which has received close attention in the recent past [95]. An approach for this estimation based on the chiral expansion uses Bayesian statistics to quantify a degree-of-believe interval [80, 82]. This ansatz is transferred to the running sums of discrete electric monopole, dipole, and quadrupole responses.

This thesis is organized in three main parts. Part I deals with the necessary theoretical basics in order to introduce the methods applied throughout the thesis. This involves mathematical concepts in Chapter 2, such as angular momentum coupling, considerations on spherical tensor operators, and the evaluation of many-nucleon matrix elements and, in particular, the particle-hole formalism rooted in second quantization, which the RPA is based on. In Chapter 3, we explain the structure of the nuclear Hamiltonian, which comprises considerations on both the general construction of the interaction in the framework of chiral EFT and the interaction applied throughout the thesis. Moreover, the free-space SRG is introduced and different single-particle bases are discussed. The part is closed with the introduction of electromagnetic multipole operators in Chapter 4, including a macroscopic view on collective excitations. Part II focuses on the methods applied throughout the thesis. In Chapter 5, the RPA equations are derived via the equations-of-motion method and the contained RPA matrices are explicitly deduced for a generic basis. The derivation of the second-order RPA and the explicit determination of its constituent matrices is the essential component of chapter 6. Furthermore, the theoretical principles of transitions in the framework of (S)RPA are presented. The peculiarities of RPA-type methods with different single-particle bases are demonstrated in Chapter 7. To this end the in-medium SRG is introduced. With the Lanczos strength function method, another approach to collective excitations is presented in Chapter 8, including the description of the NCSM as underlying many-body method. Afterwards, we present and discuss the electric monopole, dipole, and quadrupole transition strengths for selected oxygen and calcium isotopes in Part III. The model space convergences of those observables for the different single-particle bases are considered for the RPA and SRPA in Chapter 9 and Chapter 10, respectively. Moreover, the transition strengths from the Lanczos strength function method are studied in Chapter 11 for even-mass helium and oxygen isotopes. The subsequent Chapter 12 treats the uncertainty estimation in general and in particular in the context of running sums. The discussion of the applications in Part III is closed by a comparison of the different *ab initio* methods.

I

Basics

2

Mathematical Concepts

Contents

Mathematical concepts that are applied throughout the thesis, especially in the context of the characteristic coupled (S)RPA matrices, are described in the following chapter. First, the coupling of two and more angular momenta is explained and the corresponding transformation coefficients between a coupled and an uncoupled basis, the so-called Clebsch-Gordan coefficients, $3j$ symbols and $6j$ symbols, respectively, and useful properties thereof are introduced. Furthermore, spherical tensor operators and their properties are described as well as the Wigner-Eckart theorem which states that a spherical tensor can be factorized into a $3j$ symbol and a reduced matrix element which is independent of the projection of the angular momentum. The last section addresses the evaluation of many-nucleon matrix elements. For this purpose, the concepts of normal ordering and contractions are established and combined in the formulation of Wick's theorem. This can be utilized for the evaluation of matrix elements since it reduces a product of arbitrary creation and annihilation operators to a sum of all combinations of operator pairs. This chapter follows [33, 70, 76], if not stated otherwise.

2.1 Angular Momentum Coupling

The coupling (c.f. Refs. [16, 19]) of two angular momenta j_1 and j_2 with corresponding projection quantum number m_1 and m_2, respectively, to a total angular momentum J with projection M leads to the introduction of Clebsch-Gordan coefficients. These are then compared to the $3j$ symbols which show more symmetric properties. Additionally, important properties of the transformation coefficients are listed. Furthermore, the coupling of three angular momenta is briefly discussed in the context of $6j$ symbols.

Clebsch-Gordan Coefficients Dealing with a system composed of multiple angular momenta leaves a choice regarding the basis. For the calculation of matrix elements of a given operator corresponding to different observables, it is possible to use coupled $|(j_1 j_2)JM\rangle$ or uncoupled states $|j_1 m_1, j_2 m_2\rangle$, respectively. Both of these bases form a complete set of two-body states and hence can be transformed into each other. Thus, the identity operator can be expressed as dyadic products of either the coupled or uncoupled basis states

$$\begin{aligned} \mathbb{1} &= \sum_{\substack{j_1,m_1 \\ j_2,m_2}} |j_1 m_1, j_2 m_2\rangle \langle j_1 m_1, j_2 m_2| \\ &= \sum_{\substack{j_1,j_2 \\ J,M}} |(j_1 j_2)JM\rangle \langle (j_1 j_2)JM| \,. \end{aligned} \tag{2.1}$$

This expression can be used to expand either the coupled basis in terms of uncoupled states or vice versa, yielding the following relation

$$\begin{aligned} |(j_1 j_2)JM\rangle &= \sum_{\substack{j_1',m_1 \\ j_2',m_2}} \left|j_1' m_1, j_2' m_2\right\rangle \left\langle j_1' m_1, j_2' m_2\right|(j_1 j_2)JM\rangle \\ &= \sum_{m_1 m_2} |j_1 m_1, j_2 m_2\rangle \langle j_1 m_1, j_2 m_2|(j_1 j_2)JM\rangle \\ &= \sum_{m_1 m_2} \left(\begin{matrix} j_1 & j_2 \\ m_1 & m_2 \end{matrix}\middle| \begin{matrix} J \\ M \end{matrix}\right) |j_1 m_1, j_2 m_2\rangle \,, \end{aligned} \tag{2.2}$$

where the coefficients of the unitary transformation, the so called **Clebsch-Gordan coefficients**, are defined via the scalar product. In the last line of Eq. (2.2), an easily readable notation is introduced. The angular momenta of the individual states j_1 and j_2 are coupled to J, while the projections are coupled to M. Furthermore, these coefficients are chosen to be real and hence

$$\langle j_1 m_1, j_2 m_2 | (j_1 j_2) J M \rangle = \langle (j_1 j_2) J M | j_1 m_1, j_2 m_2 \rangle = \begin{pmatrix} j_1 & j_2 & \Big| & J \\ m_1 & m_2 & \Big| & M \end{pmatrix} . \tag{2.3}$$

The Clebsch-Gordan coefficients obey the orthogonality relation

$$\sum_{m_1 m_2} \begin{pmatrix} j_1 & j_2 & \Big| & J \\ m_1 & m_2 & \Big| & M \end{pmatrix} \begin{pmatrix} j_1 & j_2 & \Big| & J' \\ m_1 & m_2 & \Big| & M' \end{pmatrix} = \delta_{JJ'} \delta_{MM'} \tag{2.4}$$

and the completeness relation

$$\sum_{JM} \begin{pmatrix} j_1 & j_2 & \Big| & J \\ m_1 & m_2 & \Big| & M \end{pmatrix} \begin{pmatrix} j_1 & j_2 & \Big| & J \\ m_1' & m_2' & \Big| & M \end{pmatrix} = \delta_{m_1 m_1'} \delta_{m_2 m_2'} . \tag{2.5}$$

There are two conditions for the Clebsch-Gordan coefficients which have to be satisfied in order to ensure non-zero values: The additivity of the projection quantum numbers $m_1 + m_2 = M$ as well as the triangle inequality, i.e. $|j_1 - j_2| \leqslant J \leqslant j_1 + j_2$. Otherwise the Clebsch-Gordan coefficients are zero.

Changing the signs of the projection quantum numbers produces a phase factor including the angular momenta

$$\begin{pmatrix} j_1 & j_2 & \Big| & J \\ m_1 & m_2 & \Big| & M \end{pmatrix} = (-1)^{j_1 + j_2 - J} \cdot \begin{pmatrix} j_1 & j_2 & \Big| & J \\ -m_1 & -m_2 & \Big| & -M \end{pmatrix} . \tag{2.6}$$

The same phase factor appears when switching the first and second column in a Clebsch-Gordan coefficient, corresponding to a different coupling order

$$\begin{pmatrix} j_1 & j_2 & \Big| & J \\ m_1 & m_2 & \Big| & M \end{pmatrix} = (-1)^{j_1 + j_2 - J} \cdot \begin{pmatrix} j_2 & j_1 & \Big| & J \\ m_2 & m_1 & \Big| & M \end{pmatrix} . \tag{2.7}$$

In both cases, the absolute value of the original Clebsch-Gordan coefficient is unchanged.

In actual calculations, a normalized two-body state comprises not only the angular momentum, but additional quantum numbers, which can be summarized in a collective index a. Thus, for the basis transformation from the uncoupled to the coupled basis, we find

$$|ab\rangle = \sum_{JM} \mathcal{N}_{ab}^{-1}(J) \begin{pmatrix} j_a & j_b & \Big| & J \\ m_a & m_b & \Big| & M \end{pmatrix} |a b, JM\rangle . \tag{2.8}$$

Here we introduced a new notation for the collective index of the quantum numbers a

$$a = (a, m_a) \tag{2.9}$$

where the calligraphic letter a labels all quantum number of the single-particle state a except for the projection m_a. This notation leads to a helpful distinction of coupled and uncoupled basis in further derivations. The order of a coupled two-body state can be changed

$$|(j_2 j_1), JM\rangle = (-1)^{j_1+j_2+J+1} \, |(j_1 j_2) JM\rangle \ . \tag{2.10}$$

The phase factor arises due to the symmetry of the Clebsch-Gordan coefficients.

3j Symbol A more symmetric approach to the Clebsch-Gordan coefficients are the alternatively used **3j symbols** (c.f. Refs. [16, 19]). They are connected via a phase factor

$$\left(\begin{array}{cc|c} j_1 & j_2 & J \\ m_1 & m_2 & M \end{array}\right) = (-1)^{M+j_1-j_2} \, \hat{J} \begin{pmatrix} j_1 & j_2 & J \\ m_1 & m_2 & -M \end{pmatrix} . \tag{2.11}$$

Here, we introduced the factor $\hat{J} = \sqrt{2J+1}$ as a common abbreviation. Again, the angular momenta contained in a $3j$ symbol have to satisfy the triangle inequality and the additivity of the projection quantum numbers to zero, i.e. $m_1 + m_2 + (-M) = 0$, to ensure a non-zero value. The $3j$ symbols convey the same physics as the Clebsch-Gordan coefficients but have the feature of a more symmetric behavior. The change of the sign of the projection quantum numbers results in a symmetric phase factor

$$\begin{pmatrix} j_1 & j_2 & J \\ -m_1 & -m_2 & -M \end{pmatrix} = (-1)^{j_1+j_2+J} \begin{pmatrix} j_1 & j_2 & J \\ m_1 & m_2 & M \end{pmatrix} \tag{2.12}$$

which is similarly obtained while changing the coupling order corresponding to an odd number of permutations of the columns

$$\begin{pmatrix} j_2 & j_1 & J \\ m_2 & m_1 & M \end{pmatrix} = (-1)^{j_1+j_2+J} \begin{pmatrix} j_1 & j_2 & J \\ m_1 & m_2 & M \end{pmatrix} . \tag{2.13}$$

Thus, an even number of permutations of the columns leaves the value of the $3j$ symbol unaltered.

6j Symbol Coupling more than two angular momenta is more complicated since there exist more options for the coupling order. Omitting the details which can be found in Refs. [16, 33], the coefficients of the unitary transformation between three different sets of basis states are identified as **6j symbols**. In this case, we consider a basis transformation from an uncoupled basis to a coupled basis, in which all involved angular momenta j_1, j_2 and j_3 are coupled to a total angular momentum J. They are connected to four $3j$ symbols and and a phase factor via the explicit expression

$$\begin{aligned} \begin{Bmatrix} j_1 & j_2 & j_{12} \\ j_3 & J & j_{23} \end{Bmatrix} = \sum_{\substack{m_1 m_2 m_3 \\ m_{12} m_{23} M}} (-1)^{j_3+J+j_{23}-m_3-M-m_{23}} \begin{pmatrix} j_1 & j_2 & j_{12} \\ m_1 & m_2 & m_{12} \end{pmatrix} \begin{pmatrix} j_1 & J & j_{23} \\ m_1 & -M & m_{23} \end{pmatrix} \\ \times \begin{pmatrix} j_3 & j_2 & j_{23} \\ m_3 & m_2 & -m_{23} \end{pmatrix} \begin{pmatrix} j_3 & J & j_{12} \\ -m_3 & M & m_{12} \end{pmatrix} . \end{aligned} \tag{2.14}$$

Again, there are triangular conditions and symmetry relations resulting from the definition of the $3j$ symbols included in this notation. For example, changing two columns recovers the same value of the $6j$ symbol

$$\begin{Bmatrix} j_1 & j_2 & j_{12} \\ j_3 & J & j_{23} \end{Bmatrix} = \begin{Bmatrix} j_2 & j_1 & j_{12} \\ J & j_3 & j_{23} \end{Bmatrix} = \dots . \tag{2.15}$$

This additionally holds for the change of two angular momenta of the top row with two of them of the bottom row in any two columns

$$\begin{Bmatrix} j_1 & j_2 & j_{12} \\ j_3 & J & j_{23} \end{Bmatrix} = \begin{Bmatrix} j_3 & J & j_{12} \\ j_1 & j_2 & j_{23} \end{Bmatrix} = \dots . \tag{2.16}$$

These relations are of importance for the determination of characteristic matrices within the (S)RPA framework due to the requirement of coupled matrix elements in actual calculations.

2.2 Spherical Tensor Operators and Wigner-Eckart-Theorem

Actual calculations of matrix elements can benefit from the special transformation pattern of spherical tensor operators. Thus, certain operators used for the calculation of observables are reformulated in terms of spherical tensor operators, for example the electromagnetic operators. Furthermore, the specific transformation rules can be exploited within the particle-hole formalism (c.f. Sec. 2.3.2) concerning the creation and annihilation operators. This approach leads to an efficient calculation of observables and to a reduction of computational demand.

An operator $\hat{T}_{JM}$ is called spherical tensor operator with rank J and projection quantum number M if the following commutation relations are fulfilled

$$\left[\hat{J}_z, \hat{T}_{JM}\right] = M\hbar\, \hat{T}_{JM} \tag{2.17}$$

$$\left[\hat{J}_\pm, \hat{T}_{JM}\right] = \hbar\sqrt{(J \pm M + 1)\,(J \mp M)}\, \hat{T}_{JM\pm1}\,. \tag{2.18}$$

Here, $\hat{J}_z$ denotes the z-component of the total angular momentum operator and $\hat{J}_\pm = \hat{J}_x \pm i\hat{J}_y$ the related ladder operators which are defined as linear combinations of the remaining components of the angular momentum operator. The coupled tensor product of spherical tensor operators is defined as

$$\hat{T}_{JM} = \left[\hat{T}_{j_1}\hat{T}_{j_2}\right]_{JM} = \sum_{m_1,m_2} \left(\begin{matrix} j_1 & j_2 \\ m_1 & m_2 \end{matrix}\middle| \begin{matrix} J \\ M \end{matrix}\right) \hat{T}_{j_1 m_1}\hat{T}_{j_2 m_2}\,. \tag{2.19}$$

The spherical tensors $\hat{T}_{j_1}$ and $\hat{T}_{j_2}$ have rank j_1 and j_2, respectively. The components of the spherical tensors, $\hat{T}_{j_1 m_1}$ and $\hat{T}_{j_2 m_2}$, are connected via a Clebsch-Gordan coefficient to $\hat{T}_{JM}$, which are the $2M + 1$ components of the spherical tensor $\hat{T}_J$ of rank J.

With the aid of the Wigner-Eckart theorem [1, 4], the calculation of matrix elements of spherical tensor operators is simplified through the expression as reduced matrix elements. The theorem states that each of the spherical tensor operator's matrix elements is split into a reduced matrix element and a geometrical factor including a phase and a $3j$ symbol. The

reduced matrix element, indicated by $\langle \cdot || \cdot || \cdot \rangle$, is independent of all projection quantum numbers and still comprises the relevant physics. It holds

$$\left\langle \alpha, jm \middle| \hat{T}_{JM} \middle| \alpha', j'm' \right\rangle = (-1)^{j-m} \begin{pmatrix} j & J & j' \\ -m & M & m' \end{pmatrix} \left\langle \alpha, j \middle|\middle| \hat{T}_J \middle|\middle| \alpha', j' \right\rangle . \tag{2.20}$$

Here α and α', respectively, serve as collective indices and represent all remaining quantum numbers except for the angular momentum and its projection. The natural selection rules of the $3j$ symbol are transferred to the spherical tensor operator. Matrix elements with arbitrary m and m' can be calculated based on matrix elements with specific projection quantum numbers via the Wigner-Eckart theorem. More details on the explicit derivation of spherical tensor operators and their properties can be found in Ref. [33].

2.3 Evaluation of Many-Nucleon Matrix Elements

In order to evaluate many-nucleon matrix elements, either the traditional concept of considering explicit wave functions or the alternative of the occupation number representation can be applied. The latter concept is an abstraction and offers a powerful, efficient, and more elegant formalism for actual calculations. It can handle different particle numbers by defining particle creation and annihilation operators for which the anticommutation relations hold due to the fermionic nature of the nucleons. We first briefly introduce the basic concepts of operators and many-body states in the framework of second quantization and continue with the particle-hole formalism, which is the starting point for the random-phase approximation in Chapter 5. Afterwards, the concepts of normal ordering, contractions and Wick's theorem as a powerful tool for the actual calculation of many-body matrix elements are discussed. For this section, Refs. [41, 93] are used additionally.

2.3.1 Second Quantization

In the framework of second quantization, the fermionic creation operator $\hat{a}^\dagger$ and its Hermitian conjugate, the annihilation operator $\hat{a}$, are defined as

$$\begin{aligned} \hat{a}_i^\dagger \left|0\right\rangle &= \left|i\right\rangle \\ \hat{a}_j \left|i\right\rangle &= \delta_{ij} \left|0\right\rangle , \end{aligned} \tag{2.21}$$

with the particle vacuum $|0\rangle$, which does not contain any particles, and the single-particle state $|i\rangle$ with the collective index i for all quantum numbers. Thus, a particle with quantum numbers i is created in the so-called Fock space by applying $\hat{a}_i^\dagger$ whereas the annihilation operator $\hat{a}_j$ removes a particle in the state j if this state is occupied. Otherwise, the application of the annihilation operator on an unoccupied state leads to zero. For the fermionic creation and annihilation operators, the anticommutation relations

$$\begin{aligned} \left\{ \hat{a}_i, \hat{a}_j^\dagger \right\} &= \delta_{ij} \\ \left\{ \hat{a}_i^\dagger, \hat{a}_j^\dagger \right\} &= \{ \hat{a}_i, \hat{a}_j \} = 0 \end{aligned} \tag{2.22}$$

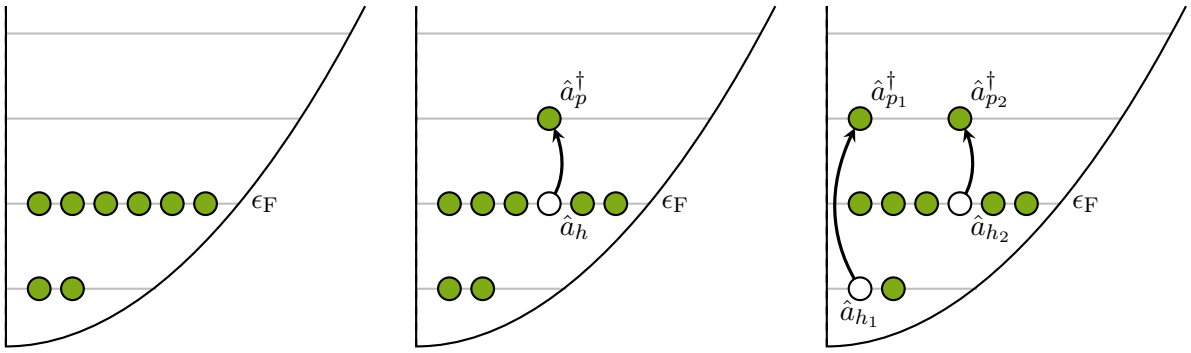

(a) Ground state of a nucleus **(b)** 1p1h excitation **(c)** 2p2h excitation

Figure 2.1: In Fig. (a), the ground state of a nucleus with 8 neutrons is shown. Fig. (b) illustrates a particle in the state $|h\rangle$ below the Fermi energy ϵ_F which is canceled while another state $|p\rangle$ with $\epsilon > \epsilon_\mathrm{F}$ is populated. This is the so-called 1p1h excitation described by the creation-annihilation operator pair $\hat{a}_p^\dagger \hat{a}_h$. In Fig. (c), two particles are excited. Thus, this process corresponds to a 2p2h excitation described by the operators $\hat{a}_{p_1}^\dagger \hat{a}_{h_1} \hat{a}_{p_2}^\dagger \hat{a}_{h_2}$.

hold. A fermionic A-body state, which is the antisymmetrized product state of A single-particle states, is a so-called Slater determinant and can be expressed in this framework as

$$|\mathrm{SD}\rangle = |i_1 i_2 \cdots i_A\rangle = \hat{a}_{i_1}^\dagger \hat{a}_{i_2}^\dagger \cdots \hat{a}_{i_A}^\dagger |0\rangle = \prod_{n=1}^{A} \hat{a}_{i_n}^\dagger |0\rangle \,. \tag{2.23}$$

This means that any A-body state can be represented in terms of creation operators that act on the vacuum state. Besides many-body states, a description of operators in second quantization, as for instance the Hamiltonian, is possible. General one- and two-body operators in second quantization are given by

$$\hat{T} = \sum_{ij} \langle i| \hat{T} |j\rangle \, \hat{a}_i^\dagger \hat{a}_j \qquad\qquad \hat{V} = \sum_{ijkl} \langle ij| \hat{V} |kl\rangle \, \hat{a}_i^\dagger \hat{a}_j^\dagger \hat{a}_l \hat{a}_k \,. \tag{2.24}$$

The explicit form of the Hamiltonian used in this thesis is discussed in Chapter 3.

2.3.2 Particle-Hole Formalism

The basis states within the random-phase approximation are constructed through particle-hole (ph) excitations of a single Slater determinant $|\mathrm{SD}\rangle$, that is for example the Hartree-Fock ground state $|\mathrm{HF}\rangle$. In second-quantized form, the operators associated with these ph excitations are represented by creation and annihilation operators. In Fig. 2.1, the ground-state configuration, the lowest possible excitation and an additional higher excitation are shown in the ph formalism for a nucleus with 8 neutrons. In the ground state, the single-particle states are filled up to the Fermi level with energy ϵ_F. Hence, the Fermi energy corresponds to the energy of the highest state that is still occupied. The single-particle states below the Fermi energy, that means the populated states, are per definition hole states while the particle states are unoccupied single-particle states with $\epsilon > \epsilon_\mathrm{F}$. The definition and notation of particle, hole and any single-particle states are summarized in Tab. 2.1.

For a ph or 1p1h (1-particle-1-hole) excitation, a particle in the initial state $|h\rangle$ is annihilated and simultaneously a particle in the unoccupied state $|p\rangle$ is created. Mathematically, this is

realized by the application of the annihilation operator $\hat{a}_h$ and the creation operator $\hat{a}_p^\dagger$ to the ground state $|\mathrm{HF}\rangle$

$$|ph\rangle = \hat{a}_p^\dagger \hat{a}_h \, |\mathrm{HF}\rangle \ . \tag{2.25}$$

In the case depicted in Fig. 2.1(b), one particle is excited from the initial state $|h\rangle$ to the final state $|p\rangle$, thus it is a 1p1h excitation. Applying more than one creation-annihilation-pair to an initial state yields a higher-order excitation, such as 2p2h, 3p3h up to an ApAh excitation. The process of a 2p2h excitation as illustrated in Fig. 2.1(c) can be expressed as

$$|p_1 h_1, p_2 h_2\rangle = \hat{a}_{p_1}^\dagger \hat{a}_{h_1} \hat{a}_{p_2}^\dagger \hat{a}_{h_2} \, |\mathrm{HF}\rangle \ . \tag{2.26}$$

The energy that is needed within the process of a ph excitation corresponds to the difference of the involved single-particle energies ϵ_p and ϵ_h of the particle and hole state, respectively,

$$\epsilon_{ph} = \epsilon_p - \epsilon_h. \tag{2.27}$$

Instead of a ph excitation, the reversed process of a hole-particle (hp) excitation is non-vanishing but only if the corresponding states are occupied or unoccupied, respectively. A ph excitation is feasible for a Hartree-Fock ground state as reference state whereas a hp excitation has the constraint of an occupied particle state and an unoccupied hole state, which is not the case for the HF ground state. In the case of a hp excitation, a particle in the state $|p\rangle$ above the Fermi energy is annihilated, while one in a state $|h\rangle$ with $\epsilon < \epsilon_\mathrm{F}$ is created. Mathematically, a creation-annihilation operator pair of the type $\hat{a}_h^\dagger \hat{a}_p$ is applied

$$|\mathrm{HF}\rangle = \hat{a}_h^\dagger \hat{a}_p \, |ph\rangle \, . \tag{2.28}$$

The amount of energy for a hp excitation is equivalent to Eq. (2.27), however this energy is released contrary to ph excitations, i.e. $\epsilon_{hp} = -\epsilon_{ph}$. Thus, an hp excitation is identified with a de-excitation. Higher order de-excitations are naturally possible as long as all involved hole states are unoccupied and all involved particle states are occupied.

In the particle-hole formalism, all (de-)excitations are performed by pairs of fermionic creation-annihilation operators $\hat{a}_p^\dagger \hat{a}_h$ or $\hat{a}_h^\dagger \hat{a}_p$. In order to provide a clear distinction between particle and hole states, a subshell closure must exist, i.e. all j orbitals are completely (un-)occupied. Otherwise, if the orbitals are partially populated, both processes of (de-)excitation can occur and an unambiguous description is not possible anymore.

type of states	single-particle energy	definition	notation
particle states	$\epsilon_p > \epsilon_\mathrm{F}$	$\hat{a}_p^\dagger \, \|\mathrm{HF}\rangle$	$\|p\rangle \, , \|p'\rangle$,...
hole states	$\epsilon_h < \epsilon_\mathrm{F}$	$\hat{a}_h^\dagger \, \|\mathrm{HF}\rangle$	$\|h\rangle \, , \|h'\rangle$,...
general single-particle states	ϵ_i	$\hat{a}_i^\dagger \, \|\mathrm{HF}\rangle$	$\|i\rangle \, , \|j\rangle \, ,..$

Table 2.1: Terminology for different types of single-particle states.

2.3.3 Normal Ordering

The first step for the evaluation of matrix elements of an operator describing an observable in the context of second quantization is the so-called normal-ordered product, where the creation and annihilation operators contained in the considered operator are rearranged. For the product

$$\Pi = \Pi\left(\{\hat{a}_i\}, \{\hat{a}_j^\dagger\}\right) \tag{2.29}$$

of a set of creation operators $\{\hat{a}_j^\dagger\}$ and annihilation operators $\{\hat{a}_i\}$ with respect to a certain reference state $|\psi_0\rangle$, we can define the normal-ordered product as

$$\mathcal{N}[\Pi] = (-1)^P \Pi\,(\text{creation} \times \text{annihilation}) \tag{2.30}$$

with P as the number of transpositions of two operators in order to arrange them in such a way that all creation operators are placed left to the annihilation operators. Normal ordering is a linear operation. The definition of normal-ordered products is not unique, since the order of the creation and annihilation operators, respectively, is not fixed and can be permuted in agreement with the anticommutation relations (2.22), which is mirrored in the phase factor. Nevertheless, we assume that all these permutations with corresponding phase factor are equivalent.

2.3.4 Contractions

For two operators $\hat{A}$ and $\hat{B}$, which can be creation or annihilation operators, the contraction is defined as

$$\overbrace{\hat{A}\hat{B}} = \hat{A}\hat{B} - \mathcal{N}[\hat{A}\hat{B}]\,. \tag{2.31}$$

The contraction of two creation or annihilation operators is zero, respectively. More generally, if two operators anticommutate, i.e. $\{\hat{A}, \hat{B}\} = 0$, their contraction vanishes, i.e. $\overbrace{\hat{A}\hat{B}} = 0$. Furthermore, the expectation value of the product of two operators $\hat{A}\hat{B}$, which are both defined with respect to the reference state $|\psi_0\rangle$, is identical to their contraction

$$\langle\psi_0|\,\hat{A}\hat{B}\,|\psi_0\rangle = \langle\psi_0|\,\overbrace{\hat{A}\hat{B}}\,|\psi_0\rangle = \overbrace{\hat{A}\hat{B}}\,, \tag{2.32}$$

since the expectation value of the normal-ordered product is zero and the contraction itself is a number.

In the framework of the ph formalism, the only non-vanishing contractions are

$$\begin{aligned} \overbrace{\hat{a}_i^\dagger \hat{a}_j} &= n_i \delta_{ij}\,, \\ \overbrace{\hat{a}_i \hat{a}_j^\dagger} &= \delta_{ij}(1 - n_i) \end{aligned} \tag{2.33}$$

with the occupation number

$$n_i = \begin{cases} 1 & \text{if } i \text{ represents a hole state} \\ 0 & \text{if } i \text{ represents a particle state}\,, \end{cases} \tag{2.34}$$

which can be summarized to the following contributions

$$\begin{aligned} \hat{a}_h^{\dagger}\hat{a}_{h'} &= \delta_{hh'}\,, \\ \hat{a}_p\hat{a}_{p'}^{\dagger} &= \delta_{pp'}\,. \end{aligned} \tag{2.35}$$

Contractions of mixed ph configurations do not occur due to the disjoint ph partitioning, i.e. $\delta_{ph} = 0$. These relations will be useful for the derivation of parts of the RPA equations in Sec. 5.2.

2.3.5 Wick's Theorem

The normal ordering of contractions can be expressed as the product of the contracted pairs, the normal-ordered product of the remaining operators and a phase factor, i.e.

$$\mathcal{N}[\hat{A}\hat{B}\hat{C}\hat{D}\hat{E}\cdots\hat{X}\hat{Y}\hat{Z}] = (-1)^P \hat{B}\hat{E}\hat{D}\hat{Y}\mathcal{N}[\hat{A}\hat{C}\cdots\hat{X}\hat{Z}] \tag{2.36}$$

with the number of operator transpositions P required for the permutation of the contractions to the left of the normal-ordered product. Here, the linearity of normal-ordered products was exploited.

With the definition for normal ordering, contractions and their combination, Wick's theorem [6] is formulated as

$$\begin{aligned}
\hat{A}\hat{B}\hat{C}\hat{D}\hat{E}\hat{F}\cdots = {} & \mathcal{N}[\hat{A}\hat{B}\hat{C}\hat{D}\hat{E}\hat{F}\cdots] \\
& + \sum_{\text{single contractions}} \mathcal{N}[\overbrace{\hat{A}\hat{B}}\hat{C}\hat{D}\hat{E}\hat{F}\cdots] \qquad \text{(all other 1-contractions)} \\
& + \sum_{\text{double contractions}} \mathcal{N}[\overbrace{\hat{A}\hat{B}}\overbrace{\hat{C}\hat{D}}\hat{E}\hat{F}\cdots] \qquad \text{(all other 2-contractions)} \\
& + \ldots \\
& + \text{all normal-ordered terms with } n \text{ contractions} \\
& + \ldots \\
& + \text{all terms with all pairs contracted.}
\end{aligned} \tag{2.37}$$

Considering Wick's theorem and additionally the vanishing expectation values of normal-ordered products, matrix elements can be evaluated via

$$\langle\psi_0|\,\hat{A}\hat{B}\hat{C}\hat{D}\hat{E}\hat{F}\cdots|\psi_0\rangle = \sum_{\substack{\text{all contraction} \\ \text{combinations}}} (-1)^c \text{ product with all pairs contracted} \tag{2.38}$$

with c as the number of contraction line crossings. Therefore, the expectation value of a product of arbitrary creation and annihilation operators can be reduced to a sum of all possible contraction pairs. An application of Wick's theorem in order to determine the matrix elements of characteristic matrices in the framework of (S)RPA can be found in Sec. 5.2.

3

Nuclear Many-Body Problem

Contents

Nuclear structure theory aims for the solution of the stationary many-body Schrödinger equation

$$\hat{H}\,|\psi_n\rangle = E_n\,|\psi_n\rangle \tag{3.1}$$

in order to get information about the nucleus, as for instance energies, radii, or electromagnetic observables as expectation values with respect to the eigenstates. Here, $\hat{H}$ denotes the Hamiltonian, E_n labels the energy eigenvalues and $|\psi_n\rangle$ the eigenstates. Techniques for an improvement of the convergence behavior are introduced in this chapter. We start with the Hamiltonian as the core of the many-body problem with the main aspects on chiral effective field theory (EFT) and explain the construction of the interaction within this framework. Additionally, the normal-ordered two-body approximation (NO2B) which provides a partial inclusion of three-body aspects at two-body level without explicitly taking them into account is motivated. Furthermore, different single-particle bases are discussed, in particular the Hartree-Fock (HF) basis resulting from the HF approximation as well as the natural orbitals. In order to reduce the model-space size in many-body calculations, the so-called similarity renormalization group (SRG) method for a pre-diagonalization of the Hamiltonian is discussed. If not stated otherwise, Refs. [14, 64, 70, 76, 78] are utilized.

3.1 The Nuclear Hamiltonian

The starting point for nuclear structure calculations is the initial Hamiltonian that is, in combination with the employed many-body method, responsible for the accuracy of such a calculation. The translationally invariant nuclear Hamiltonian

$$\begin{aligned}\hat{H} &= \hat{T} + \hat{V}_{\mathrm{NN}} + \hat{V}_{\mathrm{3N}} + \dots \\ &= \frac{1}{A}\sum_{i<j}^{A}\frac{\left(\hat{\vec{p}}_i - \hat{\vec{p}}_j\right)^2}{2m} + \sum_{i<j}^{A}\hat{V}_{ij}^{\mathrm{NN}} + \sum_{i<j<k}^{A}\hat{V}_{ijk}^{\mathrm{3N}} + \dots\end{aligned} \tag{3.2}$$

contains the intrinsic kinetic energy $\hat{T}$ and the interaction between the nucleons, namely the two-body $\hat{V}_{\mathrm{NN}}$, three-body $\hat{V}_{\mathrm{3N}}$ and higher-order interactions, respectively, that occur in a hierarchical order. In actual calculations, the Hamiltonian usually includes all contributions up to three-body level, while all higher-order contributions are neglected since they are too computationally demanding and are considered to be small [52]. For the explicit evaluation of matrix elements, the second quantization is an established method as discussed in Sec. 2.3. The Hamiltonian with three-body interaction in second quantization is given by

$$\begin{aligned}\hat{H} &= \hat{T} + \hat{V}_{\mathrm{NN}} + \hat{V}_{\mathrm{3N}} \\ &= \sum_{i,i'} t_{i,i'}\hat{c}_i^\dagger\hat{c}_{i'} + \frac{1}{4}\sum_{ij,i'j'}\bar{v}_{ij,i'j'}\hat{c}_i^\dagger\hat{c}_j^\dagger\hat{c}_{j'}\hat{c}_{i'} + \frac{1}{36}\sum_{ijk,i'j'k'}\bar{v}_{ijk,i'j'k'}^{\mathrm{3N}}\hat{c}_i^\dagger\hat{c}_j^\dagger\hat{c}_k^\dagger\hat{c}_{k'}\hat{c}_{j'}\hat{c}_{i'}\end{aligned} \tag{3.3}$$

with the matrix elements of the kinetic energy $t_{i,i'} = \langle i|\,\hat{T}\,|i'\rangle$. The antisymmetrized two-nucleon and three-nucleon interaction matrix elements are given by $\bar{v}_{ij,i'j'}$ and $\bar{v}_{ijk,i'j'k'}^{\mathrm{3N}}$, re-

spectively. The antisymmetry is mirrored in the following permutation of indices

$$\bar{v}_{ij,i'j'} = -\bar{v}_{ji,i'j'} = -\bar{v}_{ij,j'i'} = \bar{v}_{ji,j'i'}. \tag{3.4}$$

The summation indices in Eq. (3.3) include the complete single-particle basis which is still an arbitrary choice. Typical basis sets are for instance the harmonic oscillator (HO) basis, the Hartree-Fock (HF) basis, or the natural orbitals (NAT). Each single-particle basis has its own advantages which are discussed in Sec. 3.3.

The nuclear interactions which are based on chiral effective field theory (EFT) are a current research topic [85, 88]. Chiral EFT [47] provides a systematic low-momentum expansion of the interaction. This gives the opportunity for a theoretical uncertainty estimation for observables via exploiting the hierarchical order of the expansion, additionally allowing a systematic improvement. An approach for this uncertainty estimation based on the chiral expansion uses Bayesian statistics and is discussed in Sec. 12.1. Besides the two-and many-nucleon interactions, consistent electromagnetic one- and two-body current operators [39, 58, 59, 75, 88] can be deduced within the same framework. The systematic expansion of the current operators acts as input for the evaluation of electromagnetic observables such as transitions strengths, c.f. Sec. 4.2.

3.1.1 Effective Field Theory and Chiral Symmetry

The aim of *ab initio* nuclear structure theory is the description of nuclei, their structure and different properties through predicting observables such as electromagnetic observables, ground-state and excited-state energies, radii or collective excitations. Nucleons interact via the strong interaction whose fundamental degrees of freedom are quarks and gluons. The underlying theory that describes the strong interaction is quantum chromodynamics (QCD). Only for high energies the coupling constant becomes small, leading to the opportunity of a perturbative treatment of the strong interaction. This phenomenon is called asymptotic freedom. But for nuclear structure theory, the low-energy regime is of interest, where the QCD is non-perturbative. Therefore, an effective field theory is constructed as an alternative, which was developed by Weinberg [13, 18] in 1979 and holds for a certain energy scale. Within this theory, nucleons and pions are treated as degrees of freedom in combination with chiral symmetry which is the fundamental symmetry of QCD. Thus, this approach is the so-called chiral effective field theory (χEFT). Consistent two- and many-nucleon interactions as well as electromagnetic current operators are supplied in chiral EFT in terms of a systematic low-momentum expansion. Part of the expansion coefficients are the so-called low-energy constants (LECs), that are determined by fitting to experimental scattering data.

Breakdown Scale For the validity range of this effective field theory, a separation of scales is necessary, which emerges naturally as a large energy gap in the hadron spectrum between the pions with a mass of $m_\pi \simeq 135 - 140$ MeV [48] and the heavier ρ-meson, which has a mass of $m_\rho = 775$ MeV [48]. Thus, it is justified to include only nucleons and pions as degrees of freedom for the low energy regime. The mass of the ρ-meson defines the breakdown scale $\Lambda_\chi \sim m_\rho$. For energy ranges smaller than the breakdown scale, chiral EFT can be applied and thus, nuclei and their properties can be described. Upon reaching the breakdown scale, chiral EFT becomes invalid and another EFT needs to be constructed.

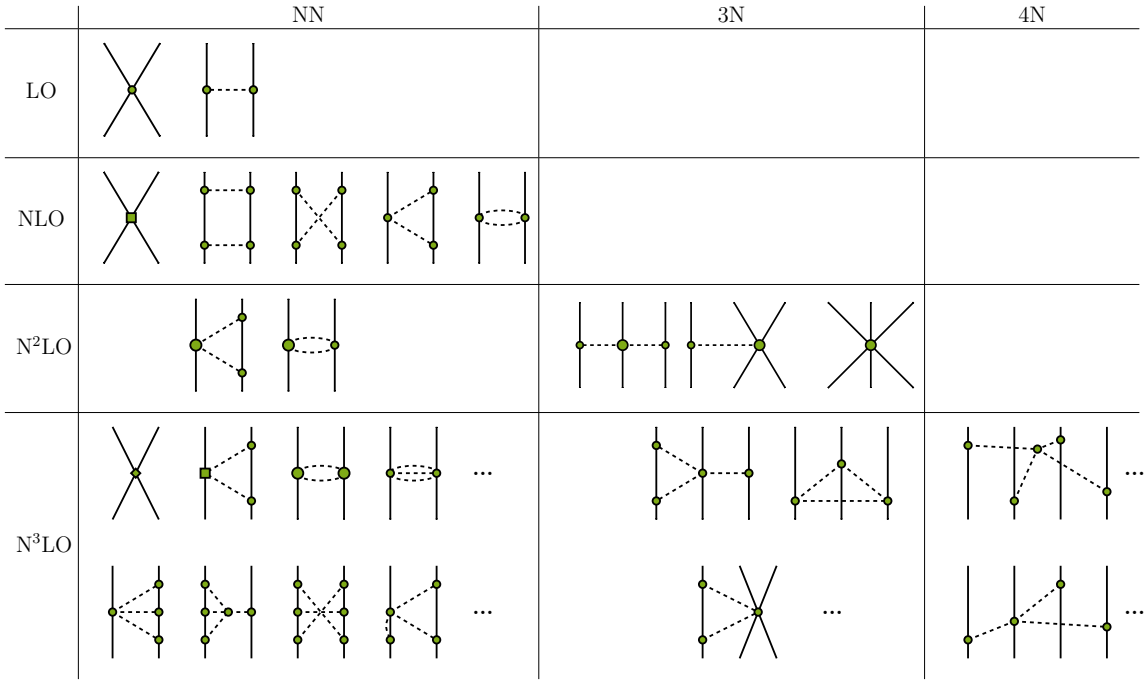

Figure 3.1: Hierarchical order of the chiral two-, three- and four-body interaction. Nucleons are depicted as solid lines whereas pions are represented as dashed lines.

Chiral Perturbation Theory The constructed most general Lagrangian that includes nucleons and pions as fundamental degrees of freedom and chiral symmetry can be expanded pertubatively, leading to the nuclear interaction. Information on nucleon-nucleon, pion-nucleon or pion-pion interactions as well as contact interactions enter the Lagrangian. Including all infinitely possible interactions is unfeasible in actual calculations. Thus, the interaction is expanded instead, using the small quantity $\left(\frac{Q}{\Lambda_\chi}\right)^n$ with the nucleon momentum Q, the breakdown scale Λ_χ, and the order n. The latter is defined by the Weinberg power counting [18] and low orders of the interaction are assumed to be more relevant, even though the sorting with respect to the chiral order is non-trivial. As mentioned before, experimental data is used for the determination of the LECs that enter the expansion coefficients. With these assumptions, the interaction is organized by the order n and the number of interacting nucleons leading to a hierarchical order as depicted in a diagrammatic way in Fig. 3.1. The interaction based on chiral EFT is shown for the two-, three- and four-body interactions for several orders n. The leading order (LO) is related to $n = 0$, whereas the next-to leading order (NLO) corresponds to $n = 2$ and the next-to-next-to leading order (N^2LO) to $n = 3$. Due to symmetry reasons, there are no contributions for $n = 1$. Different vertices represent different interactions, for instance contact interaction. By including higher orders of the interaction in practical many-body calculations, chiral EFT provides a way for systematic improvement and additionally the opportunity of the estimation of uncertainties based on the chiral order. Furthermore, a consistent discussion of many-nucleon interactions as well as electromagnetic current operators at different chiral orders can be done in the same framework.

Interactions for Applications Different chiral interactions are employed in this thesis. In the RPA framework, we mainly use non-local nucleon-nucleon (NN) interaction developed by Entem, Machleidt and Nosyk [73] plus consistent three-nucleon (3N) interactions by Hüther et al. [85] up to N^3LO with a cutoff of 500 MeV. The LECs are optimized to the ground-state

energies of ^{16}O and ^{3}H. This interaction reproduces energies and radii for p-shell nuclei up to the nickel isotopic chain and provides different chiral orders, which allow for an uncertainty estimation.

In the Lanczos framework, we additionally use the so-called N^{2}LO$_{\text{sat}}$ interaction, derived by Ekström et al. [66]. This interaction comprises NN and 3N forces at N^{2}LO and the LECs are simultaneously fitted for the overall NN+3N interaction. The experimental data for the fitting procedure includes, besides NN scattering data, binding energies and charge radii of few-nucleon systems and selected carbon and oxygen isotopes. This standard interaction provides ground-state energies and radii of *sd*-shell nuclei comparable with experimental data.

3.1.2 Normal-Ordered Two-Body Approximation

The following section is based on Refs. [52, 70, 78]. In principle, the accuracy of calculations of observables increases with the inclusion of higher-order interaction contributions in the Hamiltonian, leading additionally to a more consistent description. For most applications, three-body interactions are in fact of importance [28, 34, 44]. The problem of including full 3N interactions explicitly is the higher computational cost, which often leads to unfeasible calculations, especially in heavier nuclei. Thus, the aim of an approximation is the systematic reduction of the rank of a considered operator while maintaining most information about the system. This is the idea of the so-called normal-ordered two-body approximation (NO2B).

With the aid of the Wick theorem (2.37), a product of $2n$ operators can be split into components of normal-ordered products of operators including 0 to n contractions. Every contraction in the operator product leads to a rank that is one less than for the product containing no contractions, since the contraction of two operators yields a scalar.

We now want to motivate the application of the NO2B to the Hamiltonian. In general, the three-body interaction

$$\hat{V}_{\text{3N}} = \frac{1}{36} \sum_{ijk,i'j'k'} \bar{v}^{\text{3N}}_{ijk,i'j'k'} \hat{a}^\dagger_i \hat{a}^\dagger_j \hat{a}^\dagger_k \hat{a}_{k'} \hat{a}_{j'} \hat{a}_{i'} \tag{3.5}$$

given in Eq. (3.3) can alternatively be separated into terms corresponding to the number of contained contractions and thus with different rank

$$\hat{V}_{\text{3N}} = \hat{V}^{\text{N0B}}_{\text{3N}} + \hat{V}^{\text{N1B}}_{\text{3N}} + \hat{V}^{\text{N2B}}_{\text{3N}} + \hat{V}^{\text{N3B}}_{\text{3N}} \tag{3.6}$$

according to Wick's theorem. In the normal-ordered framework, which is so far identical to the standard representation, the three-body interaction is then approximated by the removal of the explicit 3B operator $\hat{V}^{\text{N3B}}_{\text{3N}}$, leading to

$$\hat{V}_{\text{3N}} \approx \hat{V}^{\text{N0B}}_{\text{3N}} + \hat{V}^{\text{N1B}}_{\text{3N}} + \hat{V}^{\text{N2B}}_{\text{3N}} \,. \tag{3.7}$$

Within the NO2B, effects of the 3N interaction are shifted to lower rank operators resulting in a compromise of the same computational effort as for 2N calculations and the use of an explicit 3N interaction. Additionally, the formalism is unaltered while including more contributions and, thus, more information within the NO2B. Previous work has shown NO2B to be a good approximation [52, 67].

3.2 Free-Space Similarity Renormalization Group

The free-space similarity renormalization group (SRG) [65], following Refs. [70, 76, 88], is an approach for the improvement and acceleration of the convergence properties with respect to model-space size in nuclear many-body calculations. The aim of SRG is a softened Hamiltonian achieved via a prediagonalization. This is beneficial since for larger dimension, convergence is not guaranteed.

Mathematically, a continuous unitary transformation of the bare Hamiltonian $\hat{H}_0$ or any arbitrary operator $\hat{O}_0$ is given by

$$\hat{H}_\alpha = \hat{U}_\alpha^\dagger \hat{H}_0 \hat{U}_\alpha \,, \qquad \hat{O}_\alpha = \hat{U}_\alpha^\dagger \hat{O}_0 \hat{U}_\alpha \,. \tag{3.8}$$

Here, α denotes the flow parameter. The starting point of the derivation of the SRG transformation is the derivative of the evolved Hamiltonian with respect to α

$$\frac{\mathrm{d}\hat{H}_\alpha}{\mathrm{d}\alpha} = \frac{\mathrm{d}}{\mathrm{d}\alpha}\left(\hat{U}_\alpha^\dagger \hat{H}_0 \hat{U}_\alpha\right) = \frac{\mathrm{d}\hat{U}_\alpha^\dagger}{\mathrm{d}\alpha}\hat{H}_0\hat{U}_\alpha + \hat{U}_\alpha^\dagger \underbrace{\frac{\mathrm{d}\hat{H}_0}{\mathrm{d}\alpha}}_{=0}\hat{U}_\alpha + \hat{U}_\alpha^\dagger \hat{H}_0 \frac{\mathrm{d}\hat{U}_\alpha}{\mathrm{d}\alpha} \,. \tag{3.9}$$

Since the initial Hamiltonian is independent of the flow parameter, the second term is zero. By exploiting the derivative of the unitary relation

$$0 = \frac{\mathrm{d}\mathbb{1}}{\mathrm{d}\alpha} = \frac{\mathrm{d}}{\mathrm{d}\alpha}\left(\hat{U}_\alpha^\dagger \hat{U}_\alpha\right) = \frac{\mathrm{d}\hat{U}_\alpha^\dagger}{\mathrm{d}\alpha}\hat{U}_\alpha + \hat{U}_\alpha^\dagger \frac{\mathrm{d}\hat{U}_\alpha}{\mathrm{d}\alpha} \,. \tag{3.10}$$

the derivative of the unitary operator yields

$$\frac{\mathrm{d}}{\mathrm{d}\alpha}\hat{U}_\alpha^\dagger = -\hat{U}_\alpha^\dagger \frac{\mathrm{d}\hat{U}_\alpha}{\mathrm{d}\alpha}\hat{U}_\alpha^\dagger. \tag{3.11}$$

Using these relations, we obtain the SRG flow equation

$$\begin{aligned}\frac{\mathrm{d}\hat{H}_\alpha}{\mathrm{d}\alpha} &= -\hat{U}_\alpha^\dagger \frac{\mathrm{d}\hat{U}_\alpha}{\mathrm{d}\alpha}\hat{U}_\alpha^\dagger \hat{H}_0 \hat{U}_\alpha + \hat{U}_\alpha^\dagger \hat{H}_0 \hat{U}_\alpha \hat{U}_\alpha^\dagger \frac{\mathrm{d}\hat{U}_\alpha}{\mathrm{d}\alpha} \\ &= \left[\hat{\eta}_\alpha, \hat{H}_\alpha\right]\end{aligned} \tag{3.12}$$

with the anti-hermitian generator $\hat{\eta}_\alpha = -\hat{U}_\alpha^\dagger \frac{\mathrm{d}\hat{U}_\alpha}{\mathrm{d}\alpha} = -\hat{\eta}_\alpha^\dagger$. This first-order differential equation has the initial conditions $\hat{H}_{\alpha=0} = \hat{H}_0$, $\hat{O}_{\alpha=0} = \hat{O}$ and $\hat{U}_{\alpha=0} = \mathbb{1}$.

Any arbitrary operator that is anti-hermitian is a possible choice as generator. This pertains to the following ansatz

$$\hat{\eta}_\alpha = \left[\hat{G}_\alpha, \hat{H}_\alpha\right] \tag{3.13}$$

with the generator as the commutator of a hermitian operator $\hat{G}_\alpha$ and the Hamiltonian. Originally, $\hat{G}_\alpha$ was chosen to be the diagonal part of the Hamiltonian $\hat{G}_\alpha \sim \mathrm{diag}(\hat{H}_\alpha)$ [20, 23] leading to a diagonalization of the Hamiltonian $\hat{H}_\alpha$ as obviously can be seen due to a vanishing

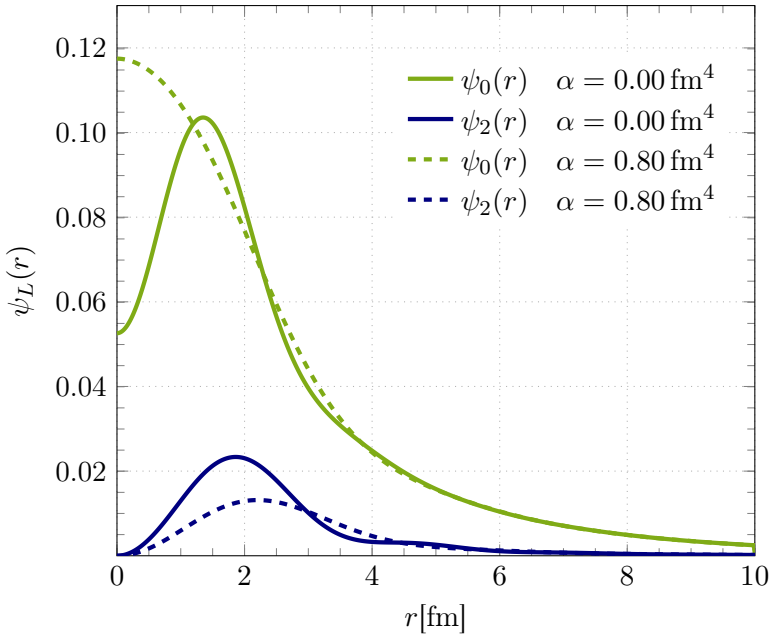

Figure 3.2: Radial wave functions $\psi_L(r)$ for $L = 0$ (S-wave, ——) and $L = 2$ (D-wave, ——) of the deuteron obtained with bare (solid) and SRG evolved (dashed) Hamiltonian.

generator which corresponds to a fix point in the SRG flow. This generator was introduced by Wegener and includes the choice of a basis.

Another possibility for $\hat{G}_\alpha$ is the intrinsic kinetic energy

$$\hat{\eta}_\alpha = (2\mu)^2 \left[\hat{T}_{\mathrm{int}}, \hat{H}_\alpha\right] \tag{3.14}$$

with the reduced mass $\mu = \frac{m_{\mathrm{N}}}{2}$, leading to a pre-diagonalized Hamiltonian with respect to the momentum basis corresponding to a decoupling of high- and low-momentum states.

Since observables are defined as expectation values with respect to the eigenstates of the Hamiltonian, they should be transformed simultaneously as well for a consistent description.

In actual calculations, the main disadvantage of the SRG are induced higher-order contributions. Due to the structure of the flow equation with its commutators, operators with higher rank occur for each step of the evaluation. For an A-body system, starting with a two- and three-body Hamiltonian leads to a SRG transformed Hamiltonian with up to A-body contributions. For the unitarity, all induced contributions up to A-body need to be taken into account, which is not feasible. Thus, the SRG transformation is truncated, leading to the violation of unitarity.

In Fig. 3.2, the wave function of the deuteron is shown for the initial and the SRG evolved Hamiltonian, whose short-range repulsion suppress the wave function at small distances in the unevolved case caused by a coupling of low- and high-momentum states. For SRG evolved interactions, the short-range correlation hole is removed leading to a decoupling of low- and high-momentum states and, thus, to a prediagonalization.

3.3 Single-Particle Bases

Besides the specification of the interaction, the single-particle basis the Hamiltonian is represented in can be chosen arbitrarily. Most derivations in the following chapters are kept on a general level and, therefore, independent of the choice of the single-particle basis, as far as possible. At a certain point within these derivations, a basis needs to be selected which leads to slightly different final mathematical expressions. This is the case because simplifications made due to symmetries can only be exploited in a specific single-particle basis.

There are several single-particle bases, for instance the harmonic oscillator (HO) basis, the Hartree-Fock (HF) basis and natural orbitals (NAT). The latter two are discussed in more detail in the following section, based on Refs. [64, 70, 78, 81], depicting the basic equations and properties.

3.3.1 Hartree-Fock Approximation

Within the Hartree-Fock method, the eigenstate of an A-body nucleus is approximated by a single Slater determinant obtained through the application of the variational principle with the single-particle states as variational degrees of freedom. As starting point in the HF method, a Slater determinant is assumed as trial state

$$|\mathrm{HF}\rangle = \hat{a}_1^\dagger \hat{a}_2^\dagger \dots \hat{a}_A^\dagger |0\rangle \ . \tag{3.15}$$

The single-particle states $|i\rangle = \hat{a}_i^\dagger |0\rangle$ are varied in order to minimize the energy functional $E[|\mathrm{HF}\rangle] = \langle \mathrm{HF}|\hat{H}|\mathrm{HF}\rangle$. The goal of the HF method is then to find this single-particle basis $\{|i\rangle\}$. The unknown HF single-particle states can be expanded in a working basis, for instance the single-particle HO basis $|\gamma_k\rangle = \hat{c}_k^\dagger |0\rangle$

$$|i\rangle = \sum_k D_k^{(i)} |\gamma_k\rangle \qquad \Leftrightarrow \qquad \hat{a}_i^\dagger = \sum_k D_k^{(i)} \hat{c}_k^\dagger \tag{3.16}$$

Here, $\hat{c}_i^\dagger$ is the creation operator in the HO basis and $\hat{a}_i^\dagger$ the creation operator in the HF basis. In order to circumvent the fact that it is not possible to determine unique coefficients $D_k^{(i)}$ or single-particle states within the energy minimization, since Slater determinants are invariant under unitary transformations among occupied single-particle states except for a global phase, single-particle densities

$$\rho_{k,k'} = \langle \mathrm{HF}| \hat{c}_{k'}^\dagger \hat{c}_k |\mathrm{HF}\rangle = \sum_{ii'} D_{k'}^{(i')*} D_k^{(i)} \langle \mathrm{HF}| \hat{a}_{i'}^\dagger \hat{a}_i |\mathrm{HF}\rangle = \sum_i^{\text{occ.}} D_{k'}^{(i)*} D_k^{(i)} \tag{3.17}$$

are used instead for the variation. Here, only occupied states are included as indicated by the summation limit "occ.". First, we have to determine the energy functional in terms of the density. Starting with the Hamiltonian (3.3), we can evaluate the expectation value in the

HF basis, leading to the energy E

$$\begin{aligned} E &= \langle \mathrm{HF} | \, \hat{H} \, | \mathrm{HF} \rangle \\ &= \sum_{i,i'} t_{i,i'} \, \langle \mathrm{HF} | \, \hat{c}_i^\dagger \hat{c}_{i'} \, | \mathrm{HF} \rangle + \sum_{ij,i'j'} \frac{1}{4} \bar{v}_{ij,i'j'} \, \langle \mathrm{HF} | \, \hat{c}_i^\dagger \hat{c}_j^\dagger \hat{c}_{j'} \hat{c}_{i'} \, | \mathrm{HF} \rangle \\ &\quad + \frac{1}{36} \sum_{ijk,i'j'k'} \bar{v}^{\mathrm{3N}}_{ijk,i'j'k'} \, \langle \mathrm{HF} | \, \hat{c}_i^\dagger \hat{c}_j^\dagger \hat{c}_k^\dagger \hat{c}_{k'} \hat{c}_{j'} \hat{c}_{i'} \, | \mathrm{HF} \rangle \; . \end{aligned} \tag{3.18}$$

The HF matrix elements are identified with the one-body, two-body and three-body density matrices

$$\rho_{i,i'} = \langle \mathrm{HF} | \, \hat{c}_{i'}^\dagger \hat{c}_i \, | \mathrm{HF} \rangle \; , \tag{3.19}$$

$$\rho_{ij,i'j'} = \langle \mathrm{HF} | \, \hat{c}_{i'}^\dagger \hat{c}_{j'}^\dagger \hat{c}_j \hat{c}_i \, | \mathrm{HF} \rangle \; , \tag{3.20}$$

$$\rho_{ijk,i'j'k'} = \langle \mathrm{HF} | \, \hat{c}_{i'}^\dagger \hat{c}_{j'}^\dagger \hat{c}_{k'}^\dagger \hat{c}_k \hat{c}_j \hat{c}_i \, | \mathrm{HF} \rangle \; . \tag{3.21}$$

If the initial and the final state are different, these matrices represent transition densities. The one-body density matrix (3.19) has some special properties. It is Hermitian, i.e.

$$\rho^*_{j,i} = \langle \psi | \, \hat{c}_i^\dagger \hat{c}_j \, | \psi \rangle^* = \langle \psi | \, \hat{c}_j^\dagger \hat{c}_i \, | \psi \rangle = \rho_{i,j} \qquad \Rightarrow \qquad \rho = \rho^\dagger \tag{3.22}$$

and its trace gives the number of particles A. Analogously, we find that higher-order density matrices are Hermitian as well.

For an HF Slater determinant, the associated density matrix is idempotent

$$\rho = \rho^2 \, . \tag{3.23}$$

This can immediately be seen by considering the structure of the density matrix which is diagonal

$$\rho = \begin{pmatrix} \rho_{hh} & \rho_{hp} \\ \rho_{ph} & \rho_{pp} \end{pmatrix} = \begin{pmatrix} \rho_{hh} & 0 \\ 0 & 0 \end{pmatrix} = \begin{pmatrix} \mathbb{1} & 0 \\ 0 & 0 \end{pmatrix} \; . \tag{3.24}$$

This is because only the entries associated with occupied single-particle states (i.e. hole states) are non-zero

$$\rho_{hh'} = \langle \mathrm{HF} | \, \hat{a}_{h'}^\dagger \hat{a}_h \, | \mathrm{HF} \rangle = \delta_{hh'} \; , \tag{3.25}$$

while all other entries, including the unoccupied single-particle states (i.e. particle states),

vanish

$$\begin{aligned}\rho_{hp} &= \langle \mathrm{HF}| \hat{a}_h^\dagger \hat{a}_p |\mathrm{HF}\rangle = 0\,,\\ \rho_{ph} &= \langle \mathrm{HF}| \hat{a}_p^\dagger \hat{a}_h |\mathrm{HF}\rangle = 0\,,\\ \rho_{pp'} &= \langle \mathrm{HF}| \hat{a}_{p'}^\dagger \hat{a}_p |\mathrm{HF}\rangle = 0\,.\end{aligned} \tag{3.26}$$

The idempotence and hermeticity influence the variation as constraints. The expectation value of the Hamiltonian in Eq. (3.18) depends on density matrices

$$E\left[\rho^1,\rho^2,\rho^3\right] = \sum_{i,i'} t_{i,i'}\rho_{i',i} + \sum_{ij,i'j'}\frac{1}{4}\bar{v}_{ij,i'j'}\rho_{i'j',ij} + \frac{1}{36}\sum_{ijk,i'j'k'}\bar{v}^{\mathrm{3N}}_{ijk,i'j'k'}\rho_{i'j'k',ijk}\,. \tag{3.27}$$

With the aid of the Slater-Condon rules [2, 3], the two-body density can be expressed in terms of one-body density matrices, since $|\mathrm{HF}\rangle$ is a single Slater determinant. Taking into account the entire two-body term in Eq. (3.27), exploiting the antisymmetry of the potential as defined in Eq. (3.4) and switching the indices i and j, we find

$$\begin{aligned}\sum_{ij,i'j'}\bar{v}_{ij,i'j'}\rho_{i'j',ij} &= \sum_{ij,i'j'}\bar{v}_{ij,i'j'}(\rho_{j',j}\rho_{i',i} - \rho_{j',i}\rho_{i',j})\\ &= 2\sum_{ij,i'j'}\bar{v}_{ij,i'j'}\rho_{j',j}\rho_{i',i}\,.\end{aligned} \tag{3.28}$$

Analogously, the three-body density matrix with respect to the HF ground state factorizes into one-body density matrices, which leads to

$$\sum_{ijk,i'j'k'}\bar{v}^{\mathrm{3N}}_{ijk,i'j'k'}\rho_{i'j'k',ijk} = 6\sum_{ijk,i'j'k'}\bar{v}^{\mathrm{3N}}_{ijk,i'j'k'}\rho_{k',k}\rho_{j',j}\rho_{i',i}\,. \tag{3.29}$$

With these considerations, the energy expectation value $E[\rho]$ in Eq. (3.27) in terms of the functional of the one-body density matrix is given by

$$E[\rho] = \sum_{i,i'} t_{i,i'}\rho_{i',i} + \sum_{ij,i'j'}\frac{1}{2}\bar{v}_{ij,i'j'}\rho_{j',j}\rho_{i',i} + \frac{1}{6}\sum_{ijk,i'j'k'}\bar{v}^{\mathrm{3N}}_{ijk,i'j'k'}\rho_{k',k}\rho_{j',j}\rho_{i',i}. \tag{3.30}$$

Stationary points of $E[\rho]$ are found through varying the energy with respect to the one-body

density

$$\begin{aligned}\delta E[\rho] &= E[\rho+\delta\rho] - E[\rho] \\ &= \sum_{i,i'} t_{i,i'}\delta\rho_{i',i} + \sum_{ij,i'j'} \bar{v}_{ij,i'j'}\delta\rho_{j',j}\rho_{i',i} + \frac{1}{2}\sum_{ijk,i'j'k'} \bar{v}^{\mathrm{3N}}_{ijk,i'j'k'}\delta\rho_{k',k}\rho_{j',j}\rho_{i',i} \\ &= \sum_{i,i'}\left(t_{i,i'} + \sum_{j,j'}\bar{v}_{ij,i'j'}\rho_{j',j} + \frac{1}{2}\sum_{jk,j'k'}\bar{v}^{\mathrm{3N}}_{ijk,i'j'k'}\rho_{k',k}\rho_{j',j}\right)\delta\rho_{i',i} \\ &\equiv \sum_{i,i'} h_{i,i'}[\rho]\,\delta\rho_{i',i}\,.\end{aligned} \tag{3.31}$$

Here, only linear terms of the density variation $\delta\rho$ are included, while higher-orders are omitted. In the last step in Eq. (3.31), the shorthand notation $h_{i,i'}[\rho]$ is introduced, describing for matrix elements of the one-body HF single-particle or mean-field Hamiltonian. It contains the kinetic energy and a density-dependent one-body potential.

For a Slater determinant, the density needs to be idempotent (3.23). This also holds for the varied density $(\rho+\delta\rho)^2 = \rho+\delta\rho$. Since the density matrix is diagonal and has a block structure (3.24), the idempotence leads to variations whose diagonal blocks are zero and whose off-diagonal blocks contains information. Thus, the variation can only connect particle and hole states or vice versa, meaning occupied and unoccupied states.

The stationary condition

$$\delta E[\rho] = 0 \tag{3.32}$$

can be rewritten as an eigenvalue problem of the mean-field Hamiltonian

$$\hat{h}[\rho]\,|i\rangle = \epsilon_i\,|i\rangle \tag{3.33}$$

with the single-particle energies ϵ_i and the single-particle HF states $|i\rangle$. The eigenvalue problem is solved iteratively since the Hamiltonian depends on the density, which itself depends on the eigenstates, which are to be determined. This procedure is done until the single-particle states do not change significantly and thus, an self-consistent solution is obtained. These single-particle states define then the HF basis.

For the HF basis, the block-diagonal structure of the density matrix (3.24) is exploited, leading to a simplification of the mean-field Hamiltonian

$$h_{i,i'}[\rho] = t_{i,i'} + \sum_{j}^{\mathrm{occ.}}\bar{v}_{ij,i'j} + \frac{1}{2}\sum_{jk}^{\mathrm{occ.}}\bar{v}^{\mathrm{3N}}_{ijk,i'jk}. \tag{3.34}$$

The associated single-particle energies are given by

$$\epsilon_i = t_{i,i} + \sum_{j}^{\mathrm{occ.}}\bar{v}_{ij,ij} + \frac{1}{2}\sum_{jk}^{\mathrm{occ.}}\bar{v}^{\mathrm{3N}}_{ijk,ijk}\,, \tag{3.35}$$

obtained with the relation of the mean-field Hamiltonian (3.31) and the energy eigenvalues

$$h_{i,i'}[\rho] = \langle i| \hat{h}[\rho] \left|i'\right\rangle = \langle i| \epsilon_{i'} \left|i'\right\rangle = \epsilon_{i'}\delta_{ii'} \,. \tag{3.36}$$

The ground-state energy corresponding to the HF Slater determinant

$$\begin{aligned} E &= \langle \mathrm{HF}| \hat{H} |\mathrm{HF}\rangle \\ &= \sum_{i}^{\mathrm{occ.}} t_{i,i} + \frac{1}{2}\sum_{ij}^{\mathrm{occ.}} \bar{v}_{ij,ij} + \frac{1}{6}\sum_{ijk}^{\mathrm{occ.}} \bar{v}^{\mathrm{3N}}_{ijk,ijk} \\ &= \sum_{i}^{\mathrm{occ.}} \epsilon_i - \frac{1}{2}\sum_{ij}^{\mathrm{occ.}} \bar{v}_{ij,ij} - \frac{1}{3}\sum_{ijk}^{\mathrm{occ.}} \bar{v}^{\mathrm{3N}}_{ijk,ijk} \end{aligned} \tag{3.37}$$

differs from the sum of the single-particle energies. In general, the HF method in this form can only be applied for closed-shell nuclei. In order to extend this approach to all nuclei, the so-called equal-filling method [36] was developed.

3.3.2 Natural Orbitals

Another established single-particle basis, according to Refs. [81, 96], are natural orbitals. They provide a fast and robust convergence behavior while yielding good results for several observables, as for instance energies, radii and certain electromagnetic properties. Natural orbitals are eigenvectors of the one-body density matrix (3.19), which is constructed with the aid of a many-body reference state. This state contains correlation effects from second-order many-body perturbation theory. Hence, this procedure leads to a perturbatively improved density matrix which includes more information about the system in form of correlations and, thus, to a more physical basis as well.

The starting point for natural orbitals is the construction of a one-body density matrix, which is obtained from a separate many-body calculation. This could be, for instance, a HF calculation. Since in that specific basis no correlations are taken into account, the HF single-particle basis and the natural orbitals are identical. Instead of a simple HF calculation or a completely correlated NCSM calculation, we construct the reference state from HF Slater determinants corrected via second-order many-body perturbation theory, leading to be

$$|\psi\rangle \approx |\psi^{(0)}\rangle + |\psi^{(1)}\rangle + |\psi^{(2)}\rangle \tag{3.38}$$

with the unperturbed state $|\psi^{(0)}\rangle$ and the first- and second-order correction $|\psi^{(1)}\rangle$ and $|\psi^{(2)}\rangle$, respectively. The one-body density matrix up to second-order is then given by

$$\rho \approx \rho^{(00)} + \rho^{(02)} + \rho^{(20)} + \rho^{(11)} \tag{3.39}$$

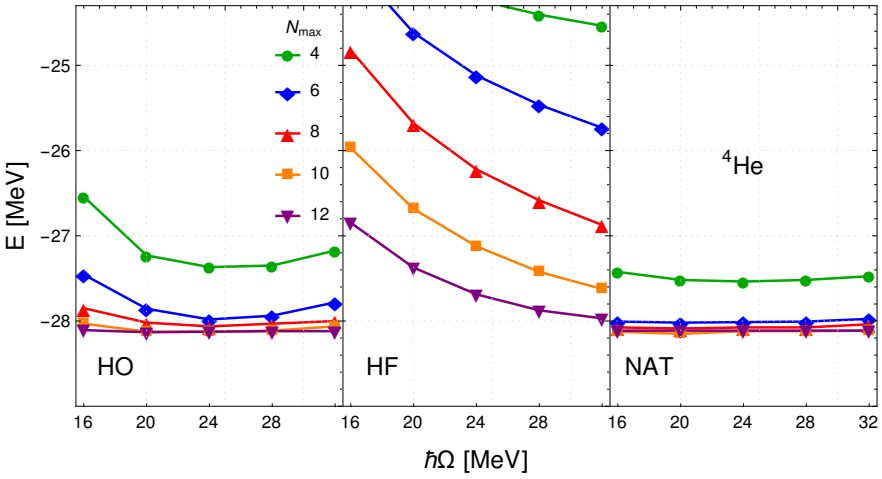

Figure 3.3: Energy depending on the frequency $\hbar\Omega$ for different single-particle bases for ^{4}He. Contrary to the HO or HF basis, natural orbitals are almost independent of $\hbar\Omega$.

with

$$\rho^{(02)}_{i',i} = \langle\psi^{(0)}|\,\hat{c}^\dagger_{i'}\hat{c}_i\,|\psi^{(2)}\rangle = \rho^{(20)}_{i,i'}\,, \tag{3.40}$$

$$\rho^{(11)}_{i,i'} = \langle\psi^{(1)}|\,\hat{c}^\dagger_{i'}\hat{c}_i\,|\psi^{(1)}\rangle\,, \tag{3.41}$$

$$\rho^{(10)}_{i,i'} = \rho^{(01)}_{i,i'} = 0\,. \tag{3.42}$$

There is no contribution to the density matrix mixing the first order corrected and the unperturbed state because of Brillouin's theorem. The density matrices (3.40)-(3.42) can be rewritten as sums of antisymmetric two-body matrix elements of the Hamiltonian and HF single-particle energies. The three-body interaction is included as matrix elements in terms of normal-ordered two-body approximation, c.f. Sec. 3.1.2.

Diagonalizing the resulting density matrix leads to the natural orbitals as used in this work. The HF single-particle basis serves as input for the evaluation of the density and thus of the natural orbitals. The underlying HF calculation is performed with respect to the HO basis as computational basis. The matrix elements of the Hamiltonian given with respect to the HO basis are transformed to the HF basis afterwards. Hence, natural orbitals can be expressed as linear combination of HF or HO basis states

$$\begin{aligned} |nljmt\rangle_{\text{NAT}} &= \sum_{n'} c^{(ljt)}_{nn'}\,|n'ljmt\rangle_{\text{HF}} \\ &= \sum_{n'} \tilde{c}^{(ljt)}_{nn'}\,|n'ljmt\rangle_{\text{HO}} \end{aligned} \tag{3.43}$$

with the respective HF and HO expansion coefficients $c^{(ljt)}_{nn'}$ and $\tilde{c}^{(ljt)}_{nn'}$. The preceding HF calculation that is used for the construction of natural orbitals is performed utilizing a truncated HO basis. Consequently, the harmonic oscillator frequency $\hbar\Omega$ occurs as a parameter both in the HF basis and the natural orbitals.

Previous work in Ref. [81] has shown that several observables evaluated in an NCSM calculation using natural orbitals are almost entirely frequency independent as illustrated in Fig. 3.3

for the ground-state energy of ^{4}He. This is in contrast to the HO and the HF basis, where the results are strongly dependent on the oscillator frequency. Considering the convergence behavior of one parameter less reduces the computational effort. Whether these benefits occur as well for strength distributions is investigated within the RPA framework in this thesis in Part III.

4

Electromagnetic Multipole Operators

Contents

Multipole moments and transitions strengths are electromagnetic observables offering a unique perspective in structure of nuclei. Nuclei interacting with a static electromagnetic field give crucial insight into a system via transition strengths and via the emerged magnetic moment due to moved charged particles and the spins of the nucleons. Coupling of nuclei to an electric field results in a charge density and, thus, to an electric moment. Transition strengths depend on the detailed form of the wave function and are in addition accessible in experiments.

The chapter introduces the interacting Hamiltonian with an external electromagnetic field and important electromagnetic observables. The derivations are briefly outlined, based on Refs. [14, 70, 76, 78]. For more details, we refer to Ref. [14].

4.1 Hamiltonian with External Electromagnetic Field

The starting point in the derivation of electromagnetic multipole operators is a Hamiltonian describing the nucleus in an external electromagnetic field which is given by

$$\begin{aligned}\hat{H}_{\text{int}} &= -\frac{1}{c}\int \mathrm{d}^3r\ \hat{j}_\mu(\vec{r})A^\mu(\vec{r}) \\ &= \int \mathrm{d}^3r\ \left(\hat{\rho}(\vec{r})\Phi(\vec{r}) - \frac{1}{c}\hat{\vec{j}}(\vec{r})\vec{A}(\vec{r})\right) \\ &= \int \mathrm{d}^3r\ \left(\hat{\rho}(\vec{r})\Phi(\vec{r}) - \hat{\vec{\mu}}(\vec{r})\cdot\vec{B}(\vec{r})\right)\end{aligned} \tag{4.1}$$

with the four-vector potential of the external field $A^\mu(\vec{r}) = (\Phi(\vec{r}), \vec{A}(\vec{r}))$ with the electric potential $\Phi(\vec{r})$ and the vector potential $\vec{A}(\vec{r})$. The first term is identified with the electric interaction and is based on the charge density $\hat{\rho}(\vec{r})$. The second term characterizes the magnetic interaction including either the current density $\hat{\vec{j}}(\vec{r})$ and the vector potential or the magnetic flux density $\vec{B}(\vec{r})$ and the magnetic moment density $\hat{\vec{\mu}}(\vec{r})$. Both descriptions are equivalent due to the relations

$$\begin{aligned}\hat{\vec{j}}(\vec{r}) &= c\vec{\nabla}\times\hat{\vec{\mu}}(\vec{r})\,, \\ \vec{B} &= \vec{\nabla}\times\vec{A}\,.\end{aligned} \tag{4.2}$$

The external field is assumed to be static and its sources are far away from the nucleus, leading to the validity of the homogeneous Maxwell equations

$$\Delta\Phi(\vec{r}) = 0\,, \tag{4.3}$$

$$\vec{\nabla}\times\vec{B}(\vec{r}) = 0\,, \tag{4.4}$$

$$\vec{\nabla}\cdot\vec{B}(\vec{r}) = 0\,, \tag{4.5}$$

with the general solution of the scalar field

$$\Phi(\vec{r}) = \sum_{\lambda,\mu} a_{\lambda\mu} r^\lambda Y_{\lambda\mu}(\theta,\phi) \tag{4.6}$$

as expansion in spherical harmonics $Y_{\lambda\mu}(\theta,\phi)$. In order to analogously find a solution for the magnetic flux $\vec{B}(\vec{r})$, a scalar field $\Xi(\vec{r})$ is introduced

$$\vec{B}(\vec{r}) = -\vec{\nabla}\Xi(\vec{r}) \qquad\qquad \Delta\Xi(\vec{r}) = 0 \tag{4.7}$$

compatible with the Maxwell equations (4.4) and (4.5). Due to the same structure as the Laplace equation (4.3), the scalar field can be expanded as well in terms of spherical harmonics

$$\Xi(\vec{r}) = \sum_{\lambda,\mu} b_{\lambda\mu} r^{\lambda} Y_{\lambda\mu}(\theta,\phi)\,. \tag{4.8}$$

With these considerations, the Hamiltonian results in

$$\begin{aligned}\hat{H}_{\text{int}} &= \sum_{\lambda,\mu} a_{\lambda\mu} \int \mathrm{d}^3 r\ \hat{\rho}(\vec{r}) r^{\lambda} Y_{\lambda\mu}(\theta,\phi) + \sum_{\lambda,\mu} b_{\lambda\mu} \int \mathrm{d}^3 r\ \hat{\vec{\mu}}(\vec{r}) \cdot \vec{\nabla} \left(r^{\lambda} Y_{\lambda\mu}(\theta,\phi) \right) \\ &= \sum_{\lambda,\mu} \left(a_{\lambda\mu} \hat{Q}_{\lambda\mu} + b_{\lambda\mu} \hat{M}_{\lambda\mu} \right)\end{aligned} \tag{4.9}$$

with the coefficients $a_{\lambda\mu}$ and $b_{\lambda\mu}$ which include various derivatives of the fields. Here, we introduced the electric and magnetic multipole operators

$$\hat{Q}_{\lambda\mu} = \int \mathrm{d}^3 r\ \hat{\rho}(\vec{r}) r^{\lambda} Y_{\lambda\mu}(\theta,\phi) \qquad\qquad \hat{M}_{\lambda\mu} = \int \mathrm{d}^3 r\ \hat{\vec{\mu}}(\vec{r}) \cdot \vec{\nabla} \left(r^{\lambda} Y_{\lambda\mu}(\theta,\phi) \right)\,. \tag{4.10}$$

Simplifying the expressions and integrating by parts, which is described in detail in Refs. [78, 88], results in a magnetic multipole operator in terms of magnetic moment density or the current density

$$\begin{aligned}\hat{M}_{\lambda\mu} &= \int \mathrm{d}^3 r\ \hat{\vec{\mu}}(\vec{r}) \cdot \vec{\nabla} \left(r^{\lambda} Y_{\lambda\mu}(\theta,\phi) \right) \\ &= \frac{1}{(\lambda+1)} \int \mathrm{d}^3 r\ \left(\vec{r} \times \left(\vec{\nabla} \times \hat{\vec{\mu}}(\vec{r}) \right) \right) \cdot \vec{\nabla} \left(r^{\lambda} Y_{\lambda\mu}(\theta,\phi) \right) \\ &= \frac{1}{c\ (\lambda+1)} \int \mathrm{d}^3 r\ \left(\vec{r} \times \hat{\vec{j}}(\vec{r}) \right) \cdot \vec{\nabla} \left(r^{\lambda} Y_{\lambda\mu}(\theta,\phi) \right)\,.\end{aligned} \tag{4.11}$$

Due to the assumption of nucleons as point particles, the charge density is characterized by

$$\hat{\rho}(\vec{r}) = \sum_{i=1}^{A} e \hat{\Pi}_{p,i}\ \delta\left(\vec{r} - \vec{r}_i\right)\,. \tag{4.12}$$

The proton projector $\hat{\Pi}_{p,i} = 1/2 + \hat{\tau}_{3,i}$ includes the third component of the isospin operator $\hat{\tau}_{3,i}$ of the i-th nucleon and, thus, indicates that only protons are responsible for the charge density, as one would naively expect. Additionally the charge depends on the coordinate of the i-th nucleon $\vec{r}_i$ with respect to the center-of-mass.

The current and magnetic moment density are identified with

$$\hat{\vec{j}}(\vec{r})_{\text{orbit}} = \sum_{i=1}^{A} e\hat{\Pi}_{p,i}\frac{1}{2}\left(\hat{\vec{v}}_i\delta\left(\vec{r}-\vec{r}_i\right)+h.c.\right) \tag{4.13}$$

$$\hat{\vec{\mu}}(\vec{r})_{\text{spin}} = \sum_{i=1}^{A}\delta\left(\vec{r}-\vec{r}_i\right)\frac{e\hbar}{2mc}\left\{\hat{\Pi}_{p,i}g_p+\hat{\Pi}_{n,i}g_n\right\}\hat{\vec{\sigma}}_i\,, \tag{4.14}$$

representing an orbit part due to moved charged particles (protons) and a spin part due to the spin contributions of nucleons. Here, the neutron projection operator $\hat{\Pi}_{n,i} = 1/2 - \hat{\tau}_{3,i}$, the nuclear magneton $\mu_{\text{N}} = {}^{e\hbar}/_{2mc}$, the gyromagnetic factors for proton and neutron, g_p and g_n, respectively, as well as the velocity $\hat{\vec{v}}_i = {}^{i}/_{\hbar}\left[\hat{H},\hat{\vec{r}}_i\right]$ contribute.

Inserting these relations into Eq. (4.10) and Eq. (4.11), the electric multipole operator is given by

$$\hat{Q}_{\lambda\mu} = e\sum_{i=1}^{A}\hat{\Pi}_{p,i}\;\hat{r}_i^{\lambda}\;Y_{\lambda\mu}(\hat{\theta}_i,\hat{\phi}_i) \tag{4.15}$$

while the magnetic multipole operator can be rewritten as

$$\hat{M}_{\lambda\mu} = \mu_{\text{N}}\sum_{i=1}^{A}\left\{\left[g_p\hat{\vec{\sigma}}_i+\frac{2}{\lambda+1}\hat{\vec{l}}_i'\right]\hat{\Pi}_{p,i}+g_{\text{n}}\hat{\vec{\sigma}}_i\hat{\Pi}_{n,i}\right\}\cdot\left(\nabla\hat{r}^{\lambda}Y_{\lambda\mu}(\hat{\theta},\hat{\phi})\right)_{\vec{r}=\vec{r}_i}\,. \tag{4.16}$$

The first term characterizes the interaction of the protons with the magnetic field, consisting of a spin and a orbital part due to the charge of the proton whereas the second term describing the neutrons interaction only contains a spin part.

4.2 Electromagnetic Observables

The determination of electromagnetic moments corresponds the calculation of expectation values of the multipole operators with respect to a state $|\psi\rangle$. In contrast, multipole transitions are defined as matrix elements including two different states $|\psi_i\rangle$ and $|\psi_f\rangle$ respectively. The angular momentum plays an important role in the framework of transitions and magnetic moments. Thus, we can divide the quantum numbers of any arbitrary state into a part concerning the angular momentum J and its projection M and a part including all remaining quantum numbers α

$$|\psi\rangle = |\alpha, JM\rangle\,. \tag{4.17}$$

Both types of observables, the static multipole moments and the multipole transitions, are briefly discussed in this chapter.

Static Multipole Moments Since the electromagnetic multipole operator is a spherical tensor operator, the application of the Wigner-Eckart theorem (2.20) leaves a choice in the

projection quantum number M. The magnetic dipole operator is then given by

$$\hat{M}_{10} = \sqrt{\frac{3}{4\pi}}\mu_{\mathrm{N}} \sum_{i=1}^{A} \left[\{ g_p \hat{\sigma}_{z,i} + \hat{l}'_{z,i} \} \hat{\Pi}_{p,i} + g_n \hat{\sigma}_{z,i} \hat{\Pi}_{n,i} \right] \tag{4.18}$$

and the electric quadrupole operator is defined as

$$\hat{Q}_{20} = \sqrt{\frac{5}{16\pi}} e \sum_{i=1}^{A} \hat{\Pi}_{p,i} \; \hat{r}_i^2 \left(3\cos^2\theta - 1 \right) \tag{4.19}$$

leading to the static electric quadrupole and magnetic dipole moments

$$Q = \sqrt{\frac{16\pi}{5}} \langle \alpha, JJ | \hat{Q}_{20} | \alpha, JJ \rangle \tag{4.20}$$

$$\mu = \sqrt{\frac{4\pi}{3}} \langle \alpha, JJ | \hat{M}_{10} | \alpha, JJ \rangle \tag{4.21}$$

respectively, for which $J = M$ is chosen by convention. Due to the Wigner-Eckart theorem, the matrix elements of arbitrary M can then be calculated.

Multipole Transitions Transitions from an initial state $|\psi_i\rangle$ to a final state $|\psi_f\rangle$ are described by matrix elements of the following pattern

$$\langle \psi_f | \, \hat{T}_{\sigma\lambda\mu} \, | \psi_i \rangle \tag{4.22}$$

with the generic electromagnetic multipole operator $\hat{T}_{\sigma\lambda\mu}$. The transition operator is a spherical tensor of rank λ which can represent either electric or magnetic transitions. The transition type is indicated by σ and its multipolarity by λ. The components of the spherical tensor are denoted by $\hat{T}_{\sigma\lambda\mu}$ with $\mu = -\lambda \ldots \lambda$. For the magnetic and electric multipole operators defined in (4.15) and (4.16), respectively, we can write $\hat{T}_{E\lambda\mu} = \hat{Q}_{\lambda\mu}$ and analogously $\hat{T}_{M\lambda\mu} = \hat{M}_{\lambda\mu}$.

The reduced transition probability or transition strength can be expressed as

$$B(\sigma\lambda : \alpha_i J_i \to \alpha_f J_f) = \frac{1}{2J_i + 1} | \langle \alpha_f J_f || \hat{T}_{\sigma\lambda} || \alpha_i J_i \rangle |^2 \tag{4.23}$$

in terms of the reduced matrix element $\langle \alpha_f J_f || \hat{T}_{\sigma\lambda} || \alpha_i J_i \rangle$ obtained by applying the Wigner-Eckart theorem introduced in Sec. 2.2. In particular, we find for the electric and magnetic transition probability

$$B\left(E\lambda : \alpha_i J_i \to \alpha_f J_f\right) = \frac{1}{2J_i + 1} | \langle \alpha_f J_f || \hat{Q}_{\lambda} || \alpha_i J_i \rangle |^2 \tag{4.24}$$

$$B\left(M\lambda : \alpha_i J_i \to \alpha_f J_f\right) = \frac{1}{2J_i + 1} | \langle \alpha_f J_f || \hat{M}_{\lambda} || \alpha_i J_i \rangle |^2 \tag{4.25}$$

with units

$$[B(\mathrm{E}\lambda)] = e^2 \mathrm{fm}^{2\lambda} \qquad [B(\mathrm{M}\lambda)] = \left(\frac{\mu_{\mathrm{N}}}{c} \right)^2 \mathrm{fm}^{2(\lambda-1)} . \tag{4.26}$$

B(E0) represents an exception, since a scalar does not mediate a transition and, thus, the operator is extended to

$$\hat{Q}_{00} = e\sum_{i=1}^{A} \hat{r}_i^2 Y_{00}(\hat{\Omega}_i) \tag{4.27}$$

with units $[B(\mathrm{E0})] = e^2\mathrm{fm}^4$. The transition probability is accessible in experiments, has tremendous importance and offers a good opportunity for the comparison of theory and experiment.

For a detailed discussion on the reduced matrix elements, we first reformulate the one-body electromagnetic operator with the aid of a tensor product (2.19)

$$\begin{aligned}\hat{T}_{\sigma\lambda} &= \sum_{jk} \langle j|\hat{T}_{\sigma\lambda}|k\rangle\, \hat{a}_j^\dagger \hat{a}_k \\ &= \frac{1}{\sqrt{2\lambda+1}} \sum_{j\hbar} \langle\, j||\hat{T}_{\sigma\lambda}||\hbar\,\rangle\, [\hat{a}_j^\dagger \hat{\tilde{a}}_\hbar]_\lambda .\end{aligned} \tag{4.28}$$

The annihilation operator is rewritten into $\hat{\tilde{a}}_\hbar$ in order to be a spherical tensor as well. This approach is explained in more detail in Sec. 5.1.2. The notation $\hbar$ represents a collective index, in which all quantum numbers except for the projection quantum number are included, as introduced in Sec. 2.1. The operator is characterized by the reduced single-particle matrix elements $\langle\, j||\hat{T}_{\sigma\lambda}||\hbar\,\rangle$. The many-body aspects emerge due to the creator and annihilator. The corresponding reduced many-body matrix element is given by

$$\langle\, \alpha_f J_f||\hat{T}_{\sigma\lambda}||\alpha_i J_i\,\rangle = \frac{1}{\sqrt{2\lambda+1}} \sum_{j\hbar} \langle\, j||\hat{T}_{\sigma\lambda}||\hbar\,\rangle\, \langle\, \alpha_f J_f||[\hat{a}_j^\dagger \hat{\tilde{a}}_\hbar]_\lambda||\alpha_i J_i\,\rangle \tag{4.29}$$

in terms of the reduced one-body transition density matrix element connecting two single-particle states $|j\rangle$ and $|\hbar\rangle$, respectively.

Reduced Single-Particle Matrix Elements of Electromagnetic Multipole Operators
The reduced single-particle matrix elements of the electric multipole operator are given by

$$\begin{aligned}\langle\, a||\hat{Q}_\lambda||b\,\rangle &= \left\langle\, n's'l'j'\middle|\middle|e\hat{r}^\lambda\, Y_{\lambda\mu}(\hat{\theta},\hat{\phi})\middle|\middle|nslj\,\right\rangle \\ &= \frac{e}{\sqrt{4\pi}} \frac{1+(-1)^{l'+\lambda+l}}{2} \hat{\lambda}\hat{j}\hat{j}'(-1)^{j'-\frac{1}{2}} \begin{pmatrix} j' & \lambda & j \\ -\frac{1}{2} & 0 & -\frac{1}{2}\end{pmatrix} \mathcal{R}^{(\lambda)}_{n'l',nl}\end{aligned} \tag{4.30}$$

where we set $s = \frac{1}{2}$ for nucleons. The abbreviation $\hat{j} = \sqrt{2j+1}$ was utilized as well as the shorthand notation for the radial integrals

$$\mathcal{R}^{(\lambda)}_{n'l',nl} = \left\langle n'l'\middle|r^\lambda\middle|nl\right\rangle = \int \mathrm{d}r\; r^2 R_{n'l'}(r) r^\lambda R_{nl}(r) \tag{4.31}$$

which are defined via the integral of the radial wave functions $R_{n'l'}(r)$ and $R_{nl}(r)$ of the final and initial single-particle states.

Analogously, the reduced single-particle matrix element of the magnetic multipole operator can be calculated via

$$\begin{aligned}\langle a||\hat{M}_\lambda||b\rangle &= \left\langle n's'l'j'\right|\left|\mu_{\mathrm{N}}\left(g_s\hat{\vec{\sigma}}+\frac{2}{\lambda+1}g_l\hat{\vec{l}}\right)\cdot\left(\vec{\nabla}\hat{r}^\lambda Y_\lambda(\hat{\Omega})\right)\right|\left|nslj\right\rangle \\ &= \mu_{\mathrm{N}}\frac{1-(-1)^{l'+\lambda+l}}{2}\frac{\hat{\lambda}\hat{j}\hat{j}'}{\sqrt{4\pi}}(-1)^{j'-\frac{1}{2}}\begin{pmatrix} j' & \lambda & j \\ -\frac{1}{2} & 0 & -\frac{1}{2}\end{pmatrix}(\lambda-\kappa) \\ &\quad\times\left[\frac{1}{2}g_s-g_l(1+\frac{\kappa}{\lambda+1})\right]\mathcal{R}^{(\lambda-1)}_{n'l',nl}\end{aligned} \tag{4.32}$$

with

$$\kappa=\left(j+\frac{1}{2}\right)(-1)^{l+j+\frac{1}{2}}+\left(j'+\frac{1}{2}\right)(-1)^{l'+j_p+\frac{1}{2}}. \tag{4.33}$$

If we perform an SRG or an IM-SRG evolution of the Hamiltonian of the considered system, the transition operators are required to be transformed additionally for consistency.

4.3 Translational Invariance and Isospin Decomposition

The coordinates of the electromagnetic operators in Eq. (4.15) and (4.16) and consequently of the multipole transitions are given relative to the center of mass of the nucleus, i.e., in the reference system of the nucleus. Thus, the translational invariant formulation contains A-body operators instead of one-body operators.

As shown in Ref. [78], for a basis that split into a relative and a center of mass part, applying one-body operators leads to the same results for the electric dipole and quadrupole operators. For electric monopole operators, the A-body formulation is only relevant for precision calculations. This is the case for the HO basis.

The electric multipole operator depends on the proton projector

$$\begin{aligned}\hat{Q}_{\lambda\mu} &= e\sum_{i=1}^{A}\hat{\Pi}_{p,i}\ \hat{r}_i^\lambda\ Y_{\lambda\mu}(\hat{\theta}_i,\hat{\phi}_i) \\ &= \frac{1}{2}e\sum_{i=1}^{A}\ \hat{r}_i^\lambda\ Y_{\lambda\mu}(\hat{\theta}_i,\hat{\phi}_i)+e\sum_{i=1}^{A}\hat{\tau}_i\ \hat{r}_i^\lambda\ Y_{\lambda\mu}(\hat{\theta}_i,\hat{\phi}_i)\end{aligned} \tag{4.34}$$

and, thus, only the last term carries information on the isospin. Due to the independence of the isospin, the first term is associated with isoscalar transition, i.e. $\Delta T=0$, which does not connect states of different isospin. The second term contains the z-projection of the isospin describing isovector transitions with $\Delta T=1$.

The electric multipole operator can be decomposed in an isoscalar and an isovector part

$$\hat{Q}_{\lambda\mu}=\hat{Q}^{\mathrm{IS}}_{\lambda\mu}+\hat{Q}^{\mathrm{IV}}_{\lambda\mu} \tag{4.35}$$

which can be additionally separated in one term concerning neutrons and one term regarding protons

$$\hat{Q}^{\mathrm{IS}}_{\lambda\mu} = \frac{1}{2}e\sum_{\pi=1}^{Z}\hat{r}^{\lambda}_{\pi}Y_{\lambda\mu}(\hat{\theta}_{\pi},\hat{\phi}_{\pi}) + \frac{1}{2}e\sum_{\nu=1}^{N}\hat{r}^{\lambda}_{\nu}Y_{\lambda\mu}(\hat{\theta}_{\nu},\hat{\phi}_{\nu}) \tag{4.36}$$

$$\hat{Q}^{\mathrm{IV}}_{\lambda\mu} = \frac{1}{2}e\sum_{\pi=1}^{Z}\hat{r}^{\lambda}_{\pi}Y_{\lambda\mu}(\hat{\theta}_{\pi},\hat{\phi}_{\pi}) - \frac{1}{2}e\sum_{\nu=1}^{N}\hat{r}^{\lambda}_{\nu}Y_{\lambda\mu}(\hat{\theta}_{\nu},\hat{\phi}_{\nu}) \tag{4.37}$$

where the electric charge e is utilized as effective charge for protons and neutrons, taking into account center-of-mass aspects of the A-body system.

The same procedure can be applied to the magnetic multipole operator $\hat{M}_{\lambda\mu}$, leading to an analogue partitioning in isoscalar and isovector. This can be found in more detail in Ref. [78], since we only discuss electric transition strengths throughout the thesis.

4.4 Collective Excitations - A Macroscopic View

Almost all nucleons are responsible for collective excitations. This is not the case for low-lying excited states which typically do not cause collective excitations. Following a specific multipole behaviour, protons and neutrons oscillate in phase when describing isoscalar electric transitions whereas they oscillate out phase when depicting isovector electric transitions from a macroscopic point of view (c.f. Refs. [24, 89]) as illustrated in Fig. 4.1. As seen in Eq. (4.36), isoscalar electric transitions are associated with in-phase oscillating neutrons and protons which is indicated by the sum of protonic and neutronic part, whereas the subtraction in Eq. (4.37) for isovector electric transitions corresponds to a collective motion from neutrons against protons, i.e. an oscillation out of phase. Therefore, these transitions occur at higher energies than isoscalar transitions of the same multipolarity, since the separation of protons and neutrons, which is essential for the anti-phase oscillation, costs additional amount of energy.

The **isoscalar monopole mode** (ISM) describes the radial oscillation of protons and neutrons in phase and, thus, of the nucleus in its entirety. Hence, it is denoted as "breathing" or "compressional" mode. On the other hand, within the **isovector monopole mode** (IVM) neutrons and protons move against each other, resulting in an oscillation out of phase.

Within the **isovector dipole mode** (IVD) the protons move against the neutrons out of phase. It is a one-dimensional collective motion which entails a separation of the nucleus' center of mass and center of charge. The **isoscalar dipole mode** (ISD) is a center-of-mass motion.

The **isoscalar quadrupole mode** (ISQ) is depicted as quadrupole deformation which describes the alternating deformation of the nucleus into prolate and oblate shape. This procedure originates from neutrons and protons oscillating in phase. Instead, the **isovector quadrupole mode** (IVQ) is associated with the out-phase quadrupole deformation, i.e. if the protons are oblate, the neutrons are prolate and vice versa.

The isoscalar and isovector magnetic transitions are described by an in-phase and out-phase oscillation of nucleons with spin-up and spin-down, respectively.

The focus of this thesis is the investigation of isoscalar monopole, isovector dipole and isoscalar quadrupole electric transitions.

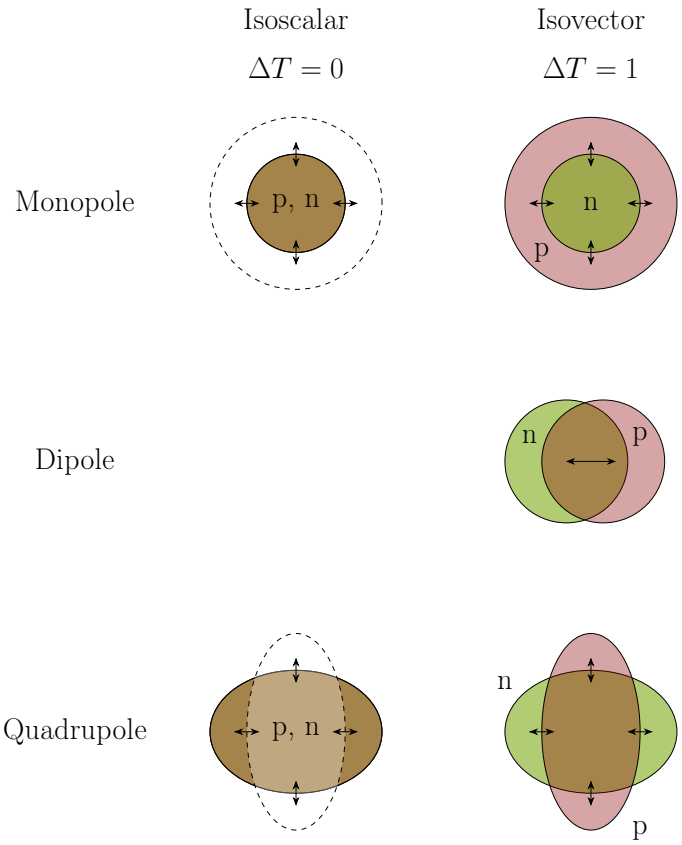

Figure 4.1: Macroscopic illustration of collective excitations.

II

Methods

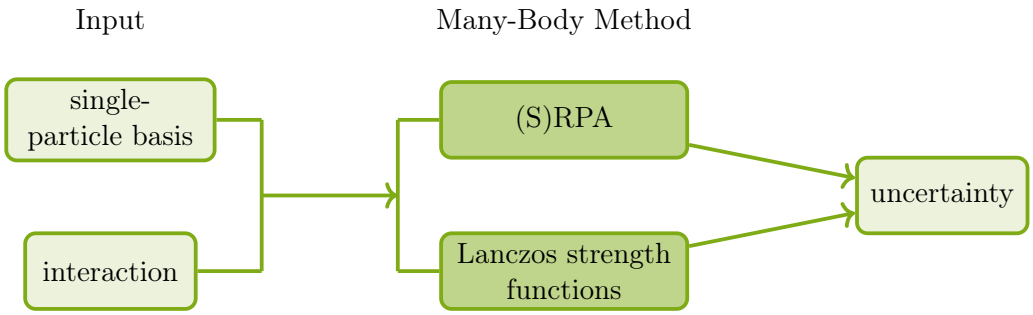

Figure II: Workflow for the determination of collective excitations. Starting with an interaction, a single-particle basis is chosen as input which is followed by the method itself, namely the (S)RPA or the Lanczos strength functions. Completing the investigation, an uncertainty estimation can be done.

The next chapters give an overview about the methods for the investigation of collective excitations employed throughout this thesis. As mentioned before and shown in Fig. II, this is the second step after choosing a single-particle basis for the calculation of strength distributions. There are two approaches for the investigation of collective excitations: The so-called random-phase approximation (RPA), which is introduced in Chapter 5, and extensions thereof, and a method based on the IT-NCSM, which is referred to as Lanczos strength function method. The first-mentioned approach applies the ph-formalism, introduced in Sec. 2.3.2, for the construction of ground and excited states. In general, ph and hp excitations are used in the framework of RPA, leading to the definition of excitation creation operators which are subsequently utilized for the derivation of the conditional equations with the aid of the equations-of-motion method and the variational principle. Depending on the specific form of the excitation creation operators, we address first- or second-order RPA. The SRPA, introduced in Chapter 6, includes additionally 2p2h (de-)excitations and is a natural emerging extension of RPA.

These methods are deduced for a generic basis. The introduction of RPA and SRPA and the derivation of their matrix equations is completed by a comparison of different input single-particle bases in Chapter 7. The discussion emphasizes the nascent peculiarities and partial simplifications.

Another access to strength distributions is an *ab initio* method, introduced in Chapter 8, which is based on an IT-NCSM calculation (c.f. Sec. 8.1). The so-called Lanczos strength function method exploits the simple Lanczos algorithm, which produces iteratively a tridiagonal matrix. This matrix can be diagonalized with standard techniques, yielding eigenstates in the Lanczos basis. These can be utilized in order to determine the transition strengths. This approach is restricted to light nuclei as the underlying IT-NCSM calculation, but allows a systematical improvement due to the *ab initio* character.

Applications of the methods for the investigation of collective excitations are presented in Part III.

5

Random-Phase Approximation

Contents

A standard tool for the description of collective excitations is the random-phase approximation (RPA). The idea of RPA was developed by David Bohm and David Pines [7, 8, 9] in quantum chemistry in the 1950s for the description of quantum many-body systems, for example electron gases.

Starting with an input single-particle basis (introduced in Sec. 3.3), it is not sufficient to use a single Slater determinant in the framework of RPA. The RPA ground state has a more complex structure and already contains correlations in form of particle-hole (ph) excitations of these basis states. Excited states are calculated as linear combinations of particle-hole and hole-particle (hp) excitations of the RPA ground state.

In the following chapter, the RPA equations are derived with the aid of the equation-of-motion method which is introduced first. Besides the full RPA, a simplification known as Tamm-Dancoff approximation (TDA) is presented. In contrast to RPA, the TDA does not contain any hp excitations. In both cases, the problem can be reduced to a matrix eigenvalue problem. All contributions to the RPA and TDA matrix, respectively, are determined for a coupled and an uncoupled single-particle basis and their properties are investigated. Additionally, the RPA with explicit three-body interaction is briefly compared to the NO2B approximation. The derivation follows Refs. [14, 17, 33, 64] and especially Ref. [70] (notation and steps) if not stated otherwise.

5.1 Derivation of RPA Equations

Several different ways of derivation lead to the RPA equations, for instance the time-dependent Hartree-Fock theory or the Green function formalism [33]. However, the following chapter addresses the derivation of the RPA equations based on the equations-of-motion method (EOM) following Refs. [33, 70]. Furthermore, different types of excitation creation operators are treated, leading to the full RPA and an approximation (TDA) and the solution exploiting the variational method is discussed.

5.1.1 Equations-of-Motion Method

For the derivation of the RPA equations with the help of the EOM method, we start with a definition of excitation creation operators (ECOs) $\hat{Q}^\dagger_\omega$ and the corresponding annihilators $\hat{Q}_\omega$

$$|\omega\rangle = \hat{Q}^\dagger_\omega |\mathrm{RPA}\rangle \qquad\qquad \hat{Q}_\omega |\omega\rangle = |\mathrm{RPA}\rangle \ . \tag{5.1}$$

The application of the ECOs on the RPA ground state $|\mathrm{RPA}\rangle$ creates excited states $|\omega\rangle$ while the annihilation operators are responsible for the reversed process of de-excitation back to the ground state. Here, the index ω represents a state including different quantum numbers $\omega = (n, J^\pi, M)$ with the number of the excited state n, the angular momentum J and its z-projection M and the parity π. For the annihilators, the additional relation

$$\hat{Q}_\omega |\mathrm{RPA}\rangle = 0 \qquad \forall\, \omega \tag{5.2}$$

holds, so a de-excitation of the ground state is not valid since the ground state is already the energetically lowest state. The operators in Eq. (5.1) can formally be expressed as dyadic

products of the ground state and the excited states

$$\hat{Q}_\omega^\dagger = |\omega\rangle \langle \mathrm{RPA}| \qquad \hat{Q}_\omega = |\mathrm{RPA}\rangle \langle \omega| \,. \tag{5.3}$$

Starting with the scalar product of excited states $|\omega\rangle$ and the ground state $|\mathrm{RPA}\rangle$ and inserting Eq. (5.1) and Eq. (5.2) yields

$$\langle \mathrm{RPA}|\omega\rangle = \langle \mathrm{RPA}| \hat{Q}_\omega^\dagger |\mathrm{RPA}\rangle = \langle \mathrm{RPA}| \hat{Q}_\omega |\mathrm{RPA}\rangle^* = 0 \qquad \forall\, \omega \,. \tag{5.4}$$

Hence, ground state and excited states are orthogonal. With these definitions and properties, the equations of motion can be derived. The starting point is the stationary Schrödinger equation

$$\hat{H} |\mathrm{RPA}\rangle = E_0 |\mathrm{RPA}\rangle \tag{5.5}$$

$$\hat{H} |\omega\rangle = E_\omega |\omega\rangle \qquad \forall \omega \tag{5.6}$$

with the ground-state energy E_0 and the excited-state energies E_ω. Combining the Schrödinger equation (5.6) with the definition of excitation creation and annihilation operators given in Eq. (5.1), we find

$$\hat{H} |\omega\rangle = \hat{H} \hat{Q}_\omega^\dagger |\mathrm{RPA}\rangle = E_\omega \hat{Q}_\omega^\dagger |\mathrm{RPA}\rangle \,. \tag{5.7}$$

The application of the creation operator to the Schrödinger equation

$$\hat{Q}_\omega^\dagger \hat{H} |\mathrm{RPA}\rangle = \hat{Q}_\omega^\dagger E_0 |\mathrm{RPA}\rangle = E_0 \hat{Q}_\omega^\dagger |\mathrm{RPA}\rangle \tag{5.8}$$

yields after subtraction of Eq. (5.7) from Eq. (5.8) the equations of motion

$$\begin{aligned} (\hat{H}\hat{Q}_\omega^\dagger - \hat{Q}_\omega^\dagger \hat{H}) |\mathrm{RPA}\rangle &= (E_\omega - E_0) \hat{Q}_\omega^\dagger |\mathrm{RPA}\rangle \\ [\hat{H}, \hat{Q}_\omega^\dagger] |\mathrm{RPA}\rangle &= (E_\omega - E_0) \hat{Q}_\omega^\dagger |\mathrm{RPA}\rangle \\ [\hat{H}, \hat{Q}_\omega^\dagger] |\mathrm{RPA}\rangle &= E_\omega^{\mathrm{RPA}} \hat{Q}_\omega^\dagger |\mathrm{RPA}\rangle \end{aligned} \tag{5.9}$$

with the commutator between the Hamiltonian and the excitation creation operator and the RPA excitation energy

$$E_\omega^{\mathrm{RPA}} = E_\omega - E_0 \tag{5.10}$$

which is the difference between the energy of the excited state and the ground-state energy. The equation of motion for the excitation creation operator $\hat{Q}_\omega^\dagger$ is then given by Eq. (5.9).

The RPA problem is exactly determined through the ground state $|\mathrm{RPA}\rangle$, the excitation energies E_ω^{RPA} and the excitation creation operators $\hat{Q}_\omega^\dagger$. Although the definition of the ground state is required within the theoretical framework, it is only presented implicitly and the explicit determination is not performed during a calculation. An advantage of the equtions-of-motion method lies in the choices of different ECOs resulting in natural extensions and systematic improvements of the method through higher-order ph excitations.

For the further derivation of the RPA equations, we consider the EOM by exploiting the variational principle, i.e., we focus on an arbitrary variation $\delta\hat{Q}$ of the excitation creation operator.

The RPA ground state and excited states are orthogonal as shown in Eq. (5.4). Dealing with an arbitrary variation of the ECO still requires the condition of being orthogonal to the ground state, since the variation spans the full model space. Thus, for the variation $\delta\hat{Q}^\dagger$, the following equation holds

$$\delta\hat{Q}\,|\mathrm{RPA}\rangle = 0\,. \tag{5.11}$$

With this condition, the overlap of the equation of motion (5.9) and the variation

$$\langle\delta\hat{Q}| = \langle\mathrm{RPA}|\,\delta\hat{Q} \tag{5.12}$$

is determined, leading to

$$\langle\mathrm{RPA}|\,\delta\hat{Q}[\hat{H},\hat{Q}^\dagger_\omega]\,|\mathrm{RPA}\rangle = \langle\mathrm{RPA}|\,\delta\hat{Q}\;E^{\mathrm{RPA}}_\omega\;\hat{Q}^\dagger_\omega\,|\mathrm{RPA}\rangle\,. \tag{5.13}$$

Subtracting vanishing terms using (5.2) yields

$$\begin{aligned}&\langle\mathrm{RPA}|\,\delta\hat{Q}[\hat{H},\hat{Q}^\dagger_\omega]\,|\mathrm{RPA}\rangle - \underbrace{\langle\mathrm{RPA}|\,[\hat{H},\hat{Q}^\dagger_\omega]}_{=0}\,\delta\hat{Q}\,|\mathrm{RPA}\rangle\\ &= E^{\mathrm{RPA}}_\omega\,\Big(\langle\mathrm{RPA}|\,\delta\hat{Q}\;\hat{Q}^\dagger_\omega\,|\mathrm{RPA}\rangle - \underbrace{\langle\mathrm{RPA}|\,\hat{Q}^\dagger_\omega}_{=0}\;\delta\hat{Q}\,|\mathrm{RPA}\rangle\Big)\,.\end{aligned} \tag{5.14}$$

These terms can be summarized in commutators which results in the generalized equation of motion

$$\langle\mathrm{RPA}|\,[\delta\hat{Q},[\hat{H},\hat{Q}^\dagger_\omega]]\,|\mathrm{RPA}\rangle = E^{\mathrm{RPA}}_\omega\;\langle\mathrm{RPA}|\,[\delta\hat{Q},\;\hat{Q}^\dagger_\omega]\,|\mathrm{RPA}\rangle\,. \tag{5.15}$$

So far, the structure of the variation as well as of the ECO are arbitrary. The general form of the EOM (5.15) is valid for any variation $\delta\hat{Q}$ which is orthogonal to the ground state as postulated in Eq. (5.11). For the next steps in the derivation, we need an ansatz for the structure of the ECOs.

5.1.2 First-Order RPA

The specific type of RPA depends on the choice of the ECOs. The standard or first-order RPA, dealt with in the following chapter, corresponds to an ECO which only contains 1p1h (de-)excitations. Restricting the ECOs to 1p1h excitations without any de-excitation in the ECOs reduces the random-phase approximation to the Tamm-Dancoff approximation (TDA) and is, thus, a simplification of the standard RPA. Additionally, the RPA ground state contains ph excitations, whereas the TDA preserves the HF ground state and allows ph contributions only for excited states. More details on the TDA are discussed in Sec. 5.1.4. Additionally including 2p2h (de-)excitations into the ECOs as improvement leads to the second-order RPA which is explained in Chapter 6. The restriction of the involved (de-)excitations to small

particle-hole model spaces yields approximate results. However, the RPA would reproduce the exact result if npnh excitations would be taken into account with $n \to A$.

As motivation of the choice of the structure of the ECOs, considerations of spherical tensors and ph and hp excitation creation operators, respectively, are done at first, followed by the specific ansatz of a first-order RPA which finally leads to the derivation of the RPA equations.

Creation and Annihilation Operators as Spherical Tensor Operators In the framework of RPA, the creation and annihilation operators always occur as pairs of fermion operators. A coupling to the correct angular momentum J with its projection quantum number M is guaranteed by using coupled pairs of fermion operators in the ECOs. Coupling the particle-hole basis to a certain angular momentum additionally leads to a reduced model space. Thus, we first make some general considerations on the relation of spherical tensors and the creation and annihilation operators and then present the further derivation of the RPA equations.

As mentioned in Sec. 2.2, the coupled basis contains a total angular momentum J and its projection M instead of the single angular momenta j_i and their corresponding z-components m_i of the single-particle states. Thus, for the following considerations, a new label for the collective index of the quantum numbers i is helpful

$$i = (i, m_i) \tag{5.16}$$

with the projection m_i and all other remaining quantum numbers i of the single-particle state i. In order to define a coupled product of a pair of fermion operators, i.e. a coupled creation operator $\hat{\mathcal{A}}^\dagger_{p\hbar}(JM)$, with the help of the coupled tensor product (2.19), we have to ensure that the involving operators, namely the creation and annihilation operators, are spherical tensors as well. As shown in App. A.2, the creation operator itself already is a spherical tensor, but for the annihilation operator some adaptions are necessary since it is not a spherical tensor. Multiplying the annihilation operator with a phase factor $(-1)^{j_i+m_i}$ and reversing the sign of the projection quantum number m_i of the operator leads to a spherical tensor

$$\hat{\tilde{a}}_i = (-1)^{j_i+m_i} \hat{a}_{i,-m_i} \tag{5.17}$$

with rank j_i. The spherical annihilation operator is denoted with a tilde. With these considerations, the coupled tensor product

$$\hat{\mathcal{A}}^\dagger_{p\hbar}(JM) = \left[\hat{a}^\dagger_p \hat{\tilde{a}}_\hbar\right]_{JM} \tag{5.18}$$

containing the spherical tensor operators $\hat{a}^\dagger_p$ and $\hat{\tilde{a}}_\hbar$ directly yields the coupled ph creation operator $\hat{\mathcal{A}}^\dagger_{p\hbar}(JM)$. The coupled tensor product can be calculated as

$$\begin{aligned}\left[\hat{a}_p^\dagger \hat{\tilde{a}}_\hbar\right]_{JM} &= \sum_{m_p,m_h} (-1)^{j_h+m_h} \begin{pmatrix} j_p & j_h & J \\ m_p & m_h & M \end{pmatrix} \hat{a}^\dagger_{p,m_p} \hat{a}_{\hbar,-m_h} \\ &= \sum_{m_p,m_h} (-1)^{j_h-m_h} \begin{pmatrix} j_p & j_h & J \\ m_p & -m_h & M \end{pmatrix} \hat{a}^\dagger_{p,m_p} \hat{a}_{\hbar,m_h}\end{aligned} \tag{5.19}$$

$$= \sum_{m_p,m_h} (-1)^{j_h-m_h} \begin{pmatrix} j_p & j_h & J \\ m_p & -m_h & M \end{pmatrix} \hat{\mathcal{A}}^\dagger_{ph} = \hat{\mathcal{A}}^\dagger_{p\hbar}(JM) \tag{5.20}$$

with a phase factor, a Clebsch-Gordan coefficient and the uncoupled ph creation operator $\hat{\mathcal{A}}^\dagger_{ph} = \hat{a}_p^\dagger \hat{a}_h$.

Analogously, a coupled annihilation operator is build. As for the single-particle annihilation operator itself, it is not sufficient to consider the Hermitian conjugate $\hat{\mathcal{A}}_{p\hbar}(JM)$ of the coupled ph excitation operator, since it is no spherical tensor as shown in App. A.2. As a consequence, the coupled annihilation operator is defined as tensor product of the spherical uncoupled annihilation operator and the creation operator

$$\hat{\tilde{\mathcal{A}}}_{p\hbar}(JM) = (-1)^{J+M} \hat{\mathcal{A}}_{p\hbar}(J,-M) = \left[\hat{\tilde{a}}_p \hat{a}_\hbar^\dagger\right]_{JM} . \tag{5.21}$$

In total, the non-spherical coupled operator $\hat{\mathcal{A}}_{p\hbar}(JM)$ is modified by a phase factor and a change of the sign of the projection quantum number M, leading to a spherical tensor operator $\hat{\tilde{\mathcal{A}}}_{p\hbar}(JM)$. A comparison of the definition of the spherical annihilation operator $\hat{\tilde{a}}_i$ (5.17) and the spherical coupled annihilation operator $\hat{\mathcal{A}}_{p\hbar}(JM)$ shows the same modifications.

In actual calculations, only one selected M is required due to spherical symmetry. Usually, we choose $M = 0$, because in this case the spherical annihilation operators are directly connected to the corresponding non-spherical ones via

$$\hat{\tilde{\mathcal{A}}}_{p\hbar}(J0) = (-1)^J \hat{\mathcal{A}}_{p\hbar}(J0) . \tag{5.22}$$

Tab. 5.1 gives an overview about the discussed coupled and uncoupled versions of the ph (de-)excitation creation operators. A discussion in more detail about the spherical creation and annihilation operators can be found in App. A.2. With these considerations we can finally make an ansatz for the excitation creation operators in the RPA framework.

Ansatz for ECOs in RPA The first-order RPA allows — as the name suggests — only 1p1h (de-)excitations in the excitation creation operator. The requirements for the ansatz for the RPA are, besides allowing $\hat{a}_p^\dagger \hat{a}_h$ and $\hat{a}_h^\dagger \hat{a}_p$ as possible excitations, additionally providing the correct quantum numbers. Hence, an ansatz for the uncoupled first-order ECOs is given

operator	definition		
$\hat{a}_i^\dagger$		-	spherical tensor
$\hat{a}_i$		-	no spherical tensor
$\hat{\tilde{a}}_i$	$(-1)^{j_i+m_i}\hat{a}_{\bar{i},-m_i}$	-	spherical tensor
$\hat{\mathcal{A}}_{ph}^\dagger$	$\hat{a}_p^\dagger \hat{a}_h$	uncoupled	
$\hat{\mathcal{A}}_{ph}$	$\hat{a}_h^\dagger \hat{a}_p$	uncoupled	
$\hat{\mathcal{A}}_{p\hbar}^\dagger(JM)$	$\left[\hat{a}_p^\dagger \hat{\tilde{a}}_\hbar\right]_{JM}$	coupled	spherical tensor
$\hat{\mathcal{A}}_{p\hbar}(JM)$	$\left(\hat{\mathcal{A}}_{p\hbar}^\dagger(JM)\right)^\dagger$	coupled	no spherical tensor
$\hat{\tilde{\mathcal{A}}}_{p\hbar}(JM)$	$\left[\hat{\tilde{a}}_p \hat{a}_\hbar^\dagger\right]_{JM}$	coupled	spherical tensor

Table 5.1: Overview of creation and annihilation operators which occur in the ph formalism. Besides the single particle and hole creation and annihilation operators, respectively, there exist operators for the combined ph (de-)excitation in the coupled and uncoupled version. These operators are partially redefined in order to obtain spherical tensor operators.

by a linear combination of ph and hp excitation creation operators

$$\begin{aligned}\hat{Q}_\omega^\dagger &= \sum_{p,h}\left(X_{ph}^\omega\ \hat{a}_p^\dagger \hat{a}_h - Y_{ph}^\omega\ \hat{a}_h^\dagger \hat{a}_p\right) \\ &= \sum_{p,h}\left(X_{ph}^\omega\ \hat{\mathcal{A}}_{ph}^\dagger - Y_{ph}^\omega\ \hat{\mathcal{A}}_{ph}\right).\end{aligned} \tag{5.23}$$

The coefficients X_{ph}^ω and Y_{ph}^ω, respectively, are the so-called forward and backward amplitudes. The corresponding coupled first-order ECOs

$$\hat{Q}_\omega^\dagger = \sum_{p,\hbar}\left(\mathcal{X}_{p\hbar}^\omega\ \hat{\mathcal{A}}_{p\hbar}^\dagger(JM) - \mathcal{Y}_{p\hbar}^\omega\ \hat{\tilde{\mathcal{A}}}_{p\hbar}(JM)\right) \tag{5.24}$$

include the spherical tensor operators $\hat{\mathcal{A}}_{p\hbar}^\dagger(JM)$ and $\hat{\tilde{\mathcal{A}}}_{p\hbar}(JM)$ defined in Eq. (5.20) and Eq. (5.21), respectively. The amplitudes $\mathcal{X}_{p\hbar}^\omega$ and $\mathcal{Y}_{p\hbar}^\omega$ in the coupled first-order ECOs differ from the uncoupled amplitudes, which is indicated by different indices.

For the following considerations, the uncoupled formulation of excitation creation operators is used. All statements made with this simplification remain valid for the coupled basis. Therefore, using the uncoupled basis is useful, since it is clearer and thus more convenient. A transformation to the coupled basis is possible at any time. Thus, the final result is converted to the coupled formulation, c.f. Sec. 5.2.1 and Sec. 5.2.2.

RPA Ground State Before we address the RPA equations, additional considerations of the connection between the first-order ECOs and the RPA ground state are done. The structure

of the ECOs is the reason why the RPA ground state already contains ph excitations of the basis state. If we apply $\hat{Q}_\omega$ to a reference state $|\mathrm{SD}\rangle$, it yields

$$\begin{aligned}\hat{Q}_\omega |\mathrm{SD}\rangle &= \sum_{p,h} \left(X_{ph}^{\omega *}\ \hat{a}_h^\dagger \hat{a}_p - Y_{ph}^{\omega *}\ \hat{a}_p^\dagger \hat{a}_h \right) |\mathrm{SD}\rangle \\ &= -\sum_{p,h} Y_{ph}^{\omega *}\ \hat{a}_p^\dagger \hat{a}_h |\mathrm{SD}\rangle \,.\end{aligned} \tag{5.25}$$

The first term evaluates to zero, because the Slater determinant does not contain particles above the Fermi level and thus $\hat{a}_h^\dagger \hat{a}_p |\mathrm{SD}\rangle = 0$. According to Eq. (5.2), the second term $\hat{a}_p^\dagger \hat{a}_h |\mathrm{SD}\rangle$ should be zero for $Y_{ph}^{\omega *} \neq 0$. However, this is not the case for the HF ground state and it can only be fulfilled if the RPA ground state $|\mathrm{RPA}\rangle$ already contains ph correlations. If $Y_{ph}^{\omega *} = 0$, the problem is reduced to a TDA, i.e. only ph excitations are allowed within the definition of the ECOs.

RPA Equations I For the further derivation of the RPA equations, the definition of the variation of the first-order ECOs $\delta\hat{Q}$ is needed in the generalized form of the equation of motion (5.15). The variation of Eq. (5.23) is given by

$$\delta\hat{Q} = \sum_{p,h} \left(\delta X_{ph}^{\omega *}\ \hat{a}_h^\dagger \hat{a}_p - \delta Y_{ph}^{\omega *}\ \hat{a}_p^\dagger \hat{a}_h \right). \tag{5.26}$$

Since the ph excitations and the hp excitations are independent among themselves and from each other, we can vary them independently and choose $\delta X_{ph}^{\omega *} = 0$ and $\delta Y_{ph}^{\omega *} = 0$, respectively. This results in two coupled equations for the ph and hp excitations

$$\begin{aligned}\delta X_{ph}^{\omega *}: &\quad \langle \mathrm{RPA}| \left[\hat{a}_h^\dagger \hat{a}_p, [\hat{H}, \hat{Q}_\omega^\dagger]\right] |\mathrm{RPA}\rangle = E_\omega^{\mathrm{RPA}} \langle \mathrm{RPA}| \left[\hat{a}_h^\dagger \hat{a}_p, \hat{Q}_\omega^\dagger\right] |\mathrm{RPA}\rangle \\ \delta Y_{ph}^{\omega *}: &\quad \langle \mathrm{RPA}| \left[\hat{a}_p^\dagger \hat{a}_h, [\hat{H}, \hat{Q}_\omega^\dagger]\right] |\mathrm{RPA}\rangle = E_\omega^{\mathrm{RPA}} \langle \mathrm{RPA}| \left[\hat{a}_p^\dagger \hat{a}_h, \hat{Q}_\omega^\dagger\right] |\mathrm{RPA}\rangle\end{aligned} \tag{5.27}$$

These equations determine the amplitudes X_{ph}^ω and Y_{ph}^ω. Since the RPA ground state $|\mathrm{RPA}\rangle$ is unknown, the equations of determination are not directly solvable but only an iterative solution is possible.

So far, the EOMs (5.27) are derived in an exact analytical way. Within the iterative solution, the (de-)excitation creation operators and the ground state are obtained simultaneously in a self-consistent way. The first step in this framework is assuming a solution. With this, the above equations are solved, achieving a new solution which is then again used as starting point. This procedure stops when a solution is obtained which is self-consistent. This approach is referred to as self-consistent RPA [22]. Since this type of solving costs more effort, strictly speaking the number of iterations times the effort, the EOM expectation values (5.27) in the standard RPA are approximated within the so called quasi-boson approximation.

Quasi-Boson Approximation (QBA) The EOMs (5.27) depend on the expectation value with respect to the RPA ground state $|\mathrm{RPA}\rangle$. For a comparison with the QBA, the expectation

value is evaluated to

$$\begin{aligned}
&\langle \mathrm{RPA}|[\hat{a}_h^\dagger \hat{a}_p, \hat{Q}_\omega^\dagger]\,|\mathrm{RPA}\rangle \\
&\quad = \sum_{p',h'} X_{p'h'}^{\omega} \langle \mathrm{RPA}|\,[\hat{a}_h^\dagger \hat{a}_p, \hat{a}_{p'}^\dagger \hat{a}_{h'}]\,|\mathrm{RPA}\rangle + 0 \\
&\quad = \sum_{p',h'} X_{p'h'}^{\omega} \left(\delta_{pp'}\delta_{hh'} - \delta_{pp'} \langle \mathrm{RPA}|\,\hat{a}_{h'}\hat{a}_h^\dagger\,|\mathrm{RPA}\rangle - \delta_{hh'} \langle \mathrm{RPA}|\,\hat{a}_{p'}^\dagger \hat{a}_p\,|\mathrm{RPA}\rangle\right) \\
&\quad = X_{ph}^{\omega} - \sum_{h'} X_{ph'}^{\omega} \langle \mathrm{RPA}|\,\hat{a}_{h'}\hat{a}_h^\dagger\,|\mathrm{RPA}\rangle - \sum_{p'} X_{p'h}^{\omega} \langle \mathrm{RPA}|\,\hat{a}_{p'}^\dagger \hat{a}_p\,|\mathrm{RPA}\rangle
\end{aligned} \tag{5.28}$$

Here, the second and third term can be neglected, since they are expected to be small if there is no phase correlation between the matrix elements and the coefficients of excited states. Furthermore, this is also the origin of the name random phase approximation.

As we can see here, the rank of a commutator between two operators is one lower than the rank of the product of the involved operators. For instance, the commutator of two one-body operators is again a one-body operator. Thus, two-body correlations of the ground state have smaller impact which is important if the QBA and hence not the exact wave function for the ground state is used.

Another way to motivate this behavior is the introduction of an approximation. Regarding the fermion operators in Eq. (5.27), we notice that only pairs of them occur. The assumption made within this approximation is that an even number of fermion operators behave as boson-like operators. Mathematically, the expectation value is evaluated with a single Slater determinant $|\mathrm{SD}\rangle$ instead of the RPA ground state, since the RPA ground state in the equation of motion is substituted by the one originated in for instance the HF framework. This results in

$$\begin{aligned}
\langle \mathrm{RPA}|\,[\hat{a}_h^\dagger \hat{a}_p, \hat{a}_{p'}^\dagger \hat{a}_{h'}]\,|\mathrm{RPA}\rangle &\overset{\mathrm{QBA}}{\approx} \langle \mathrm{SD}|\,[\hat{a}_h^\dagger \hat{a}_p, \hat{a}_{p'}^\dagger \hat{a}_{h'}]\,|\mathrm{SD}\rangle \\
&= \langle \mathrm{SD}|\,(\delta_{pp'}\hat{a}_h^\dagger \hat{a}_{h'} - \delta_{hh'}\hat{a}_{p'}^\dagger \hat{a}_p)\,|\mathrm{SD}\rangle \\
&= \delta_{pp'}\delta_{hh'}.
\end{aligned} \tag{5.29}$$

Here, the commutator

$$\left[\hat{a}_h^\dagger \hat{a}_p, \hat{a}_{p'}^\dagger \hat{a}_{h'}\right] = \delta_{pp'}\hat{a}_h^\dagger \hat{a}_{h'} - \delta_{hh'}\hat{a}_{p'}^\dagger \hat{a}_p \tag{5.30}$$

is exactly determined. The detailed derivation of this commutator is shown in App. A.1. The second term in Eq. (5.29) is zero since $\hat{a}_p\,|\mathrm{SD}\rangle = 0$.

We can define new boson-like operators B_i and B_j containing fermionic ph operators

$$B_i = \hat{a}_{h'}^\dagger \hat{a}_{p'} \qquad i = (h', p') \tag{5.31}$$

$$B_j^\dagger = \hat{a}_p^\dagger \hat{a}_h \qquad j = (h, p) \tag{5.32}$$

for which the basic bosonic commutator yields

$$\left[B_i, B_j^\dagger\right] = \delta_{ij}. \tag{5.33}$$

with $\delta_{ij} = \delta_{pp'}\delta_{hh'}$, c.f. Refs. [64, 70]. The name quasi-boson approximation originates from the fact that the expectation values of the commutator in Eq. (5.30) with a single Slater determinant instead of the RPA ground state can be identified with a commutator of two bosonic operators. But the QBA is still an approximation, since operator contributions form the fermionic creators and annihilators are neglected. It would be exact if the ph pair operators were real bosonic operators.

RPA Equations II In order to derive the final result for the RPA equations, Eq. (5.27) is used including the QBA, leading to

$$\begin{aligned}
\langle \mathrm{SD}| \left[\hat{a}_h^\dagger \hat{a}_p, [\hat{H}, \hat{Q}_\omega^\dagger]\right] |\mathrm{SD}\rangle &= E_\omega^{\mathrm{RPA}} \langle \mathrm{SD}| \left[\hat{a}_h^\dagger \hat{a}_p, \hat{Q}_\omega^\dagger\right] |\mathrm{SD}\rangle \\
\langle \mathrm{SD}| \left[\hat{a}_p^\dagger \hat{a}_h, [\hat{H}, \hat{Q}_\omega^\dagger]\right] |\mathrm{SD}\rangle &= E_\omega^{\mathrm{RPA}} \langle \mathrm{SD}| \left[\hat{a}_p^\dagger \hat{a}_h, \hat{Q}_\omega^\dagger\right] |\mathrm{SD}\rangle
\end{aligned} \tag{5.34}$$

The QBA allows for some simplifications since it is known that $\hat{a}_p |\mathrm{SD}\rangle = 0$ and $\langle \mathrm{SD}| \hat{a}_p^\dagger = 0$. Hence the (outer) commutators in the above equations only have one non-zero term. The right-hand side of the first equation is evaluated by inserting the definition of the excitation creation operators (5.23)

$$\begin{aligned}
&\langle \mathrm{SD}| \hat{a}_h^\dagger \hat{a}_p [\hat{H}, \hat{Q}_\omega^\dagger] |\mathrm{SD}\rangle \\
&\quad = E_\omega^{\mathrm{RPA}} \langle \mathrm{SD}| \hat{a}_h^\dagger \hat{a}_p \hat{Q}_\omega^\dagger |\mathrm{SD}\rangle \\
&\quad = E_\omega^{\mathrm{RPA}} \sum_{p',h'} \left(X_{p'h'}^\omega \langle \mathrm{SD}| \hat{a}_h^\dagger \hat{a}_p \hat{a}_{p'}^\dagger \hat{a}_{h'} |\mathrm{SD}\rangle - Y_{p'h'}^\omega \langle \mathrm{SD}| \hat{a}_h^\dagger \hat{a}_p \hat{a}_{h'}^\dagger \hat{a}_{p'} |\mathrm{SD}\rangle \right) \\
&\quad = E_\omega^{\mathrm{RPA}} \sum_{p',h'} \left(X_{p'h'}^\omega \delta_{hh'} \delta_{pp'} - Y_{p'h'}^\omega \cdot 0 \right) \\
&\quad = E_\omega^{\mathrm{RPA}} \, X_{ph}^\omega \,,
\end{aligned} \tag{5.35}$$

connecting the expectation value to the X_{ph}^ω-amplitude. Analogously, the right-hand side of the second equation results in

$$\begin{aligned}
&\langle \mathrm{SD}| [\hat{H}, \hat{Q}_\omega^\dagger] \hat{a}_p^\dagger \hat{a}_h |\mathrm{SD}\rangle \\
&\quad = E_\omega^{\mathrm{RPA}} \langle \mathrm{SD}| \hat{Q}_\omega^\dagger \hat{a}_p^\dagger \hat{a}_h |\mathrm{SD}\rangle \\
&\quad = E_\omega^{\mathrm{RPA}} \sum_{p',h'} \left(X_{p'h'}^\omega \langle \mathrm{SD}| \hat{a}_{p'}^\dagger \hat{a}_{h'} \hat{a}_p^\dagger \hat{a}_h |\mathrm{SD}\rangle - Y_{p'h'}^\omega \langle \mathrm{SD}| \hat{a}_{h'}^\dagger \hat{a}_{p'} \hat{a}_p^\dagger \hat{a}_h |\mathrm{SD}\rangle \right) \\
&\quad = E_\omega^{\mathrm{RPA}} \sum_{p',h'} \left(X_{p'h'}^\omega \cdot 0 - Y_{p'h'}^\omega \delta_{hh'} \delta_{pp'} \right) = -E_\omega^{\mathrm{RPA}} \, Y_{ph}^\omega \,,
\end{aligned} \tag{5.36}$$

which gives a relation to the Y^{ω}_{ph}-amplitude. In summary, we find the relations

$$\begin{aligned}\langle \mathrm{SD}|\, \hat{a}^{\dagger}_h \hat{a}_p [\hat{H}, \hat{Q}^{\dagger}_{\omega}]\, |\mathrm{SD}\rangle &= E^{\mathrm{RPA}}_{\omega}\, X^{\omega}_{ph}\,, \\ \langle \mathrm{SD}|\, [\hat{H}, \hat{Q}^{\dagger}_{\omega}] \hat{a}^{\dagger}_p \hat{a}_h\, |\mathrm{SD}\rangle &= -E^{\mathrm{RPA}}_{\omega}\, Y^{\omega}_{ph}\,.\end{aligned} \tag{5.37}$$

In order to standardize the results, the second equation is reformulated to bring it to a similar form as the first one

$$\langle \mathrm{SD}|\, \hat{a}^{\dagger}_h \hat{a}_p [\hat{H}, \hat{Q}_{\omega}]\, |\mathrm{SD}\rangle^{*} = E^{\mathrm{RPA}}_{\omega}\, Y^{\omega}_{ph}\,. \tag{5.38}$$

With all these considerations, we obtain

$$\begin{aligned}\langle \mathrm{SD}|\, \hat{a}^{\dagger}_h \hat{a}_p [\hat{H}, \hat{Q}^{\dagger}_{\omega}]\, |\mathrm{SD}\rangle \;\; &= E^{\mathrm{RPA}}_{\omega}\, X^{\omega}_{ph}\,, \\ \langle \mathrm{SD}|\, \hat{a}^{\dagger}_h \hat{a}_p [\hat{H}, \hat{Q}_{\omega}]\, |\mathrm{SD}\rangle^{*} &= E^{\mathrm{RPA}}_{\omega}\, Y^{\omega}_{ph}\,.\end{aligned} \tag{5.39}$$

The last step in the derivation of the RPA equations is inserting the definition of the ph-excitation creation operator (5.23) which gives the final result

$$\sum_{p',h'} (X^{\omega}_{p'h'} \underbrace{\langle \mathrm{SD}|\, \hat{a}^{\dagger}_h \hat{a}_p [\hat{H}, \hat{a}^{\dagger}_{p'} \hat{a}_{h'}]\, |\mathrm{SD}\rangle}_{A_{ph,p'h'}} - Y^{\omega}_{p'h'} \underbrace{\langle \mathrm{SD}|\, \hat{a}^{\dagger}_h \hat{a}_p [\hat{H}, \hat{a}^{\dagger}_{h'} \hat{a}_{p'}]\, |\mathrm{SD}\rangle)}_{-B_{ph,p'h'}} = E^{\mathrm{RPA}}_{\omega}\, X^{\omega}_{ph}\,, \tag{5.40}$$

$$\sum_{p',h'} (X^{\omega *}_{p'h'} \underbrace{\langle \mathrm{SD}|\, \hat{a}^{\dagger}_h \hat{a}_p [\hat{H}, \hat{a}^{\dagger}_{h'} \hat{a}_{p'}]\, |\mathrm{SD}\rangle}_{-B_{ph,p'h'}} - Y^{\omega *}_{p'h'} \underbrace{\langle \mathrm{SD}|\, \hat{a}^{\dagger}_h \hat{a}_p [\hat{H}, \hat{a}^{\dagger}_{p'} \hat{a}_{h'}]\, |\mathrm{SD}\rangle)^{*}}_{A_{ph,p'h'}} = E^{\mathrm{RPA}}_{\omega}\, Y^{\omega}_{ph}\,, \tag{5.41}$$

where the same expectation values occur in both equations and are abbreviated with $A_{ph,p'h'}$ and $B_{ph,p'h'}$ leading to

$$\begin{aligned}\sum_{p',h'} \left(X^{\omega}_{p'h'}\; A_{ph,p'h'} + Y^{\omega}_{p'h'}\; B_{ph,p'h'} \right) &= E^{\mathrm{RPA}}_{\omega}\, X^{\omega}_{ph}\,, \\ \sum_{p',h'} \left(-X^{\omega}_{p'h'}\; B^{*}_{ph,p'h'} - Y^{\omega}_{p'h'}\; A^{*}_{ph,p'h'} \right) &= E^{\mathrm{RPA}}_{\omega}\, Y^{\omega}_{ph}\,.\end{aligned} \tag{5.42}$$

The A and B matrices are expectation values of the form

$$A_{ph,p'h'} = \langle \mathrm{SD}|\, \hat{a}^{\dagger}_h \hat{a}_p [\hat{H}, \hat{a}^{\dagger}_{p'} \hat{a}_{h'}]\, |\mathrm{SD}\rangle \tag{5.43}$$

$$B_{ph,p'h'} = -\langle \mathrm{SD}|\, \hat{a}^{\dagger}_h \hat{a}_p [\hat{H}, \hat{a}^{\dagger}_{h'} \hat{a}_{p'}]\, |\mathrm{SD}\rangle\,. \tag{5.44}$$

The B matrix is the so-called correlation matrix. Replacing the definitions of the RPA

matrices leads to a more compact version of the RPA equations

$$\begin{aligned} \sum_j \left(A_{i,j}\, X_j^\omega + B_{i,j}\, Y_j^\omega \right) &= E_\omega^{\mathrm{RPA}}\, X_i^\omega \\ \sum_j \left(-B_{i,j}^*\, X_j^\omega - A_{i,j}^*\, Y_j^\omega \right) &= E_\omega^{\mathrm{RPA}}\, Y_i^\omega \end{aligned} \tag{5.45}$$

where the collective indices $i = (p, h)$ and $j = (p', h')$ are used for the matrix notation. Finally, these equations are expressed in matrix form as

$$\begin{pmatrix} A & B \\ -B^* & -A^* \end{pmatrix} \begin{pmatrix} X^\omega \\ Y^\omega \end{pmatrix} = E_\omega^{\mathrm{RPA}} \begin{pmatrix} X^\omega \\ Y^\omega \end{pmatrix}. \tag{5.46}$$

The RPA equations are reduced to an eigenvalue problem. The solution consists of the eigenenergies E_ω^{RPA} and the forward and backward amplitudes X^ω and Y^ω, allowing for the calculation of further properties as for instance transition strengths or the dipole polarizability. The matrix A is Hermitian whereas the B-matrix is symmetric. Thus, the RPA supermatrix

$$R = \begin{pmatrix} A & B \\ -B^* & -A^* \end{pmatrix} \tag{5.47}$$

is non-Hermitian, and the eigenvalues are not necessarily real. The RPA supermatrix has block structure and its dimension is $(2n) \times (2n)$ with the number n of ph pairs, indicated by the indices p and h, since the submatrices A and B have dimension $n \times n$.

Before we determine the explicit form of the A and B matrix in Sec. 5.2, we discuss a few properties of the RPA equations.

5.1.3 Properties of RPA Eigenvalue Problem

The solution of the RPA eigenvalue problem, following Refs. [33, 64, 70], yields both amplitudes as eigenvector and additionally the eigenenergy. For every eigenvector (X^ω, Y^ω) with corresponding energy eigenvalue E_ω^{RPA} we find a second solution with eigenvector $(X^{\omega *}, Y^{\omega *})$ with corresponding eigenenergy $-E_\omega^{\mathrm{RPA}*}$. This can easily be shown by inserting the new solution in the RPA matrix equation (5.46), yielding a complex conjugate version of the original equation. Since the energy eigenvalue corresponds to a negative excitation energy, the second solution is not physical. The reason for the second solution lies in the block structure and the non-hermiticity of the RPA supermatrix and the solutions with positive energy eigenvalue already form a complete set of eigenstates.

Although the RPA problem is a non-hermitian eigenvalue problem, its solutions obey the orthogonality relation

$$\delta_{\omega\omega'} = \sum_{p,h} X_{ph}^{\omega' *} X_{ph}^\omega - Y_{ph}^{\omega' *} Y_{ph}^\omega \tag{5.48}$$

and the completeness relation

$$\delta_{ph}\delta_{p'h'} = \sum_{\omega} X^{\omega *}_{ph} X^{\omega}_{p'h'} - Y^{\omega *}_{ph} Y^{\omega}_{p'h'} \,. \tag{5.49}$$

For the energy of the RPA ground state $|\mathrm{RPA}\rangle$, we find

$$\langle \mathrm{RPA}| \, \hat{H} \, |\mathrm{RPA}\rangle = \langle \mathrm{SD}| \, \hat{H} \, |\mathrm{SD}\rangle - \sum_{\omega} E^{\mathrm{RPA}}_{\omega} \sum_{p,h} |Y^{\omega}_{ph}|^2 \,. \tag{5.50}$$

Thus, the energy of the RPA ground state is lower than the ground state energy. Utilizing Eq. (5.2), the RPA ground state can be constructed to

$$|\mathrm{RPA}\rangle = N_0 \exp\Big(\frac{1}{2} \sum_{\substack{ph \\ p'h'}} Z_{ph,p'h'} \hat{a}^{\dagger}_{p} \hat{a}_{h} \hat{a}^{\dagger}_{p'} \hat{a}_{h'} \Big) \, |\mathrm{SD}\rangle \tag{5.51}$$

with

$$\sum_{p,h} X^{\omega *}_{ph} Z_{ph,p'h'} = Y^{\omega *}_{p'h'} \qquad \forall \, \omega \tag{5.52}$$

as coefficients. The creation and annihilation operators are part of the exponent. This structure is characteristic for coherent states.

5.1.4 Tamm-Dancoff Approximation

A simplification of the standard RPA is the so-called Tamm-Dancoff approximation (TDA), which is less sophisticated since it only contains the ph part in the excitation creation operator. Besides the excitation creation operator in the uncoupled and coupled version, the TDA ground state and the TDA equations are discussed in the following.

TDA Excitation Creation Operator The uncoupled TDA excitation creation operator is defined as linear combination of ph excitations

$$\hat{Q}^{\dagger}_{\omega} = \sum_{p,h} X^{\omega}_{ph} \; \hat{a}^{\dagger}_{p} \hat{a}_{h} = \sum_{p,h} X^{\omega}_{ph} \; \hat{\mathcal{A}}^{\dagger}_{ph}. \tag{5.53}$$

Analogously, the coupled TDA excitation operator is given by

$$\hat{Q}^{\dagger}_{\omega} = \sum_{p,h} X^{\omega}_{p\hbar} \; \hat{\mathcal{A}}^{\dagger}_{p\hbar}(JM). \tag{5.54}$$

This corresponds to the definition of the ECO in the RPA (5.23) with the amplitude $Y^{\omega}_{ph} = 0$ to ensure that only ph excitations are allowed.

Analogous to standard RPA, in the TDA framework it is required that a further de-excitation of the energetically lowest possible state, which is the ground state $|\mathrm{TDA}\rangle$,

$$\hat{Q}_\omega \, |\mathrm{TDA}\rangle = 0 \qquad \forall\, \omega \tag{5.55}$$

is not physical.

TDA ground state According to Eq. (5.25), the RPA ground state is not equivalent to a single Slater determinant because of missing ph correlations. With Eq. (5.55) follows $\hat{a}_h^\dagger \hat{a}_p \, |\mathrm{TDA}\rangle = 0$ which holds true for a single Slater determinant $|\mathrm{SD}\rangle$ and thus

$$|\mathrm{TDA}\rangle = |\mathrm{SD}\rangle \ . \tag{5.56}$$

Therefore, a single Slater determinant fulfills the condition of the TDA ground state.

TDA equations As mentioned before, there are no hp excitations and thus the Y_{ph}^ω amplitudes are zero. Consequently, the B matrix does not exist for the TDA, which originally arises due to the hp excitations in the RPA ECOs. Thus, the TDA eigenvalue problem reduces to

$$AX^\omega = E_\omega^{\mathrm{TDA}} \, X^\omega, \tag{5.57}$$

which can be easily seen in the derivation of RPA equations with $Y_{ph}^\omega = 0$.

5.2 Determination of RPA Matrices

The RPA eigenvalue problem (5.46) depends on the A and B matrix which themselves consist of nested commutators of the ph (de-)excitation creation operator and the Hamiltonian. In the following chapter, these RPA matrices are determined for both the coupled and uncoupled ECOs, respectively, for the sake of completeness. As mentioned before, the transformation of the uncoupled to the coupled version is possible at any time. In actual calculations, the coupled basis is used. We start with some general considerations on the commutators of the Hamiltonian and ph creation operators on operator level, before we derive the explicit form of the uncoupled A matrix which we finally convert to the coupled formulation. Afterwards, the same procedure is done for the B matrix.

5.2.1 Explicit Form of the A Matrix

The A matrix (5.43) contains a commutator of the Hamiltonian and pairs of creation and annihilation operators. The starting point is a Hamiltonian $\hat{H}$ with kinetic energy $\hat{T}$ and a two-body interaction $\hat{V}_{\mathrm{NN}}$ which is given in Eq. (3.3). The result for an additional three-body interaction $\hat{V}_{\mathrm{3N}}$ is presented in the next Sec. 5.3. First, the inner commutator of the Hamiltonian and the particle-hole creation operator of the form $\hat{a}_{p'}^\dagger \hat{a}_{h'}$ is evaluated

$$\begin{aligned} \left[\hat{H}, \hat{a}_{p'}^\dagger \hat{a}_{h'}\right] &= \left[\hat{T} + \hat{V}_{\mathrm{NN}}\right] \\ &= \left[\hat{T}, \hat{a}_{p'}^\dagger \hat{a}_{h'}\right] + \left[\hat{V}_{\mathrm{NN}}, \hat{a}_{p'}^\dagger \hat{a}_{h'}\right] . \end{aligned} \tag{5.58}$$

The claim is to leave the derivation general as long as possible. Thus, the (anti-)commutator relations given in App. A.1 are applied and the first term in Eq. (5.58) is calculated to

$$\begin{aligned}\left[\hat{T}, \hat{a}^\dagger_{p'}\hat{a}_{h'}\right] &= \sum_{i,i'} t_{ii'} \left[\hat{a}^\dagger_i \hat{a}_{i'}, \hat{a}^\dagger_{p'}\hat{a}_{h'}\right] \\ &= \sum_i \left(t_{p',i}\hat{a}^\dagger_i \hat{a}_{h'} - t_{i,h'}\hat{a}^\dagger_{p'}\hat{a}_i\right).\end{aligned} \tag{5.59}$$

Analogously, the commutator of the two-body interaction and the ph excitation operator yields

$$\begin{aligned}\left[\hat{V}_{\mathrm{NN}}, \hat{a}^\dagger_{p'}\hat{a}_{h'}\right] &= \frac{1}{4}\sum_{ij,i'j'} \bar{v}_{ij,i'j'} \left[\hat{a}^\dagger_i \hat{a}^\dagger_j \hat{a}_{j'}\hat{a}_{i'}, \hat{a}^\dagger_{p'}\hat{a}_{h'}\right] \\ &= \frac{1}{4}\sum_{ij,i'j'} \bar{v}_{ij,i'j'} \left(\hat{a}^\dagger_i \hat{a}^\dagger_j \left[\hat{a}_{j'}\hat{a}_{i'}, \hat{a}^\dagger_{p'}\hat{a}_{h'}\right] + \left[\hat{a}^\dagger_i \hat{a}^\dagger_j, \hat{a}^\dagger_{p'}\hat{a}_{h'}\right]\hat{a}_{j'}\hat{a}_{i'}\right) \\ &= \frac{1}{4}\sum_{ij,j'} \left(\bar{v}_{ij,p'j'} - \bar{v}_{ij,j'p'}\right)\hat{a}^\dagger_i \hat{a}^\dagger_j \hat{a}_{j'}\hat{a}_{h'} + \frac{1}{4}\sum_{i,i'j'} \left(\bar{v}_{ih',i'j'} - \bar{v}_{ih',j'i'}\right)\hat{a}^\dagger_{p'}\hat{a}^\dagger_j \hat{a}_{j'}\hat{a}_{i'} \\ &= \frac{1}{2}\sum_{ij,j'} \bar{v}_{ij,p'j'}\hat{a}^\dagger_i \hat{a}^\dagger_j \hat{a}_{j'}\hat{a}_{h'} + \frac{1}{2}\sum_{i,i'j'} \bar{v}_{ih',i'j'}\hat{a}^\dagger_{p'}\hat{a}^\dagger_i \hat{a}_{j'}\hat{a}_{i'},\end{aligned} \tag{5.60}$$

where the product rule for commutators (A.4) as well as the properties of the antisymmetrized matrix elements of the potential energy (3.4) are applied. Furthermore, some indices are renamed. The commutators containing two creation or annihilation operators and a ph excitation creation operator are determined with the product rule and standard (anti-)commutation relations as follows

$$\begin{aligned}\left[\hat{a}_{j'}\hat{a}_{i'}, \hat{a}^\dagger_{p'}\hat{a}_{h'}\right] &= \hat{a}_{j'}\left[\hat{a}_{i'}, \hat{a}^\dagger_{p'}\hat{a}_{h'}\right] + \left[\hat{a}_{j'}, \hat{a}^\dagger_{p'}\hat{a}_{h'}\right]\hat{a}_{i'} \\ &= \delta_{i'p'}\hat{a}_{j'}\hat{a}_{h'} + \delta_{j'p'}\hat{a}_{h'}\hat{a}_{i'}\end{aligned} \tag{5.61}$$

and

$$\begin{aligned}\left[\hat{a}^\dagger_i \hat{a}^\dagger_j, \hat{a}^\dagger_{p'}\hat{a}_{h'}\right] &= \hat{a}^\dagger_i \left[\hat{a}^\dagger_j, \hat{a}^\dagger_{p'}\hat{a}_{h'}\right] + \left[\hat{a}^\dagger_i, \hat{a}^\dagger_{p'}\hat{a}_{h'}\right]\hat{a}^\dagger_j \\ &= -\delta_{h'j}\hat{a}^\dagger_i \hat{a}^\dagger_{p'} - \delta_{h'i}\hat{a}^\dagger_{p'}\hat{a}^\dagger_j.\end{aligned} \tag{5.62}$$

So far, the evaluation of the commutators contained in the RPA matrices is on operator-level, i.e. universally valid. For the A matrix, expectation values of a hole-particle excitation

creation operator and the commutator of Hamiltonian and $\hat{a}^\dagger_{p'}\hat{a}_{h'}$ of the form

$$\begin{aligned} A_{ph,p'h'} &= \langle \mathrm{SD}|\, \hat{a}^\dagger_h \hat{a}_p \left[\hat{H}, \hat{a}^\dagger_{p'}\hat{a}_{h'}\right] |\mathrm{SD}\rangle \\ &= \langle \mathrm{SD}|\, \hat{a}^\dagger_h \hat{a}_p \left[\hat{T} + \hat{V}_{\mathrm{NN}}, \hat{a}^\dagger_{p'}\hat{a}_{h'}\right] |\mathrm{SD}\rangle \\ &= \sum_i t_{p',i} \langle \mathrm{SD}|\, \hat{a}^\dagger_h \hat{a}_p \hat{a}^\dagger_i \hat{a}_{h'} |\mathrm{SD}\rangle - \sum_i t_{i,h'} \langle \mathrm{SD}|\, \hat{a}^\dagger_h \hat{a}_p \hat{a}^\dagger_{p'} \hat{a}_i |\mathrm{SD}\rangle \\ &+ \frac{1}{2}\sum_{ij,j'} \bar{v}_{ij,p'j'} \langle \mathrm{SD}|\, \hat{a}^\dagger_h \hat{a}_p \hat{a}^\dagger_i \hat{a}^\dagger_j \hat{a}_{j'} \hat{a}_{h'} |\mathrm{SD}\rangle + \frac{1}{2}\sum_{i,i'j'} \bar{v}_{ih',i'j'} \langle \mathrm{SD}|\, \hat{a}^\dagger_h \hat{a}_p \hat{a}^\dagger_{p'} \hat{a}^\dagger_i \hat{a}_{j'} \hat{a}_{i'} |\mathrm{SD}\rangle \end{aligned} \tag{5.63}$$

are relevant. Here, we inserted the definition of the Hamiltonian and the previous results. The expectation values in Eq. (5.63) are non-zero only if one included creation operator populates a particle (hole) state while a corresponding annihilation operator eliminates the same state. Thus, only pairs of matching excitation creation and annihilation operators are considered. Mapping a pair of these operators to a single-particle basis state yields either δ_{ij} or 0 if the involved states are already (un-)occupied. Furthermore, particle and hole states are disjoint, i.e., $\delta_{ph} = 0$. With these considerations, the expectation value in the first term in Eq. (5.63) can be expressed with Wick's theorem in terms of contractions to

$$\begin{aligned} \langle \mathrm{SD}|\, \hat{a}^\dagger_h \hat{a}_p \hat{a}^\dagger_i \hat{a}_{h'} |\mathrm{SD}\rangle &= \hat{a}^\dagger_h \hat{a}_p \hat{a}^\dagger_i \hat{a}_{h'} + \hat{a}^\dagger_h \hat{a}_p \hat{a}^\dagger_i \hat{a}_{h'} \\ &= (-1)^0 \delta_{hp}\delta_{ih'} + (-1)^0 \delta_{hh'}\delta_{pi} \\ &= \delta_{hh'}\delta_{pi}\,. \end{aligned} \tag{5.64}$$

Analogously, the second expectation value yields

$$\begin{aligned} \langle \mathrm{SD}|\, \hat{a}^\dagger_h \hat{a}_p \hat{a}^\dagger_{p'} \hat{a}_i |\mathrm{SD}\rangle &= \hat{a}^\dagger_h \hat{a}_p \hat{a}^\dagger_{p'} \hat{a}_i + \hat{a}^\dagger_h \hat{a}_p \hat{a}^\dagger_{p'} \hat{a}_i \\ &= (-1)^0 \delta_{hp}\delta_{ip'} + (-1)^2 \delta_{pp'}\delta_{hi} \\ &= \delta_{pp'}\delta_{hi} \end{aligned} \tag{5.65}$$

where contractions of the sort $\hat{a}^\dagger_h \hat{a}_p$ are omitted because they result in δ_{ph} which is zero. The third scalar product is evaluated to

$$\begin{aligned} \langle \mathrm{SD}|\, \hat{a}^\dagger_h \hat{a}_p \hat{a}^\dagger_i \hat{a}^\dagger_j \hat{a}_{j'} \hat{a}_{h'} |\mathrm{SD}\rangle &= \hat{a}^\dagger_h \hat{a}_p \hat{a}^\dagger_i \hat{a}^\dagger_j \hat{a}_{j'} \hat{a}_{h'} + \hat{a}^\dagger_h \hat{a}_p \hat{a}^\dagger_i \hat{a}^\dagger_j \hat{a}_{j'} \hat{a}_{h'} \\ &+ \hat{a}^\dagger_h \hat{a}_p \hat{a}^\dagger_i \hat{a}^\dagger_j \hat{a}_{j'} \hat{a}_{h'} + \hat{a}^\dagger_h \hat{a}_p \hat{a}^\dagger_i \hat{a}^\dagger_j \hat{a}_{j'} \hat{a}_{h'} \\ &= (-1)^1 \delta_{hj'}\delta_{pi}\delta_{jh'} + (-1)^2 \delta_{hj'}\delta_{pj}\delta_{ih'} \\ &+ (-1)^0 \delta_{hh'}\delta_{pi}\delta_{jj'} + (-1)^1 \delta_{hh'}\delta_{pj}\delta_{ij'} \end{aligned} \tag{5.66}$$

whereas the last expectation value results in

$$\begin{aligned}\langle \mathrm{SD}|\, \hat{a}_h^\dagger \hat{a}_p \hat{a}_{p'}^\dagger \hat{a}_i^\dagger \hat{a}_{j'} \hat{a}_{i'} \,|\mathrm{SD}\rangle &= \hat{a}_h^\dagger \hat{a}_p \hat{a}_{p'}^\dagger \hat{a}_i^\dagger \hat{a}_{j'} \hat{a}_{i'} + \hat{a}_h^\dagger \hat{a}_p \hat{a}_{p'}^\dagger \hat{a}_i^\dagger \hat{a}_{j'} \hat{a}_{i'} \\ &\quad + \hat{a}_h^\dagger \hat{a}_p \hat{a}_{p'}^\dagger \hat{a}_i^\dagger \hat{a}_{j'} \hat{a}_{i'} + \hat{a}_h^\dagger \hat{a}_p \hat{a}_{p'}^\dagger \hat{a}_i^\dagger \hat{a}_{j'} \hat{a}_{i'} \\ &= (-1)^1 \delta_{hj'} \delta_{pp'} \delta_{ii'} + 0 \\ &\quad + (-1)^0 \delta_{hi'} \delta_{pp'} \delta_{ij'} + 0\,. \end{aligned} \tag{5.67}$$

Here, the second and the fourth term evaluate to zero, since contractions of the form $\hat{a}_p^\dagger \hat{a}_i$ are zero according to Eq. (2.35). With these considerations, the terms of the A matrix in Eq. (5.63) yield

$$\sum_i t_{p',i} \langle \mathrm{SD}|\, \hat{a}_h^\dagger \hat{a}_p \hat{a}_i^\dagger \hat{a}_{h'} \,|\mathrm{SD}\rangle = \sum_i t_{p',i} \delta_{hh'} \delta_{pi} = t_{p,p'} \delta_{hh'} \tag{5.68}$$

$$-\sum_i t_{i,h'} \langle \mathrm{SD}|\, \hat{a}_h^\dagger \hat{a}_p \hat{a}_{p'}^\dagger \hat{a}_i \,|\mathrm{SD}\rangle = \sum_i t_{i,h'} \delta_{pp'} \delta_{hi} = -t_{h',h} \delta_{pp'} \tag{5.69}$$

$$\begin{aligned}&\frac{1}{2} \sum_{ij,j'} \bar{v}_{ij,p'j'} \langle \mathrm{SD}|\, \hat{a}_h^\dagger \hat{a}_p \hat{a}_i^\dagger \hat{a}_j^\dagger \hat{a}_{j'} \hat{a}_{h'} \,|\mathrm{SD}\rangle \\ &\quad = \frac{1}{2} \sum_{ij,j'} \bar{v}_{ij,p'j'} \left[-\delta_{hj'} \delta_{pi} \delta_{jh'} + \delta_{hj'} \delta_{pj} \delta_{ih'} + \delta_{hh'} \delta_{pi} \delta_{jj'} - \delta_{hh'} \delta_{pj} \delta_{ij'} \right] \\ &\quad = \frac{1}{2} \left[-\bar{v}_{ph',p'h} + \bar{v}_{h'p,p'h} + \delta_{hh'} \sum_i^{\text{occ.}} \left(\bar{v}_{pi,p'i} - \bar{v}_{ip,p'i} \right) \right] \\ &\quad = -\bar{v}_{ph',p'h} + \delta_{hh'} \sum_i^{\text{occ.}} \bar{v}_{pi,p'i} \end{aligned} \tag{5.70}$$

$$\begin{aligned}&\frac{1}{2} \sum_{i,i'j'} \bar{v}_{ih',i'j'} \langle \mathrm{SD}|\, \hat{a}_h^\dagger \hat{a}_p \hat{a}_{p'}^\dagger \hat{a}_i^\dagger \hat{a}_{j'} \hat{a}_{i'} \,|\mathrm{SD}\rangle \\ &\quad = \frac{1}{2} \sum_{i,i'j'} \bar{v}_{ih',i'j'} \left[-\delta_{hj'} \delta_{pp'} \delta_{ii'} + \delta_{hi'} \delta_{pp'} \delta_{ij'} \right] \\ &\quad = \frac{1}{2} \left[-\delta_{pp'} \sum_i^{\text{occ.}} \left(\bar{v}_{ih',ih} - \bar{v}_{ih',hi} \right) \right] \\ &\quad = -\delta_{pp'} \sum_i^{\text{occ.}} \bar{v}_{ih',ih}\,. \end{aligned} \tag{5.71}$$

Here we used the antisymmetry (3.4) of the interaction to further simplify the terms. Finally, we obtain the A matrix

$$
\begin{aligned}
A_{ph,p'h'} &= \langle \mathrm{SD} | \, \hat{a}_h^\dagger \hat{a}_p [\hat{H}, \hat{a}_{p'}^\dagger \hat{a}_{h'}] \, | \mathrm{SD} \rangle \\
&= t_{p,p'} \delta_{hh'} - t_{h',h} \delta_{pp'} + \delta_{hh'} \sum_i^{\text{occ.}} \bar{v}_{pi,p'i} - \delta_{pp'} \sum_i^{\text{occ.}} \bar{v}_{h'i,hi} + \bar{v}_{ph',hp'} \\
&= \epsilon_{p,p'} \delta_{hh'} - \epsilon_{h',h} \delta_{pp'} + \bar{v}_{ph',hp'}
\end{aligned}
\tag{5.72}
$$

with the elements of the Fock operator

$$
\epsilon_{i,i'} = t_{i,i'} + \sum_h^{\text{occ.}} \bar{v}_{i'h,ih} \tag{5.73}
$$

that are abbreviated analogously to the HF framework introduced in Sec. 3.3.1. For a generic basis the one-body part is not necessarily diagonal contrary to the HF case which is discussed in Sec. 7.1.

Coupled Formulation As mentioned before, the uncoupled excitation creation operator is used for lucidity. For actual calculations, the coupled formulation is mandatory. The uncoupled and coupled ph states, respectively, are defined as

$$
\begin{aligned}
|ph\rangle = |pm_p, \hbar m_h\rangle &= \hat{\mathcal{A}}_{p\hbar}^\dagger \, |\mathrm{SD}\rangle \\
|p\hbar, JM\rangle &= \mathcal{N}_{p\hbar} \hat{\mathcal{A}}_{p\hbar}^\dagger (JM) \, |\mathrm{SD}\rangle
\end{aligned}
\tag{5.74}
$$

and thus, the expression of the uncoupled states expanded in the coupled basis according to (2.2) is given by

$$
|ij\rangle = \sum_{JM} \begin{pmatrix} j_i & j_j \\ m_i & m_j \end{pmatrix} \begin{vmatrix} J \\ M \end{pmatrix} \mathcal{N}_{ij}^{-1} \, |ij, JM\rangle \, . \tag{5.75}
$$

Here, the normalization factor

$$
\mathcal{N}_{ij} = \frac{\sqrt{1 + (-1)^J \delta_{ij}}}{1 + \delta_{ij}} \tag{5.76}
$$

is introduced in order to ensure correct normalization for the case of two identical states. For $i = j$ and odd J, the normalization factor becomes zero. Since these combinations of states do not occur in our basis [70], we can simplify the normalization factor to

$$
\mathcal{N}_{ij} = \frac{1}{\sqrt{1 + \delta_{ij}}} \tag{5.77}
$$

which is 1 if the single-particle angular momenta are not identical and $2^{-\frac{1}{2}}$ otherwise. Substituting the uncoupled excitation creation operator in the A matrix (5.43) by the coupled

ones (5.24)

$$\hat{Q}^\dagger_\omega = \sum_{p,\hbar} \left(\mathcal{X}^\omega_{p\hbar}\ \hat{\mathcal{A}}^\dagger_{p\hbar}(JM) - \mathcal{Y}^\omega_{p\hbar}\ \hat{\tilde{\mathcal{A}}}_{p\hbar}(JM) \right) \tag{5.78}$$

with the associated variation

$$\begin{aligned} \delta Q &= \sum_{p,\hbar} (\mathcal{X}^{\omega *}_{p\hbar}\ (\hat{\mathcal{A}}^\dagger_{p\hbar}(JM))^\dagger - \mathcal{Y}^{\omega *}_{p\hbar}\ (\hat{\tilde{\mathcal{A}}}_{p\hbar}(JM))^\dagger) \\ &= \sum_{p,\hbar} (\mathcal{X}^{\omega *}_{p\hbar}\ \hat{\mathcal{A}}_{p\hbar}(JM) - \mathcal{Y}^{\omega *}_{p\hbar}\ \hat{\tilde{\mathcal{A}}}^\dagger_{p\hbar}(JM)) \end{aligned} \tag{5.79}$$

The coupled A matrix is then given by

$$\begin{aligned} A^J_{p\hbar,p'\hbar'} &= \langle \mathrm{SD} |\, \hat{\mathcal{A}}_{p\hbar}(JM) [\hat{H}, \hat{\mathcal{A}}^\dagger_{p'\hbar'}(JM)] \,| \mathrm{SD} \rangle \\ &= \sum_{m_p, m_h} \sum_{m_{p'}, m_{h'}} (-1)^{j_h - m_h} (-1)^{j_{h'} - m_{h'}} \begin{pmatrix} j_p & j_h \\ m_p & -m_h \end{pmatrix} \begin{pmatrix} j_{p'} & j_{h'} \\ m_{p'} & -m_{h'} \end{pmatrix} \begin{pmatrix} J \\ M \end{pmatrix} \\ &\qquad \times \langle \mathrm{SD} |\, \hat{a}^\dagger_h \hat{a}_p [\hat{H}, \hat{a}^\dagger_{p'} \hat{a}_{h'}] \,| \mathrm{SD} \rangle \ . \end{aligned} \tag{5.80}$$

Here, the definition of the coupled creation and annihilation operators (5.20) was inserted, leading to a phase factor and Clebsch-Gordan coefficients due to the construction as coupled tensor product. The matrix element was already evaluated in Eq. (5.72), yielding for the coupled A matrix

$$\begin{aligned} &= \sum_{m_p, m_h} \sum_{m_{p'}, m_{h'}} (-1)^{j_h - m_h} (-1)^{j_{h'} - m_{h'}} \begin{pmatrix} j_p & j_h \\ m_p & -m_h \end{pmatrix} \begin{pmatrix} j_{p'} & j_{h'} \\ m_{p'} & -m_{h'} \end{pmatrix} \begin{pmatrix} J \\ M \end{pmatrix} \\ &\qquad \times (\bar{v}_{ph',hp'} + \underbrace{t_{p,p'}\delta_{hh'} + \delta_{hh'} \sum_i^{\text{occ.}} \bar{v}_{pi,p'i}}_{\epsilon_{p,p'}\delta_{hh'}} \underbrace{- t_{h',h}\delta_{pp'} - \delta_{pp'} \sum_i^{\text{occ.}} \bar{v}_{h'i,hi}}_{-\epsilon_{h',h}\delta_{pp'}}). \end{aligned} \tag{5.81}$$

The kinetic energy matrix elements $t_{i,i'}$ and the ones of the potential energy are still with respect to the uncoupled basis. Due to spherical symmetry, it is sufficient to consider only one certain M as mentioned earlier. The choice of $M = 0$ together with the additivity of the projection quantum numbers in Clebsch-Gordan coefficients results in two equalities for the single-particle projections, namely $m_p = m_h$ and $m_{p'} = m_{h'}$. For a full expression of the A matrix in the coupled basis, the matrix elements of kinetic and potential energy needs to be transformed as well. Therefore, we start with Eq. (5.81) and insert the expression of the uncoupled states expanded in the coupled basis (5.75). The normalization factor is 1, since the contained Kronecker delta δ_{ph} is zero. For the transformation of the matrix elements of

the first term in Eq. (5.81) in the coupled basis, we obtain

$$\begin{aligned}\bar{v}_{ph',hp'} &= \langle ph'| \hat{V}_{\mathrm{NN}} |hp'\rangle \\ &= \sum_{J'M'} \sum_{J''M''} \begin{pmatrix} j_p & j_{h'} & J' \\ m_p & m_{h'} & M' \end{pmatrix} \begin{pmatrix} j_h & j_{p'} & J'' \\ m_h & m_{p'} & M'' \end{pmatrix} \langle p\hbar', J'M'| \hat{V}_{\mathrm{NN}} |\hbar p', J''M''\rangle \\ &= \sum_{J'M'} \begin{pmatrix} j_p & j_{h'} & J' \\ m_p & m_{h'} & M' \end{pmatrix} \begin{pmatrix} j_h & j_{p'} & J' \\ m_h & m_{p'} & M' \end{pmatrix} \langle p\hbar', J'| \hat{V}_{\mathrm{NN}} |\hbar p', J'\rangle ,\end{aligned} \tag{5.82}$$

where the Wigner-Eckart theorem (2.20) was applied to the matrix element of the scalar two-body interaction operator V, yielding an M-independent matrix element which is diagonal in J and M (see Eq. (8.12) in Ref. [33])

$$\langle p\hbar', J'M'| \hat{V}_{\mathrm{NN}} |\hbar p', J''M''\rangle = \delta_{J'J''}\delta_{M'M''} \langle p\hbar', J'| \hat{V}_{\mathrm{NN}} |\hbar p', J''\rangle . \tag{5.83}$$

Inserting this result into Eq. (5.81) leads to

$$\begin{aligned}\mathrm{term1} &= \sum_{\substack{m_p m_h \\ m_{p'} m_{h'}}} (-1)^{j_h - m_h} (-1)^{j_{h'} - m_{h'}} \begin{pmatrix} j_p & j_h & J \\ m_p & -m_h & M \end{pmatrix} \begin{pmatrix} j_{p'} & j_{h'} & J \\ m_{p'} & -m_{h'} & M \end{pmatrix} \langle ph'| \hat{V}_{\mathrm{NN}} |hp'\rangle \\ &= \sum_{\substack{m_p m_h \\ m_{p'} m_{h'}}} \sum_{J'M'} \begin{pmatrix} j_p & j_h & J \\ m_p & -m_h & M \end{pmatrix} \begin{pmatrix} j_{p'} & j_{h'} & J \\ m_{p'} & -m_{h'} & M \end{pmatrix} \begin{pmatrix} j_p & j_{h'} & J' \\ m_p & m_{h'} & M' \end{pmatrix} \begin{pmatrix} j_h & j_{p'} & J' \\ m_h & m_{p'} & M' \end{pmatrix} \\ &\qquad \times (-1)^{j_h - m_h} (-1)^{j_{h'} - m_{h'}} \langle p\hbar', J'| \hat{V}_{\mathrm{NN}} |\hbar p', J'\rangle .\end{aligned} \tag{5.84}$$

In a next step, we can sum over M while dividing by $\hat{J}^2 = 2J + 1$, since the matrix element is independent of M. Furthermore, the sign of $m_h \to -m_h$ and $m_{h'} \to -m_{h'}$, respectively are reversed, resulting in

$$\begin{aligned}&= \sum_{\substack{m_p m_h \\ m_{p'} m_{h'}}} \sum_{J'M'} \sum_{M} \begin{pmatrix} j_p & j_h & J \\ m_p & m_h & M \end{pmatrix} \begin{pmatrix} j_{p'} & j_{h'} & J \\ m_{p'} & m_{h'} & M \end{pmatrix} \begin{pmatrix} j_p & j_{h'} & J' \\ m_p & -m_{h'} & M' \end{pmatrix} \begin{pmatrix} j_h & j_{p'} & J' \\ -m_h & m_{p'} & M' \end{pmatrix} \\ &\qquad \times \frac{1}{2J+1} (-1)^{j_h + m_h} (-1)^{j_{h'} + m_{h'}} \langle p\hbar', J'| \hat{V}_{\mathrm{NN}} |\hbar p', J'\rangle .\end{aligned} \tag{5.85}$$

The Clebsch-Gordan coefficients are expressed via $3j$ symbols (2.11), yielding

$$\begin{aligned}&\begin{pmatrix} j_p & j_h & J \\ m_p & m_h & M \end{pmatrix} \begin{pmatrix} j_{p'} & j_{h'} & J \\ m_{p'} & m_{h'} & M \end{pmatrix} \begin{pmatrix} j_p & j_{h'} & J' \\ m_p & -m_{h'} & M' \end{pmatrix} \begin{pmatrix} j_h & j_{p'} & J' \\ -m_h & m_{p'} & M' \end{pmatrix} \\ &= \hat{J}^2 \hat{J}'^2 \begin{pmatrix} j_p & j_h & J \\ m_p & m_h & -M \end{pmatrix} \begin{pmatrix} j_{p'} & j_{h'} & J \\ m_{p'} & m_{h'} & -M \end{pmatrix} \begin{pmatrix} j_p & j_{h'} & J' \\ m_p & -m_{h'} & -M' \end{pmatrix} \begin{pmatrix} j_{p'} & j_h & J' \\ -m_{p'} & m_h & M' \end{pmatrix} .\end{aligned} \tag{5.86}$$

In the last $3j$ symbol, we used the symmetry properties (2.12) and (2.13). The phase factors occurring due to the conversion into $3j$ symbols and the symmetry properties can be summarized to $+1$. Reversing the signs of M, M' and $m_{p'}$ leads to an expression which can be identified with a $6j$ symbol

$$\begin{aligned}\text{term1} =& \sum_{J'}(2J'+1)\sum_{M,M'}\sum_{\substack{m_p m_h\\ m_{p'}m_{h'}}}(-1)^{j_h+m_h}(-1)^{j_{h'}+m_{h'}}\left\langle p\hbar', J'\right|\hat{V}_{\mathrm{NN}}\left|\hbar p', J'\right\rangle \\ &\times\begin{pmatrix} j_p & j_h & J\\ m_p & m_h & M\end{pmatrix}\begin{pmatrix} j_{p'} & j_{h'} & J\\ -m_{p'} & m_{h'} & M\end{pmatrix}\begin{pmatrix} j_p & j_{h'} & J'\\ m_p & -m_{h'} & M'\end{pmatrix}\begin{pmatrix} j_{p'} & j_h & J'\\ m_{p'} & m_h & -M'\end{pmatrix} \\ =&\sum_{J'}(2J'+1)(-1)^{j_h+j_{p'}+J'}\begin{Bmatrix} j_p & j_h & J\\ j_{p'} & j_{h'} & J'\end{Bmatrix}\left\langle p\hbar', J'\right|\hat{V}_{\mathrm{NN}}\left|\hbar p', J'\right\rangle \end{aligned} \tag{5.87}$$

The phase factor is derived in App. A.3. Thus, the final result for the coupled A matrix is given by

$$\begin{aligned}A^J_{p\hbar,p'\hbar'} =& \sum_{m_p,m_h}\sum_{m_{p'},m_{h'}}(-1)^{j_h-m_h}(-1)^{j_{h'}-m_{h'}}\left(\begin{array}{cc|c} j_p & j_h & J\\ m_p & -m_h & M\end{array}\right)\left(\begin{array}{cc|c} j_{p'} & j_{h'} & J\\ m_{p'} & -m_{h'} & M\end{array}\right) \\ &\times\left(\epsilon_{p,p'}\delta_{hh'}-\epsilon_{h',h}\delta_{pp'}\right) \\ &+\sum_{J'}(2J'+1)(-1)^{j_h+j_{p'}+J'}\begin{Bmatrix} j_p & j_h & J\\ j_{p'} & j_{h'} & J'\end{Bmatrix}\left\langle p\hbar', J'\right|\hat{V}_{\mathrm{NN}}\left|\hbar p', J'\right\rangle \end{aligned} \tag{5.88}$$

for a generic single-particle basis.

5.2.2 Explicit Form of the B Matrix

The B matrix (5.44) consists of a product of the hp excitation creation operator and a commutator of the Hamiltonian and the hp excitation creation operator

$$B_{ph,p'h'} = -\left\langle \mathrm{SD}\right|\hat{a}^\dagger_h\hat{a}_p[\hat{H},\hat{a}^\dagger_{h'}\hat{a}_{p'}]\left|\mathrm{SD}\right\rangle. \tag{5.89}$$

Analogously to the A matrix in Sec. 5.2.1, the commutator is evaluated and the expectation value is determined. In comparison to the A matrix, the B matrix contains the commutator of the Hamiltonian and the hp excitation creation operator instead of the operator causing a ph excitation. Since the derivation of the A matrix (5.63) includes only operators and thus is the most general way, the results are valid for arbitrary indices of the ECOs which can be

renamed. Starting from Eq. (5.63) and changing the indices $p' \leftrightarrow h'$, we obtain

$$\begin{aligned} B_{ph,p'h'} =& - \langle \mathrm{SD}| \hat{a}_h^\dagger \hat{a}_p [\hat{H}, \hat{a}_{h'}^\dagger \hat{a}_{p'}] |\mathrm{SD}\rangle \\ =& - \sum_i t_{h',i} \langle \mathrm{SD}| \hat{a}_h^\dagger \hat{a}_p \hat{a}_i^\dagger \hat{a}_{p'} |\mathrm{SD}\rangle + \sum_i t_{i,p'} \langle \mathrm{SD}| \hat{a}_h^\dagger \hat{a}_p \hat{a}_{h'}^\dagger \hat{a}_i |\mathrm{SD}\rangle \\ & - \frac{1}{2} \sum_{ij,j'} \bar{v}_{ij,h'j'} \langle \mathrm{SD}| \hat{a}_h^\dagger \hat{a}_p \hat{a}_i^\dagger \hat{a}_j^\dagger \hat{a}_{j'} \hat{a}_{p'} |\mathrm{SD}\rangle - \frac{1}{2} \sum_{i,i'j'} \bar{v}_{ip',i'j'} \langle \mathrm{SD}| \hat{a}_h^\dagger \hat{a}_p \hat{a}_{h'}^\dagger \hat{a}_i^\dagger \hat{a}_{j'} \hat{a}_{i'} |\mathrm{SD}\rangle \end{aligned} \tag{5.90}$$

for a two-body Hamiltonian. The first and the third term yield zero because they contain $\hat{a}_p |\mathrm{SD}\rangle = 0$. The other contribution of the kinetic energy, i.e., the second term, becomes zero as well. In this case, all possible contractions vanish, since either the particle annihilator is contracted with another annihilator or with a hole creator. Therefore, the only contributing term to the B matrix in Eq. (5.90) is the last one, whose expectation value can be evaluated with Wick's theorem in terms of contractions to

$$\begin{aligned} \langle \mathrm{SD}| \hat{a}_h^\dagger \hat{a}_p \hat{a}_{h'}^\dagger \hat{a}_i^\dagger \hat{a}_{j'} \hat{a}_{i'} |\mathrm{SD}\rangle &= \overbrace{\hat{a}_h^\dagger \hat{a}_p \hat{a}_{h'}^\dagger \hat{a}_i^\dagger \hat{a}_{j'} \hat{a}_{i'}} + \overbrace{\hat{a}_h^\dagger \hat{a}_p \hat{a}_{h'}^\dagger \hat{a}_i^\dagger \hat{a}_{j'} \hat{a}_{i'}} \\ &= (-1)^2 \delta_{hj'} \delta_{pi} \delta_{h'i'} + (-1)^1 \delta_{hi'} \delta_{pi} \delta_{h'j'} \,. \end{aligned} \tag{5.91}$$

All other contractions vanish, because particle and hole states are disjoint. Inserting the result of the expectation value into the definition of the B matrix leads to

$$\begin{aligned} & -\frac{1}{2} \sum_{i,i'j'} \bar{v}_{ip',i'j'} \langle \mathrm{SD}| \hat{a}_h^\dagger \hat{a}_p \hat{a}_{h'}^\dagger \hat{a}_i^\dagger \hat{a}_{j'} \hat{a}_{i'} |\mathrm{SD}\rangle \\ &= -\frac{1}{2} \sum_{i,i'j'} \bar{v}_{ip',i'j'} \left[(-1)^2 \delta_{hj'} \delta_{pi} \delta_{h'i'} + (-1)^1 \delta_{hi'} \delta_{pi} \delta_{h'j'} \right] \\ &= -\frac{1}{2} \left[\bar{v}_{pp',h'h} - \bar{v}_{pp',hh'} \right] = \bar{v}_{pp',hh'} \,. \end{aligned} \tag{5.92}$$

Since this is the only contribution to the B matrix, the final results is given by

$$\begin{aligned} B_{ph,p'h'} &= - \langle \mathrm{SD}| \hat{a}_h^\dagger \hat{a}_p [\hat{H}, \hat{a}_{h'}^\dagger \hat{a}_{p'}] |\mathrm{SD}\rangle \\ &= \bar{v}_{pp',hh'} \,. \end{aligned} \tag{5.93}$$

Coupled Formulation Analogous to the A matrix, the uncoupled excitation creation operators and their variation are substituted by the coupled ones given in Eq. (5.78) and Eq. (5.79) for the coupled formulation of the B matrix. Thus, the B matrix reads

$$B^J_{p\hbar,p'\hbar'} = - \langle \mathrm{SD}| \hat{\mathcal{A}}_{p\hbar}(JM) [\hat{H}, \hat{\tilde{\mathcal{A}}}_{p'\hbar'}(JM)] |\mathrm{SD}\rangle \tag{5.94}$$

with the Hermitian conjugate of the coupled excitation creation operator $\hat{\mathcal{A}}_{p\hbar}(JM)$ and the coupled annihilation operator $\hat{\tilde{\mathcal{A}}}_{p\hbar}(JM) = (-1)^{J+M} \hat{\mathcal{A}}_{p\hbar}(J,-M)$ given in Eq. (5.20) and

Eq. (5.21), respectively. Inserting these definitions, we obtain

$$
\begin{aligned}
&= -\sum_{m_p,m_h}\sum_{m_{p'},m_{h'}} \begin{pmatrix} j_p & j_h \\ m_p & -m_h \end{pmatrix}\!\!\begin{vmatrix} J \\ M \end{vmatrix} \begin{pmatrix} j_{p'} & j_{h'} \\ m_{p'} & -m_{h'} \end{pmatrix}\!\!\begin{vmatrix} J \\ -M \end{vmatrix} \\
&\qquad \times (-1)^{j_h-m_h}(-1)^{j_{h'}-m_{h'}}(-1)^{J+M} \left\langle \mathrm{SD}\right| \hat{a}_h^\dagger \hat{a}_p [\hat{H}, \hat{a}_{h'}^\dagger \hat{a}_{p'}] \left|\mathrm{SD}\right\rangle \\
&= \sum_{m_p,m_h}\sum_{m_{p'},m_{h'}} \begin{pmatrix} j_p & j_h \\ m_p & -m_h \end{pmatrix}\!\!\begin{vmatrix} J \\ M \end{vmatrix} \begin{pmatrix} j_{p'} & j_{h'} \\ m_{p'} & -m_{h'} \end{pmatrix}\!\!\begin{vmatrix} J \\ -M \end{vmatrix} \\
&\qquad \times (-1)^{j_h-m_h}(-1)^{j_{h'}-m_{h'}}(-1)^{J+M}\ \bar{v}_{pp',hh'}.
\end{aligned}
\tag{5.95}
$$

The matrix element was evaluated in the previous chapter which in combination with the Wigner-Eckart theorem (5.83), yields

$$
\begin{aligned}
&= \sum_{\substack{m_p m_h \\ m_{p'} m_{h'}}}\sum_{J'M'} \begin{pmatrix} j_p & j_h \\ m_p & -m_h \end{pmatrix}\!\!\begin{vmatrix} J \\ M \end{vmatrix} \begin{pmatrix} j_{p'} & j_{h'} \\ m_{p'} & -m_{h'} \end{pmatrix}\!\!\begin{vmatrix} J \\ -M \end{vmatrix} \begin{pmatrix} j_p & j_{p'} \\ m_p & m_{p'} \end{pmatrix}\!\!\begin{vmatrix} J' \\ M' \end{vmatrix} \\
&\qquad \times \begin{pmatrix} j_h & j_{h'} \\ m_h & m_{h'} \end{pmatrix}\!\!\begin{vmatrix} J' \\ M' \end{vmatrix}\ \mathcal{N}_{pp'}^{-1}\mathcal{N}_{hh'}^{-1}(-1)^{j_h-m_h}(-1)^{j_{h'}-m_{h'}}(-1)^{J+M} \\
&\qquad \times \left\langle pp', J'\right| \hat{V}_{\mathrm{NN}} \left|hh', J'\right\rangle .
\end{aligned}
\tag{5.96}
$$

As for the A matrix, an additional sum over M is added while dividing by $\hat{J}^2 = 2J+1$, since the matrix element is independent of M. Moreover, the signs of m_h and $m_{h'}$ are reversed, leading to

$$
\begin{aligned}
&= \sum_{\substack{m_p m_h \\ m_{p'} m_{h'}}}\sum_{J'M'}\sum_{M} \begin{pmatrix} j_p & j_h \\ m_p & m_h \end{pmatrix}\!\!\begin{vmatrix} J \\ M \end{vmatrix} \begin{pmatrix} j_{p'} & j_{h'} \\ m_{p'} & m_{h'} \end{pmatrix}\!\!\begin{vmatrix} J \\ -M \end{vmatrix} \begin{pmatrix} j_p & j_{p'} \\ m_p & m_{p'} \end{pmatrix}\!\!\begin{vmatrix} J' \\ M' \end{vmatrix} \\
&\qquad \times \begin{pmatrix} j_h & j_{h'} \\ -m_h & -m_{h'} \end{pmatrix}\!\!\begin{vmatrix} J' \\ M' \end{vmatrix}\ (-1)^{j_h+m_h}(-1)^{j_{h'}+m_{h'}}(-1)^{J+M} \\
&\qquad \times \frac{1}{\hat{J}^2}\mathcal{N}_{pp'}^{-1}\mathcal{N}_{hh'}^{-1}\ \left\langle pp', J'\right| \hat{V}_{\mathrm{NN}} \left|hh', J'\right\rangle
\end{aligned}
\tag{5.97}
$$

The next step is the replacement of the Clebsch-Gordan coefficients by $3j$ symbols where we use the symmetry property for reversing the sign of the m quantum numbers in the last $3j$ symbol resulting in an additional phase factor. Including the phase factors stemming from

the conversion to a $3j$ symbol and the symmetry properties, we find

$$\begin{aligned}
&= \sum_{\substack{m_p m_h \\ m_{p'} m_{h'}}} \sum_{J'M'} \sum_{M} \begin{pmatrix} j_p & j_h & J \\ m_p & m_h & -M \end{pmatrix} \begin{pmatrix} j_{p'} & j_{h'} & J \\ m_{p'} & m_{h'} & M \end{pmatrix} \begin{pmatrix} j_p & j_{p'} & J' \\ m_p & m_{p'} & -M' \end{pmatrix} \\
&\quad \times \begin{pmatrix} j_h & j_{h'} & J' \\ m_h & m_{h'} & M' \end{pmatrix} \mathcal{N}_{pp'}^{-1} \mathcal{N}_{hh'}^{-1} \hat{J'}^2 (-1)^{J+M} (-1)^{J'+M'} \\
&\quad \times \left\langle pp', J' \right| \hat{V}_{\mathrm{NN}} \left| \hbar\hbar', J' \right\rangle
\end{aligned} \tag{5.98}$$

In the last step, the $3j$ symbols are summarized to a $6j$ symbol and the definition of the normalization factors are inserted, leading to

$$\begin{aligned}
B^J_{p\hbar,p'\hbar'} &= (-1)^{j_h + j_{p'} + J} \sqrt{(1+\delta_{pp'})(1+\delta_{hh'})} \\
&\quad \times \sum_{J'} (-1)^{J'} (2J'+1) \begin{Bmatrix} j_p & j_h & J \\ j_{h'} & j_{p'} & J' \end{Bmatrix} \left\langle pp', J' \right| \hat{V}_{\mathrm{NN}} \left| \hbar\hbar', J' \right\rangle .
\end{aligned} \tag{5.99}$$

5.3 RPA with Three-Body Interaction

So far, the explicit form of the first-order RPA matrices is derived for a two-body Hamiltonian. Additionally including the three-body interaction $\hat{V}_{\mathrm{3N}}$ in the Hamiltonian leads to more complex expressions for the involved commutators in the definition of the A matrix. The derivation is only motivated but not presented in detail here. We refer to Ref. [70] for further information. For the commutator of the Hamiltonian and hp creation operator (5.58), one additional term arises

$$\begin{aligned}
\left[\hat{H}, \hat{a}^\dagger_{p'} \hat{a}_{h'}\right] &= \left[\hat{T} + \hat{V}_{\mathrm{NN}} + \hat{V}_{\mathrm{3N}}, \hat{a}^\dagger_{p'} \hat{a}_{h'}\right] \\
&= \left[\hat{T}, \hat{a}^\dagger_{p'} \hat{a}_{h'}\right] + \left[\hat{V}_{\mathrm{NN}}, \hat{a}^\dagger_{p'} \hat{a}_{h'}\right] + \left[\hat{V}_{\mathrm{3N}}, \hat{a}^\dagger_{p'} \hat{a}_{h'}\right] .
\end{aligned} \tag{5.100}$$

The evaluation of the additional commutator yields

$$\begin{aligned}
\left[\hat{V}_{\mathrm{3N}}, \hat{a}^\dagger_{p'} \hat{a}_{h'}\right] &= \frac{1}{36} \sum_{ijk,i'j'k'} \bar{v}^{\mathrm{3N}}_{ijk,i'j'k'} \left[\hat{a}^\dagger_i \hat{a}^\dagger_j \hat{a}^\dagger_k \hat{a}_{k'} \hat{a}_{j'} \hat{a}_{i'}, \hat{a}^\dagger_{p'} \hat{a}_{h'}\right] \\
&= \frac{1}{12} \sum_{ijk,j'k'} \bar{v}^{\mathrm{3N}}_{ijk,p'j'k'} \hat{a}^\dagger_i \hat{a}^\dagger_j \hat{a}^\dagger_k \hat{a}_{k'} \hat{a}_{j'} \hat{a}_{h'} - \frac{1}{12} \sum_{jk,i'j'k'} \bar{v}^{\mathrm{3N}}_{h'jk,i'j'k'} \hat{a}^\dagger_{p'} \hat{a}^\dagger_j \hat{a}^\dagger_k \hat{a}_{k'} \hat{a}_{j'} \hat{a}_{i'}
\end{aligned} \tag{5.101}$$

The three-body part of the A matrix

$$\begin{aligned}\langle \mathrm{SD}|\, \hat{a}_h^\dagger \hat{a}_p [\hat{V}_{\mathrm{3N}}, \hat{a}_{p'}^\dagger \hat{a}_{h'}]\, |\mathrm{SD}\rangle = \frac{1}{12} \sum_{ijk,j'k'} \bar{v}^{\mathrm{3N}}_{ijk,p'j'k'} \langle \mathrm{SD}|\, \hat{a}_h^\dagger \hat{a}_p \hat{a}_i^\dagger \hat{a}_j^\dagger \hat{a}_k^\dagger \hat{a}_{k'} \hat{a}_{j'} \hat{a}_{h'}\, |\mathrm{SD}\rangle \\ - \frac{1}{12} \sum_{jk,i'j'k'} \bar{v}^{\mathrm{3N}}_{h'jk,i'j'k'} \langle \mathrm{SD}|\, \hat{a}_h^\dagger \hat{a}_p \hat{a}_{p'}^\dagger \hat{a}_j^\dagger \hat{a}_k^\dagger \hat{a}_{k'} \hat{a}_{j'} \hat{a}_{i'}\, |\mathrm{SD}\rangle\end{aligned} \tag{5.102}$$

can analogously to the two-body case be calculated with the aid of contractions. The full A matrix including a three-body Hamiltonian has further three-body contributions

$$A_{ph,p'h'} = A^{\mathrm{2B}}_{ph,p'h'} + \sum_i^{\mathrm{occ.}} \bar{v}^{\mathrm{3N}}_{ph'i,hp'i} + \frac{1}{2}\delta_{hh'} \sum_{i,j}^{\mathrm{occ.}} \bar{v}^{\mathrm{3N}}_{pij,p'ij} - \frac{1}{2}\delta_{pp'} \sum_{i,j}^{\mathrm{occ.}} \bar{v}^{\mathrm{3N}}_{h'ij,hij}\,. \tag{5.103}$$

Here, $A^{\mathrm{2B}}_{ph,p'h'}$ is the A matrix for a two-body Hamiltonian which is given by Eq. (5.72). Analogously, the B matrix is as well extended by a term including the explicit three-body interaction

$$B_{ph,p'h'} = B^{\mathrm{2B}}_{ph,p'h'} + \sum_i^{\mathrm{occ.}} \bar{v}^{\mathrm{3N}}_{pp'i,hh'i}\,. \tag{5.104}$$

Comparing the results of the explicit three-body contributions to the normal-ordered three-body interaction, it can be shown that they are identical (c.f. Ref. [70]). Thus, for the first-order RPA, utilizing the NO2B truncated Hamiltonian is no approximation, but exact.

6

Second-Order Random-Phase Approximation

Contents

The second-order random-phase approximation (SRPA) [43] is an extension of standard RPA which includes additionally to 1p1h excitations some higher-order correlations, namely 2p2h excitations. Thus, the model space is enlarged yielding improved results. Starting analogously to first-order RPA with some abbreviations and the construction of creation and annihilation operators to fulfill the conditions of spherical tensor operators, the second-order excitation creation operator is defined. Furthermore, the SRPA equations are deduced and the expressions for the more complex second-order A matrix are presented in m-scheme and coupled representation. A brief outlook is given regarding the inclusion of three-body interactions. The chapter is completed by the introduction of transitions in the framework of (S)RPA. The derivation follows Refs. [43, 70] (notation and steps) if not stated otherwise.

6.1 Derivation of SRPA Equations

The second-order excitation creation operator contains on the one hand the part originating from RPA and on the other hand a 2p2h contribution

$$\begin{aligned}\hat{Q}^\dagger_\omega &= \sum_{p_1,h_1} \left(X^\omega_{p_1h_1}\, \hat{\mathcal{A}}^\dagger_{p_1h_1} - Y^\omega_{p_1h_1}\, \hat{\mathcal{A}}_{p_1h_1} \right) + \sum_{\substack{p_1,h_1\\p_2,h_2}} \left(X^\omega_{p_1h_1,p_2h_2}\, \hat{\mathcal{A}}^\dagger_{p_1h_1,p_2h_2} - Y^\omega_{p_1h_1,p_2h_2}\, \hat{\mathcal{A}}_{p_1h_1,p_2h_2} \right) \\ &= \underbrace{\sum_{p_1,h_1} \left(X^\omega_{p_1h_1}\, \hat{a}^\dagger_{p_1}\hat{a}_{h_1} - Y^\omega_{p_1h_1}\, \hat{a}^\dagger_{h_1}\hat{a}_{p_1} \right)}_{\hat{Q}^\dagger_{\omega,\mathrm{RPA}}} \\ &\quad + \sum_{\substack{p_1,h_1\\p_2,h_2}} \left(X^\omega_{p_1h_1,p_2h_2}\, \hat{a}^\dagger_{p_1}\hat{a}_{h_1}\hat{a}^\dagger_{p_2}\hat{a}_{h_2} - Y^\omega_{p_1h_1,p_2h_2}\, \hat{a}^\dagger_{h_1}\hat{a}_{p_1}\hat{a}^\dagger_{h_2}\hat{a}_{p_2} \right). \end{aligned} \tag{6.1}$$

The first term indicates the RPA ECO given in Eq. (5.23), the second term gives rise to the 2p2h excitation and thus consists of two creators and annihilators, respectively. Furthermore, two new amplitudes are introduced which are summarized with the original amplitudes as follows

$$X^\omega = \begin{pmatrix} X^\omega_{p_1h_1} \\ X^\omega_{p_1h_1,p_2h_2} \end{pmatrix} = \begin{pmatrix} X^\omega_1 \\ X^\omega_2 \end{pmatrix} \qquad Y^\omega = \begin{pmatrix} Y^\omega_{p_1h_1} \\ Y^\omega_{p_1h_1,p_2h_2} \end{pmatrix} = \begin{pmatrix} Y^\omega_1 \\ Y^\omega_2 \end{pmatrix} \tag{6.2}$$

The amplitude vector which originates from standard RPA is updated by the new amplitudes stemming from the second-order contributions. Since the physical process described by these amplitudes stays the same but at different orders, it is a legitimate approach.

For lucidity of the following derivation, we introduce an abbreviation

$$\hat{\mathcal{A}}^\dagger_{2,i} = \hat{\mathcal{A}}^\dagger_{(p_1p_2)J_p(\hbar_1\hbar_2)J_h} \qquad i = (p_1p_2)J_p(\hbar_1\hbar_2)J_h \tag{6.3}$$

where the first index labels the order and the second index collects the involved particles and holes and the coupled angular momenta. The uncoupled analogue is abbreviated as

$$\hat{\mathcal{A}}^\dagger_{2,i} = \hat{\mathcal{A}}^\dagger_{p_1p_2h_1h_2} \qquad i = p_1p_2h_1h_2 \tag{6.4}$$

allowing for a clear and direct distinction between 1p1h and 2p2h excitations. The 1p1h excitation creation operator, which was denoted as $\hat{\mathcal{A}}^\dagger_{ph}$ in standard RPA, is written as $\hat{\mathcal{A}}^\dagger_{1,i}$ with $i = p_1h_1$ within the new notation. Thus, the SRPA ECO in Eq. (6.1) can be summarized as follows

$$\hat{Q}^\dagger_\omega = \hat{Q}^\dagger_{1,\omega} + \hat{Q}^\dagger_{2,\omega}\,. \tag{6.5}$$

As preliminary considerations, the SRPA matrices contain more entries in order to describe the 2p2h excitations according to the extension of the amplitude vectors. While the first-order A and B matrices read

$$A_{\mathrm{RPA}} = (A_{11}) \qquad\qquad B_{\mathrm{RPA}} = (B_{11}) \tag{6.6}$$

the SRPA-matrices are given by

$$A_{\mathrm{SRPA}} = \begin{pmatrix} A_{11} & A_{12} \\ A_{21} & A_{22} \end{pmatrix} \qquad\qquad B_{\mathrm{SRPA}} = \begin{pmatrix} B_{11} & B_{12} \\ B_{21} & B_{22} \end{pmatrix}\,. \tag{6.7}$$

The matrices on the diagonal describe the pure 1p1h and 2p2h space. On the off-diagonal we find mixtures of both spaces. The dimension of the RPA-matrix is $N_1 \times N_1$ with the number of 1p1h configurations N_1. The 2p2h space is described by the $N_2 \times N_2$- dimensional A_{22} matrix with the number N_2 of 2p2h configurations. The coupling of 1p1h and 2p2h states is represented by the block matrix A_{12}, which has a dimension of $N_1 \times N_2$. Thus, the matrices are split by their ph rank.

In SRPA, the model space is extended by 2p2h contributions. Aiming the full model space which includes 1p1h up to ApAh excitations would yield the exact result. Hence, the second-order RPA is the natural extension of the standard RPA, improving the model systematically since more information of the full model space is included.

As for the standard RPA, the SRPA equations are formally deduced in the uncoupled formulation for reasons of simplicity. However, it is possible to switch at any step to the coupled formulation which is needed for actual calculations. In the following, the creation and annihilation operators in the uncoupled formulation, the so-called m-scheme, and the coupled representation are presented. Afterwards, some basic commutation relations are calculated. With the help of these considerations, the SRPA equations are derived.

6.1.1 Coupled Creation and Annihilation Operators for SRPA

The structure of the SRPA ECOs is more complex because of the extension of the RPA, as mentioned before. Thus, also the ph and hp excitation creation operators for the SRPA have to be extended to second order. In standard RPA, the coupled ph creation operator is given by

$$\hat{\mathcal{A}}^\dagger_{p\bar{h}}(JM) = \left[\hat{a}^\dagger_p \hat{\tilde{a}}_{\bar{h}}\right]_{JM}\,. \tag{6.8}$$

For the coupled 2p2h (de-)excitation operators, the creation and annihilation operator need to be adjusted as done in standard RPA in order to obtain the correct angular momentum. There are two ways for the construction of the operators. Either two of the RPA-type ph excitation creation operators are combined or a total particle creation operator, resulting from

the coupling of two particle creators, and a total hole de-excitation operator, obtained by the coupling of two hole creators, are merged. We focus on the latter construction of a 2p2h excitation operator.

The pair creator or pp creator

$$\begin{aligned}\hat{\mathcal{K}}^\dagger_{p_1,p_2}(J_pM_p) &= \mathcal{N}_{p_1,p_2}\left[\hat{a}^\dagger_{p_1}\hat{a}^\dagger_{p_2}\right]_{J_pM_p} \\ &= \mathcal{N}_{p_1,p_2}\sum_{m_{p_1},m_{p_2}}\left(\begin{matrix} j_{p_1} & j_{p_2} \\ m_{p_1} & m_{p_2}\end{matrix}\middle|\begin{matrix} J_p \\ M_p\end{matrix}\right)\hat{a}^\dagger_{p_1,m_{p_1}}\hat{a}^\dagger_{p_2,m_{p_2}}\end{aligned} \tag{6.9}$$

is defined as tensor product of two particle creation operators which couple to the total angular momentum J_p with the normalization factor

$$\mathcal{N}_{p_1,p_2} = \mathcal{N}_{p_2,p_1} = \frac{\sqrt{1+(-1)^{J_p}\delta_{p_1p_2}}}{1+\delta_{p_1p_2}} \tag{6.10}$$

as already discussed in the context of the RPA matrices (5.77). It can be simplified to

$$\mathcal{N}_{p_1,p_2} = \mathcal{N}_{p_2,p_1} = \frac{1}{\sqrt{1+\delta_{p_1p_2}}}\,, \tag{6.11}$$

yielding 1 if p_1 and p_2 are not identical and $2^{-\frac{1}{2}}$ otherwise. The pair creator (6.9) contains besides the single-particle creation operators a Clebsch-Gordan coefficient but no phase factor contrary to standard RPA. There, it arises from the reformulation of the annihilation operator as spherical tensor. Since we consider creation operators, this phase factor is absent. Furthermore, the normalization factor in RPA yields 1 due to the disjointness of particle and hole states.

The pair creator can be rewritten using symmetry properties of the Clebsch-Gordan coefficients given in Eq. (2.7), where a changing of two rows leads to a phase factor. This results in

$$\begin{aligned}\hat{\mathcal{K}}^\dagger_{p_1,p_2}(J_pM_p) &= \mathcal{N}_{p_1,p_2}\left[\hat{a}^\dagger_{p_1}\hat{a}^\dagger_{p_2}\right]_{J_pM_p} \\ &= \mathcal{N}_{p_1,p_2}\sum_{m_{p_1},m_{p_2}}\left(\begin{matrix} j_{p_1} & j_{p_2} \\ m_{p_1} & m_{p_2}\end{matrix}\middle|\begin{matrix} J_p \\ M_p\end{matrix}\right)\hat{a}^\dagger_{p_1,m_{p_1}}\hat{a}^\dagger_{p_2,m_{p_2}} \\ &= \mathcal{N}_{p_1,p_2}\sum_{m_{p_1},m_{p_2}}(-1)^{j_{p_1}+j_{p_2}-J}\left(\begin{matrix} j_{p_2} & j_{p_1} \\ m_{p_2} & m_{p_1}\end{matrix}\middle|\begin{matrix} J_p \\ M_p\end{matrix}\right)\hat{a}^\dagger_{p_1,m_{p_1}}\hat{a}^\dagger_{p_2,m_{p_2}} \\ &= \mathcal{N}_{p_1,p_2}\sum_{m_{p_1},m_{p_2}}(-1)^{j_{p_1}+j_{p_2}-J+1}\left(\begin{matrix} j_{p_2} & j_{p_1} \\ m_{p_2} & m_{p_1}\end{matrix}\middle|\begin{matrix} J_p \\ M_p\end{matrix}\right)\hat{a}^\dagger_{p_2,m_{p_2}}\hat{a}^\dagger_{p_1,m_{p_1}} \\ &= (-1)^{j_{p_1}+j_{p_2}-J+1}\mathcal{N}_{p_1,p_2}\left[\hat{a}^\dagger_{p_2}\hat{a}^\dagger_{p_1}\right]_{J_pM_p} \\ &= (-1)^{j_{p_1}+j_{p_2}-J+1}\hat{\mathcal{K}}^\dagger_{p_2,p_1}(J_pM_p)\,.\end{aligned} \tag{6.12}$$

Thus, changing the two particles p_1 and p_2 in the pair creator leads to a phase factor. For the construction of the ECOs, it is sufficient to consider only one of the pair creators since the pair creator and the version with the interchanged particles are not linear independent. Thus, an ordering of the states $p_1 < p_2$ according to Ref. [43] is necessary.

Analogously to first-order RPA, the pair annihilator can be considered as adjoint of the pair creator

$$\begin{aligned}
\hat{\mathcal{K}}_{p_1,p_2}(J_pM_p) &= \hat{\mathcal{K}}^{\dagger}_{p_1,p_2}(J_pM_p)^{\dagger} \\
&= \mathcal{N}_{p_1,p_2} \sum_{m_{p_1},m_{p_2}} \begin{pmatrix} j_{p_1} & j_{p_2} \\ m_{p_1} & m_{p_2} \end{pmatrix} \begin{matrix} J_p \\ M_p \end{matrix} \hat{a}_{p_2,m_{p_2}} \hat{a}_{p_1,m_{p_1}} \\
&= (-1)^{j_{p_1}+j_{p_2}-J_p} \mathcal{N}_{p_1,p_2} \sum_{m_{p_1},m_{p_2}} \begin{pmatrix} j_{p_2} & j_{p_1} \\ m_{p_2} & m_{p_1} \end{pmatrix} \begin{matrix} J_p \\ M_p \end{matrix} \hat{a}_{p_2,m_{p_2}} \hat{a}_{p_1,m_{p_1}} \\
&= (-1)^{j_{p_1}+j_{p_2}-J_p} \mathcal{N}_{p_1,p_2} \left[\hat{a}_{p_2}\hat{a}_{p_1}\right]_{J_pM_p} ,
\end{aligned} \tag{6.13}$$

yielding a phase factor and the tensor product of the two considered annihilation operators. Here, the symmetry of the Clebsch-Gordan coefficients is applied. The pair annihilator $\hat{\mathcal{K}}_{p_1,p_2}(J_pM_p)$ is no spherical tensor. This problem emerged already in standard RPA and is solved by an additional phase factor (5.17), leading to

$$\begin{aligned}
\hat{\tilde{\mathcal{K}}}_{p_1,p_2}(J_pM_p) &= (-1)^{J_p+M_p} \hat{\mathcal{K}}_{p_1,p_2}(J_p - M_p) \\
&= (-1)^{j_{p_1}+j_{p_2}+M_p} \mathcal{N}_{p_1,p_2} \left[\hat{a}_{p_2}\hat{a}_{p_1}\right]_{J_p-M_p} .
\end{aligned} \tag{6.14}$$

The redefined pair annihilation operator $\hat{\tilde{\mathcal{K}}}_{p_1,p_2}(J_pM_p)$ then fulfills the conditions of spherical tensor operators and is used as the coupled pair annihilation operator. Starting alternatively with the coupling of spherical tensor operators $[\hat{\tilde{a}}_{p_1}\hat{\tilde{a}}_{p_2}]_{J_pM_p}$ would result in a coupled pair annihilator fulfilling the spherical tensor requirements automatically without an additional phase factor. Similarly, the hole-hole (hh) creation and annihilation operators can be deduced. Therefore, only the indices in the pair creator and annihilator are replaced by the hole indices.

For the construction of the 2p2h excitation creation operators in Eq. (6.1), the tensor product of the pp pair creator and the hh pair annihilator is calculated. The two particle states couple to an angular momentum J_p while the angular momenta of the hole states couple to J_h. The total angular momentum, obtained by coupling J_p and J_h, is given by J and its projection

quantum number M. The 2p2h excitation creation operator is evaluated to

$$
\begin{aligned}
&\hat{\mathcal{A}}^{\dagger}_{(p_1p_2)J_p(\hbar_1\hbar_2)J_h} \\
&\quad= \left[\hat{\mathcal{K}}^{\dagger}_{p_1,p_2}\hat{\tilde{\mathcal{K}}}_{\hbar_1,\hbar_2}\right]_{JM} \\
&\quad= \sum_{M_p,M_h} \left(\begin{matrix} J_p & J_h \\ M_p & M_h \end{matrix}\middle| \begin{matrix} J \\ M \end{matrix}\right) \hat{\mathcal{K}}^{\dagger}_{p_1,p_2}\hat{\tilde{\mathcal{K}}}_{\hbar_1,\hbar_2} \\
&\quad= \mathcal{N}_{p_1,p_2}\mathcal{N}_{\hbar_1,\hbar_2} \sum_{M_p,M_h} \left(\begin{matrix} J_p & J_h \\ M_p & M_h \end{matrix}\middle| \begin{matrix} J \\ M \end{matrix}\right) \sum_{m_{p_1},m_{p_2}} \left(\begin{matrix} j_{p_1} & j_{p_2} \\ m_{p_1} & m_{p_2} \end{matrix}\middle| \begin{matrix} J_p \\ M_p \end{matrix}\right) \hat{a}^{\dagger}_{p_1,m_{p_1}}\hat{a}^{\dagger}_{p_2,m_{p_2}} \\
&\qquad\qquad \times (-1)^{j_{h_1}+j_{h_2}+M_h} \sum_{m_{h_1},m_{h_2}} \left(\begin{matrix} j_{h_2} & j_{h_1} \\ m_{h_2} & m_{h_1} \end{matrix}\middle| \begin{matrix} J_h \\ -M_h \end{matrix}\right) \hat{a}_{\hbar_2,m_{h_2}}\hat{a}_{\hbar_1,m_{h_1}} \\
&\quad= \mathcal{N}_{p_1,p_2}\mathcal{N}_{\hbar_1,\hbar_2} \sum_{M_p,M_h} (-1)^{J_h-M_h} \left(\begin{matrix} J_p & J_h \\ M_p & -M_h \end{matrix}\middle| \begin{matrix} J \\ M \end{matrix}\right) \sum_{m_{p_1},m_{p_2}} \left(\begin{matrix} j_{p_1} & j_{p_2} \\ m_{p_1} & m_{p_2} \end{matrix}\middle| \begin{matrix} J_p \\ M_p \end{matrix}\right) \\
&\qquad\qquad \times \sum_{m_{h_1},m_{h_2}} \left(\begin{matrix} j_{h_1} & j_{h_2} \\ m_{h_1} & m_{h_2} \end{matrix}\middle| \begin{matrix} J_h \\ M_h \end{matrix}\right) \hat{a}^{\dagger}_{p_1,m_{p_1}}\hat{a}^{\dagger}_{p_2,m_{p_2}}\hat{a}_{\hbar_2,m_{h_2}}\hat{a}_{\hbar_1,m_{h_1}}
\end{aligned}
\tag{6.15}
$$

and thus has a more complex structure than the 2p2h excitation creation operator. Besides two creation and annihilation operators, three Clebsch-Gordan coefficients arising from the construction of the coupled creation and annihilation operators and a phase factor complete the definition of the 2p2h excitation creation operator. In the last step, the sum over M_h is reordered as done several times before leading to a change of the sign of the hole angular momentums projection number M_h. Furthermore, the phase factor is summarized, since there occurs an additional one by applying the symmetry properties of a Clebsch-Gordan coefficient

$$
(-1)^{j_{h_1}+j_{h_2}-M_h}\,(-1)^{j_{h_1}+j_{h_2}+J_h} = (-1)^{2j_{h_1}+2j_{h_2}+J_h-M_h} = (-1)^{J_h-M_h}. \tag{6.16}
$$

The single-particle angular momentum j_i is a half-integer leading to the fact that twice the single-particle angular momentum $2j_i$ is an odd integer. The phase factor contains the sum of both hole single-particle angular momenta $2(j_{h_1}+j_{h_2})$ which is an even number and the phase factor can be simplified. In Eq. (6.15), the particle creation and hole annihilation operators

$$
\hat{\mathcal{A}}^{\dagger}_{p_1p_2h_1h_2} = \hat{a}^{\dagger}_{p_1,m_{p_1}}\hat{a}^{\dagger}_{p_2,m_{p_2}}\hat{a}_{\hbar_2,m_{h_2}}\hat{a}_{\hbar_1,m_{h_1}} \tag{6.17}
$$

represent the uncoupled 2p2h creation operator in m-scheme. The coupled annihilation operator for 2p2h excitations reads

$$
\hat{\tilde{\mathcal{A}}}_{(p_1p_2)J_p(\hbar_1\hbar_2)J_h}(JM) = (-1)^{J+M}\hat{\mathcal{A}}_{(p_1p_2)J_p(\hbar_1\hbar_2)J_h}(J-M) \tag{6.18}
$$

analogously to Eq. (5.21) in RPA, and without further simplification. It is constructed via the adjoint of the creation operator including a phase factor in order to pay attention to

spherical tensor operators.

6.1.2 Commutation Relations including 1p1h and 2p2h Operators

As we know from the RPA equations, commutators of the Hamiltonian and excitation creation operators play an important role within the derivation. In the following section, some basic commutator relations are deduced for the excitation creation operators derived in the last section. The uncoupled 2p2h excitation operator is given as product of two 1p1h excitation operators

$$\hat{\mathcal{A}}^\dagger_{2,i} = \hat{\mathcal{A}}^\dagger_{1,i_1}\hat{\mathcal{A}}^\dagger_{1,i_2} \tag{6.19}$$

where the short-hand notation, introduced in Eq. (6.4), was exploited. The 2p2h excitation creation operator usually couples the particle states and the hole states, respectively, which are finally coupled to a total angular momentum. Hence, they are coupled in the so-called pp-hh scheme. On the other hand, the 1p1h excitation creation operators couples particles to holes and thus the coupling of several 1p1h operators employs the ph-ph scheme. Consequently there are two options for the sequence of the creators and annihilators which show no differences between organizing particles and holes or ph pairs as long as we consider ph pairs

$$\hat{\mathcal{A}}^\dagger_{p_1p_2h_1h_2} = \hat{a}^\dagger_{p_1}\hat{a}^\dagger_{p_2}\hat{a}_{h_2}\hat{a}_{h_1} = \hat{a}^\dagger_{p_1}\hat{a}_{h_1}\hat{a}^\dagger_{p_2}\hat{a}_{h_2} = \hat{\mathcal{A}}^\dagger_{p_1h_1}\hat{\mathcal{A}}^\dagger_{p_2h_2}\,. \tag{6.20}$$

This simplification is only valid in the uncoupled representation. The coupled 1p1h and 2p2h excitation creation operators include Clebsch-Gordan coefficients which take the different coupling order into account. With these considerations, the commutators of two second-order creators on m-scheme level becomes

$$\begin{aligned}\left[\hat{\mathcal{A}}^\dagger_{2,i},\hat{\mathcal{A}}^\dagger_{2,j}\right] &= \left[\hat{\mathcal{A}}^\dagger_{1,i_1}\hat{\mathcal{A}}^\dagger_{1,i_2},\hat{\mathcal{A}}^\dagger_{1,j_1}\hat{\mathcal{A}}^\dagger_{1,j_2}\right]\\ &= \hat{\mathcal{A}}^\dagger_{1,i_1}\left[\hat{\mathcal{A}}^\dagger_{1,i_2},\hat{\mathcal{A}}^\dagger_{1,j_1}\right]\hat{\mathcal{A}}^\dagger_{1,j_2} + \hat{\mathcal{A}}^\dagger_{1,i_1}\hat{\mathcal{A}}^\dagger_{1,j_1}\left[\hat{\mathcal{A}}^\dagger_{1,i_2},\hat{\mathcal{A}}^\dagger_{1,j_2}\right]\\ &+ \left[\hat{\mathcal{A}}^\dagger_{1,i_1},\hat{\mathcal{A}}^\dagger_{1,j_1}\right]\hat{\mathcal{A}}^\dagger_{1,j_2}\hat{\mathcal{A}}^\dagger_{1,i_2} + \hat{\mathcal{A}}^\dagger_{1,j_1}\left[\hat{\mathcal{A}}^\dagger_{1,i_1},\hat{\mathcal{A}}^\dagger_{1,j_2}\right]\hat{\mathcal{A}}^\dagger_{1,i_2} = 0\end{aligned} \tag{6.21}$$

The commutator of the creation operators associated with a 2p2h excitation is zero according to Eq. (A.6) with $p' \leftrightarrow h'$, since only commutators proportional to $\delta_{ph} = 0$ appear. Another helpful relation considers the commutator of the annihilation operators. Taking the adjoint results in

$$\left[\hat{\mathcal{A}}_{2,i},\hat{\mathcal{A}}_{2,j}\right] = \left[\hat{\mathcal{A}}^\dagger_{2,i},\hat{\mathcal{A}}^\dagger_{2,j}\right]^\dagger = 0. \tag{6.22}$$

Furthermore, the commutator of a first- and second-order creation operator

$$\left[\hat{\mathcal{A}}^\dagger_{1,i},\hat{\mathcal{A}}^\dagger_{2,j}\right] = \left[\hat{\mathcal{A}}^\dagger_{1,i},\hat{\mathcal{A}}^\dagger_{1,j_1}\hat{\mathcal{A}}^\dagger_{1,j_2}\right] = \hat{\mathcal{A}}^\dagger_{1,j_1}\left[\hat{\mathcal{A}}^\dagger_{1,i},\hat{\mathcal{A}}^\dagger_{1,j_2}\right] + \left[\hat{\mathcal{A}}^\dagger_{1,i},\hat{\mathcal{A}}^\dagger_{1,j_1}\right]\hat{\mathcal{A}}^\dagger_{1,j_2} = 0 \tag{6.23}$$

as well as the corresponding annihilators

$$\left[\hat{\mathcal{A}}_{1,i},\hat{\mathcal{A}}_{2,j}\right] = -\left[\hat{\mathcal{A}}^\dagger_{1,i},\hat{\mathcal{A}}^\dagger_{2,j}\right]^\dagger = 0 \tag{6.24}$$

are calculated to zero. Consequently, the expectation values of these commutators vanish as well. The last interesting case contains operators with mixed orders and a combination of creation and annihilation operator, for instance

$$\left[\hat{\mathcal{A}}^\dagger_{1,i}, \hat{\mathcal{A}}_{2,j}\right] = \left[\hat{\mathcal{A}}^\dagger_{1,i}, \hat{\mathcal{A}}_{1,j_1}\hat{\mathcal{A}}_{1,j_2}\right] = \hat{\mathcal{A}}_{1,j_1}\left[\hat{\mathcal{A}}^\dagger_{1,i}, \hat{\mathcal{A}}_{1,j_2}\right] + \left[\hat{\mathcal{A}}^\dagger_{1,i}, \hat{\mathcal{A}}_{1,j_1}\right]\hat{\mathcal{A}}_{1,j_2}. \tag{6.25}$$

This commutator can be non-zero. In contrast, the expectation value is indeed zero

$$\langle \mathrm{SD}| \left[\hat{\mathcal{A}}^\dagger_{1,i}, \hat{\mathcal{A}}_{2,j}\right] |\mathrm{SD}\rangle = 0, \tag{6.26}$$

since the commutator evaluates to Eq. (A.6) which in combination with the remaining annihilation operator leads to δ_{ph}=0 among others. Generally, only operators of the same order can provide Kronecker deltas that result in a non-vanishing matrix element.

6.1.3 The SRPA Matrix Equation

The derivation of the RPA equations are generally valid as far as we operate on operator-level and make no specific choice of the ECOs. The difference between the standard RPA and the consideration of higher-order excitations takes place in specific chosen ECOs. Thus, we start with the equation of motion (5.15)

$$\langle \mathrm{RPA}| \left[\delta\hat{Q}, [\hat{H}, \hat{Q}^\dagger_\omega]\right] |\mathrm{RPA}\rangle = E^{\mathrm{SRPA}}_\omega \ \langle \mathrm{RPA}| \left[\delta\hat{Q}, \ \hat{Q}^\dagger_\omega\right] |\mathrm{RPA}\rangle \tag{6.27}$$

with the SRPA excitation energy E^{SRPA}_ω, the second-order excitation creation operator $\hat{Q}^\dagger_\omega$ and its variation $\delta\hat{Q}$. Furthermore, applying the quasi-boson approximation which implies the replacement of the expectation value concerning the RPA ground state $|\mathrm{RPA}\rangle$ by the one regarding an arbitrary Slater determinant is still not order-dependent. As seen in the definition of the second-order ECOs in Eq. (6.1), the excitation creation operator is a sum of 1p1h and 2p2h (de-)excitations. That is the reasons why for the corresponding variation holds the same. The extended ECOs and corresponding variation are given by

$$\begin{aligned}
\hat{Q}^\dagger_\omega &= \hat{Q}^\dagger_{1,\omega} + \hat{Q}^\dagger_{2,\omega} = \sum_i \left(X^\omega_{1,i}\ \hat{\mathcal{A}}^\dagger_{1,i} - Y^\omega_{1,i}\ \hat{\mathcal{A}}_{1,i}\right) + \sum_j \left(X^\omega_{2,j}\ \hat{\mathcal{A}}^\dagger_{2,j} - Y^\omega_{2,j}\ \hat{\mathcal{A}}_{2,j}\right), \\
\delta\hat{Q} &= \delta\hat{Q}_{1,\omega} + \delta\hat{Q}_{2,\omega} = \sum_i \left(\delta X^{\omega*}_{1,i}\ \hat{\mathcal{A}}_{1,i} - \delta Y^{\omega*}_{1,i}\ \hat{\mathcal{A}}^\dagger_{1,i}\right) + \sum_j \left(\delta X^{\omega*}_{2,j}\hat{\mathcal{A}}_{2,j} - \delta Y^{\omega*}_{2,j}\hat{\mathcal{A}}^\dagger_{2,j}\right)
\end{aligned} \tag{6.28}$$

Inserting these definitions in the equation of motion results in four equations, due to four different amplitudes, while we had only two each in standard RPA

$$\delta X^\omega_1: \qquad \langle \mathrm{SD}| \left[\hat{\mathcal{A}}_{1,i}, [\hat{H}, \hat{Q}^\dagger_\omega]\right] |\mathrm{SD}\rangle = E^{\mathrm{SRPA}}_\omega \langle \mathrm{SD}| \left[\hat{\mathcal{A}}_{1,i}, \hat{Q}^\dagger_\omega\right] |\mathrm{SD}\rangle\ , \tag{6.29}$$

$$\delta Y^\omega_1: \qquad \langle \mathrm{SD}| \left[\hat{\mathcal{A}}^\dagger_{1,i}, [\hat{H}, \hat{Q}^\dagger_\omega]\right] |\mathrm{SD}\rangle = E^{\mathrm{SRPA}}_\omega \langle \mathrm{SD}| \left[\hat{\mathcal{A}}^\dagger_{1,i}, \hat{Q}^\dagger_\omega\right] |\mathrm{SD}\rangle\ , \tag{6.30}$$

$$\delta X^\omega_2: \qquad \langle \mathrm{SD}| \left[\hat{\mathcal{A}}_{2,i}, \left[\hat{H}, \hat{Q}^\dagger_\omega\right]\right] |\mathrm{SD}\rangle = E^{\mathrm{SRPA}}_\omega \langle \mathrm{SD}| \left[\hat{\mathcal{A}}_{2,i}, \hat{Q}^\dagger_\omega\right] |\mathrm{SD}\rangle\ , \tag{6.31}$$

$$\delta Y^\omega_2: \qquad \langle \mathrm{SD}| \left[\hat{\mathcal{A}}^\dagger_{2,i}, [\hat{H}, \hat{Q}^\dagger_\omega]\right] |\mathrm{SD}\rangle = E^{\mathrm{SRPA}}_\omega \langle \mathrm{SD}| \left[\hat{\mathcal{A}}^\dagger_{2,i}, \hat{Q}^\dagger_\omega\right] |\mathrm{SD}\rangle\ . \tag{6.32}$$

The commutators are evaluated in detail in App. A.4. Here, we only summarize the results: The right-hand side of each equation yields the amplitude corresponding to each variation, i.e. the first equation of motion which corresponds to the variation δX_1^ω leads to the forward amplitude $X_{1,i}^\omega$. The commutators contained in the left-hand side are more complicated. The first and second equation consists of a part that is identified with the A and B matrix from standard RPA and a part connecting the 1p1h with the 2p2h space. The latter two equations comprise new introduced matrices A_{12} and A_{22} that couple 1p1h or 2p2h (de-)excitations with 2p2h (de-)excitations.

The obtained equations of motions (6.29) - (6.32) are finally summarized to

$$\begin{aligned}
\delta X_1^\omega: &\quad E_\omega^{\mathrm{SRPA}}\, X_{1,i}^\omega = \sum_j X_{1,j}^\omega\,(A_{11})_{ij} + Y_{1,j}^\omega\,(B_{11})_{ij} + X_{2,j}^\omega\,(A_{12})_{ij} \\
\delta Y_1^\omega: &\quad E_\omega^{\mathrm{SRPA}}\, Y_{1,i}^\omega = -\sum_j X_{1,j}^\omega\,(B_{11})_{ij}^* - Y_{1,j}^\omega\,(A_{11})_{ij}^* - Y_{2,j}^\omega\,(A_{12})_{ij}^* \\
\delta X_2^\omega: &\quad E_\omega^{\mathrm{SRPA}}\, X_{2,i}^\omega = \sum_j X_{1,j}^\omega\,(A_{12})_{ij} + X_{2,j}^\omega\,(A_{22})_{ij} \\
\delta Y_2^\omega: &\quad E_\omega^{\mathrm{SRPA}}\, Y_{2,i}^\omega = \sum_j -Y_{1,j}^\omega\,(A_{21})_{ij}^* - Y_{2,j}^\omega\,(A_{22})_{ij}^*
\end{aligned} \tag{6.33}$$

with the (S)RPA A matrices

$$(A_{11})_{ij} = \langle \mathrm{SD}|\,[\hat{\mathcal{A}}_{1,i}, [\hat{H}, \hat{\mathcal{A}}_{1,j}^\dagger]]\,|\mathrm{SD}\rangle \tag{6.34}$$

$$(A_{12})_{ij} = \langle \mathrm{SD}|\,[\hat{\mathcal{A}}_{1,i}, [\hat{H}, \hat{\mathcal{A}}_{2,j}^\dagger]]\,|\mathrm{SD}\rangle \tag{6.35}$$

$$(A_{21})_{ij} = \langle \mathrm{SD}|\,[\hat{\mathcal{A}}_{2,i}, [\hat{H}, \hat{\mathcal{A}}_{1,j}^\dagger]]\,|\mathrm{SD}\rangle = (A_{12})_{ij}^T \tag{6.36}$$

$$(A_{22})_{ij} = \langle \mathrm{SD}|\,[\hat{\mathcal{A}}_{2,i}, [\hat{H}, \hat{\mathcal{A}}_{2,j}^\dagger]]\,|\mathrm{SD}\rangle \tag{6.37}$$

and B matrices

$$(B_{11})_{ij} = -\langle \mathrm{SD}|\,[\hat{\mathcal{A}}_{1,i}, [\hat{H}, \hat{\mathcal{A}}_{1,j}]]\,|\mathrm{SD}\rangle \tag{6.38}$$

$$(B_{12})_{ij} = -\langle \mathrm{SD}|\,[\hat{\mathcal{A}}_{1,i}, [\hat{H}, \hat{\mathcal{A}}_{2,j}]]\,|\mathrm{SD}\rangle \tag{6.39}$$

$$(B_{21})_{ij} = -\langle \mathrm{SD}|\,[\hat{\mathcal{A}}_{2,i}, [\hat{H}, \hat{\mathcal{A}}_{1,j}]]\,|\mathrm{SD}\rangle = (B_{12})_{ij}^T \tag{6.40}$$

$$(B_{22})_{ij} = -\langle \mathrm{SD}|\,[\hat{\mathcal{A}}_{2,i}, [\hat{H}, \hat{\mathcal{A}}_{2,j}]]\,|\mathrm{SD}\rangle \tag{6.41}$$

As discussed in more detail in App. A.4, all B matrices except for the B_{11} known from RPA are zero for a two-body Hamiltonian.

The equations of motion in Eq. (6.33) can now be reformulated to the SRPA eigenvalue

problem in matrix notation

$$\left(\begin{array}{cc|cc} A_{11} & A_{12} & B_{11} & 0 \\ A_{21} & A_{22} & 0 & 0 \\ \hline -B_{11}^* & 0 & -A_{11}^* & -A_{12}^* \\ 0 & 0 & -A_{21}^* & -A_{22}^* \end{array}\right) \begin{pmatrix} X_1^\omega \\ X_2^\omega \\ Y_1^\omega \\ Y_2^\omega \end{pmatrix} = E_\omega^{\mathrm{SRPA}} \begin{pmatrix} X_1^\omega \\ X_2^\omega \\ Y_1^\omega \\ Y_2^\omega \end{pmatrix} \tag{6.42}$$

The structure of the A matrix is as expected, the B matrix has only non-zero entries for the first block associated with the 1p1h space

$$B = \begin{pmatrix} B_{11} & 0 \\ 0 & 0 \end{pmatrix}. \tag{6.43}$$

This holds true for a two-body Hamiltonian. Including a higher-order interaction leads to a more complex structure of the B matrix as discussed in the explanation for vanishing block matrices of the B matrix.

6.2 Determination of SRPA Matrices

The next step is the evaluation of the block matrices of the A matrix. The B matrix remains unaffected by the inclusion of 2p2h contributions as long as we deal with a two-body Hamiltonian. There exist different approaches for the determination of the SRPA A matrix, namely the straight-forward evaluation of the expectation values given in Eq. (6.35) for the A_{12} matrix and in Eq. (6.37) for the A_{22} matrix with the aid of Wick's theorem in terms of contractions or via a more elegant diagrammatic formalism. The derivation via the diagrams is suitable especially for complicated and lengthy matrix elements as in the case of SRPA where we deal with up to 8 creation or annihilation operators. In the diagrammatic approach, only non-zero contributions are considered whereas in the straight-forward evaluation, the contractions leads to Kronecker deltas which depend on the particle-hole structure of the considered creation and annihilation operators. For a detailed description of the diagrams occurring in SRPA and the resulting matrix elements in m-scheme, we refer to Ref. [70].

6.2.1 Explicit Form of the A_{12} Matrix

The explicit form of the A_{12} matrix is given in this section in m-scheme and in the coupled representation. They can be converted into each other. The A_{12} matrix couples 1p1h states to 2p2h states and thus contains 6 different particle and hole states.

m-scheme Representation The A_{12} matrix, derived in Ref. [70] via diagrams and motivated in App. A.6 via contractions, is defined as

$$\begin{aligned} A_{12,\mathrm{uncoupled}} &\equiv [A_{12}]_{ph;p_1p_2h_1h_2} \\ &= (1 - P(h_1, h_2))\, \delta_{hh_1}\, \bar{v}_{ph_2,p_1p_2} - (1 - P(p_1, p_2))\, \delta_{pp_1}\, \bar{v}_{h_1h_2,hp_2} \\ &+ (1 - P(p_1, p_2))\, (1 - P(h_1, h_2))\, \delta_{hh_1} \delta_{pp_1} \epsilon_{h_2p_2} \end{aligned} \tag{6.44}$$

with the operator $P(p_1, p_2)$ changing the indices p_1 and p_2. In the first term, the particle p interacts with an intermediate ph state (where $h = h_1$ or $h = h_2$) while the hole h propagates free. The second term is the opposite, meaning a free propagation of a particle while the hole h interacts with an intermediate ph state. The third term contains the off-diagonal elements of the Fock operator (5.73) that will be interesting for IM-SRG evolved matrix elements and the natural orbitals, respectively. Due to the diagonality of the HF single-particle energies, this contribution vanishes in the HF framework.

Coupled Representation For the conversion of the m-scheme A_{12} matrix in the coupled basis, the coupled excitation creation operators needs to be applied. The A_{12} matrix is defined in Eq. (6.35) via the expectation value

$$(A_{12})_{ij} = \langle \mathrm{SD} | \left[\hat{\mathcal{A}}_{1,i}, [\hat{H}, \hat{\mathcal{A}}^\dagger_{2,j}] \right] | \mathrm{SD} \rangle \ .$$

Inserting the definition for the coupled ECOs (6.15), summarizing the phase factors and Clebsch-Gordan coefficients to a $6j$ symbol while exploiting the symmetry properties, and transforming the matrix elements of the Hamiltonian to the coupled basis, we find

$$\begin{aligned}
A_{12,\mathrm{coupled}} &\equiv [A_{12}]_{p\hbar;p_1p_2\hbar_1\hbar_2 J_p J_h} \\
&= \langle p\hbar, J | \, \hat{H} \, | (p_1 p_2, J_p) \, (\hbar_1 \hbar_2, J_h) \, , J \rangle \\
&= \left(1 - (-1)^{j_{h_1} + j_{h_2} - J_h} P(h_1, h_2)\right) \delta_{h h_1} (-1)^{j_p + j_{h_2} + J + J_h} \left(1 + \delta_{h_1 h_2}\right)^{-\frac{1}{2}} \hat{J}_p \hat{J}_h \\
&\quad \times \begin{Bmatrix} J_p & J & J_h \\ j_{h_1} & j_{h_2} & j_p \end{Bmatrix} \langle p_1 p_2, J_p | \, \hat{V}_{\mathrm{NN}} \, | p \hbar_2, J_p \rangle \\
&\quad - \left(1 - (-1)^{j_{p_1} + j_{p_2} - J_p} P(p_1, p_2)\right) \delta_{p p_1} (-1)^{j_{p_1} + j_{p_2} + J + J_h} \left(1 + \delta_{p_1 p_2}\right)^{-\frac{1}{2}} \hat{J}_p \hat{J}_h \\
&\quad \times \begin{Bmatrix} J_h & J & J_p \\ j_{p_1} & j_{p_2} & j_h \end{Bmatrix} \langle \hbar p_2, J_h | \, \hat{V}_{\mathrm{NN}} \, | \hbar_1 \hbar_2, J_h \rangle \\
&\quad + \sum_{m_p, m_h} (-1)^{j_h - m_h} \begin{pmatrix} j_p & j_h \\ m_p & -m_h \end{pmatrix} \begin{matrix} J \\ M \end{matrix} \mathcal{N}_{p_1,p_2} \mathcal{N}_{\hbar_1,\hbar_2} \sum_{M_p, M_h} \begin{pmatrix} J_p & J_h \\ M_p & -M_h \end{pmatrix} \begin{matrix} J \\ M \end{matrix} \\
&\quad \times (-1)^{J_h - M_h} \sum_{m_{p_1}, m_{p_2}} \begin{pmatrix} j_{p_1} & j_{p_2} \\ m_{p_1} & m_{p_2} \end{pmatrix} \begin{matrix} J_p \\ M_p \end{matrix} \sum_{m_{h_1}, m_{h_2}} \begin{pmatrix} j_{h_1} & j_{h_2} \\ m_{h_1} & m_{h_2} \end{pmatrix} \begin{matrix} J_h \\ M_h \end{matrix} \\
&\quad \times \left(1 - P(p_1, p_2)\right) \left(1 - P(h_1, h_2)\right) \delta_{h h_1} \delta_{p p_1} \epsilon_{h_2 p_2}
\end{aligned} \tag{6.45}$$

as definition of the coupled A_{12} matrix for a generic basis. The structure of the coupled and m-scheme A_{12} matrix are similar.

6.2.2 Explicit Form of the A_{22} Matrix

The explicit form of the A_{22} matrix is more complex due to the coupling of 2p2h states to 2p2h states. Thus, it includes 8 different particle and hole states. As for the other (S)RPA-matrices, the A_{22} matrix in m-scheme and in the coupled representation and can be converted into each other.

m-scheme Representation The A_{22} matrix, derived in Ref. [70] via diagrams, is defined as

$$\begin{aligned}
A_{22,\text{uncoupled}} &\equiv [A_{22}]_{p_1p_2h_1h_2;p_1'p_2'h_1'h_2'} \\
&= \left(\epsilon_{p_1,p_1'}\delta_{p_2'p_2} + \epsilon_{p_2,p_2'}\delta_{p_1'p_1} - \epsilon_{p_1'p_2}\delta_{p_1p_2'} - \epsilon_{p_2'p_1}\delta_{p_1'p_2}\right)\delta_{h_1'h_1}\delta_{h_2'h_2} \\
&\quad - \left(\epsilon_{h_1,h_1'}\delta_{h_2'h_2} + \epsilon_{h_2,h_2'}\delta_{h_1'h_1} - \epsilon_{h_1h_2'}\delta_{h_1'h_2} - \epsilon_{h_1'h_2}\delta_{h_1h_2'}\right)\delta_{p_1'p_1}\delta_{p_2'p_2} \\
&\quad - \left(1 - P(p_1', p_2')\right)\left(1 - P(h_1', h_2')\right)\left(1 - P(p_1, p_2)\right)\left(1 - P(h_1, h_2)\right) \\
&\quad \times \delta_{h_1'h_1}\delta_{p_1'p_1}\bar{v}_{h_2p_2',h_2'p_2} + \delta_{p_2'p_2}\delta_{p_1'p_1}\bar{v}_{h_1h_2,h_1'h_2'} + \delta_{h_1'h_1}\delta_{h_2'h_2}\bar{v}_{p_2'p_1',p_2p_1} \,.
\end{aligned} \tag{6.46}$$

The A_{22} matrix consists of eight terms which describe free propagation of all or a certain amount of particles and holes while the remaining interact. In the first terms, a 2p2h state propagates freely, the next terms describe a ph pair propagating and simultaneously the other ph pair interacting, followed by a free propagation of two particles whereas the two holes interact and vice versa.

Coupled Representation The A_{22} matrix is defined in Eq. (6.37) via the expectation value

$$(A_{22})_{ij} = \langle \text{SD}| \left[\hat{\mathcal{A}}_{2,i}, [\hat{H}, \hat{\mathcal{A}}^\dagger_{2,j}]\right] |\text{SD}\rangle \,.$$

The strategy for the determination of the coupled A_{22} matrix, which is briefly motivated in App. A.7, is the same as for the A_{12} matrix. The coupled excitation creation operators are applied, yielding an amount of Clebsch-Gordan coefficients and phase factors. Furthermore, the matrix elements of the Hamiltonian are transformed to the coupled basis, resulting in additional Clebsch-Gordan coefficients. With the aid of their symmetry properties, the completeness and orthogonality relation and rewriting into nj symbols with $n = 3, 6, 12$, the coupled A_{22} matrix becomes

$$\begin{aligned}
A_{22,\text{coupled}} &\equiv [A_{22}]_{p_1p_2\hbar_1\hbar_2J_pJ_h;p_1'p_2'\hbar_1'\hbar_2'J_{p'}J_{h'}} \\
&= A_{22}^{\text{SPE}} + A_{22}^{\hbar_1\hbar_2} + A_{22}^{p_1p_2} + A_{22}^{p_1\hbar_1}
\end{aligned} \tag{6.47}$$

with the following abbreviations:

$$
\begin{aligned}
A_{22}^{\mathrm{SPE}} = \mathcal{N}_{p_1,p_2}\mathcal{N}_{h_1,h_2}\mathcal{N}_{p_1',p_2'}\mathcal{N}_{h_1',h_2'} \sum_{\substack{M_pM_h\\M_{p'}M_{h'}}} \sum_{\substack{m_{p_1}m_{p_2}\\m_{p_1'}m_{p_2'}}} \sum_{\substack{m_{h_1}m_{h_2}\\m_{h_1'}m_{h_2'}}} (-1)^{J_h-M_h}(-1)^{J_{h'}-M_{h'}} \\
\times \begin{pmatrix} J_p & J_h \\ M_p & -M_h \end{pmatrix}\begin{pmatrix} j_{p_1} & j_{p_2} \\ m_{p_1} & m_{p_2} \end{pmatrix}\begin{pmatrix} j_{h_1} & j_{h_2} \\ m_{h_1} & m_{h_2} \end{pmatrix}\begin{pmatrix} J_{p'} & J_{h'} \\ M_{p'} & -M_{h'} \end{pmatrix}\Big|\begin{matrix} J \\ M \end{matrix}\Big) \\
\times \begin{pmatrix} j_{p_1'} & j_{p_2'} \\ m_{p_1'} & m_{p_2'} \end{pmatrix}\begin{pmatrix} j_{h_1'} & j_{h_2'} \\ m_{h_1'} & m_{h_2'} \end{pmatrix}\Big|\begin{matrix} J_{p'} \\ M_{p'} \end{matrix}\Big)\Big|\begin{matrix} J_{h'} \\ M_{h'} \end{matrix}\Big) \\
\times [\Big(\epsilon_{p_1,p_1'}\delta_{p_2'p_2} + \epsilon_{p_2,p_2'}\delta_{p_1'p_1} - \epsilon_{p_1'p_2}\delta_{p_1p_2'} - \epsilon_{p_2'p_1}\delta_{p_1'p_2}\Big)\delta_{h_1'h_1}\delta_{h_2'h_2} \\
- \Big(\epsilon_{h_1,h_1'}\delta_{h_2'h_2} + \epsilon_{h_2,h_2'}\delta_{h_1'h_1} - \epsilon_{h_1h_2'}\delta_{h_1'h_2} - \epsilon_{h_1'h_2}\delta_{h_1h_2'}\Big)\delta_{p_1'p_1}\delta_{p_2'p_2}]
\end{aligned}
\tag{6.48}
$$

$$
A_{22}^{\hbar_1\hbar_2} = \delta_{p_1'p_1}\delta_{p_2'p_2}\delta_{J_{p'}J_p}\delta_{J_{h'}J_h}\left(1+(-1)^{J_p}\delta_{p_1p_2}\right)(1+\delta_{p_1p_2})^{-1}\left\langle \hbar_1'\hbar_2', J_h\right|\hat{V}_{\mathrm{NN}}\left|\hbar_1\hbar_2, J_h\right\rangle \tag{6.49}
$$

$$
A_{22}^{p_1p_2} = \delta_{h_1'h_1}\delta_{h_2'h_2}\delta_{J_{p'}J_p}\delta_{J_{h'}J_h}\left(1+(-1)^{J_h}\delta_{h_1h_2}\right)(1+\delta_{h_1h_2})^{-1}\left\langle p_1p_2, J_p\right|\hat{V}_{\mathrm{NN}}\left|p_1'p_2', J_p\right\rangle \tag{6.50}
$$

$$
\begin{aligned}
A_{22}^{p_1\hbar_1} = &\left(1-(-1)^{j_{p_1}+j_{p_2}-J_p}P(p_1,p_2)\right)(1+\delta_{p_1p_2})^{-\frac{1}{2}} \\
&\times \left(1-(-1)^{j_{h_1}+j_{h_2}-J_h}P(h_1,h_2)\right)(1+\delta_{h_1h_2})^{-\frac{1}{2}} \\
&\times \left(1-(-1)^{j_{p_1'}+j_{p_2'}-J_{p'}}P(p_1',p_2')\right)\left(1+\delta_{p_1'p_2'}\right)^{-\frac{1}{2}} \\
&\times \left(1-(-1)^{j_{h_1'}+j_{h_2'}-J_{h'}}P(h_1',h_2')\right)\left(1+\delta_{h_1'h_2'}\right)^{-\frac{1}{2}} \\
&\times \delta_{p_2'p_2}\delta_{h_2'h_2}(-1)^{1+j_{p_1}+j_{p_2}+j_{h_1}+j_{h_2}}\hat{J}_p\hat{J}_{p'}\hat{J}_h\hat{J}_{h'} \\
&\times \sum_L (-1)^{J_h-J_{h'}+J-L}(2L+1)\begin{Bmatrix} J_p & J_{p'} & L \\ J_{h'} & J_h & J \end{Bmatrix}\begin{Bmatrix} J_p & J_{p'} & L \\ j_{p_1'} & j_{p_1} & j_{p_2} \end{Bmatrix}\begin{Bmatrix} J_h & J_{h'} & L \\ j_{h_1'} & j_{h_1} & j_{h_2} \end{Bmatrix} \\
&\times \sum_{J_1} (-1)^{j_{h_1}+j_{p_1'}-J_1}(2J_1+1)\begin{Bmatrix} j_{p_1} & j_{h_1'} & J_1 \\ j_{h_1} & j_{p_1'} & L \end{Bmatrix}\left\langle p_1\hbar_1', J_1\right|\hat{V}_{\mathrm{NN}}\left|p_1'\hbar_1, J_1\right\rangle .
\end{aligned}
\tag{6.51}
$$

As in the previous section, the structure stays the same between the coupled and m-scheme formulation. The free propagation is described by the Kronecker delta and the interaction by the matrix element. The only permutations occur for a ph propagation while the other ph pair interacts.

6.3 Explicit Three-Body Interaction

In contrast to first-order RPA, the SRPA does not reduce the case of including a three-body interaction to the case of using a normal-ordered two-body approximation. Besides a modified B matrix which is mirrored in non-vanishing block matrices B_{12} and B_{22} as mentioned in the derivation of the SRPA equations in Sec. 6.1.3, the A matrix experiences an alteration as well. For more information about SRPA including three-body interactions, we refer to Ref. [70]. Taking into account the three-body interactions is once again a compromise between a more precise result and more effort due to an extended formalism.

6.4 Transitions in the Framework of RPA

In order to consider transitions in the framework of RPA, the transition matrix element is derived. Furthermore, a possibility for the comparison of discrete calculated strength distributions to continuous experimental distributions is introduced. Finally, the sum rules are discussed which allow for a comparison of different approaches in the context of collective excitations. This section is based on Refs. [33, 49, 70].

6.4.1 Transition Matrix Element

The matrix element that enters the definition of a transition strength from an initial excited state $|\omega\rangle$ to the correlated RPA ground state $|\mathrm{RPA}\rangle$ is defined as

$$R^{(\omega)} = \langle \mathrm{RPA}| \hat{T}_{\sigma\lambda\mu} |\omega\rangle \tag{6.52}$$

with the generic electromagnetic multipole operator $\hat{T}_{\sigma\lambda\mu}$ introduced in Eq. (4.22). The excited state can be written in terms of the ph creation and annihilation operators and the RPA forward and backward amplitudes

$$|\omega\rangle = \hat{Q}^\dagger_\omega |\mathrm{RPA}\rangle = \sum_{p,h} \left(X^\omega_{p\hbar} \hat{\mathcal{A}}^\dagger_{p\hbar}(JM) - Y^\omega_{p\hbar} \hat{\tilde{\mathcal{A}}}_{p\hbar}(JM) \right) |\mathrm{RPA}\rangle \ , \tag{6.53}$$

leading to the transition matrix element

$$\begin{aligned} R^{(\omega)} &= \langle \mathrm{RPA}| \hat{T}_{\sigma\lambda} \hat{Q}^\dagger_\omega |\mathrm{RPA}\rangle \\ &= \langle \mathrm{RPA}| [\hat{T}_{\sigma\lambda}, \hat{Q}^\dagger_\omega] |\mathrm{RPA}\rangle \ , \end{aligned} \tag{6.54}$$

where we used $\hat{Q}_\omega |\mathrm{RPA}\rangle = 0$ as in Eq. (5.2) enabling the introduction of a commutator. This approach is generally valid and independent of the actual form of $\hat{T}_{\sigma\lambda}$ and $\hat{Q}^\dagger_\omega$. The reformulation of a set of operators into a commutator is known from the EOM and is an

established method in the framework of RPA. Due to the reduced rank of the involved operators, the computational cost is lower and as well the formalistic demand. Furthermore, the introduction of a commutator allows for the application of the QBA.

Within QBA, the RPA ground state $|\mathrm{RPA}\rangle$ is substituted by an uncorrelated Slater determinant, yielding as transition matrix element

$$\langle \mathrm{RPA}| \left[\hat{T}_{\sigma\lambda}, \hat{Q}^{\dagger}_{\omega}\right] |\mathrm{RPA}\rangle \overset{\mathrm{QBA}}{\approx} \langle \mathrm{SD}| \left[\hat{T}_{\sigma\lambda}, \hat{Q}^{\dagger}_{\omega}\right] |\mathrm{SD}\rangle \,. \tag{6.55}$$

The ECO in the commutator contains the coupled ph creator and annihilator. Thus, we can split the commutator and evaluate the matrix element for the commutator of the electromagnetic operator $\hat{T}_{\lambda\mu}$ given in Eq. (4.28) and the coupled ph creation operator

$$\langle \mathrm{SD}| \left[\hat{T}_{\sigma\lambda}, \hat{\mathcal{A}}^{\dagger}_{p'\hbar'}(JM)\right] |\mathrm{SD}\rangle = \hat{\lambda}^{-1} \sum_{p,h} \langle p||\hat{T}_{\sigma\lambda}||h\rangle \, \delta_{\lambda J}\delta_{\mu,-M}(-1)^{j_p+j_h+M+1}\delta_{pp'}\delta_{hh'} \tag{6.56}$$

and analogously for the coupled ph annihilation operator

$$\langle \mathrm{SD}| \left[\hat{T}_{\sigma\lambda}, \hat{\tilde{\mathcal{A}}}_{p'\hbar'}(JM)\right] |\mathrm{SD}\rangle = \hat{\lambda}^{-1} \sum_{p,h} \langle p||\hat{T}_{\sigma\lambda}||h\rangle \, \delta_{\lambda J}\delta_{\mu,-M}(-1)^{J+M+1}\delta_{pp'}\delta_{hh'} \,. \tag{6.57}$$

Combining these results, applying the Wigner-Eckart theorem (2.20) to the left-hand side, which leads to a reduced matrix element, and exploiting the following symmetry property

$$\langle h||\hat{T}_{\sigma\lambda}||p\rangle = (-1)^{j_p+j_h+1} \langle p||\hat{T}_{\sigma\lambda}||h\rangle \,, \tag{6.58}$$

the transition matrix elements in QBA read

$$\langle \mathrm{RPA}||\hat{T}_{\sigma\lambda}||\omega\rangle = \delta_{\lambda J} \sum_{p,h} \langle p||\hat{T}_{\sigma\lambda}||h\rangle \left((-1)^{\lambda} X^{\omega}_{p\hbar} + Y^{\omega}_{p\hbar}\right) . \tag{6.59}$$

In the framework of TDA, only the first term remains since it holds $Y^{\omega}_{p\hbar} = 0$.

An IM-SRG or free-space SRG transformed electromagnetic operator contains a two-body contribution due to the induced higher-order terms arising during the evolution. Thus, the two-body transition matrix element needs to be taken into account for those aforementioned operators for a consistent description of collective excitations. These matrix elements are derived in Ref. [98] and only given here for completeness. The coupled RPA two-body matrix element reads

$$\begin{aligned}\langle \mathrm{RPA}|\hat{T}_{\sigma\lambda}|\omega, J\rangle = \sum_{J_1 J_2} \sum_{p\hbar\mathfrak{b}} \hat{J}_1 \hat{J}_2 \mathcal{N}^{-1}_{p\mathfrak{b}} \mathcal{N}^{-1}_{\hbar\mathfrak{b}} \begin{Bmatrix} j_p & j_h & J \\ J_1 & J_2 & j_b \end{Bmatrix} \\ \Big(X^{\omega}_{p\hbar}(-1)^{J_2-j_p-j_b} \langle \hbar\mathfrak{b}, J_1|\hat{T}_{\sigma\lambda}|p\mathfrak{b}, J_2\rangle \\ + \, Y^{\omega}_{p\hbar}(-1)^{J+J_1+j_p-j_b} \langle p\mathfrak{b}, J_2|\hat{T}_{\sigma\lambda}|\hbar\mathfrak{b}, J_1\rangle \Big) \,.\end{aligned} \tag{6.60}$$

The coupled SRPA two-body matrix element is given by

$$\begin{aligned}\langle \mathrm{SRPA}|\hat{T}_{\sigma\lambda}|\omega, J\rangle = &\langle \mathrm{RPA}, J_G = 0|\hat{T}_{\sigma\lambda}|\omega, J\rangle \\ &+ \sum_{\substack{pp' \\ \hbar\hbar'}} \Big(\mathcal{X}^{\omega}_{p\hbar,p'\hbar'}(-1)^{J_h - J_p + J} \left\langle \hbar\hbar', J_h \middle| \hat{T}_{\sigma\lambda} \middle| pp', J_p \right\rangle \\ &+ \mathcal{Y}^{\omega}_{p\hbar,p'\hbar'} \left\langle pp', J_p \middle| \hat{T}_{\sigma\lambda} \middle| \hbar\hbar', J_h \right\rangle \Big)\end{aligned} \tag{6.61}$$

with the first term being identical to the RPA two-body matrix element.

6.4.2 Lorentz Curves

The experimental data on collective excitations are continuous distributions. In contrast, the theoretical calculation provides a discrete spectrum with one calculated strength per any eigenstate

$$R(E;\sigma\lambda) = \sum_{\omega} |\left\langle \omega||\hat{T}_{\sigma\lambda}||\mathrm{RPA}\right\rangle|^2 \delta(E - E_\omega) \tag{6.62}$$

In order to enable a comparison of the calculated discrete excitation spectrum from (S)RPA to the continuous experimental distributions, we convolve the discrete theoretical values with a Lorentzian, leading to a smoothed-out strength function

$$R(E;\sigma\lambda) = \sum_{\omega} \frac{\Gamma}{\pi} \frac{|\left\langle \omega||\hat{T}_{\sigma\lambda}||\mathrm{RPA}\right\rangle|^2}{((E - E_\omega)^2 + \Gamma^2)} \tag{6.63}$$

The width Γ of the Lorentzian is chosen to be $\Gamma = 1\,\mathrm{MeV}$ for all calculations throughout this thesis. The discrete as well as the smoothed-out distribution are both referred to as $R(E;\sigma\lambda)$, since both can be distinguished easily.

6.4.3 Sum Rules

The sum rules allow for a comparison of different approaches of collective excitations. The general definition of sum rules is given by

$$S_k = \sum_{\omega} (E_\omega - E_0)^k \left\langle \omega||\hat{T}_{\sigma\lambda\mu}||\mathrm{RPA}\right\rangle \tag{6.64}$$

where $k = 1$ is denoted as energy-weighted sum rule (EWSR) and $k = 0$ is associated with the non energy-weighted sum rule (NEWSR).

Energy-Weighted Sum Rule The RPA satisfies the energy-weighted sum rule

$$\sum_{\omega} E^{\mathrm{RPA}}_{\omega} |\left\langle \omega||\hat{T}_{\sigma\lambda}||\mathrm{RPA}\right\rangle|^2 = \frac{1}{2}\hat{\lambda}^2 \left\langle \mathrm{SD}\right| [\hat{T}^{\dagger}_{\sigma\lambda\mu}, \hat{H}, \hat{T}_{\sigma\lambda\mu}] \left|\mathrm{SD}\right\rangle \tag{6.65}$$

with the Hermitian conjugate $\hat{T}^{\dagger}_{\sigma\lambda\mu}$ of the electromagnetic multipole operator and $\omega = n\lambda^{\pi}$ since $\lambda = J$. The double commutator is defined as

$$\left[\hat{A},\hat{B},\hat{C}\right] = \frac{1}{2}\left(\left[\left[\hat{A},\left[\hat{B},\hat{C}\right]\right] + \left[\left[\hat{A},\hat{B}\right],\hat{C}\right]\right]\right) . \tag{6.66}$$

With this definition, the proof of the EWSR (6.65) is straight-forward and can be found in Refs. [70, 49]. As a side product, a more handy reformulation for the EWSR is provided

$$\sum_{\omega} E^{\mathrm{RPA}}_{\omega} |\left\langle \omega||\hat{T}_{\sigma\lambda}||\mathrm{RPA}\right\rangle|^2 = p^{\lambda^T}\left(A - (-1)^{\lambda}B\right)p^{\lambda} \tag{6.67}$$

with the abbreviation

$$p^{\lambda}_{ij} = (-1)^{\lambda}\left\langle i||\hat{T}_{\sigma\lambda}||j\right\rangle \tag{6.68}$$

which avoids the actual calculation of the double commutator and, thus, is more convenient. The left-hand side of the EWSR only depends on the RPA results, for instance energy $E^{\mathrm{RPA}}_{\omega}$, RPA ground state $|\mathrm{RPA}\rangle$ and excited state $|\omega\rangle$, whereas the right-hand side carries information about the input parameters such as the Hamiltonian $\hat{H}$ (explicitly or as part of the RPA matrices A and B) and the Slater determinant $|\mathrm{SD}\rangle$. This structure allows for a crosscheck of the actual RPA calculation.

We use a one-body transition operator. Therefore, the two-body part of the excitation creation operator $\hat{Q}^{\dagger}_{\omega}$ does not play a role in the calculation and the EWSR is obeyed for RPA and SRPA, at least for HF single-particle states or natural orbitals. Due to the peculiarity that we are not able to calculate all solutions of the SRPA eigenvalue problem, since the 2p2h space is too large and needs to be truncated, the EWSR is only valid up to a certain accuracy in SRPA calculations, because as well high-lying energies that are omitted can cause a contribution to the strength.

Non Energy-Weighted Sum Rule The TDA satisfies the non energy-weighted sum rule

$$\sum_{\omega} |\left\langle \omega||\hat{T}_{\sigma\lambda}||\mathrm{SD}\right\rangle|^2 = \sum_{i,j} |\left\langle i||\hat{T}_{\sigma\lambda}||j\right\rangle|^2 \tag{6.69}$$

which is less complicated since the TDA ground state is identical to a Slater determinant. Again, the left-hand side depends on the TDA wave function while the right-hand side corresponds to the matrix element of the electromagnetic multipole operator. For the same reasons as in the case of the EWSR, the NEWSR is additionally valid for the second-order TDA.

Due to the peculiarity that the IM-(S)RPA reduces to an IM-(S)TDA, whose discussion in more detail is part of Chapter 7, both sum rules should be obeyed within a certain accuracy for matrix elements of an IM-transformed Hamiltonian. This is not the case for the other single-particle bases.

7

RPA-type Methods - A Comparison

Contents

All methods introduced so far are briefly compared and the main differences are stated. Furthermore, peculiarities for different single-particle bases are discussed.

The summary of all considered ph excitations and extensions is depicted in Tab. 7.1. Besides the type, the excitation creation operator $\hat{Q}^\dagger_\omega$ and its corresponding variation $\delta\hat{Q}$ are shown. The TDA (c.f. Sec. 5.1.4) includes exclusively ph excitations and consequently the excitation creation operator contains only one term which is affiliated with the forward amplitude $\mathcal{X}^\omega_{p\hbar}$. Thus, the TDA eigenvalue problem is manageable, since only one matrix is involved in the TDA equations. It can be shown that the TDA ground state is identical to the single Slater determinant $|\mathrm{SD}\rangle$.

The RPA (c.f. Sec. 5) permits additionally hp excitations to the ph excitations from TDA. As a result, the excitation creation operator has a further term which is associated with the backward amplitude $\mathcal{Y}^\omega_{p\hbar}$. In consequence the RPA equations are more complex and a second matrix occurs in the derivation. The RPA ground state $|\mathrm{RPA}\rangle$ includes already 1p1h excitations and thus, the single Slater determinant is not a valid choice. However, the quasi-boson approximation is applied leading to a substitution of the RPA ground state by the single Slater determinant in expectation values. It can be shown (c.f. Ref. [70]) that the RPA including explicit three-body interactions is identical to the case in which the normal-ordered two-body approximation is applied.

The SRPA (c.f. Sec. 6) is a natural extension of the RPA since the model space of considered excitations is enlarged to 2p2h excitations. In comparison to RPA, the excitation creation operator has a more complex structure and includes also a forward and backward amplitude for these excitations, $\mathcal{X}^\omega_{p_1\hbar_1,p_2\hbar_2}$ and $\mathcal{Y}^\omega_{p_1\hbar_1,p_2\hbar_2}$, respectively. The SRPA equations become more lengthy, since besides the new submatrix associated with the 2p2h space two matrices corresponding to a coupling of 1p1h and 2p2h space emerge. Including a three-body interaction would yield to additional contributions in the involved matrices.

Naively one would expect a better description due to a systematical improvement with extending the model space of excitations. How the different approaches and extensions, respectively, perform in actual calculations and for different single-particle bases and input matrix elements can be seen in Part III.

type	$\hat{Q}^\dagger_\omega$	variation $\delta\hat{Q}$
TDA	$\sum_{p,\hbar} \mathcal{X}^\omega_{p\hbar}\ \hat{\mathcal{A}}^\dagger_{p\hbar}(JM)$	$\hat{\mathcal{A}}_{p\hbar}(JM)$
RPA	$\sum_{p,\hbar}[\mathcal{X}^\omega_{p\hbar}\ \hat{\mathcal{A}}^\dagger_{p\hbar}(JM)$	$\hat{\mathcal{A}}_{p\hbar}(JM)$
	$-\mathcal{Y}^\omega_{p\hbar}\ \hat{\tilde{\mathcal{A}}}_{p\hbar}(JM)]$	$\hat{\tilde{\mathcal{A}}}^\dagger_{p\hbar}(JM)$
SRPA	$\hat{Q}^\dagger_{\omega,\mathrm{RPA}}$	$\hat{\mathcal{A}}_{p\hbar}(JM), \hat{\tilde{\mathcal{A}}}^\dagger_{p\hbar}(JM)$
	$+\sum_{\substack{p_1,\hbar_1\\p_2,\hbar_2}}[\mathcal{X}^\omega_{p_1\hbar_1,p_2\hbar_2}\ \hat{\mathcal{A}}^\dagger_{(p_1p_2)J_p(\hbar_1\hbar_2)J_h}$	$\hat{\mathcal{A}}_{(p_1p_2)J_p(\hbar_1\hbar_2)J_h}$
	$-\mathcal{Y}^\omega_{p_1\hbar_1,p_2\hbar_2}\ \hat{\tilde{\mathcal{A}}}_{(p_1p_2)J_p(\hbar_1\hbar_2)J_h}]$	$\hat{\tilde{\mathcal{A}}}^\dagger_{(p_1p_2)J_p(\hbar_1\hbar_2)J_h}$

Table 7.1: Excitation creation operators and their variations for different theories. The ph creation and annihilation operators are given in Tab. 5.1.

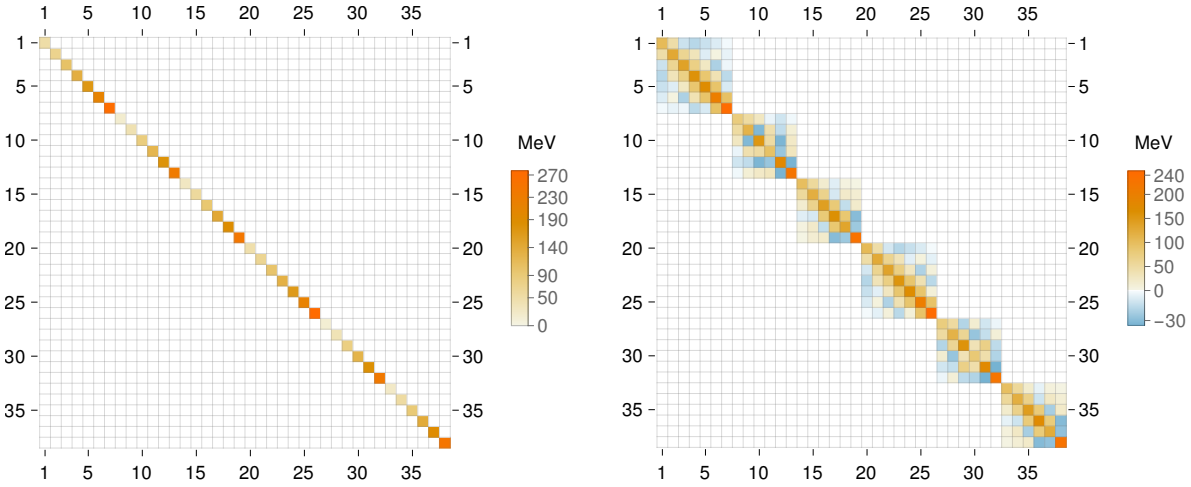

(a) HF **(b)** NAT

Figure 7.1: Representation of the A_{11} matrix one-body contribution for HF (left) and NAT (right). The choice of the HF single-particle basis leads to a diagonal structure whereas natural orbitals show additional non-diagonal behavior.

7.1 Peculiarities of HF-(S)RPA

The results and peculiarities for the (S)RPA matrices in the framework of HF are motivated. In the case of an HF single-particle basis as input choice, the definition of the diagonal single-particle energies (3.35) is inserted, yielding to further simplifications

$$\begin{aligned} A^{\mathrm{HF}}_{ph,p'h'} &= \langle \mathrm{HF} | \, \hat{a}^\dagger_h \hat{a}_p [\hat{H}, \hat{a}^\dagger_{p'} \hat{a}_{h'}] \, | \mathrm{HF} \rangle \\ &= (\epsilon_p - \epsilon_h) \, \delta_{pp'} \delta_{hh'} + \bar{v}_{ph',hp'} \, . \end{aligned} \tag{7.1}$$

Therefore, the A matrix in m-scheme of the HF-RPA is diagonal in the contribution depending on the single-particle energies as well. This is shown in Fig. 7.1. For the coupled formulation of the A matrix, we find

$$\begin{aligned} A^{J,\mathrm{HF}}_{p\hbar,p'\hbar'} &= (\epsilon_p - \epsilon_h) \, \delta_{pp'} \delta_{hh'} \\ &\quad + \sum_{J'} (2J'+1)(-1)^{j_h + j_{p'} + J'} \begin{Bmatrix} j_p & j_h & J \\ j_{p'} & j_{h'} & J' \end{Bmatrix} \left\langle p\hbar', J' \right| \hat{V}_{\mathrm{NN}} \left| \hbar p', J' \right\rangle \end{aligned} \tag{7.2}$$

since the diagonality of the single-particle energies leads to identical Clebsch-Gordan coefficients yielding one by summation. The B matrix remains unmodified compared to a generic basis and is given by Eq. (5.93) and Eq. (5.99).

The SRPA submatrices can be simplified in the HF framework. Since the HF single-particle energies (3.35) are diagonal, the last term in Eq. (6.44) is zero. Thus, the A_{12} matrix consists only of 2B contributions. For the A_{22} matrix (6.46), the term containing the single-particle energies can be summarized due to the diagonality of the single-particle energies, yielding

$$A^{\mathrm{SPE}}_{22} = \delta_{h'_1 h_1} \delta_{p'_1 p_1} \delta_{p'_2 p_2} \delta_{h'_2 h_2} \left(\epsilon_{p_1} + \epsilon_{p_2} - \epsilon_{h_1} - \epsilon_{h_2} \right) . \tag{7.3}$$

Furthermore, the non-diagonal terms including ϵ_{p_i,p_j} vanish. The 2B contributions remain unchanged.

7.2 In-Medium (S)RPA

For the discussion of the peculiarities of the IM-(S)RPA, we first present general aspects of the IM-SRG.

7.2.1 In-Medium Similarity Renormalization Group

The in-medium similarity renormalization group (IM-SRG) method, following Refs. [70, 86, 88], is used for solving the many-body Schrödinger equation via combining SRG principles and mechanisms available in second quantization. The SRG approach discussed in Sec. 3.2 is denoted as free-space SRG in order to specify the difference between both concepts.

Within the IM-SRG framework, all operators are represented in normal-ordering with respect to a certain reference state. For the Hamiltonian, the application of NO2B has shown to be a good approximation (c.f. Ref. [52]) as introduced in Sec. 3.1.2. Contrary to free-space SRG, an A-body system is SRG evolved, which is indicated by the phrase in-medium. The aim of free-space SRG is the pre-diagonalization of the Hamiltonian and thus the improvement of convergence of a subsequent many-body calculation by an incomplete decoupling of high- and low-momentum states. Instead, the A-body reference state in the IM-SRG framework is required to decouple entirely from all its ph excitations. The reference state is obtained in a previous HF or NCSM calculation. However, the flow-equation for the IM-SRG evolution remains the same as for the free-space SRG

$$\frac{\mathrm{d}\hat{H}(s)}{\mathrm{d}s} = \left[\hat{\eta}(s), \hat{H}(s)\right] \tag{7.4}$$

with the continuous unitary transformation of the (normal-ordered) Hamiltonian

$$\hat{H}(s) = \hat{U}^\dagger(s)\hat{H}_0\hat{U}(s)\,. \tag{7.5}$$

For a better distinction, the flow parameter s instead of α is used for the IM-SRG evolution. As in the free-space SRG, induced higher-order terms occur during the evolution and are omitted.

The procedure of IM-SRG is schematically illustrated in Fig. 7.2. In the ph formalism, the Hamiltonian has block structure. The point of interest is the reference state which we aim to decouple from ph excitations. The initial unevolved Hamiltonian that corresponds to the flow parameter $s = 0$ exhibits contributions associated with coupling between the reference state and 1p1h and 2p2h excitations, respectively. A fully IM-SRG evolved Hamiltonian ($s \to \infty$) does not contain these contributions, they are suppressed since the reference state is decoupled from all ph excitations.

For this decoupling procedure, the Hamiltonian is split into a diagonal and an off-diagonal part

$$\hat{H} = \hat{H}_\mathrm{d} + \hat{H}_\mathrm{od}\,. \tag{7.6}$$

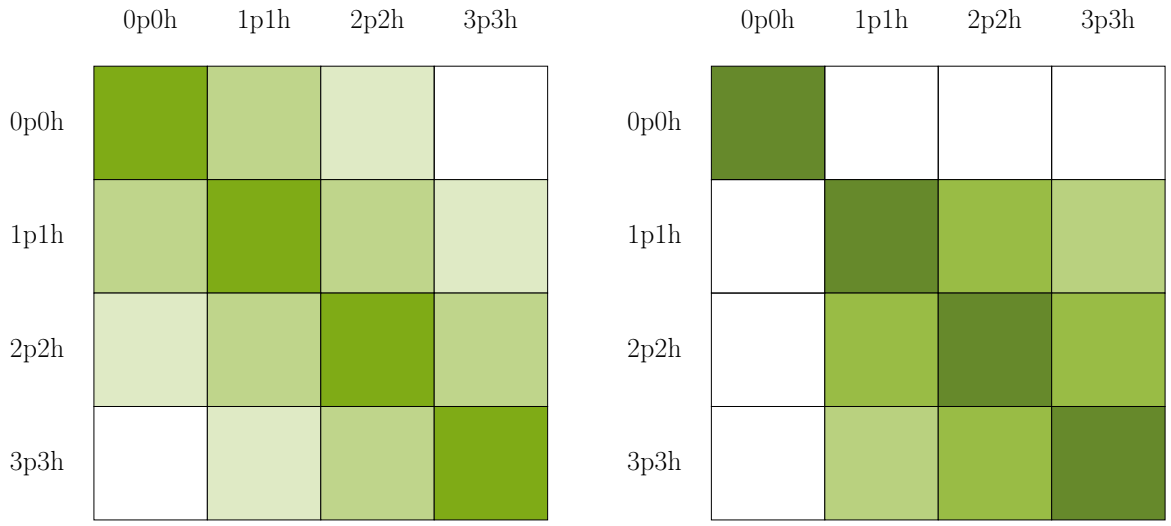

(a) unevolved Hamiltonian **(b)** IM-SRG evolved Hamiltonian

Figure 7.2: Schematic representation of decoupling process within IM-SRG. The final IM-SRG evolved Hamiltonian (right) exhibits less to none coupling of the reference state with ph excitations in contrast to the initial unevolved Hamiltonian (left).

The off-diagonal part consists of the contributions that are associated with the coupling of the reference state to 1p1h and 2p2h excitations.

As in free-space SRG, the generator can be chosen arbitrarily, for instance the Wegner generator (3.13), the White or imaginary-time generator [68]. All these generators lead to a decoupling form the reference state although the properties of the evolution differ. In principle, the same fix point is reached during the flow for a good choice of truncation parameter.

Another similarity of free-space and IM-SRG is the need of simultaneous evolution of arbitrary operators

$$\frac{\mathrm{d}\hat{O}(s)}{\mathrm{d}s} = \left[\hat{\eta}(s), \hat{O}(s)\right] \tag{7.7}$$

if other observables than the energy are of interest. This is the case for the transitions obtained within the RPA framework.

7.2.2 Peculiarities of IM-(S)RPA

For the case of an IM-transformed Hamiltonian in the framework of RPA, no further simplifications can be applied for the A and B matrix deduced in Sec. 5.2 for a generic basis. Thus, the coupled A and B matrix are determined via Eq. (5.88) and Eq. (5.99).

As discussed in the previous section, the IM-SRG transformation suppresses the off-diagonal matrix elements of the form $\bar{v}_{pp',hh'}$. These are exactly the contributions to the B matrix. Utilizing matrix elements from IM-SRG leads to a vanishing B matrix and, thus, to a reduction to TDA since all backward amplitudes Y^{ω}_{ph} are zero. In Fig. 7.3, the B matrix is illustrated for HF-RPA and for IM-HF-RPA. We observe a clear suppression of the B matrix for IM-based matrix elements.

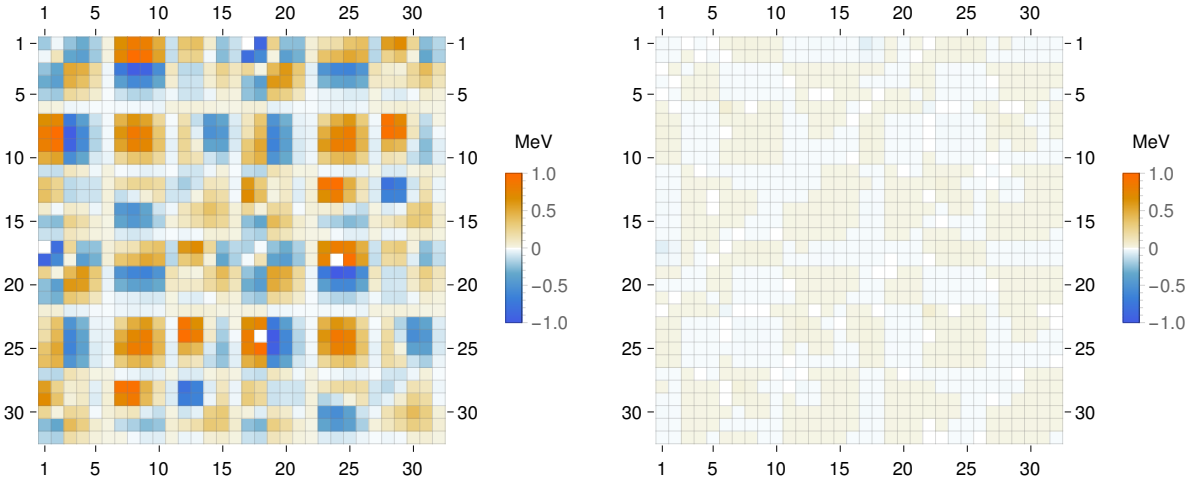

(a) HF **(b)** IM-HF

Figure 7.3: Representation of the B matrix for HF (left) and IM-HF, where all matrix elements are significantly suppressed.

Furthermore, the A_{12} matrix comprises a term proportional to ϵ_{p_1,h_1}, representing the off-diagonal part of the Hamiltonian which is suppressed within IM-SRG as well.

8

Lanczos Strength Functions

Contents

The Lanczos strength function method is an *ab initio* approach for the investigation of collective excitations, based on the Lanczos strength-function method by Whitehead [15] in combination with an importance-truncated no-core shell model (IT-NCSM) calculation. The advantage of this technique lies in the computational efficiency of the calculation of transition strengths and additionally in being an *ab initio* access. The application of Lanczos strength functions is restricted to light nuclei as they are based on the (IT-)NCSM and, thus, have the same limitations. First, the NCSM is introduced and the general concept of the underlying Lanczos algorithm is explained. Furthermore, the Lanczos strength function method is introduced. If not stated otherwise, this chapter follows Refs. [71, 77, 78].

8.1 No-Core Shell Model

Within the no-core shell model (NCSM) [38, 55, 57] ground-state as well as excited-state energies and the associated wave functions can be calculated and, thus, a wide range of observables as expectation values or matrix elements with respect to the wave functions. Since the model-space size and, connected to that, the computational cost grows factorially with the number of nucleons, the application of the NCSM is limited to light nuclei.

The Schrödinger equation (3.1) can be transformed to a matrix eigenvalue problem that is solved with the aid of the Lanczos algorithm through a truncation of the model space. The exact solution of the eigenvalue problem is obtained by an infinite basis. Since this is not feasible in practical calculations, the model-space size is increased stepwise via the truncation parameter leading to a solution that is converged or can be extrapolated to a converged result using exponential functions or artificial neural networks [94].

In NCSM calculations, the harmonic oscillator (HO) basis is preferred as starting point. Thus, the model space is spanned by Slater determinants of single-particle HO states. The truncation parameter is the unperturbed excitation energy $N_{\max}\hbar\Omega$ with the oscillator frequency $\hbar\Omega$ and the total single-particle excitation quanta $N_{\max}$. For ^{16}O, the unperturbed and one excited configuration are illustrated in Fig. 8.1. The first consists of single-particle configurations, which fill the lowest states, the 0s and 0p shell, respectively. This is the only Slater determinant for ^{16}O in the lowest energy configuration, i. e. $N_{\max} = 0$, since the shells are completely filled, i.e., a closed-shell nucleus. For other nuclei without shell closure, there exists more than one Slater determinant since the nucleons can occupy different states within the shell. Within the excited configuration, neutrons and protons are excited to higher-energy shells. In Fig. 8.1(b), two neutrons and two protons are excited to higher-energy shells. Two

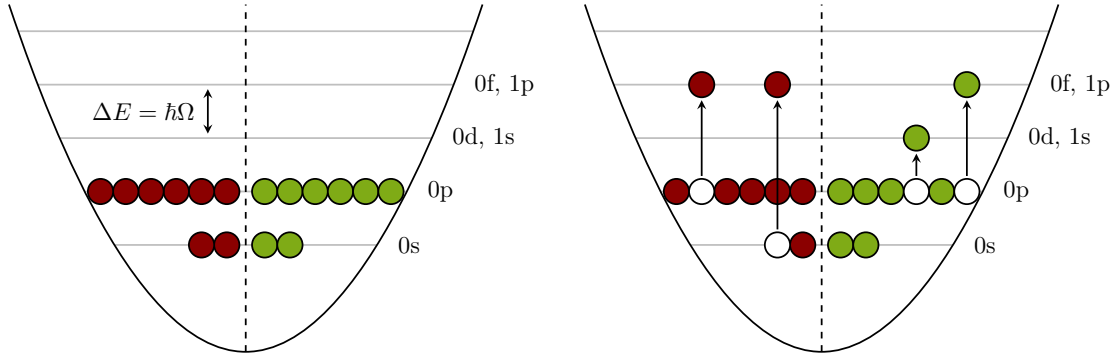

(a) unperturbed configuration **(b)** excited configuration

Figure 8.1: Unperturbed (left) and excited configuration (right) for ^{16}O. The excitation energy is $8\hbar\Omega$. Green circles denote neutrons and red circles protons.

adjacent shells differ by an energy of $\hbar\Omega$ and the total excitation energy sums all HO excitation quanta, leading to a total excitation energy of $8\hbar\Omega$ in our case. Thus, the basis is spanned by all configurations associated with $N_{\max} \leq 8\hbar\Omega$. Due to the variational principle, the calculated eigenenergies in the NCSM framework are an upper bound to the exact results. This is not the case for other observables such as electromagnetic observables.

As mentioned before, the NCSM is restricted to light nuclei. The approach can be extended to larger model-space sizes and slightly heavier nuclei via the importance-truncated no-core shell model (IT-NCSM). The idea is to include only basis states that are physically relevant. The NCSM calculation yields the eigenstates

$$|\psi_n\rangle = \sum_i C_i^{(n)} |\phi_i\rangle \tag{8.1}$$

where many coefficients $C_i^{(n)}$ almost vanish. With the aid of an importance measure

$$\kappa_i = \frac{\langle\phi_i| \hat{H} |\psi_{\text{ref}}\rangle}{\epsilon_{\text{ref}} - \epsilon_i} \tag{8.2}$$

with basis states $|\phi_i\rangle$, the most important basis states can be selected in order to reduce the model-space size and thus computational demand. The importance measure is deduced in multiconfigurational perturbation theory. Here, the reference state $|\psi_{\text{ref}}\rangle$ is approximated by a chosen target state, for instance the ground state. The IT-NCSM model space includes only basis states for which the importance measure is larger than a certain threshold $|\kappa_i| > \kappa_{\min}$.

The solving procedure of an IT-NCSM calculation is iterative. A NCSM calculation in a small model space is done for a chosen target state and a threshold yielding the reference state. The IT-NCSM model space includes $(N_{\max} + 2)$ basis states that are physically relevant, i.e. that are truncated by the importance measure. The following IT-NCSM calculation produces a new reference state which is again used for the construction of the model space and a subsequent IT-NCSM calculation. This procedure is done for a sequence of different importance thresholds $\kappa_{\min}$ which are then extrapolated to $\kappa_{\min} \to 0$ since this is associated with the exact result.

8.2 General Concept: Lanczos Algorithm

The Lanczos algorithm [5, 11] is suitable for the determination of extreme eigenvalues and associated eigenvectors of a Hermitian matrix A. With the help of the iterative approach and the aforementioned matrix A, a tridiagonal matrix T_m with dimension $m \times m$ is produced after m steps

$$T_m = \begin{pmatrix} \alpha_1 & \beta_1 & & & & \\ \beta_1 & \alpha_2 & \beta_2 & & & \\ & \ddots & \ddots & \ddots & & \\ & & & & & \beta_{m-1} \\ & & & & \beta_{m-1} & \alpha_m \end{pmatrix}. \tag{8.3}$$

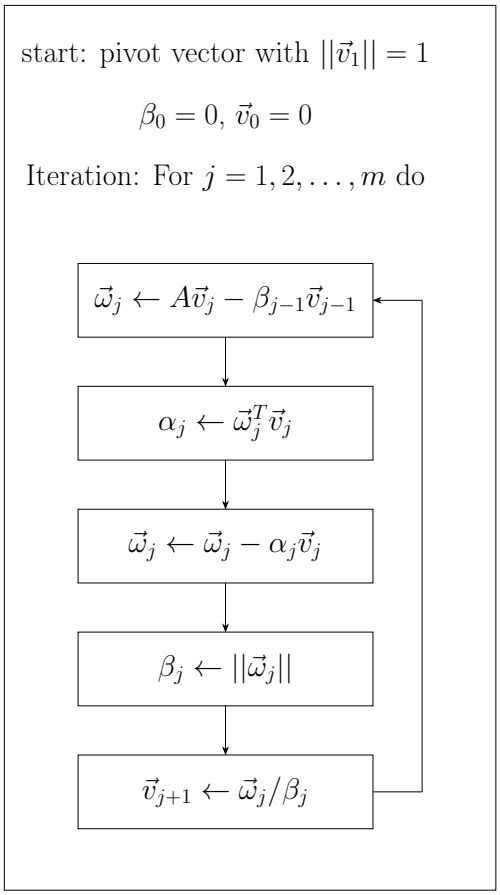

Figure 8.2: Iterations within the simple Lanczos algorithm. As starting point, a random but normalized pivot vector is chosen. A tridiagonal matrix with matrix elements β_j and α_j is constructed within the m iteration steps.

This matrix can be diagonalized with the aid of standard approaches. The eigenvalues of T_m and A are identical. Formally, the Lanczos algorithm projects a Lanczos vector $\vec{v}_j$ onto a Krylov subspace.

The Lanczos algorithm with its iterations is schematically depicted in Fig. 8.2. First, the considered Hermitian matrix A, an arbitrary but normalized vector $\vec{v}_1$ and the number of iterations m need to be set. Furthermore, the initial value for the matrix element β_0 and the first Lanczos vector $\vec{v}_0$ are chosen to be zero. Within the actual algorithm, the matrix elements α_j and β_j of the tridiagonal matrix are calculated via a projection of the current Lanczos vector $\vec{v}_j$ on a Krylov subspace which is indicated by the multiplication $A\vec{v}_j$ of matrix and vector and the subsequent reorthogonalization with respect to the previous two Lanczos vectors. Afterwards, the temporary vector $\vec{\omega}_j$ is normalized, yielding the new Lanczos vector $\vec{v}_{j+1}$. This algorithm shows low computational effort, since only two Lanczos vectors and the current vector $\vec{\omega}_j$ need to be stored simultaneously as long if we are only interested in the eigenvalues and not in the eigenvectors. Otherwise, all Lanczos vectors are important, since they build the columns of a transformation matrix required for the transformation of the eigenvectors of the tridiagonal matrix in the original basis, leading to approximated eigenvectors of the input matrix. The matrix T_m can be diagonalized using standard techniques in the Lanczos basis. The transformation matrix is unitary if T_m and A have the same dimension. In this specific case, the exact eigenvectors of A can be determined. Besides the memory efficiency, only vector multiplication is necessary, except for the projection onto a Krylov subspace associated with the matrix-vector multiplication. Thus, the Lanczos algorithm is feasible for large sparse matrices. The eigenvalues of the tridiagonal matrix converge rapidly with the

iteration steps m to the eigenvalues of the input matrix A. Every iteration step corresponds to a new eigenvalue, starting with the most extreme eigenvalues converging first.

A peculiarity of the algorithm is the loss of orthogonality of the Lanczos vectors due to round-off errors which is manifested in multiplicities of copied eigenvalues. For a full reorthogonalization in order to eliminate these remnants, all Lanczos vectors are required resulting in more computational effort. Therefor, a Lanczos vector $\vec{v}_{j+1}$ is only orthogonalized with respect to the previous $n \leq m$ ones $\vec{v}_{j-n\ldots j}$, yielding a partial reorthogonalization. The reorthogonalization itself employs a Gram-Schmidt approach. The copied eigenvalues emerge in later iteration steps of the algorithm while applying the partial reorthogonalization. A full suppression is only achieved by a full reorthoganlization. For a detailed discussion of the reorthogonalization procedure and the occurence of multiplicities of eigenvalues, we refer to Ref. [78].

8.3 The Lanczos Method for Strength Functions

In order to investigate strength distributions in an *ab initio* framework, the IT-NCSM is combined with the Lanczos strength function method [15]. The starting point for the Lanczos algorithm is the definition of a pivot state

$$|v_1\rangle = \frac{1}{\sqrt{\tilde{S}}}\hat{T}_{\sigma\lambda}\,|\psi_0\rangle \tag{8.4}$$

where the ground-state eigenvector $|\psi_0\rangle$ is obtained by a previous IT-NCSM calculation. In principle, any other *ab initio* method could be used in order to determine the initial state. The transition operator $\hat{T}_{\sigma\lambda}$ acts on the ground-state and is defined as electromagnetic multipole operator with multipolarity λ and type σ as introduced in Sec. 4.2. In order to ensure a normalization, we introduce the factor

$$\begin{aligned}\tilde{S} &= \langle\psi_0|\,\hat{T}^{\dagger}_{\sigma\lambda}\hat{T}_{\sigma\lambda}\,|\psi_0\rangle \\ &= \sum_n \langle\psi_0|\,\hat{T}^{\dagger}_{\sigma\lambda}\,|\psi_n\rangle\,\langle\psi_n|\,\hat{T}_{\sigma\lambda}\,|\psi_0\rangle \\ &= \sum_n |\,\langle\psi_n|\,\hat{T}_{\sigma\lambda}\,|\psi_0\rangle\,|^2\end{aligned}$$

which depends on the transition strength between the ground state $|\psi_0\rangle$ and an arbitrary excited state $|\psi_n\rangle$. The next step is the application of the Lanczos algorithm with the pivot state (8.4) as first Lanczos vector and the Hamiltonian as input matrix which is modified in order to be tridiagonal. This tridiagonal matrix can subsequently be diagonalized using standard methods, yielding the eigenvalues E_n and corresponding eigenstates $|E_n\rangle$ which are given as superposition of the Lanczos vectors

$$|E_n\rangle = \sum_{i=1}^{m} C_i^{(n)}\,|v_i\rangle \tag{8.5}$$

leading to m approximated eigenvectors for the input Hamiltonian. The first coefficient

$$C_1^{(n)} = \langle v_1|E_n\rangle = \frac{1}{\sqrt{\tilde{S}}}\,\langle E_n|\,\hat{T}_{\sigma\lambda}\,|\psi_0\rangle \tag{8.6}$$

is of interest since it depends on the matrix element associated with a transition between an eigenstate and the ground state. Exploiting the Wigner-Eckart theorem (2.20), the reduced transition matrix element $\langle \psi_0 || \hat{T}_\lambda || E_n \rangle$ can be calculated, leading to the discrete reduced strength distribution

$$R(E^*, \sigma\lambda) = \sum_n |\langle \psi_0 || \hat{T}_{\sigma\lambda} || E_n \rangle|^2 \delta(E^* - (E_n - E_0)). \tag{8.7}$$

As seen in Eq. (8.6), the transition matrix element consists of the coefficients obtained within the Lanczos algorithm $C_1^{(n)}$ and the strength of the pivot state $\tilde{S}$.

For the special case of transitions to a ground state with $J_0 = 0$, the approximated excited states exhibit an angular momentum equal to the multipolarity $J_n = \lambda$, which simplifies the reduced transition matrix element to

$$\langle E_n || \hat{T}_{\sigma\lambda} || \psi_0 \rangle = \sqrt{(2\lambda + 1)\tilde{S}}\, C_1^{(n)} \tag{8.8}$$

As briefly motivated in Sec. 6.4.2, the discrete strength distribution is folded with a Lorentzian in order to mimic continuum effects and resolution allowing for a comparison with experimental data.

III

Application

Nucleus	ISM	IVD	ISQ
^{16}O	21.13 ± 0.14 [25]	[12]	19.76 ± 0.22 [25]
^{40}Ca	19.18 ± 0.37 [27]		
	20.2 ± 0.1 [84]		18.0 ± 0.1 [83]
^{48}Ca	$19.88^{+0.14}_{-0.18}$ [46]		
	19.5 ± 0.1 [84]		19.0 ± 0.2 [83]

Table 8.1: Experimental centroid energies of nuclei. For the other nuclei considered in this work, no data is available. All values are given in MeV.

The next chapters discuss the applications of many-body methods for the investigation of collective excitations. For that purpose, the results obtained within the different approaches are analyzed separately first. This involves considerations on the model-space convergence both of the employed single-particle bases and of the method itself. We use different single-particle bases and examine the impact of ground-state correlations on first-order RPA calculations by the IM-RPA. Furthermore, the state-of-the-art chiral interaction, the non-local NN+3N interaction by Hüther [85], is applied for collective excitations for the first time. We investigate the electric isoscalar monopole, isovector dipole, and isoscalar quadrupole strength distributions of the oxygen isotopes ^{16}O and ^{24}O and of the calcium isotopes ^{40}Ca and ^{48}Ca with RPA-type methods. Within the Lanczos framework, both even-mass helium and oxygen isotopes, ^{4}He to ^{8}He and ^{16}O to ^{24}O, respectively, are analyzed. The isotopes are chosen regarding to different limitations of the approach.

Another aspect of this part of the thesis is the uncertainty estimation. This has become a point of interest during the last years, since a better comparability with experimental data can be achieved. We introduce an ansatz for the uncertainty estimation, which is rooted in Bayesian statistics in combination with the chiral expansion of the interaction.

Afterwards, the responses of the two oxygen isotopes ^{16}O and ^{24}O, obtained with three different methods, are compared focusing fragmentation, fine structure, centroid energies (CE) and experimental data. One observable that can easily be compared to experiment is the centroid energy. The experimental centroid energies are summarized in Tab. 8.1. The theoretical counterpart is given by

$$E_{\mathrm{CE}} = \frac{\sum_\omega E_\omega B_\omega(\sigma\lambda)}{\sum_\omega B_\omega(\sigma\lambda)} \tag{III.1}$$

with the RPA energy eigenvalues E_ω and the corresponding strengths $B_\omega(\sigma\lambda)$.

9

Collective Excitations with RPA

Contents

In this chapter, we investigate the electric isoscalar monopole (ISM), isovector dipole (IVD) and isoscalar quadrupole (ISQ) transition strengths of oxygen and calcium isotopes with subshell closures within the RPA framework for different single-particle bases. All sections are similarly structured. First, some general aspects of the model-space size are given and different chiral orders of the interaction are compared. Afterwards, we examine the model-space convergence for several truncation parameters. If not stated otherwise, we use the following model-space truncations and interaction: The non-local NN+3N interaction at N^{3}LO in NO2B approximation is SRG-evolved with $\alpha = 0.08$ fm^4. Furthermore, we choose the oscillator frequency $\hbar\Omega = 20$ MeV, $e_{\max} = 12$, $l_{\max} = 8$ and $E_{3\max} = 14$ for the truncation of the single-particle basis and vary these parameters systematically in the following sections.

9.1 HF-RPA

The HF basis has been the standard choice in the RPA framework for decades, since it is a computationally cheap method. The HF many-body state can be written as single Slater determinant and the single-particle energies are diagonal, leading to simplifications in the RPA framework, for instance in the underlying matrices discussed in Chapter 7. First, we examine the model-space size. In Fig. 9.1, the cumulative number of 1p1h states of ^{16}O and ^{40}Ca is illustrated for different electric modes. The energy E_{ph} is the maximum energy of 1p1h excitations. We recognize systematics for the different modes and the two nuclei: The number of 1p1h states for a full RPA model space is larger for the heavier nucleus as well as the more complex mode due to the higher-rank electromagnetic operator in Eq. (4.15). For the isoscalar quadrupole strength of the calcium isotope, about 2.5 times the number of 1p1h states is needed in comparison to ^{16}O in order to include the full model space. This also becomes important in the SRPA framework in Chapter 10. In the RPA framework, however, a full calculation without energy truncation of the 1p1h excitations is trivial for calcium isotopes. In the case of ^{40}Ca, both RPA matrices A and B have a dimension of 190×190.

After these considerations, we first discuss the TDA as simplification of the RPA. Afterwards, different chiral orders of the interaction are compared and the model-space convergence is examined.

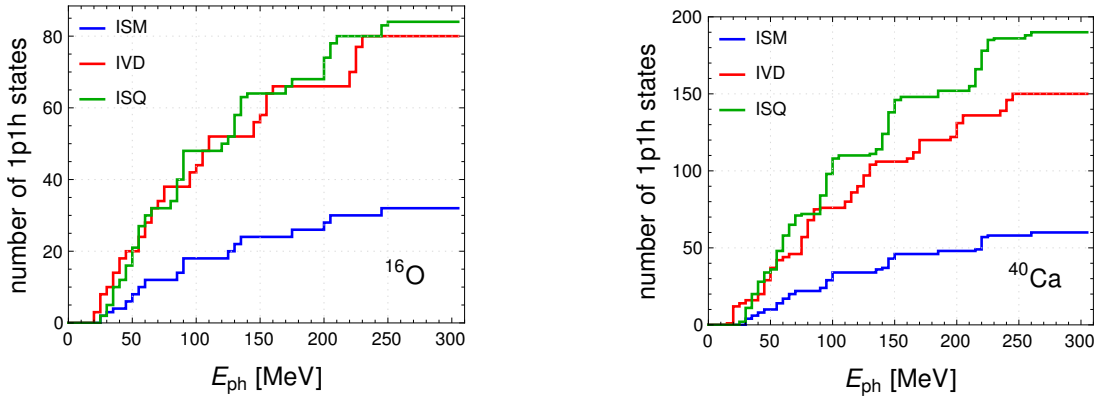

Figure 9.1: Cumulative number of 1p1h states of the isoscalar monopole (——), isovector dipole (——) and isoscalar quadrupole (——) strength distributions depending on the excitation energy threshold for ^{16}O and ^{40}Ca.

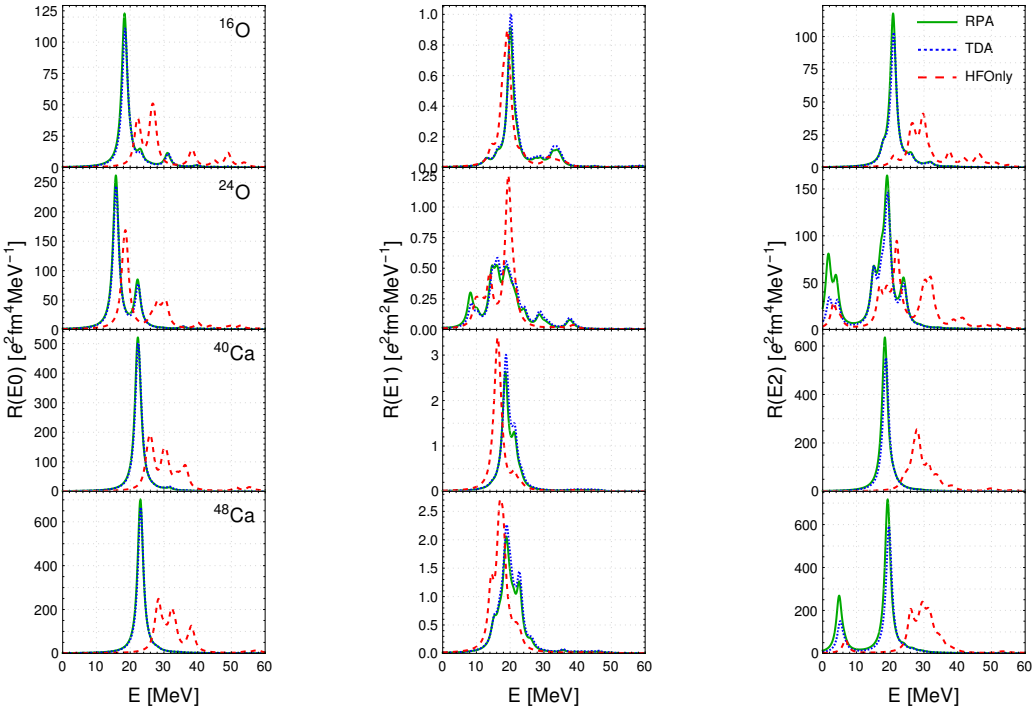

Figure 9.2: Electric ISM (left), IVD (middle) and ISQ (right) response of oxygen and calcium isotopes obtained by RPA (——), TDA (·····), and HFOnly (- - -) calculations. Here, we used an SRG flow parameter of $\alpha = 0.04$ fm^4.

9.1.1 Tamm-Dancoff Approximation

The TDA is a simplification of the RPA. The underlying excitation creation operator includes only ph excitations and, thus, the B matrix is non-existent. As a consequence, the Y^{ω}_{ph} are zero as well. In Fig. 9.2, the TDA (·····) response is compared to the full RPA (——) response and additionally to the HF (- - -) response. The TDA and RPA responses are almost identical for the ISM mode. For this case, both differ only slightly in the peak height. The structure and the peak position are the same when going from TDA to RPA. This behavior is found for all nuclei. The TDA vs. RPA differences in the IVD and ISQ are almost not noticeable, except for low-lying states of the ISQ response. This little difference is remarkable. The HF response only takes the diagonal elements of the A matrix into account. Since in this section we focus on the HF single-particle basis, the HF response depends on the ph excitation energies (c.f. Sec. 7.1). For the ISM and ISQ mode, the HF response deviates strongly from the TDA and RPA results for all nuclei. The deviation contains both a shift in the peak position to higher energies as well as a different overall shape. Contrary, the IVD response shows similarities for the different types of calculation. The peak position is shifted by only a few MeV to smaller energies. The response structure is comparable as well. The reason for the discrepancy between HF response and TDA or RPA response lies in the construction. The HF response contains the uncoupled ph excitation energies, whereas the TDA and RPA response comprise the coupled ones. The collectivity arises due to the coupled ph excitations. Thus, the HF response does not capture collectivity, which is observed in a shift in energy as well as a reduced transition strengths.

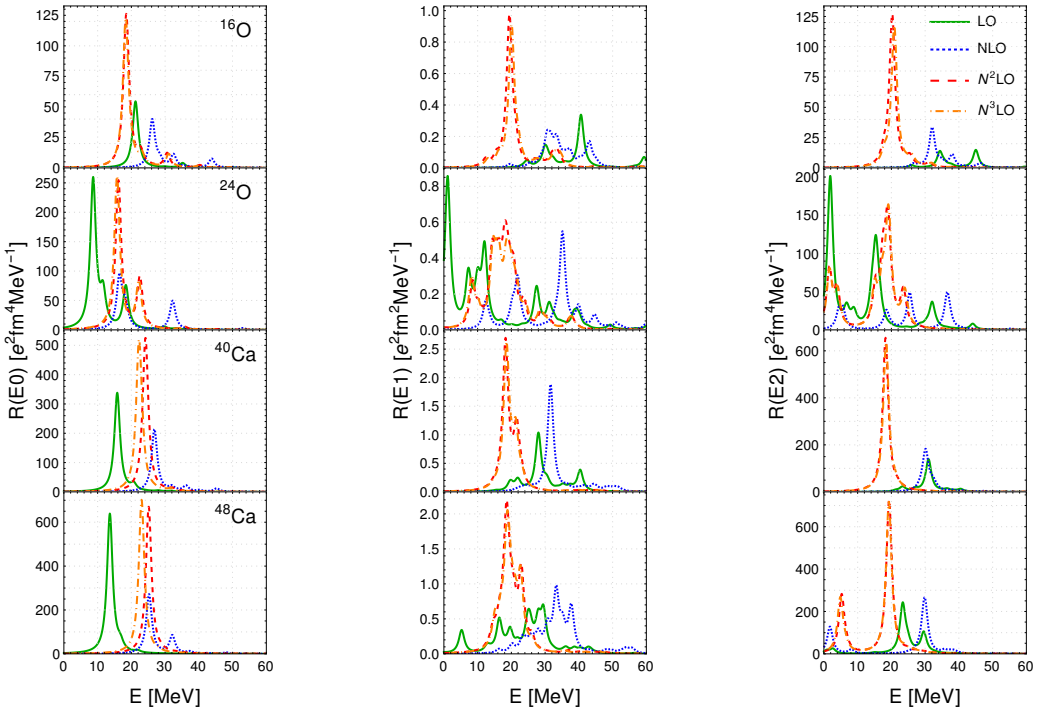

Figure 9.3: Electric ISM (left), IVD (middle) and ISQ (right) response of oxygen and calcium isotopes for the different chiral orders LO (——), NLO (·····), N^2LO (- - - -) and N^3LO (-·-·-) obtained by HF-RPA calculations with a SRG flow parameter of $\alpha = 0.04$ fm^4.

9.1.2 Chiral Interaction

Traditionally, phenomenological interactions were used for RPA calculations. This has been advanced to interactions from chiral EFT for a consistent description of both ground-state properties of nuclei and collective excitations. The non-local NN+3N interaction by Hüther [85] has been applied for different observables and we apply it for the first time in the context of collective excitations. In Fig. 9.3, the strength distributions are shown for the different chiral orders from LO up to N^3LO. The corresponding centroid energies are given in Tab. 9.1. In particular, the leading and next-to-leading chiral orders generate strength distributions that are strongly shifted in the peak position and, thus, in the centroid energies. Except for the ISM mode of the calcium isotopes, the overall shape of the strength distributions deviates as well. The peak height for the ISM mode of ^{24}O and ^{48}Ca is comparable to higher chiral orders when going from LO to N^2LO or higher. For the other cases, the height of the responses obtained with the smallest two chiral orders are only a fractional amount thereof. Higher chiral orders (N^2LO and N^3LO) are in good agreement with each other and the experiment, which deviates about $2-5$ MeV. However, they show a few deviations in the centroid energy of around 2 MeV for the ISM mode of the calcium isotopes. For the other modes, the difference is less than 0.5 MeV and, thus, negligible.

The discrepancy between LO and NLO on one hand and the two higher orders N^2LO and N^3LO on the other hand can be traced back to the inclusion of 3N forces. In Fig. 3.1, the hierarchy of the chiral interaction is shown. Up to NLO, only two-body interactions are involved. For higher orders, additional three-body interactions arise, leading to a significantly better description of collective excitations by a tendential shift of the transition strengths to-

Nucleus	mode	LO	NLO	N^{2}LO	N^{3}LO	N^{3}LO
			$\alpha = 0.04$ fm^4			$\alpha = 0.08$ fm^4
^{16}O	ISM	22.48	30.45	20.32	20.05	23.29
	IVD	39.53	37.60	21.93	22.68	26.79
	ISQ	39.69	34.90	20.78	21.39	24.24
^{24}O	ISM	11.50	22.37	18.40	17.77	19.30
	IVD	13.94	32.17	18.37	18.28	21.42
	ISQ	11.06	23.24	14.36	14.53	16.43
^{40}Ca	ISM	16.38	29.11	24.44	22.56	23.66
	IVD	30.70	34.69	19.94	20.04	23.00
	ISQ	30.83	31.27	18.49	18.61	20.36
^{48}Ca	ISM	13.96	27.73	25.39	23.17	23.82
	IVD	23.68	34.02	20.42	20.36	23.21
	ISQ	23.49	22.06	15.72	15.63	16.79

Table 9.1: Centroid energies of different oxygen and calcium isotopes and response types for chiral orders up to N^{3}LO with a SRG flow parameter of $\alpha = 0.04$ fm^4 and for the highest chiral order with $\alpha = 0.08$ fm^4 (right column). All values are given in MeV.

wards lower energies. This is in accordance with previous investigations, which apply different interactions. For a systematic comparison of transition strengths, which employ a two-body, a two-body plus induced three-body and a two-body plus initial three-body interaction, we refer to Ref. [70]. The inclusion of three-body forces is crucial for a more precise description of strength distributions. Thus, we perform all HF-RPA calculations with interactions of order N^{3}LO and only include lower chiral orders for the uncertainty estimation.

9.1.3 Model-Space Convergence

For the model-space convergence behavior, we fix all parameters and truncations except for the one we want to test. The parameters differ in their role: The single-particle truncation $e_{\max}$ describes the size of the model space. Thus, an increased $e_{\max}$ corresponds to a larger model space and, as a consequence, to an improved result. For the SRG flow parameter and the oscillator frequency, a larger value is not automatically associated with a better convergence behavior. In case of the SRG evolution, a balance between pre-diagonalization and induced many-body forces has to be found.

SRG Flow Parameter Dependence The chiral NN+3N interaction is SRG-evolved with a certain flow parameter α. The responses for $\alpha = 0.04$ fm^4 (——) and $\alpha = 0.08$ fm^4 (·····) are shown in Fig. 9.4. A larger flow parameter leads to a shift of the strength distributions to higher energies. This shift of around 3 MeV is larger than the shift for the two highest orders of chiral EFT and almost the same for the different response modes and nuclei. The only exception is the ISM mode of the calcium isotopes, which tends to be robust against the variation of the SRG flow parameter. For low-lying strengths, the shift is less pronounced, which can be seen in the ISQ mode of ^{48}Ca and ^{24}O. The pre-diagonalization within the SRG evolution leads to a softened Hamiltonian and, thus, to both higher binding energies due to smaller ground-state energies and as a result to larger single-particle excitations, which are given in Tab. 9.2. Increased single-particle excitations leads to a shift of the transition

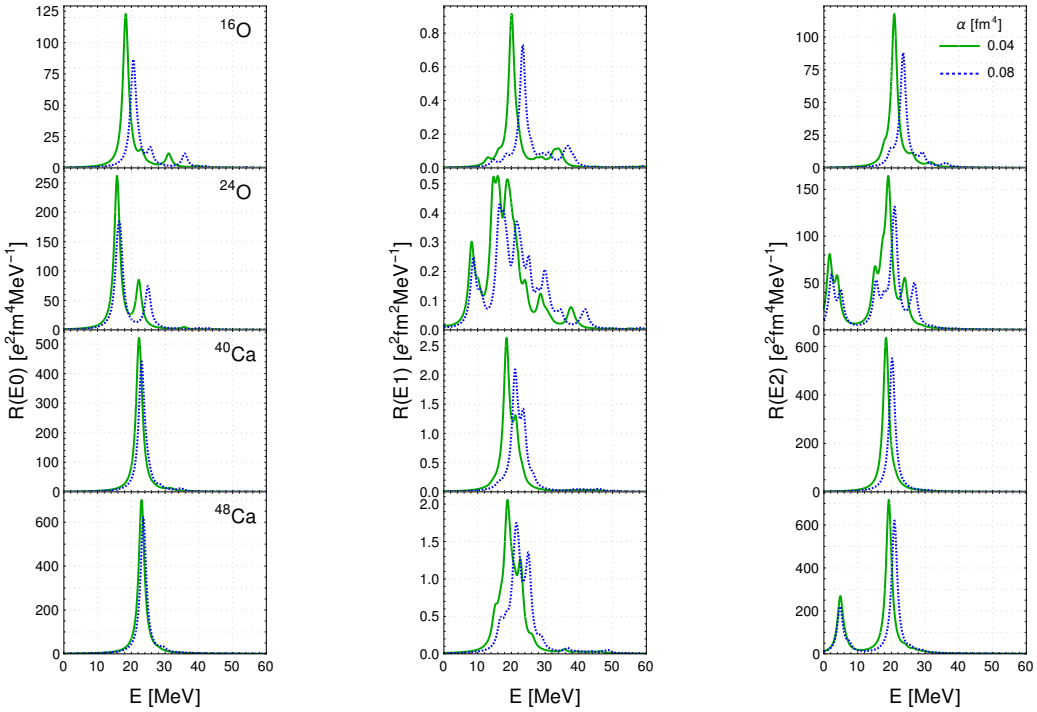

Figure 9.4: Electric ISM (left), IVD (middle) and ISQ (right) response of oxygen and calcium isotopes for different SRG flow parameters $\alpha = 0.04$ fm^4 (——) and $\alpha = 0.08$ fm^4 (·····).

strengths to higher energies. The excitations, which are responsible for the low-lying ISQ response, are located close to the Fermi gap which is almost unaltered by the SRG evolution.

Oscillator Frequency Dependence The dependence of the strength distributions on the oscillator frequency is shown in Fig. 9.5 for $\hbar\Omega = 16$ MeV (——), $\hbar\Omega = 20$ MeV (·····), and $\hbar\Omega = 24$ MeV (- - - -). The strength distributions are typically shifted towards higher energies with increased $\hbar\Omega$. While for the IVD and ISQ response, the shift is about 1.5 MeV, the shift in the ISM response up to 5 MeV is more pronounced for all considered nuclei, especially for the calcium isotopes. The robustness of low-lying strengths as observed for the variation of the SRG flow parameter cannot be reproduced. The ground-state energies are almost unchanged for a variation of $\hbar\Omega$ (< 1 MeV) and, thus, smaller than for a variation of the flow parameter. Therefore we conclude that not the binding energies are important for a convergence in the RPA framework, but the single-particle energies and their deviation. The oscillator frequency is no direct model-space truncation parameter, but still a basis parameter. For sufficiently large model spaces, the strength distributions would be independent of $\hbar\Omega$ (c.f. next paragraph).

Single-Particle Truncation The convergence behavior of RPA calculations with respect to the single-particle truncation is shown in Fig. 9.6 for $e_{\max} = 12$ (——) and $e_{\max} = 14$ (·····). The corresponding centroid energies are summarized in Tab. 9.3. We observe a slight shift of the strength distributions to lower excitation energies for higher $e_{\max}$, i.e., larger model spaces. This effect of about 1 MeV is more pronounced for ^{24}O than for the other nuclei. The

$\alpha = 0.04$ fm^4					$\alpha = 0.08$ fm^4				
particle	hole	E_p	E_h	E_{ph}	particle	hole	E_p	E_h	E_{ph}
0d3/2	0s1/2	23.12	-18.31	41.43	0d3/2	0s1/2	24.34	-23.72	48.05
1d3/2	0s1/2	36.54	-18.31	54.85	1d3/2	0s1/2	37.38	-23.72	61.10
2d3/2	0s1/2	62.07	-18.31	80.38	2d3/2	0s1/2	62.72	-23.72	86.43
3d3/2	0s1/2	98.27	-18.31	116.58	3d3/2	0s1/2	98.83	-23.72	122.55
4d3/2	0s1/2	147.99	-18.31	166.3	4d3/2	0s1/2	148.85	-23.72	172.57
5d3/2	0s1/2	219.70	-18.31	238.01	5d3/2	0s1/2	221.39	-23.72	245.11
0d5/2	0s1/2	19.07	-18.31	37.38	0d5/2	0s1/2	19.38	-23.72	43.09
1d5/2	0s1/2	33.20	-18.31	51.51	1d5/2	0s1/2	33.74	-23.72	57.46
2d5/2	0s1/2	58.62	-18.31	76.93	2d5/2	0s1/2	58.69	-23.72	82.41
3d5/2	0s1/2	95.10	-18.31	113.41	3d5/2	0s1/2	94.88	-23.72	118.6
4d5/2	0s1/2	145.17	-18.31	163.48	4d5/2	0s1/2	145.21	-23.72	168.93
5d5/2	0s1/2	218.23	-18.31	236.54	5d5/2	0s1/2	218.83	-23.72	242.55
1p3/2	0p1/2	26.30	5.49	20.81	1p3/2	0p1/2	27.04	4.43	22.61
2p3/2	0p1/2	48.74	5.49	43.24	2p3/2	0p1/2	48.73	4.43	44.30
3p3/2	0p1/2	83.04	5.49	77.55	3p3/2	0p1/2	82.83	4.43	78.40
4p3/2	0p1/2	131.21	5.49	125.71	4p3/2	0p1/2	131.07	4.43	126.64

Table 9.2: Particle-hole configurations with corresponding energies for the ISQ response of ^{16}O for different SRG flow parameter. The ground-state energy is calculated to -53.60 MeV for $\alpha = 0.04$ fm^4 and -79.52 MeV for $\alpha = 0.08$ fm^4. The energies are given in MeV.

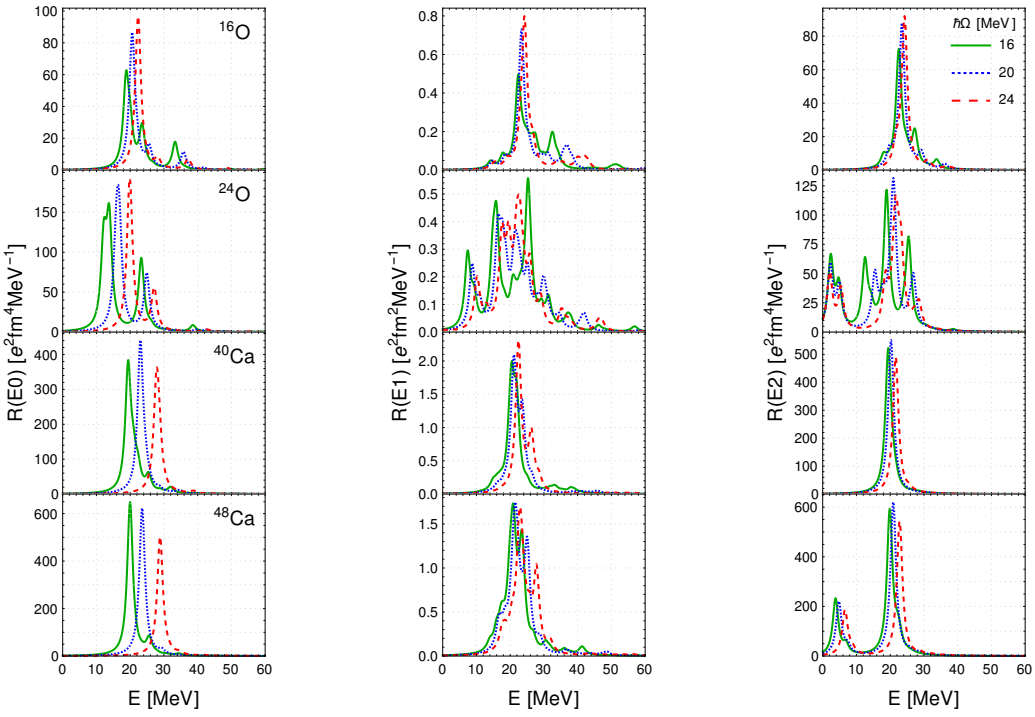

Figure 9.5: Electric ISM (left), IVD (middle) and ISQ (right) response of oxygen and calcium isotopes for different oscillator frequencies $\hbar\Omega = 16$ MeV (——), $\hbar\Omega = 20$ MeV (·····), and $\hbar\Omega = 24$ MeV (- - -).

Nucleus	mode	$\hbar\Omega$ 16 MeV	20 MeV	24 MeV	20 MeV		
			$e_{\max} = 12$		$e_{\max} = 14$		
			$E_{3\max} = 14$			$E_{3\max} = 16$	$E_{3\max} = 18$
^{16}O	ISM	22.83	23.29	24.16	23.04	23.24	23.24
	IVD	26.68	26.79	27.03	26.73	26.79	26.79
	ISQ	24.02	24.24	24.63	24.11	24.23	24.23
^{24}O	ISM	16.95	19.30	22.02	18.31	18.91	18.78
	IVD	20.66	21.42	22.38	21.05	21.33	21.31
	ISQ	15.47	16.43	17.48	15.97	16.34	16.32
^{40}Ca	ISM	21.16	23.66	28.30	23.37	22.27	21.74
	IVD	22.27	23.00	24.37	22.85	22.67	22.57
	ISQ	19.79	20.36	21.82	20.24	20.10	20.03
^{48}Ca	ISM	20.90	23.82	29.14	23.38	22.21	21.67
	IVD	22.44	23.21	24.70	23.03	22.86	22.76
	ISQ	15.94	16.79	18.82	16.59	16.38	16.34

Table 9.3: Centroid energies in MeV of different oxygen and calcium isotopes and response types for varied oscillator frequencies $\hbar\Omega$ with a single-particle truncation of $e_{\max} = 12$ and for $\hbar\Omega = 20$ MeV with $e_{\max} = 14$.

convergence behavior in total is not comparable to those of varying the SRG flow parameter or the oscillator frequencies, since the transition strengths tend to be converged with respect to the single-particle truncation and for the discussed exceptions, the dependence is less pronounced. The low-lying ISQ responses seem to be unaffected of the different single-particle truncations. In principle, the calculations need a larger model space in order to obtain fully converged results. For RPA calculations, a single-particle truncation of $e_{\max} = 14$ or larger is still feasible. One reason for this lies in the equality of the inclusion of full 3N forces and the NO2B approximation within the RPA framework. However, we also perform RPA calculations, which are build on results of the IM-SRG, and SRPA calculations, which both are computationally more expensive. Thus, we choose $e_{\max} = 12$, if not stated otherwise.

Furthermore, larger single-particle truncations $e_{\max}$ and, thus, larger model spaces could also reduce the influence of the oscillator frequency on the results. As mentioned before, this frequency is no truncation parameter but a basis parameter. For model-space sizes that are sufficiently large, the strength distributions would be independent of $\hbar\Omega$. Previous work in Ref. [31] has shown a connection between larger model-space sizes and a less pronounced dependence on the oscillator frequency. However, due to the limitations in the computing power, we are not able to reduce the dependencies in $\hbar\Omega$ and $e_{\max}$.

Truncation of 3N interaction The dependence on the truncation of the 3N model space is shown in Fig. 9.7 for $E_{3\max} = 14$ (——), $E_{3\max} = 16$ (·····), and $E_{3\max} = 18$ (- - -) with corresponding centroid energies given in Tab. 9.3. The shapes and peak positions of the ISM, IVD and ISQ response of the oxygen isotopes and the ISQ response of the calcium isotopes are stable against the variation of $E_{3\max}$. For both calcium isotopes, the IVD mode is as well converged with respect to $E_{3\max}$. There are slight deviations for the smallest value of the truncation parameter. The only noticeable shift in the peak positions is observed for the ISM mode of the calcium isotopes. Nevertheless, this shift amounts to 0.5 MeV and is, thus, negligible. Therefore, we restrict ourselves to a 3N truncation of $E_{3\max} = 14$.

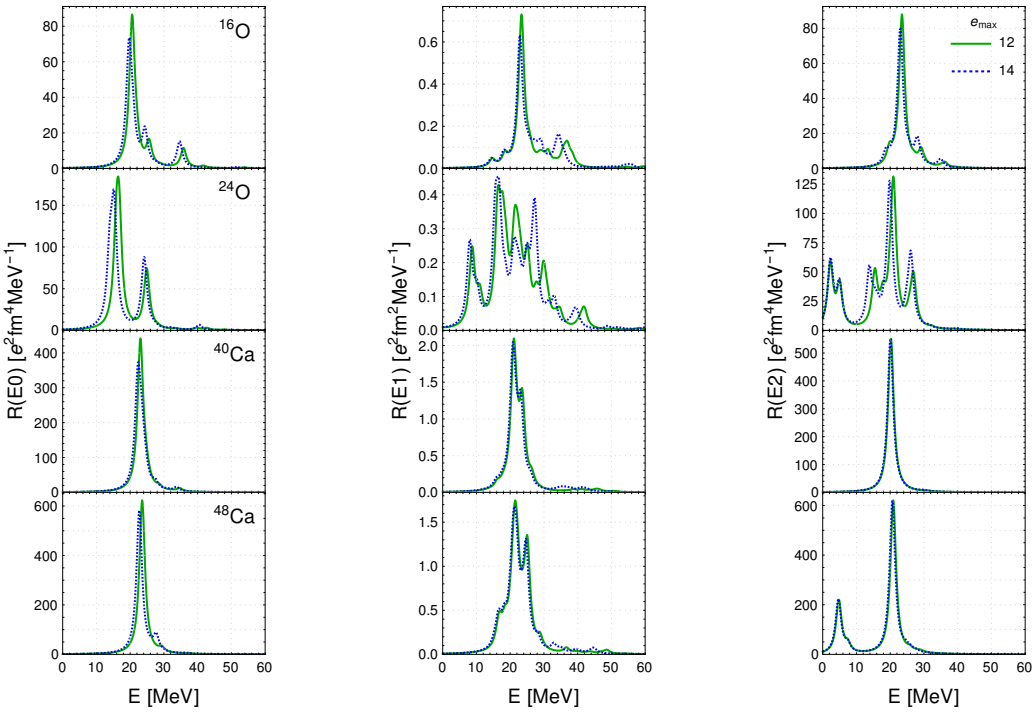

Figure 9.6: Electric ISM (left), IVD (middle) and ISQ (right) response of oxygen and calcium isotopes for different model-space truncations $e_{\max} = 12$ (——) and $e_{\max} = 14$ (·····).

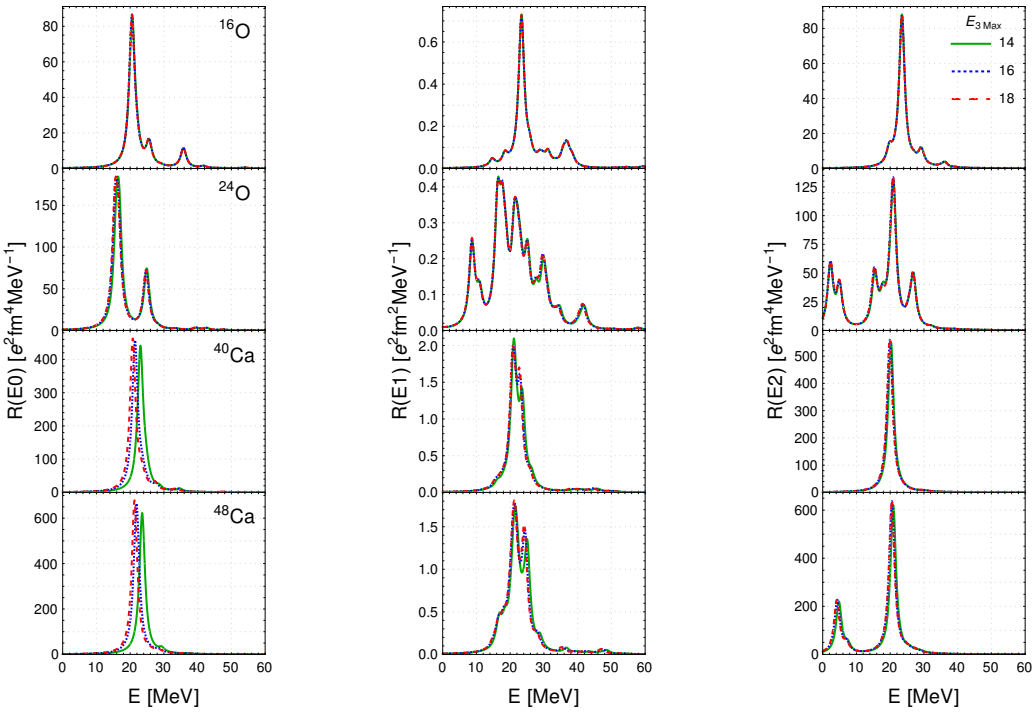

Figure 9.7: Electric ISM (left), IVD (middle) and ISQ (right) response of oxygen and calcium isotopes for different cuts of the 3N model space $E_{3\max} = 14$ (——), $E_{3\max} = 16$ (·····), and $E_{3\max} = 18$ (- - -).

9.2 NAT-RPA

Natural orbitals have the advantage of independence with respect to the oscillator frequency for ground-state properties, such as energies and radii [81]. In this section will be investigated if this is also the case for collective excitations. We start with some considerations on the model-space size analogously to HF-RPA. The cumulative number of 1p1h states depending on the excitation energy threshold is illustrated in Fig. 9.8 for ^{16}O and ^{40}Ca. The overall behavior is similar to the number of 1p1h excitations within HF-RPA, c.f. Fig. 9.1. For both cases, when considering heavier nuclei or a response type including an underlying higher-order electromagnetic operator, more 1p1h excitations need to be included in order to describe the full model space. For the NAT basis, however, the increase is more smooth compared to HF. The number of 1p1h excitations for a full model space remains unaltered for both bases, but the corresponding excitation energy thresholds differ. For NAT, the full model space is already obtained for energies around 220 MeV, whereas an energy threshold of around 250 MeV is needed for the HF basis for the case of ^{16}O. After these considerations, we continue with NAT-RPA results for different interaction orders and model-space truncations.

9.2.1 Chiral Interaction

The dependence of the response on different chiral orders LO up to N^{3}LO is depicted in Fig. 9.9. The NAT-RPA calculations behave similarly as the ones obtained by HF-RPA, c.f. Fig. 9.3. The two lowest orders of the chiral interaction show a strong shift in the peak position and the corresponding centroid energies compared to the higher orders. Furthermore, the overall shape and the peak height varies between the two lowest and the two highest orders of chiral interaction. The only exception is the ISM response of the calcium isotopes. Again, the strength distributions are almost stable against varying the chiral orders N^{2}LO and N^{3}LO, except for a small difference for the calcium isotopes, which amounts to 2 MeV. This behavior can be traced back to the inclusion of three-body interactions within the chiral hierarchy in those orders. A more detailed discussion is conducted in the context of HF-RPA in Sec. 9.1.2.

9.2.2 Model-Space Convergence

As for the HF-RPA, we investigate the model-space convergence for the natural orbitals based RPA. The same parameters and truncations are varied and discussed.

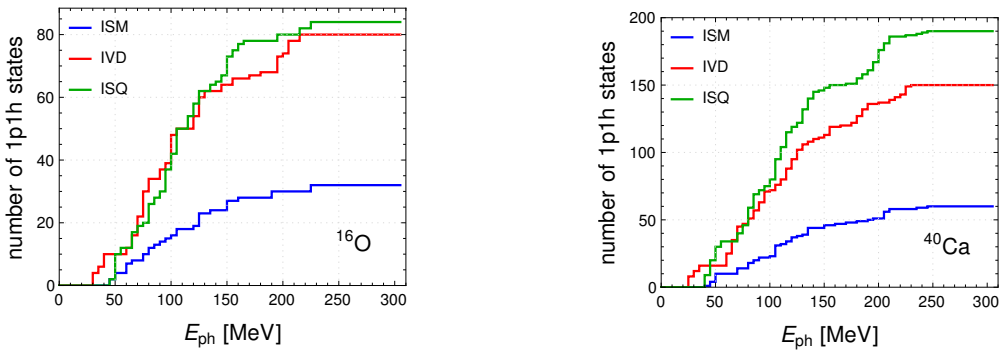

Figure 9.8: Cumulative number of 1p1h states of the isoscalar monopole (——), isovector dipole (——) and isoscalar quadrupole (——) strength distributions depending on the excitation energy threshold for ^{16}O and ^{40}Ca.

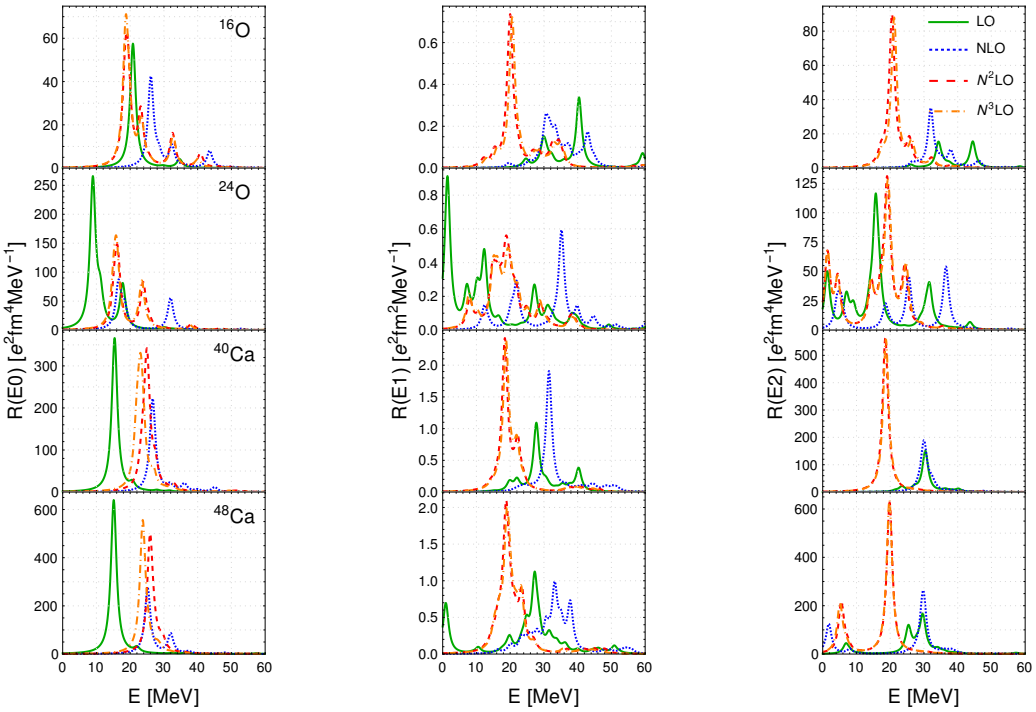

Figure 9.9: Electric ISM (left), IVD (middle) and ISQ (right) response of oxygen and calcium isotopes for the different chiral orders LO (——), NLO (·····), N^{2}LO (- - - -) and N^{3}LO (-·-·-) obtained by NAT-RPA calculations. Here, we use a SRG flow parameter of $\alpha = 0.04$ fm^4.

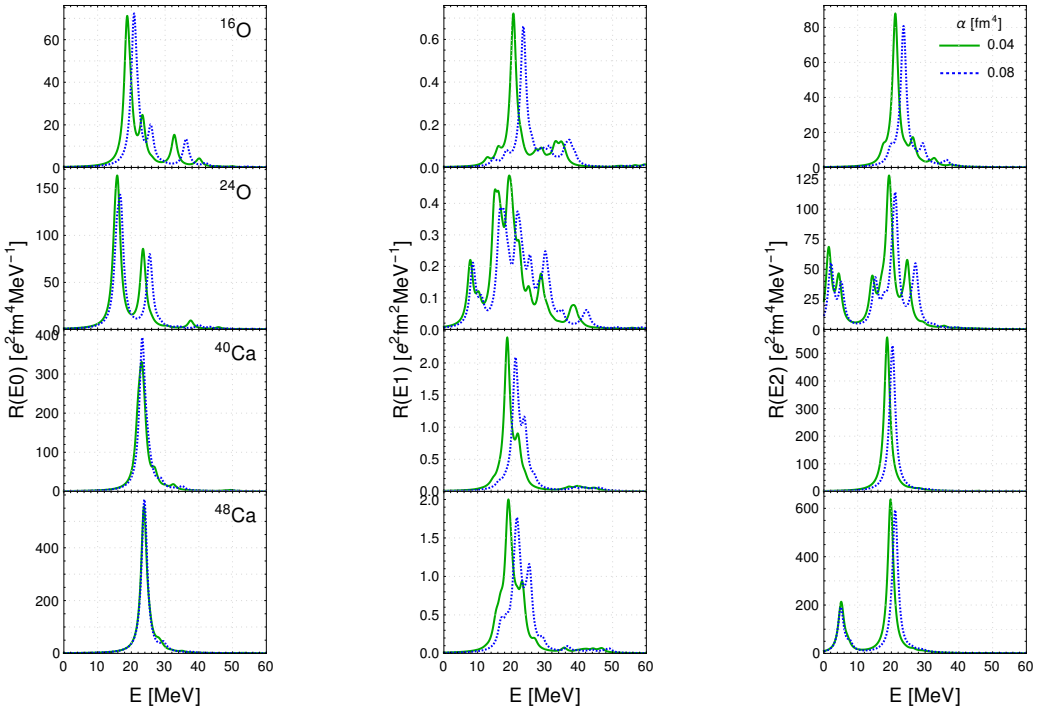

Figure 9.10: Electric ISM (left), IVD (middle) and ISQ (right) response of oxygen and calcium isotopes for different SRG flow parameters $\alpha = 0.04$ fm^4 (——) and $\alpha = 0.08$ fm^4 (·····).

SRG Flow Parameter Dependence In Fig. 9.10, the isoscalar monopole, isovector dipole, and isoscalar quadrupole response of oxygen and calcium isotopes are shown for two different SRG flow parameters $\alpha = 0.04$ fm^4 (——) and $\alpha = 0.08$ fm^4 (·····). Again, the strength distributions are shifted to higher energies for a larger flow parameter α. The shift of 3 MeV is for both the isovector dipole mode as well as for lighter nuclei, such as ^{16}O, larger than for the other types and nuclei. The ISM response of both calcium isotopes is almost robust against a variation of the flow parameter. The amount of the energy shift is larger than the one obtained by a variation of $e_{\max}$ and comparable to a variation of $\hbar\Omega$, except for the ISM response. The low-lying ISQ response tends to be independent of the flow parameter for the same reasons as for HF-RPA.

Single-Particle Truncation and Truncation of 3N Interaction The influence of varying the single-particle truncation in RPA calculations is illustrated in Fig. 9.11. For larger model-space sizes, the strength distributions are slightly shifted towards lower energies. The overall shape remains robust, except for the IVD response of ^{24}O. The shift of less than 0.5 MeV is almost negligible and, thus, smaller than the dependence of the SRG flow parameter and the convergence behavior is comparable to the results obtained with HF-RPA. Thus, the conclusion remains the same: The larger the model space, the better converged results.

The convergence behavior of the strength distributions with respect to the truncation of the 3N model space is not shown here, since the results are similar to the HF-RPA case. Again, the only noticeable deviation between different 3N truncations is observed for the ISM response of the calcium isotopes. The shift of less than 1.5 MeV is for the two higher $E_{3\max}$ negligible.

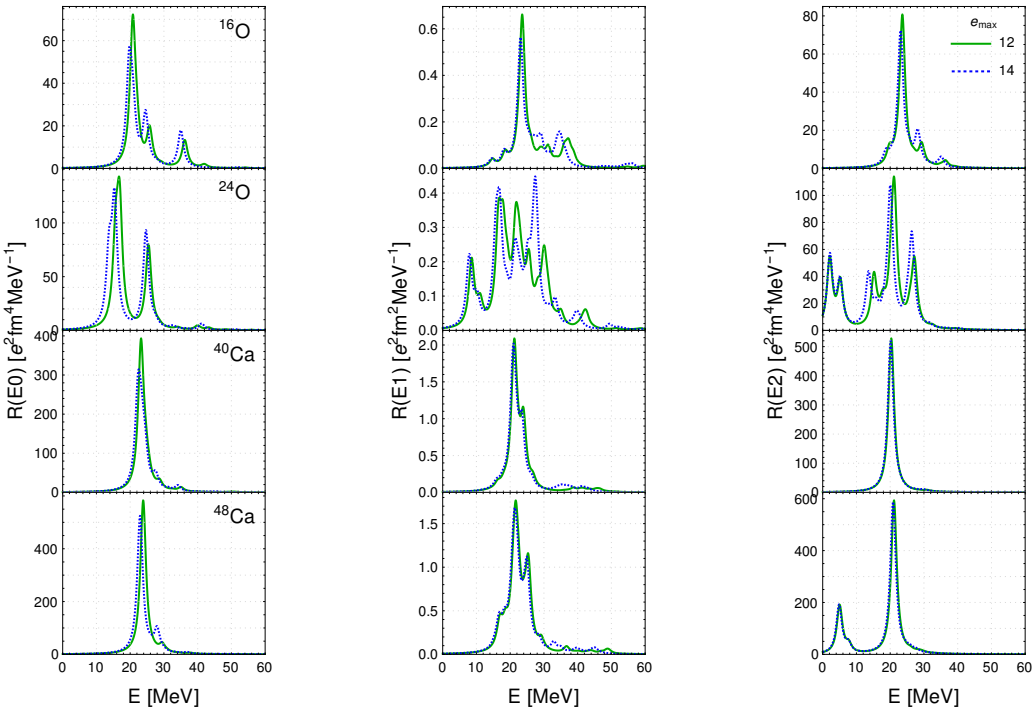

Figure 9.11: Electric ISM (left), IVD (middle) and ISQ (right) response of oxygen and calcium isotopes for different model-space truncations $e_{\max} = 12$ (——) and $e_{\max} = 14$ (·····).

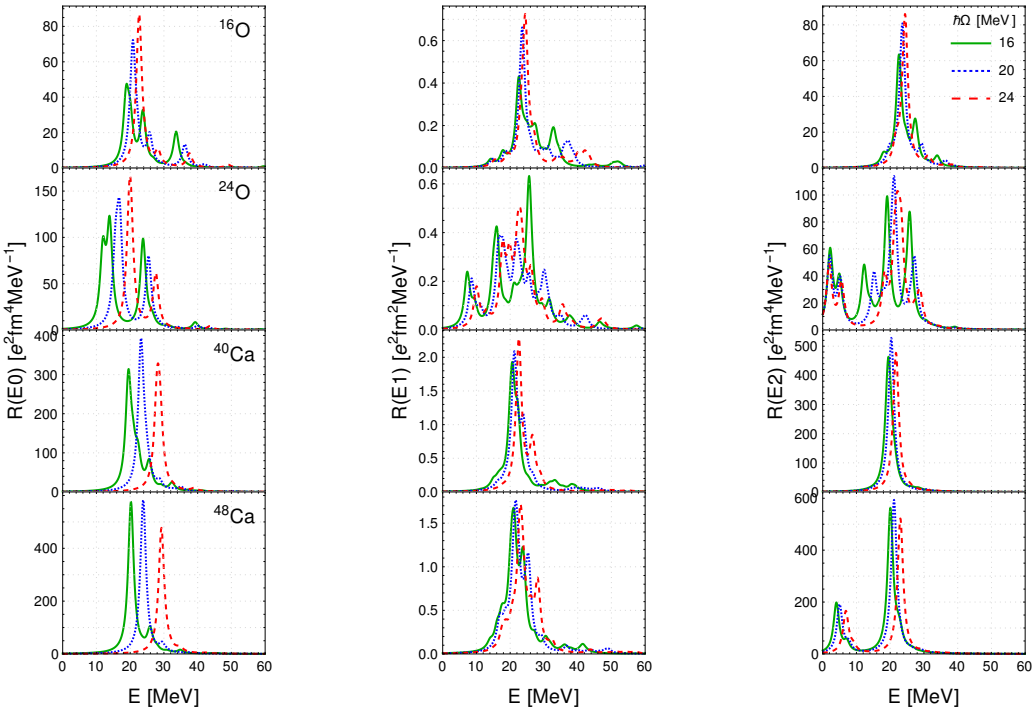

Figure 9.12: Electric ISM (left), IVD (middle) and ISQ (right) response of oxygen and calcium isotopes for different oscillator frequencies $\hbar\Omega = 16$ MeV (——), $\hbar\Omega = 20$ MeV (·····), and $\hbar\Omega = 24$ MeV (- - -).

Oscillator Frequency Dependence In Fig. 9.12, the ISM, IVD, and ISQ transition strengths are illustrated for different oscillator frequencies $\hbar\Omega$ for $e_{\max} = 12$. Contrary to the expectations, the strength distributions depend on $\hbar\Omega$ for natural orbitals. For higher frequencies, the responses are shifted to larger excitation energies. The shift up to 4.5 MeV for the ISM mode is more pronounced than for the other modes. This is comparable to the results from HF-RPA. In order to explain the dependence and find a possibility how to get rid of it, we first investigate the ground-state properties.

The radial proton wave functions of ^{16}O are depicted in Fig. 9.13 for different single-particle truncations $e_{\max}$. The wave functions of low-lying orbitals, which are occupied in ^{16}O, are independent of the oscillator frequency within the natural orbitals. The frequency dependence starts at $n = 3$ for $e_{\max} = 12$. For $e_{\max} = 14$, the wave function of $3s_{1/2}$ is almost converged with respect to $\hbar\Omega$ in contrast to the smaller $e_{\max} = 12$. Higher orbitals still experience a frequency dependence. However, for small distances r, the wave functions are converged. For $e_{\max} = 16$, the wave functions of higher-lying orbitals are less dependent on the frequency. Summarizing, with increasing $e_{\max}$ the frequency dependence is slightly shifted to orbitals with higher n. Up to now, observables based on natural orbitals, which only include low-lying states in the calculation, have been investigated [81]. These observables are independent of the oscillator frequency, since the latter has no influence on the used low-lying states. For RPA calculations, the situation is different.

The single-particle spectrum of ^{16}O is shown in Fig. 9.14 for proton (——) and neutron (——) states. The lowest three orbitals are occupied (solid lines). All orbitals with higher energy are unoccupied, which is indicated by the dashed lines. We restrict ourselves to a certain single-particle energy. In principle, more unoccupied orbitals are available. The Fermi gap, which is the energy difference between occupied and unoccupied states, is with 20 MeV visible for both protons and neutrons. For both nucleon types, the single-particle spectra are similar with almost the same distance between particle and hole states. However, the whole spectrum is shifted to slightly lower energies for neutrons.

The RPA is based on the ph formalism and, therefore, the ph excitation energies play a crucial role. For an isoscalar monopole transition, the orbital angular momentum remains unaltered. Other transition types include a change in l. Thus, for $e_{\max} = 12$, the quantum number n can change for the energetically lowest orbital $0s_{1/2}$ up to $n = 6$ because of the relation $e_{\max} = 2n + l$. The other occupied orbitals $0p_{1/2}$ and $0p_{3/2}$ can be excited up to $n = 5$. The possible excitations are shown in Fig. 9.15, yielding 32 ph configurations in total, which is in accordance with Fig. 9.8. A proton or neutron in the energetically lowest state $0s_{1/2}$ can be excited via 6 different possibilities. The highest possible orbital for protons has a single-particle energy of 175.37 MeV. Together with the energy of the lowest hole state, the ph excitation energy yields $E_{ph} = 193.52$ MeV. The energies of hole and particle states and the corresponding ph excitation energies are presented in Tab. 9.4. If we perform a full RPA calculation, i.e., we do not truncate the ph excitation energy, we realize that the $5s_{1/2}$ and $6s_{1/2}$ states are included according to Fig. 9.8. But the radial wave functions of those orbitals are strongly frequency dependent. Thus, including these excitations in the RPA framework for a complete description of the ISM response, the frequency dependence of the radial wave functions is transferred to the RPA strength distributions. For larger model-space sizes, the influence of $\hbar\Omega$ to the wave functions is shifted towards higher orbitals. Thus, the idea is to shift this dependence to higher orbitals by increasing $e_{\max}$ while restricting the subsequent RPA calculation to smaller model spaces, which is consequently more unaffected by a variation of $\hbar\Omega$.

In order to exclude a potential frequency dependence induced by $E_{3\max}$, we investigate the radial wave functions on NN-level. These are shown in Fig. 9.16. We observe already on two-

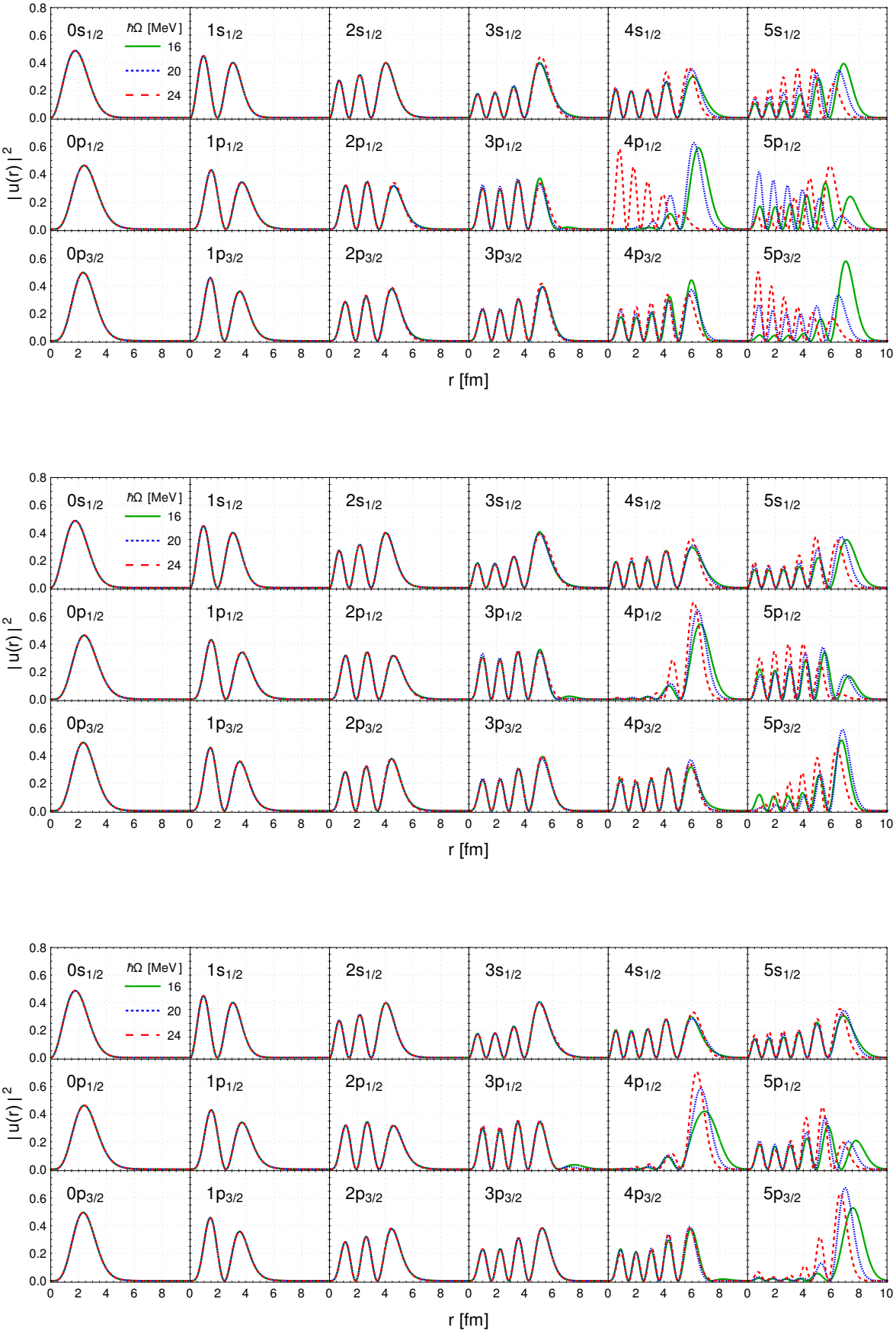

Figure 9.13: Radial proton wave functions of ^{16}O for $e_{\max} = 12$ (above), $e_{\max} = 14$ (center), and $e_{\max} = 16$ (below) for different oscillator frequencies $\hbar\Omega = 16$ MeV (——), $\hbar\Omega = 20$ MeV (·····), and $\hbar\Omega = 24$ MeV (- - -).

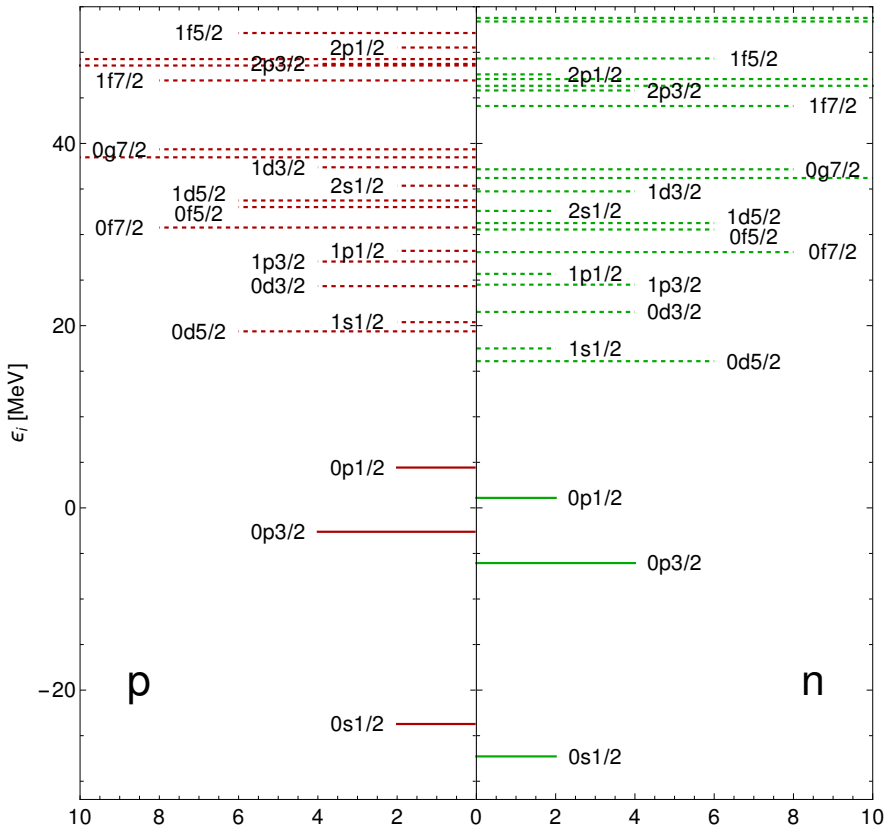

Figure 9.14: Single-particle spectrum of ^{16}O for protons (left, red) and neutrons (right, green). The single-particle energies depending on the occupation number are shown. The spectroscopic notation of the corresponding orbitals is given as well. The lowest three orbitals are occupied and the dashed orbitals are unoccupied.

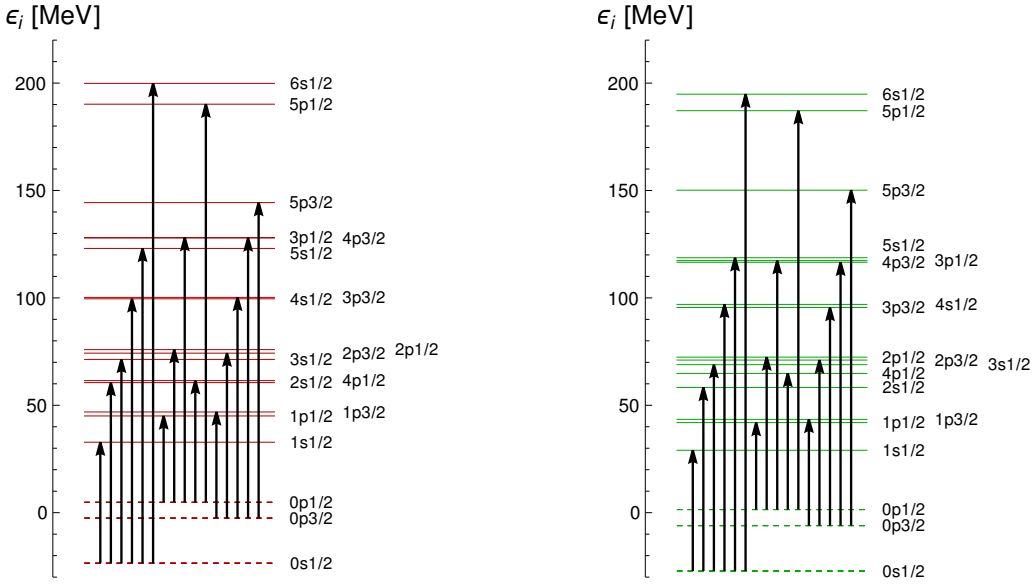

Figure 9.15: Possible ph excitations for an ISM transition of ^{16}O. There are 16 possibilities for protons (left, red) as well as for neutrons (right, green), which leads to a total number of 1p1h excitations of 32.

protons					neutrons				
particle	hole	E_p	E_h	E_{ph}	particle	hole	E_p	E_h	E_{ph}
1s1/2	0s1/2	32.80	-23.53	56.34	1s1/2	0s1/2	29.05	-27.16	56.21
2s1/2	0s1/2	60.55	-23.53	84.08	2s1/2	0s1/2	58.30	-27.16	85.46
3s1/2	0s1/2	71.36	-23.53	94.89	3s1/2	0s1/2	68.90	-27.16	96.06
4s1/2	0s1/2	99.57	-23.53	123.10	4s1/2	0s1/2	96.97	-27.16	124.13
5s1/2	0s1/2	123.03	-23.53	146.56	5s1/2	0s1/2	118.70	-27.16	145.86
6s1/2	0s1/2	199.87	-23.53	223.41	6s1/2	0s1/2	194.83	-27.16	221.99
1p1/2	0p1/2	45.03	4.82	40.21	1p1/2	0p1/2	41.94	1.45	40.49
2p1/2	0p1/2	75.92	4.82	71.09	2p1/2	0p1/2	72.42	1.45	70.97
3p1/2	0p1/2	128.07	4.82	123.25	3p1/2	0p1/2	117.35	1.45	115.90
4p1/2	0p1/2	61.48	4.82	56.66	4p1/2	0p1/2	64.82	1.45	63.37
5p1/2	0p1/2	190.18	4.82	185.35	5p1/2	0p1/2	187.15	1.45	185.69
1p3/2	0p3/2	46.89	-2.54	49.42	1p3/2	0p3/2	43.44	-6.02	49.46
2p3/2	0p3/2	74.27	-2.54	76.81	2p3/2	0p3/2	71.04	-6.02	77.06
3p3/2	0p3/2	100.24	-2.54	102.77	3p3/2	0p3/2	95.52	-6.02	101.54
4p3/2	0p3/2	127.89	-2.54	130.43	4p3/2	0p3/2	116.59	-6.02	122.61
5p3/2	0p3/2	144.36	-2.54	146.89	5p3/2	0p3/2	150.13	-6.02	156.15

Table 9.4: Particle-hole configurations with corresponding energies for ISM response of ^{16}O for protons (left) and neutrons (right). The energies are given in MeV.

body level a frequency dependence for higher-lying orbitals, which is shifted with increasing $e_{\max}$. For $e_{\max} = 16$, the $n = 5$ states are still noticeably frequency dependent. Thus, the single-particle truncation $e_{\max}$ should be increased further, which reaches computational limitations. Therefore, we recommend a basis optimization, which not only includes low-lying states but also higher-lying states in order to gain the features of frequency independence for collective excitations as well.

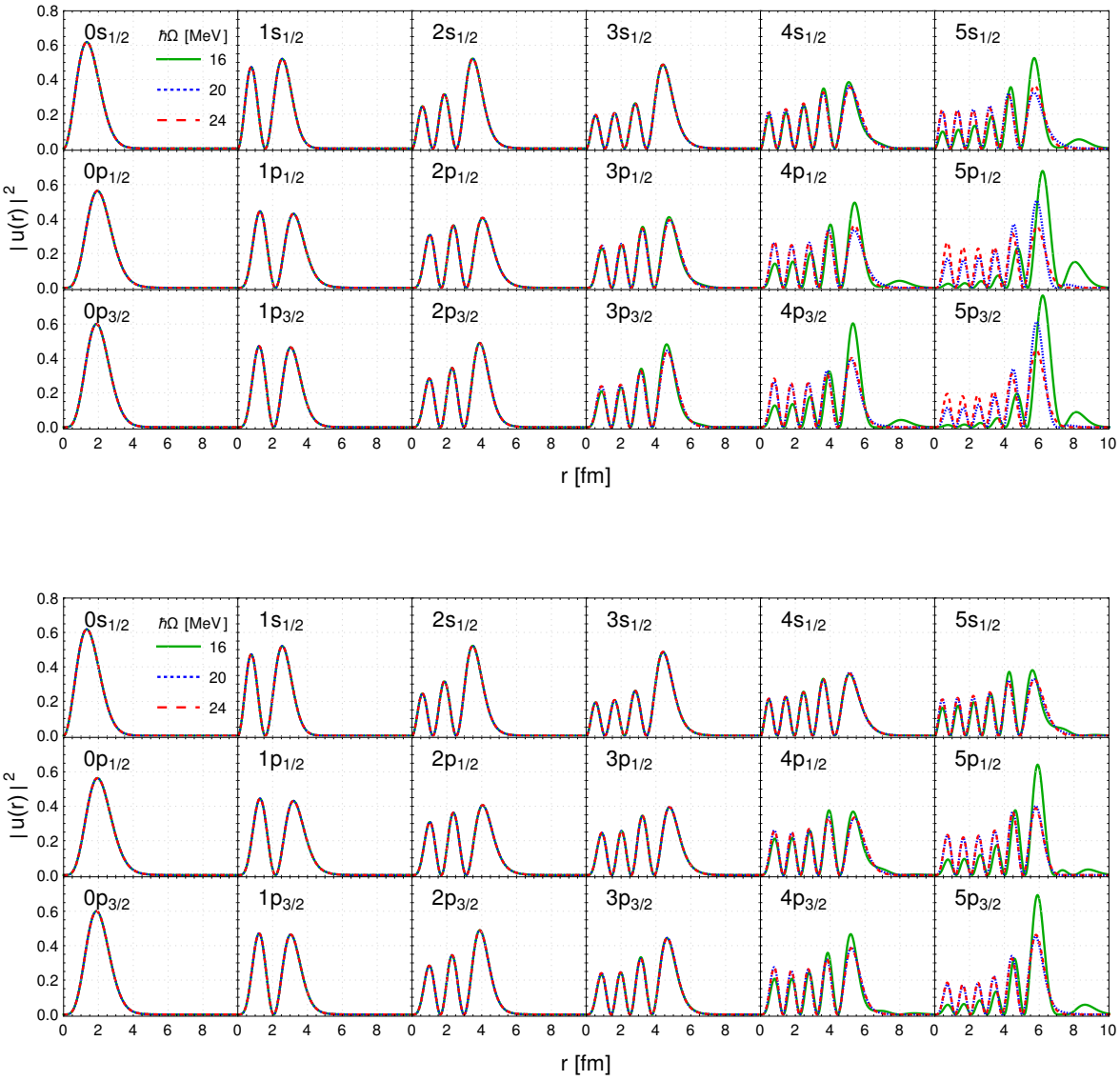

Figure 9.16: Radial neutron wave functions on two-body level of ^{16}O for $e_{\max} = 14$ (above) and $e_{\max} = 16$ (below) for different oscillator frequencies $\hbar\Omega = 16$ MeV (——), $\hbar\Omega = 20$ MeV (·····), and $\hbar\Omega = 24$ MeV (- - - -).

9.3 IM-RPA

An RPA calculation based on IM-SRG matrix elements includes ground-state correlations. The corresponding A and B matrices contain off-diagonal contributions as discussed in Sec. 7.2.

The following strength distributions are obtained by an RPA calculation which uses an IM-SRG evolved Hamiltonian together with HF matrix elements of the electromagnetic operators instead of IM-SRG evolved matrix elements. This inconsistency occurs since the implementation of IM-SRG evolved non-scalar operators is part of current research [97]. The transition energies, i.e., the eigenvalues, are unaffected by this, but the transition strengths are influenced in the process.

First, we examine the RPA model-space size. In Fig. 9.17, the cumulative number of 1p1h states for the ISM, IVD, and ISQ response of ^{16}O and ^{40}Ca is shown for different single-particle bases. On the left-hand side, we compare the 1p1h states of HF and the IM-HF matrix elements and on the right-hand side, we contrast the ones for NAT and IM-NAT matrix elements. For all depicted cases, the standard and the in-medium RPA results are equal in the maximum number of 1p1h states and similar in the energy intervals between the appearance of new 1p1h excitations. However, the corresponding excitation energy differs around 10 MeV. After these considerations, we discuss the different chiral order of the interaction within NAT-RPA and analyse the convergence with respect to the model-space truncation and other characteristic parameters.

9.3.1 Chiral Interaction

The convergence of the IM-RPA response with respect to the chiral order is investigated in Fig. 9.18. The isoscalar monopole, isovector dipole, and isoscalar quadrupole response at N^{2}LO and N^{3}LO is shown for in-medium input matrix elements based on HF and NAT. We observe a stability against both chiral orders, independent of the isotope, the response type and the underlying single-particle basis, as we have seen in the previous sections. The only exception is the ISM response of the calcium isotopes, where the higher chiral order leads to a shift of the strength distribution to smaller energies. The shift amounts to about 2 MeV.

9.3.2 Model-Space Convergence

The convergence behavior with respect to different truncation and other characteristic parameters is examined in the following section.

IM-SRG Flow Parameter Dependence The IM-SRG, which produces the input for the IM-RPA, decouples the ground-state from its particle-hole configurations via a flow equation, c.f. Eq.(7.4). The flow parameter s characterizes the Hamiltonian $\hat{H}(s)$, which is utilized to calculate the transitions strengths via IM-RPA. In Fig. 9.19(a), the convergence of the IM-HF-RPA response of ^{16}O with respect to the iterations steps $s = 0.0$ (——), $s = 0.2$ (·····), $s = 0.5$ (- - - -), $s = 1.0$ (-·-·-), and $s = 2.5$ (——) is illustrated. A flow parameter of $s = 0$ corresponds to the standard HF-RPA calculation. We observe a fast convergence of the IM-HF strengths. The first iteration step of the IM-SRG evolution shifts the strength distributions to higher energies. The following flow parameters, starting at $s = 0.5$ up to $s = 2.5$, result in a slight upward energy shift of the responses and lead to an almost converged IM-HF-RPA result for all transition types. The IM-SRG transformation of the ground-state energy E_0 depending on the flow parameter is shown in Fig. 9.19(b). This energy converges marginally slower than

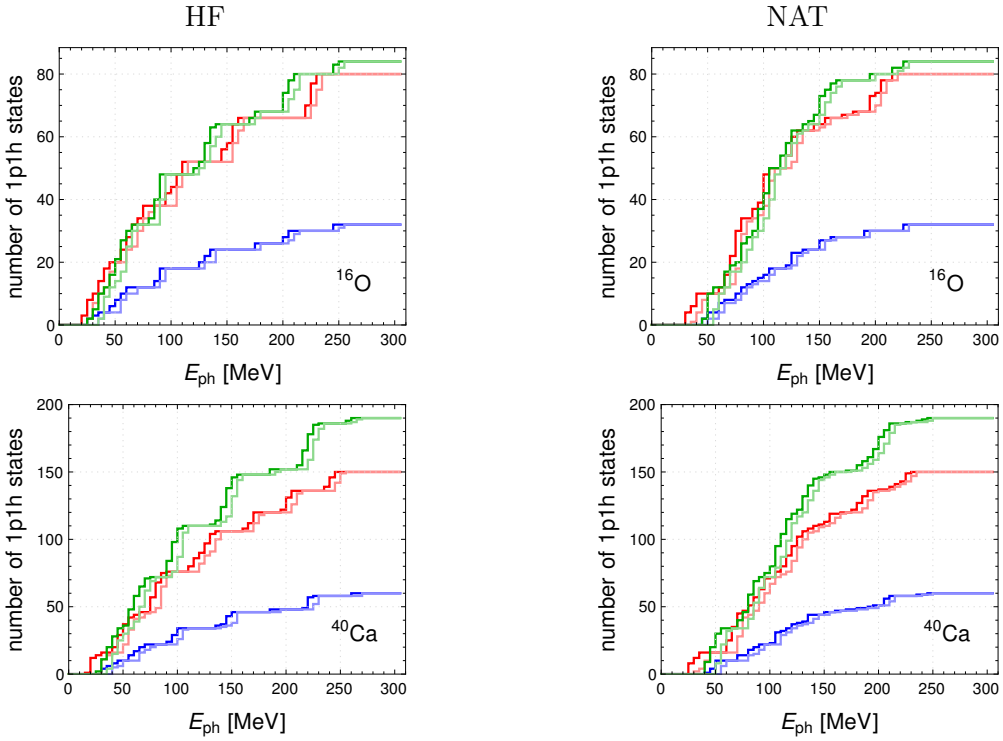

Figure 9.17: Cumulative number of 1p1h states of the ISM (——), IVD (——) and ISQ (——) strength distributions depending on the excitation energy threshold for ^{16}O (above) and ^{40}Ca (below). The left column compares the number of 1p1h excitations for HF and IM-HF matrix elements, whereas the right column shows the results obtained for NAT and IM-NAT matrix elements. The more transparent lines represent the IM results.

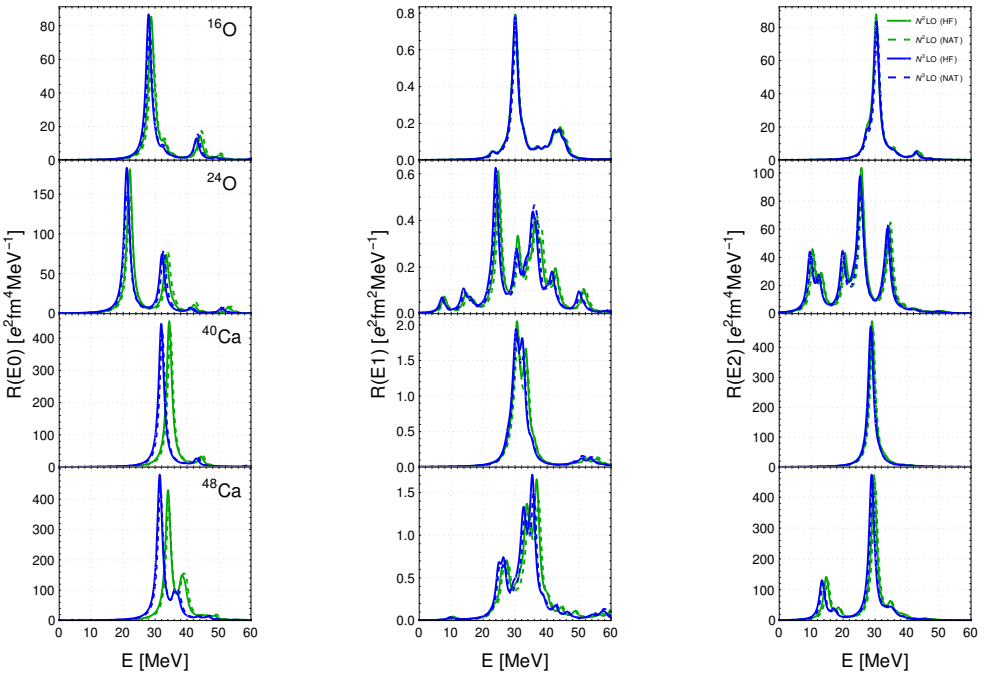

Figure 9.18: Electric ISM (left), IVD (middle) and ISQ (right) response of oxygen and calcium isotopes for the different chiral orders N^{2}LO (——) and N^{3}LO (——) obtained by IM-HF-RPA (solid line) and IM-NAT-RPA (dashed line) calculations.

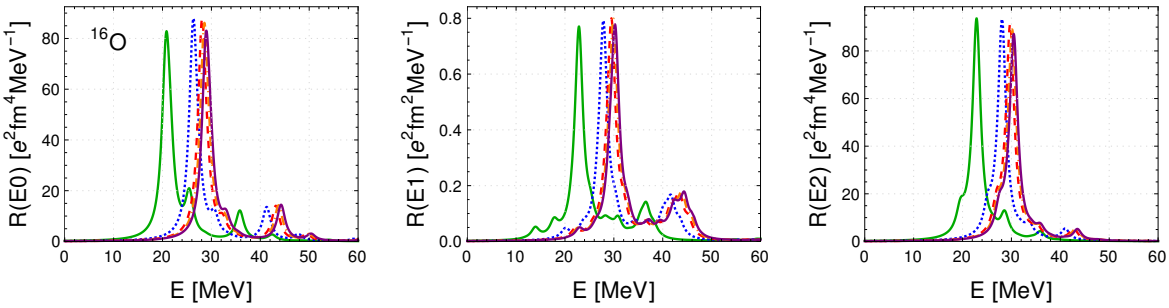

(a) Electric ISM (left), IVD (middle) and ISQ (right) response of ^{16}O for different flow parameters $s = 0.0$ (——), $s = 0.2$ (·····), $s = 0.5$ (- - - -), $s = 1.0$ (-·-·-), and $s = 2.5$ (——). The calculation was obtained by an IM-HF-RPA calculation with an underlying interaction at N^{2}LO, $\alpha = 0.08$ fm^4, $e_{\max} = 12$, $l_{\max} = 8$, $\hbar\Omega = 20$ MeV, and $E_{3\max} = 14$. A flow parameter of $s = 0.0$ corresponds to the HF-RPA response.

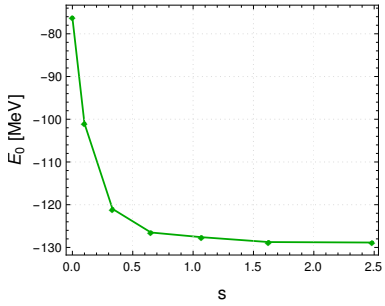

(b) Ground state energy of ^{16}O for different IM-SRG flow parameter s. For larger values of s, the calculated ground-state energy is with -128.85 MeV comparable to the experimental value of 127.6 MeV [30].

Figure 9.19: Strength distributions and ground state energy of ^{16}O depending on iteration steps of the IM-SRG evolution.

the strength distributions. However, for a flow parameter of $s = 2.5$, the ground-state energy is converged and amounts to -128.85 MeV, which is compatible to the experimental value of 127.6 MeV [30]. For all in-medium calculations, we use the White Generator.

Free-Space SRG Flow Parameter Dependence In Fig. 9.20, the ISM, IVD, and ISQ IM-HF-RPA responses are shown for different free-space SRG flow parameter $\alpha = 0.04$ fm^4 (——) and $\alpha = 0.08$ fm^4 (——). The dashed lines represent the IM-NAT-RPA results. The strength distributions of oxygen isotopes experience a slight downward shift in the transition energies for larger SRG flow parameters. The calcium isotopes are more affected by the different α. With around 5 MeV for the ISM mode and around 2 MeV for the ISQ response, the energy shifts are larger compared to the shifts of the oxygen isotopes. The convergence behavior of the IVD mode of the calcium isotopes is comparable to the oxygen isotopes. The shift is compatible for both bases, IM-HF and IM-NAT, respectively, and is contrary to the investigation in standard RPA, where we found an upward energy shift for larger SRG flow parameters.

Single-Particle Truncation The convergence behavior of the different response types with respect to the single-particle truncation is illustrated in Fig. 9.21 for $e_{\max} = 12$ (——) and $e_{\max} = 14$ (——). Analogously to HF-RPA and NAT-RPA, the responses are shifted to slightly lower transition energies with increasing $e_{\max}$. This shift amounts to 3 MeV and is, thus, comparable to the influence of the SRG flow parameter, which mainly yields for the ISM mode. The other modes tend to be robust against a variation of $e_{\max}$. The overall shape remains same, except for the IVD response of ^{24}O and the ISM response of ^{48}Ca.

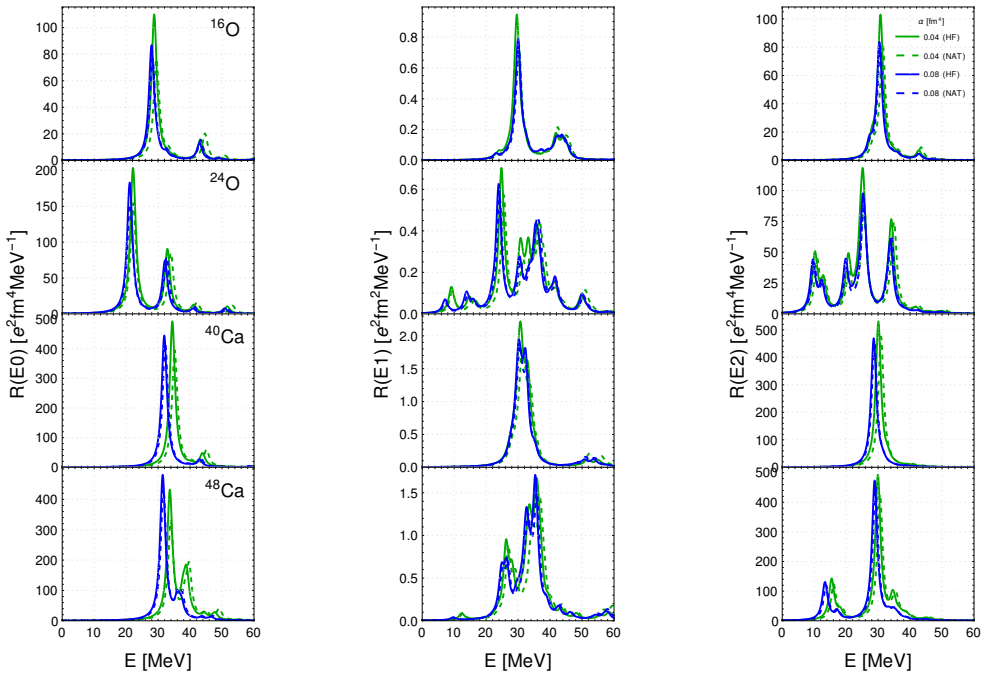

Figure 9.20: Electric ISM (left), IVD (middle) and ISQ (right) response of oxygen and calcium isotopes for different SRG flow parameters $\alpha = 0.04$ fm^4 (——) and $\alpha = 0.08$ fm^4 (——) for an IM-HF-RPA calculation. The dashed lines represent the corresponding IM-NAT-RPA results.

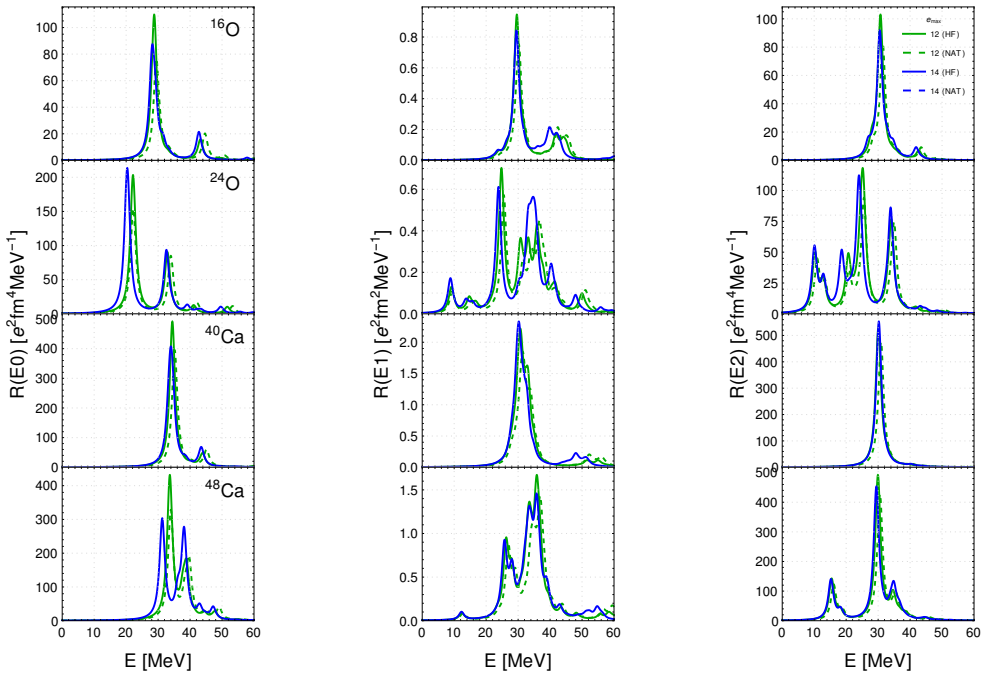

Figure 9.21: Electric ISM (left), IVD (middle) and ISQ (right) response of oxygen and calcium isotopes for different model-space truncations $e_{\max} = 12$ (——) and $e_{\max} = 14$ (——) for an IM-HF-RPA calculation. The dashed lines represent the corresponding IM-NAT-RPA results. Here, we use an SRG flow parameter of $\alpha = 0.04$ fm^4.

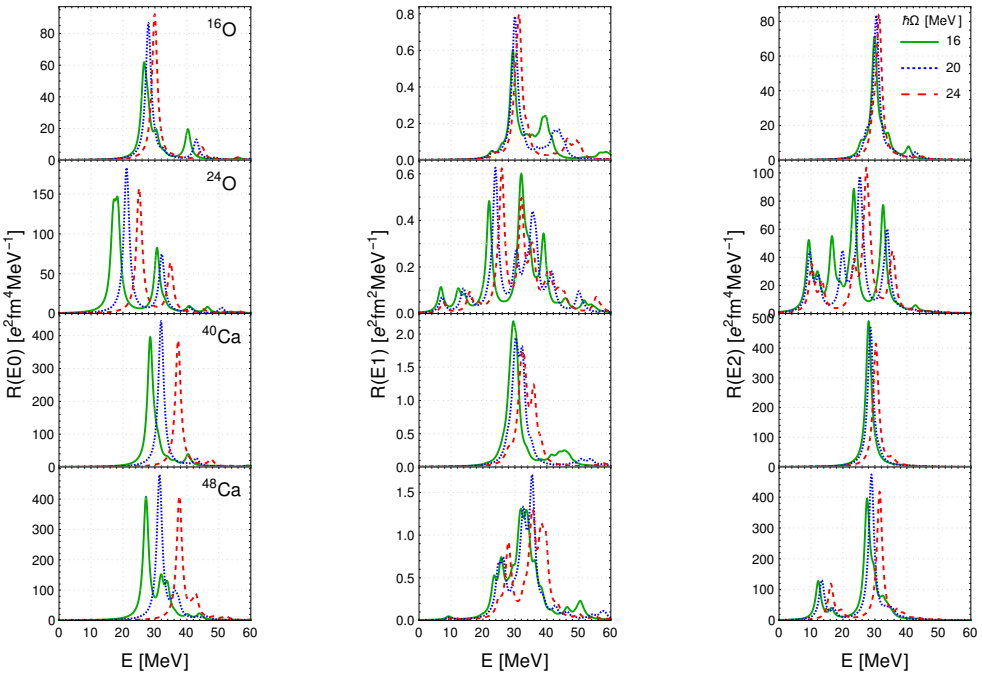

Figure 9.22: Electric ISM (left), IVD (middle) and ISQ (right) response of oxygen and calcium isotopes for different oscillator frequencies $\hbar\Omega = 16$ MeV (——), $\hbar\Omega = 20$ MeV (·····), and $\hbar\Omega = 24$ MeV (- - - -) for an IM-HF-RPA calculation. The result obtained with IM-NAT-RPA are very similar.

Oscillator Frequency Dependence The influence of the oscillator frequency of IM-HF-RPA calculations is shown in Fig. 9.22 for the ISM, IVD, and ISQ response of oxygen and calcium isotopes. We compare the results for $\hbar\Omega = 16$ MeV (——), $\hbar\Omega = 20$ MeV (·····), and $\hbar\Omega = 24$ MeV (- - - -). Larger oscillator frequencies shift the strength distributions to larger transition energies. This behavior is already known from the standard HF- and NAT-RPA. The shift of about 5 MeV is more noticeable for the ISM transition strengths than for the other types. Enlarging the model space would reduce the dependence, since this artifact is caused by too small model spaces.

9.4 Comparison of Different Types of RPA

So far, we discussed the standard and IM-correlated RPA separately. In the following section, both methods are compared to each other. In Fig. 9.23, the isoscalar monopole, isovector dipole, and isoscalar quadrupole resonances of oxygen and calcium isotopes are illustrated for the HF- (——) and IM- (·····) RPA based on the HF basis. The analogous results with natural orbitals are depicted in Fig. 9.24. The observed systematic between both methods is equal throughout all nuclei, transition modes, and underlying single-particle bases. The transition strengths are significantly shifted to larger energies when including ground-state correlations from IM-SRG in first-order RPA. The overall structure slightly deviates between both methods. The shape of the ISM response remains almost unaltered except for small changes of the descending tail of the strong peak of ^{16}O and ^{48}Ca. However, the ISQ response is slightly compressed, resulting in smaller peak heights for all nuclei. The largest deviations in the detailed structure of the transition strengths is given for the IVD response. Especially the IVD mode of ^{24}O exhibits remarkable changes. For the HF-RPA, we find a broadened

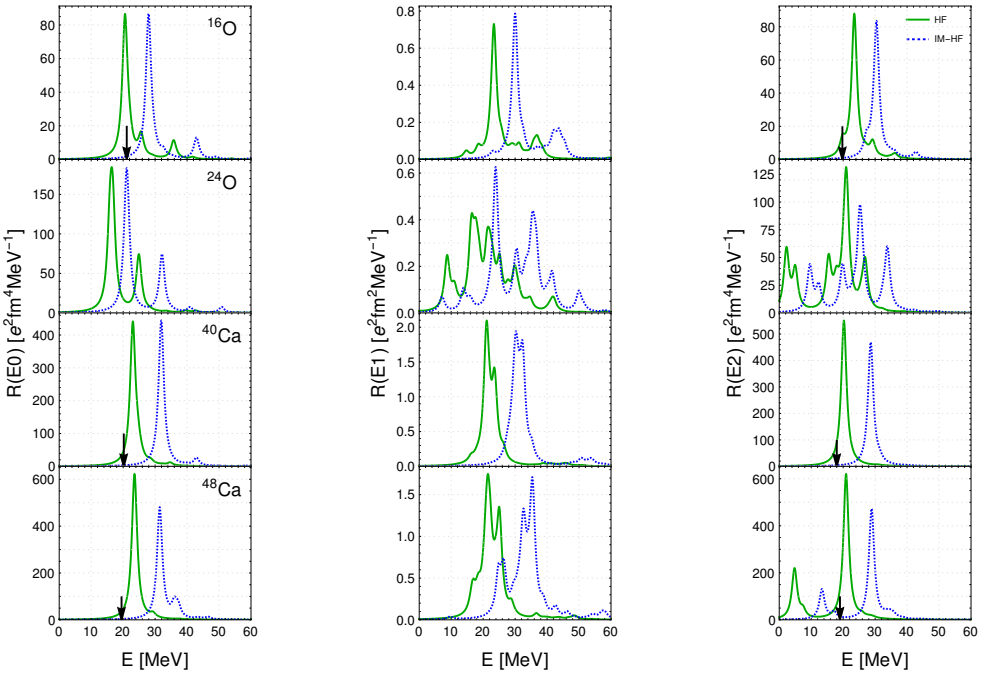

Figure 9.23: Electric ISM (left), IVD (middle) and ISQ (right) response of oxygen and calcium isotopes obtained by HF-RPA (——) and IM-HF-RPA (·····) calculations. The experimental centroid energies from Tab. 8.1 are shown by black arrows.

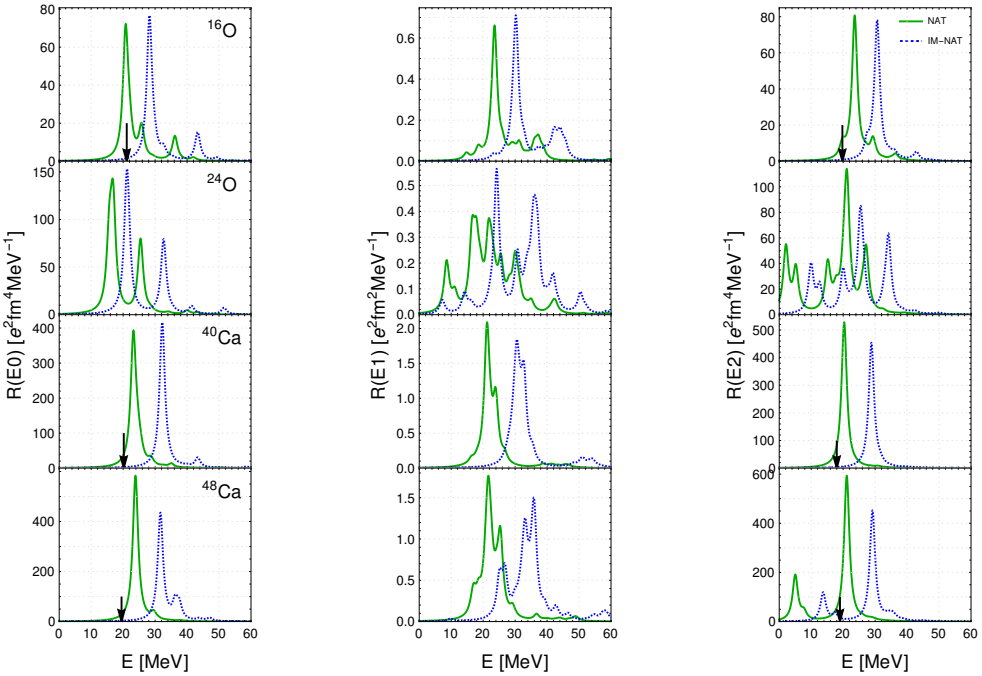

Figure 9.24: Electric ISM (left), IVD (middle) and ISQ (right) response of oxygen and calcium isotopes obtained by NAT-RPA (——) and IM-NAT-RPA (·····) calculations. The arrows indicate the experimental centroid energies.

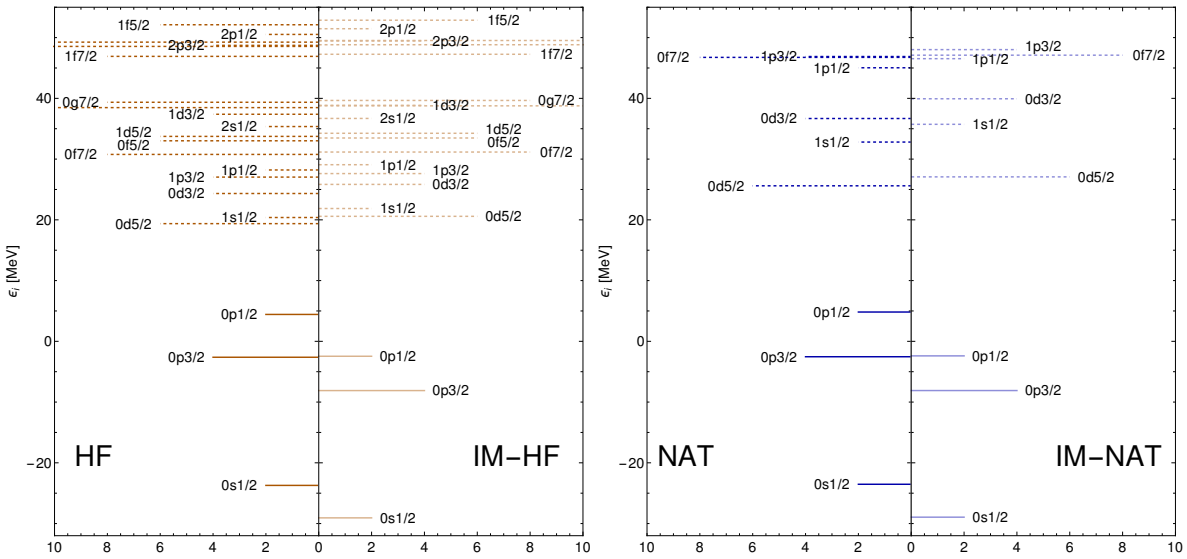

Figure 9.25: Single-particle spectra of ^{16}O for proton states regarding the HF (——), the IM-HF (both left), the NAT (——), and the IM-NAT (both right) basis. The more transparent lines represent the IM results. Occupied states are indicated by a solid line, whereas a dashed line indicates unoccupied states.

distribution around the resonance region, which separates in two more pronounced peaks for the IM response.

As already seen in Sec. 9.2, both single-particle bases, HF and NAT, respectively, show only slight deviations regarding the centroid energies and overall structure of the transition strengths throughout all nuclei and transition modes. The observed behavior between standard and correlated RPA results is as well comparable for different SRG flow parameters and model-space sizes. This is not discussed here in further detail.

In order to find an explanation for the upward energy shift of the transition strengths when going from standard HF- or NAT-RPA to the in-medium counterparts, we examine the level schemes in Fig. 9.25. On the left-hand side, the single-particle spectra of ^{16}O with respect to the HF (——) and IM-HF basis are presented. The right-hand side shows the NAT (——) and IM-NAT single-particle spectra. The more transparent lines represent the results obtained with IM-RPA. We show the various single-particle spectra of ^{16}O as an example, but the overall behavior is similar for other nuclei and different truncation parameters. We observe two remarkable things: First, comparing the single-particle spectrum of HF or NAT basis with its in-medium counterparts, we find a larger Fermi gap for IM-SRG evolved matrix elements. In this case, the single-particle energies of the occupied states are lowered. This is similar to the lowering of the ground-state energies with IM-SRG. All unoccupied states are comparable in the corresponding single-particle energy and the distance between two consecutive (un-)occupied levels is almost equal. This pertains for both single-particle bases, HF and NAT, respectively. However, the energy shift is less than 5 MeV within the (IM-)NAT basis and even smaller for the (IM-)HF basis. The second remark concerns the comparison of the uncorrelated HF and NAT basis. Here, the single-particle energies of the occupied states are very similar for both, HF and NAT. However, the structure of the unoccupied single-particle spectra deviates strongly. For NAT, already the first unoccupied state $0d_{5/2}$ has a larger single-particle energy compared to HF and the difference to the second unoccupied state $1s_{1/2}$, which is contained in the ph configurations in RPA, amounts to more than 10 MeV. For HF, both states lie almost on top of each other. This causes a stretching of the NAT spectrum

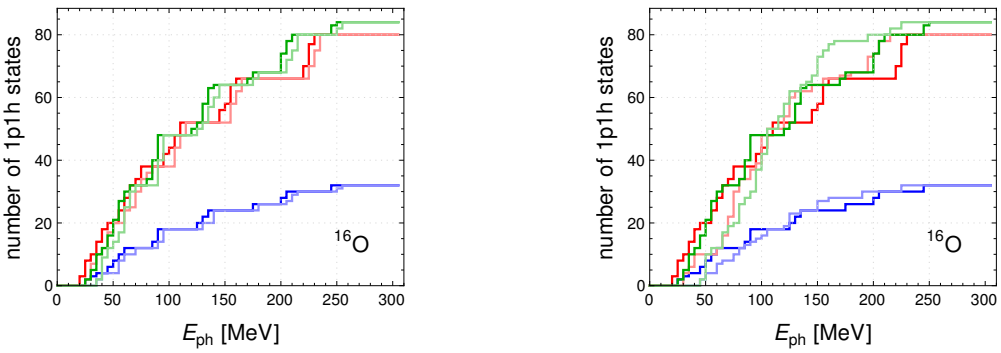

Figure 9.26: Cumulative number of 1p1h states of the ISM (——), IVD (——) and ISQ (——) strength distributions depending on the excitation energy threshold of ^{16}O for the comparison of HF and an IM-HF (transparent line) basis (left) and for the comparison of HF and NAT (transparent line) basis (right).

and a compression of the HF spectrum, respectively. Due to the unchanged single-particle energies of the occupied states and the increased ones for, at least, the first unoccupied NAT state, we find a widened Fermi gap as well. The Fermi gap, of course, plays an important role since ph excitations need a certain amount of energy.

However, this cannot be the only reason for the energy shift of the RPA responses comparing the HF- with the IM-RPA. Thus, we focus on the cumulative number of 1p1h excitations next, which is already shown in Fig. 9.17 for the uncorrelated RPA with the in-medium counterpart. For an easier comparison, we present this again in Fig. 9.26 (left) and contrast the cumulative number of 1p1h excitations within HF- and NAT-RPA calculations (right). We observe that the whole step function is shifted upwards in the energy threshold while being similar in the energy intervals between the different numbers of 1p1h excitations. Thus, the 1p1h states, which contribute to the IM-RPA calculation appear at almost 10 MeV larger excitation energies than for HF-RPA, which corresponds to the widening of the Fermi gap. This corresponds exactly to the energy shift, which we find for the transition strengths in Fig. 9.23.

However, the NAT vs. HF case is different. For lower excitation energy thresholds up to around 120 MeV, the 1p1h excitations appear for HF matrix elements almost 20 MeV less. After this threshold, the behavior is reversed. For the ISM mode, the energy shift is not as pronounced as for the other modes. In contrast to the previous case of the comparison of HF with IM-HF matrix elements (and analogously for NAT), this is no pure shift in the excitation energy threshold, which causes the transition strengths to remain almost unaltered as discussed in Sec. 9.2.

10

Collective Excitations with SRPA

Contents

The SRPA is a natural extension of the RPA and includes not only the 1p1h (de-)excitations, but additional 2p2h (de-)excitations. Their impact on the ISM, IVD, and ISQ response of oxygen and calcium isotopes is investigated throughout this chapter. We focus on the same transition modes, nuclei, and truncation parameters as for first-order RPA, allowing for a comparison of both methods. Thus, if not stated otherwise, we use the non-local NN+3N interaction at N^{3}LO [85] in NO2B approximation, which is SRG-evolved with $\alpha = 0.08$ fm^4. Moreover, we choose $\hbar\Omega = 20$ MeV, $e_{\max} = 12$, $l_{\max} = 8$ and $E_{3\max} = 14$ and vary these parameters systematically for different single-particle bases in the following sections.

10.1 HF-SRPA

The SRPA model space is several orders of magnitude larger than the RPA model space. In Fig. 10.1, the cumulative number of 2p2h excitations is shown. In addition to less than 100 1p1h configurations for ^{16}O, we obtain between 10^4 and 10^5 2p2h states for the different transition modes in increasing order, starting with the ISM mode. For ^{40}Ca, the SRPA model space is even larger: Besides the less than 200 states needed for the full description of the RPA model space, the full SRPA model space consists of already more than 10^5 2p2h states for the ISM mode. The SRPA model space for the other modes is even larger. These large model spaces cause an enormous computational effort, which is not feasible without additional truncations or approximative methods. Thus, we introduce a new model-space truncation for the SRPA model space, the so-called $E_{2\mathrm{p2hMax}}$, which is given by

$$E_{2\mathrm{p2hMax}} \geq \epsilon_{p_1} - \epsilon_{h_1} + \epsilon_{p_2} - \epsilon_{h_2} \tag{10.1}$$

with the single-particle energies ϵ_i. Thus, we include only 2p2h excitations up to the threshold $E_{2\mathrm{p2hMax}}$, which can be chosen differently for each nucleus. With $E_{2\mathrm{p2hMax}} = 0$ MeV we reproduce the first-order RPA calculation. The dependence on $E_{2\mathrm{p2hMax}}$ is shown for the example of the ISM response of oxygen and calcium isotopes in Fig. 10.2. For all nuclei, we find convergence with respect to the SRPA model-space truncation. Increasing the model space causes a downward energy shift, which amounts to a few MeV for oxygen and to around 7 MeV for calcium, comparing $E_{2\mathrm{p2hMax}}$ between 100 MeV and 250 MeV. But the two largest truncations show no difference. The SRPA calculation for the ISM mode is possible for $E_{2\mathrm{p2hMax}} = 250$ MeV with increased computational time: We need more than 24h (48h) for the SRPA calculation of oxygen (calcium) isotopes in those large model spaces on a cluster node. Those estimations vary obviously with the other truncations and parameters,

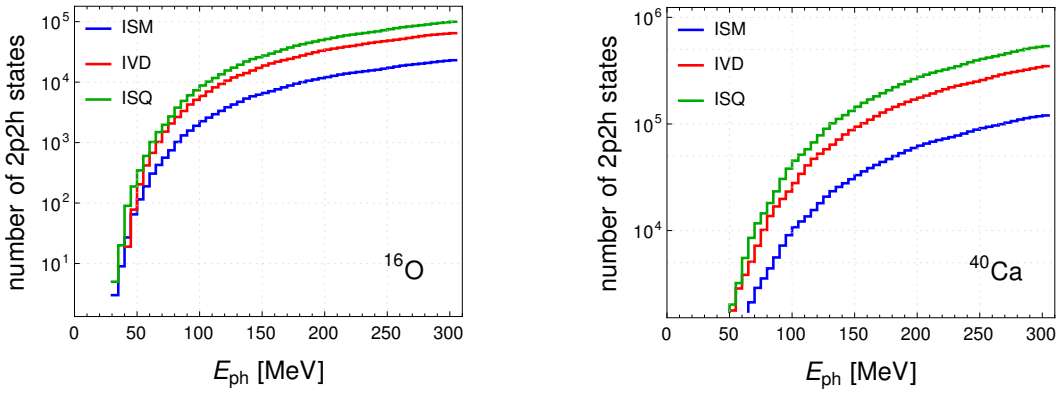

Figure 10.1: Cumulative number of 2p2h states of the isoscalar monopole (——), isovector dipole (——) and isoscalar quadrupole (——) strength distributions depending on the excitation energy threshold for ^{16}O and ^{40}Ca.

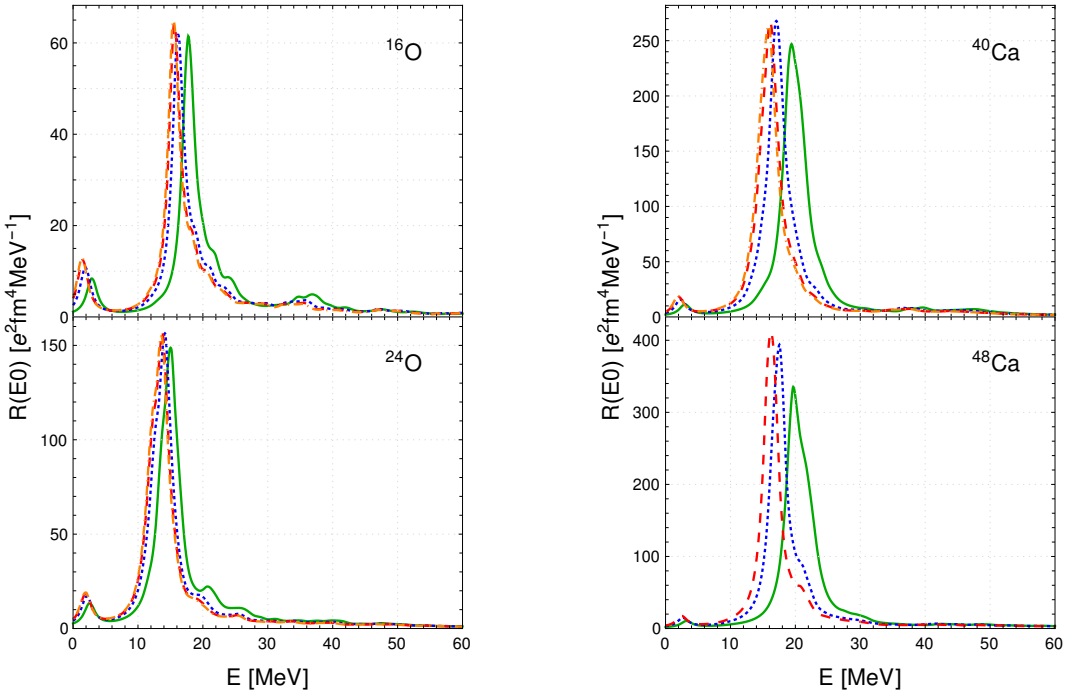

Figure 10.2: Isoscalar monopole response of oxygen (left) and calcium (right) isotopes for different SRPA model-space truncations $E_{\text{2p2hMax}} = \{50\ (\text{——}), 80\ (\cdots\cdots), 100\ (\text{- - -}), 150\ (\text{-·-·}), 200\ (\text{——})\}$.

such as the SRG flow parameter and the single-particle truncation. The difference in the computational time between oxygen and calcium isotopes can be explained with Fig. 10.1. About one order of magnitude more 2p2h states are needed for ^{40}Ca than for ^{16}O for a SRPA model space truncated at $E_{\text{2p2hMax}} = 250$ MeV. The calculation of other modes for oxygen are possible as well for $E_{\text{2p2hMax}} = 250$ MeV, but require even more computational time. However, those large model spaces cannot be reached for the calculation of other modes for calcium due to memory reasons.

If not stated otherwise, we restrict ourselves to model-space sizes of $E_{\text{2p2hMax}} = 200$ MeV for the oxygen isotopes (or if not feasible $E_{\text{2p2hMax}} = 150$ MeV due to a time limit of 24h) and of $E_{\text{2p2hMax}} = 100$ MeV for the calcium isotopes. We keep in mind that the transition strengths for the calcium isotopes are not yet converged in those model spaces. The difference to a converged SRPA model space amounts to about 7 MeV towards higher energies.

The dependence on the same model-space truncations and characteristic parameters as for first-order RPA calculations is investigated.

Oscillator Frequency Dependence In Fig. 10.3, the electric isoscalar monopole, isovector dipole and isoscalar quadrupole strengths distributions are shown for oxygen and calcium isotopes for variations of the oscillator frequency, for which we choose $\hbar\Omega = 16$ MeV (——), $\hbar\Omega = 20$ MeV (·····), and $\hbar\Omega = 24$ MeV (- - -). Comparing to the convergence behavior of first-order RPA, which is illustrated in Fig. 9.5, and SRPA, we find almost no differences. For larger $\hbar\Omega$, the strength distributions are shifted to larger transition energies by a similar extent or even less.

Single-Particle Truncation The impact of different single-particle truncations $e_{\text{max}} = 12$ (——) and $e_{\text{max}} = 14$ (·····) on the transition strengths is illustrated in Fig. 10.4. The larger model-

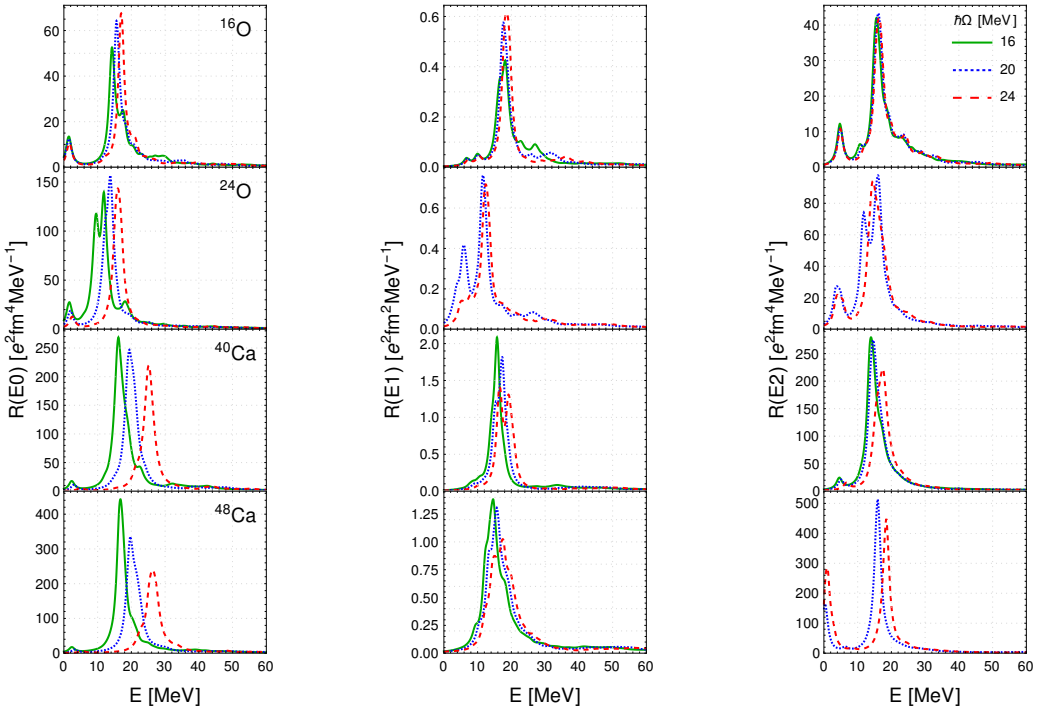

Figure 10.3: Electric ISM (left), IVD (middle) and ISQ (right) response of oxygen and calcium isotopes for different oscillator frequencies $\hbar\Omega = 16$ MeV (——), $\hbar\Omega = 20$ MeV (·····), and $\hbar\Omega = 24$ MeV (- - -). Except for the ISQ response of ^{24}O, where we use $E_{\mathrm{2p2hMax}} = 150$ MeV, we employ $E_{\mathrm{2p2hMax}} = 200$ MeV for the other oxygen isotopes and $E_{\mathrm{2p2hMax}} = 100$ MeV for the calcium isotopes. The strength distributions for $\hbar\Omega = 16$ MeV are missing due to computational time limits.

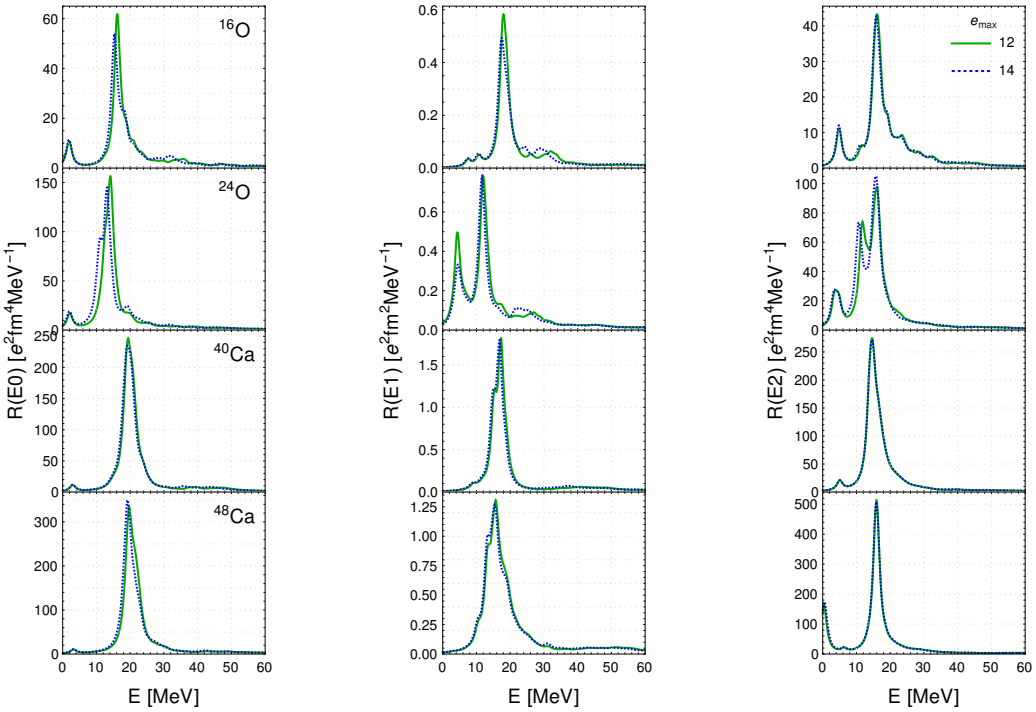

Figure 10.4: Electric ISM (left), IVD (middle) and ISQ (right) response of oxygen and calcium isotopes for different model-space truncations $e_{\max} = 12$ (——) and $e_{\max} = 14$ (·····). We utilize $E_{\mathrm{2p2hMax}} = 150$ MeV for the oxygen isotopes and $E_{\mathrm{2p2hMax}} = 100$ MeV for the calcium isotopes.

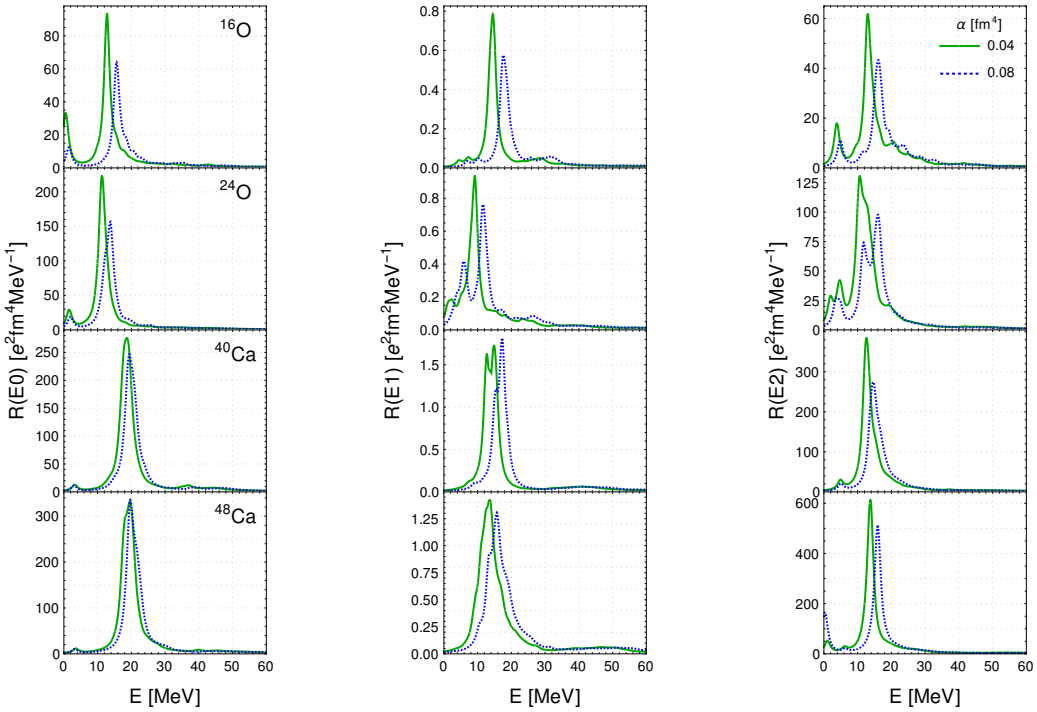

Figure 10.5: Electric ISM (left), IVD (middle) and ISQ (right) response for oxygen and calcium isotopes for different SRG flow parameters $\alpha = 0.04$ fm^4 (——) and $\alpha = 0.08$ fm^4 (·····). Except for the ISM response of ^{24}O, where we use $E_{2\text{p2hMax}} = 150$ MeV, we employ $E_{2\text{p2hMax}} = 200$ MeV for the other oxygen isotopes and $E_{2\text{p2hMax}} = 100$ MeV for the calcium isotopes.

space size associated with $e_{\max} = 14$ causes a marginal shift towards lower energies of ISM mode of the oxygen isotopes. In total, the transition strengths are robust against a variation of $e_{\max}$. Again, the convergence behavior is similar when comparing to first-order RPA in Fig. 9.6. The difference between both methods is particularly noticeable for ^{24}O, for which the change in $e_{\max}$ leads to a smaller shift of the transition strengths obtained with second-order than in first-order RPA. The other nuclei and transition modes are already stable against a variation of the single-particle model space in HF-RPA.

SRG Flow Parameter Dependence The convergence for the ISM, IVD, and ISQ response for oxygen and calcium isotopes with respect to the SRG flow parameter is depicted in Fig. 10.5. We focus on $\alpha = 0.04$ fm^4 and $\alpha = 0.08$ fm^4 as in previous discussions. For the larger flow parameter $\alpha = 0.08$ fm^4, which corresponds to a softer Hamiltonian, the ISM, IVD, and ISQ response of the different nuclei is shifted to higher transition energies. The shift is smaller for the ISM mode of the calcium isotopes than for the other modes and nuclei. This convergence behavior is comparable to first-order RPA. However, the difference in the transition strengths between both SRG flow parameters is slightly larger in SRPA than in first-order RPA. This is contrary to the influence of the oscillator frequency and the single-particle truncation. For these parameters we find an improvement in convergence with the inclusion of second-order ph excitations. Thus, it is not clear, which SRG flow parameter is more advantageous overall. A tradeoff between a softer Hamiltonian and induced many-body forces needs to be found.

In summary, the convergence behavior of the transition strengths obtained by an IM-HF-SRPA

calculation is comparable to the first-order counterpart. A variation of the oscillator frequency and the single-particle truncation even indicates a slightly more converged result. Thus, the inclusion of 2p2h excitations is crucial for a description of collective excitations. However, the transition strengths behave differently for a variation of the SRG flow parameter. Here, we find slightly larger shifts for different α. Furthermore, enlarging the model space by increased $e_{\max}$ could fix the dependence on $\hbar\Omega$.

10.2 NAT-SRPA

For first-order RPA calculations, we observed a similar behavior of the results with respect to a variation of the different truncation parameters as for an HF basis and natural orbitals. In this section, we focus on NAT-SRPA and discuss the results, comparing with HF-SRPA and NAT-RPA.

The cumulative number of 2p2h states depending on the excitation energy of ^{16}O and ^{40}Ca is shown in Fig. 10.6 for three different modes. In contrast to HF-SRPA, 2p2h contributions appear at higher excitation energy thresholds in NAT-SRPA calculations. For the ISM response of ^{16}O, a HF-SRPA calculation with $E_{\text{2p2hMax}} = 100$ MeV yields 1406 2p2h states, whereas we find 125 2p2h states for the NAT-SRPA. The difference for the ISQ response amounts to almost one order of magnitude at this energy threshold. For excitation energies larger than $E_{\text{2p2hMax}} = 200$ MeV, the HF- and the NAT-SRPA are comparable. For ^{40}Ca, the energy difference for the same number of 2p2h states amounts to 20 MeV comparing both single-particle bases. In principle, a larger E_{2p2hMax} can be chosen in order to include the same number of 2p2h states as in HF-SRPA in the formalism. For an optimized calculation, the energy threshold could be adjusted to another value for the different response types in order to find a balance between computational time and effort on the one hand and convergence on the other hand.

A variation of the excitation energy threshold is depicted in Fig. 10.7 for the isoscalar monopole mode of oxygen and calcium isotopes. As for the HF case, we observe convergence with respect to the SRPA model-space truncation for oxygen isotopes. Enlarging this truncation from 200 MeV to 250 MeV leads to no significant difference. This additionally holds for the other modes. Therefore we choose $E_{\text{2p2hMax}} = 200$ MeV for the oxygen isotopes and modes, if not stated otherwise.

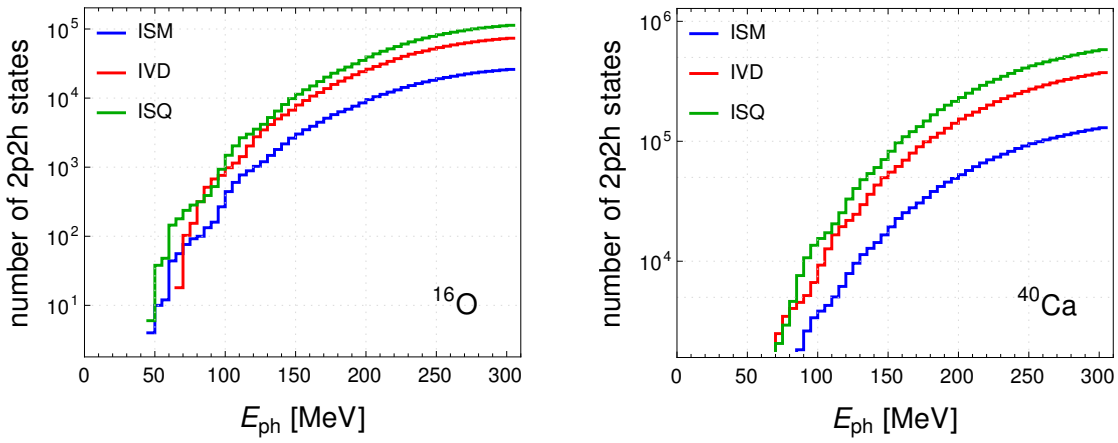

Figure 10.6: Cumulative number of 2p2h states of the isoscalar monopole (——), isovector dipole (——) and isoscalar quadrupole (——) strength distributions depending on the excitation energy threshold for ^{16}O and ^{40}Ca.

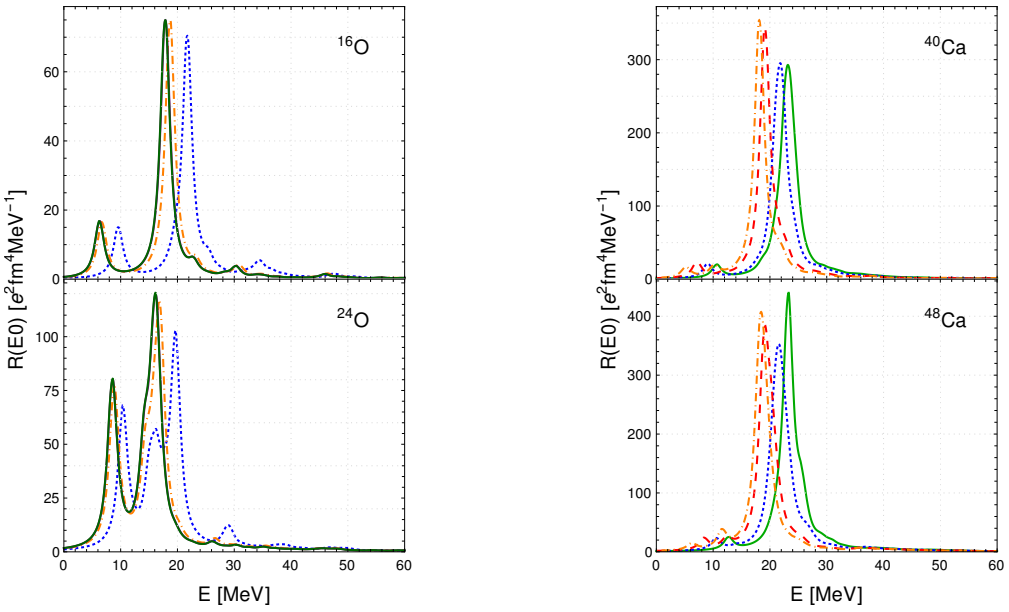

Figure 10.7: Isoscalar monopole response of oxygen (left) and calcium (right) isotopes for different SRPA model-space truncations $E_{\mathrm{2p2hMax}} = \{80\,(\text{——}), 100\,(\cdots\cdots), 130\,(\text{- - -}), 150\,(\text{-·-·}), 200\,(\text{——}), 250\,(\text{——})\}$.

For an analysis of NAT-SRPA transition strengths and a comparison with other bases and orders of the method, we need an impression of the convergence behavior with respect to truncation parameters. We vary the same parameters as for the previous methods.

Oscillator Frequency Dependence The impact of different oscillator frequencies on the ISM, IVD, and ISQ mode is investigated in Fig. 10.8 for oxygen and calcium isotopes. We compare the transition strengths for frequencies of $\hbar\Omega = 16$ MeV (——), $\hbar\Omega = 20$ MeV (⋯⋯), and $\hbar\Omega = 24$ MeV (- - -). For ^{16}O, the dependency is reduced and the transition strengths are almost converged, which can be observed for all three response types. For ^{24}O and the calcium isotopes, the discrepancy found in NAT-RPA in Fig. 9.12 for different $\hbar\Omega$ can be reproduced. The transition strengths are shifted to larger excitation energies with increasing $\hbar\Omega$, where the shifts amounts to 3 MeV and, thus, is comparable in size.

Single-Particle Truncation The convergence behavior with respect to the single-particle truncation is illustrated in Fig. 10.9 for $e_{\max} = 12$ (——) and $e_{\max} = 14$ (⋯⋯). We observe a convergence for this truncation parameter. The dependency with respect to the single-particle model-space size is reduced when going from NAT-RPA or HF-SRPA to NAT-SRPA. The inclusion of second-order excitations within SRPA leads to an improvement.

SRG Flow Parameter Dependence In Fig. 10.10, the ISM, IVD, and ISQ transition strengths are shown for SRG flow parameters of $\alpha = 0.04$ fm^4 (——) and $\alpha = 0.08$ fm^4 (⋯⋯) for oxygen and calcium isotopes. The responses are shifted to larger excitation energies for larger SRG flow parameters. The shifts are slightly larger in size than for NAT-RPA, but comparable with HF-SRPA. In contrast to the other truncation parameters so far, an improvement regarding the convergence behavior does not take place for the SRG flow parameter, which was already the case within HF-SRPA. Again, a tradeoff between a softer Hamiltonian and induced many-body forces guides the choice of α.

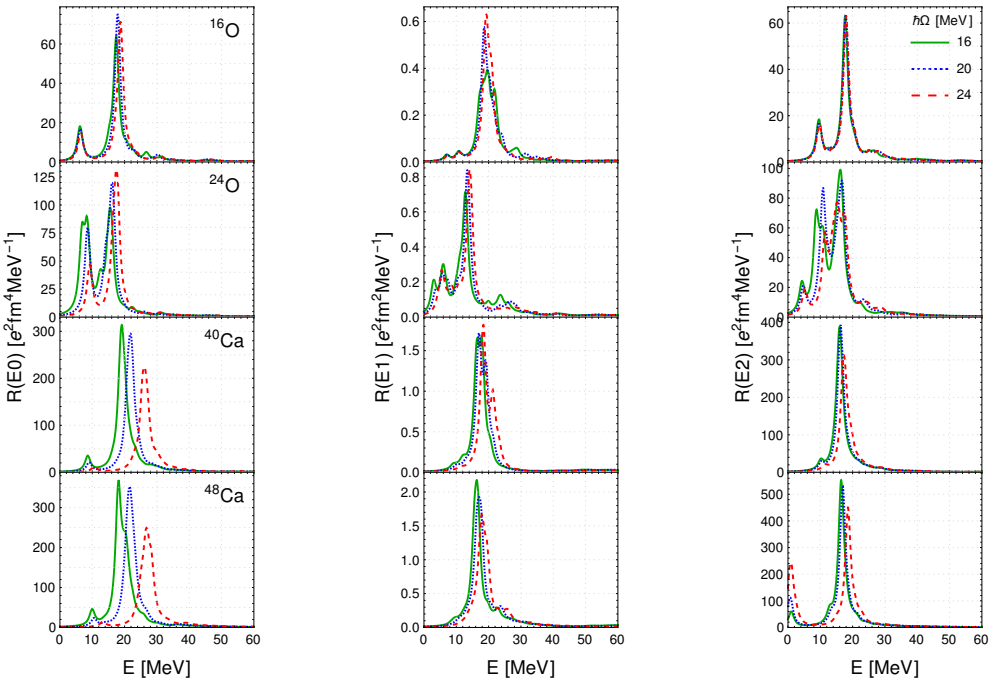

Figure 10.8: Electric ISM (left), IVD (middle) and ISQ (right) response of oxygen and calcium isotopes for different oscillator frequencies $\hbar\Omega = 16$ MeV (——), $\hbar\Omega = 20$ MeV (·····), and $\hbar\Omega = 24$ MeV (- - - -). Except for the IVD response of ^{24}O and the ISQ response of both oxygen isotopes, where we use $E_{\mathrm{2p2hMax}} = 150$ MeV, we employ $E_{\mathrm{2p2hMax}} = 200$ MeV for the other oxygen isotopes and $E_{\mathrm{2p2hMax}} = 100$ MeV for the calcium isotopes.

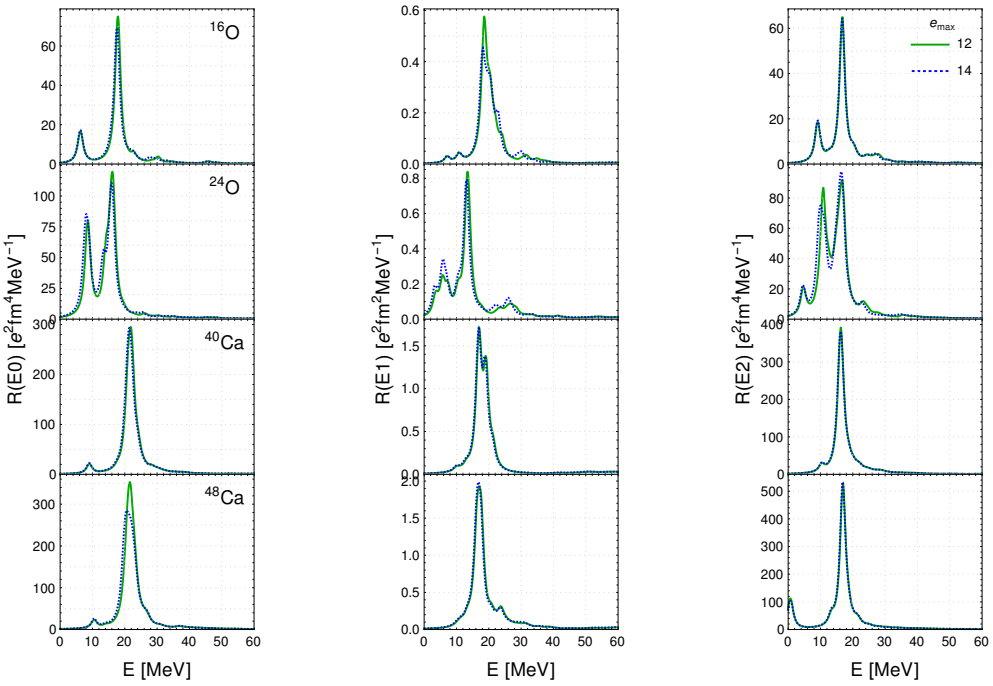

Figure 10.9: Electric ISM (left), IVD (middle) and ISQ (right) response of oxygen and calcium isotopes for different model-space truncations $e_{\max} = 12$ (——) and $e_{\max} = 14$ (·····). For the IVD and ISQ response of ^{24}O, we employ $E_{\mathrm{2p2hMax}} = 150$ MeV. For the other responses of the oxygen (calcium) isotopes, $E_{\mathrm{2p2hMax}} = 200$ MeV ($E_{\mathrm{2p2hMax}} = 100$ MeV) is utilized.

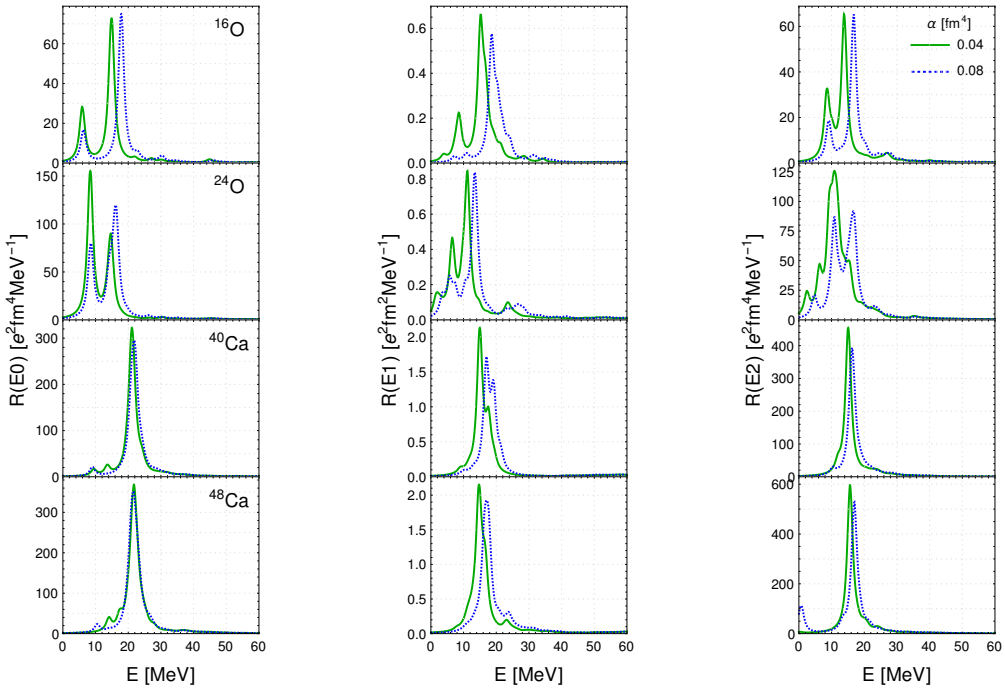

Figure 10.10: Electric ISM (left), IVD (middle) and ISQ (right) response of oxygen and calcium isotopes for different SRG flow parameters $\alpha = 0.04$ fm^4 (——) and $\alpha = 0.08$ fm^4 (·····). The choice of E_{2p2hMax} is the same as in Fig. 10.9.

In summary, we find a similar pattern as for HF-SRPA. The inclusion of 2p2h excitations is crucial for the description of transition strengths. The convergence behavior with respect to the model-space size e_{max} and the oscillator frequency $\hbar\Omega$ improves when going to NAT-SRPA. For ^{16}O, the transition strengths tend to be independent of $\hbar\Omega$. The SRG flow parameter is again an exception, since it is not a truncation parameter of the type, for which a larger value corresponds to a larger model space and where we could, thus, expect an improvement.

10.3 IM-SRPA

For first-order RPA calculations we found a similar convergence behavior and structure of the transition strengths for IM-HF and IM-NAT matrix elements. Now we focus on the second-order IM-HF and IM-NAT calculations and investigate the model-space convergence.

First, the number of 2p2h excitations is analyzed. In Fig. 10.11, the cumulative number of 2p2h states of the ISM, IVD, and ISQ response of ^{16}O and ^{40}Ca is shown. On the left-hand side, the HF- and IM-HF cases are compared, whereas the right-hand side contrasts NAT and IM-NAT results. As for first-order RPA, the cumulative number of 2p2h states is equal for the standard and in-medium SRPA for sufficient large SRPA model spaces. The excitation energy at which the 2p2h states appear differs for the standard and in-medium SRPA about 20 MeV for HF and about 15 MeV for NAT. In Fig. 10.12, the isoscalar monopole transition strengths of the oxygen isotopes obtained within IM-NAT-SRPA is illustrated for different SRPA model-space sizes. The transition strengths are converged with respect to the two largest model-space truncations. For smaller E_{2p2hMax}, the responses are shifted to larger energies.

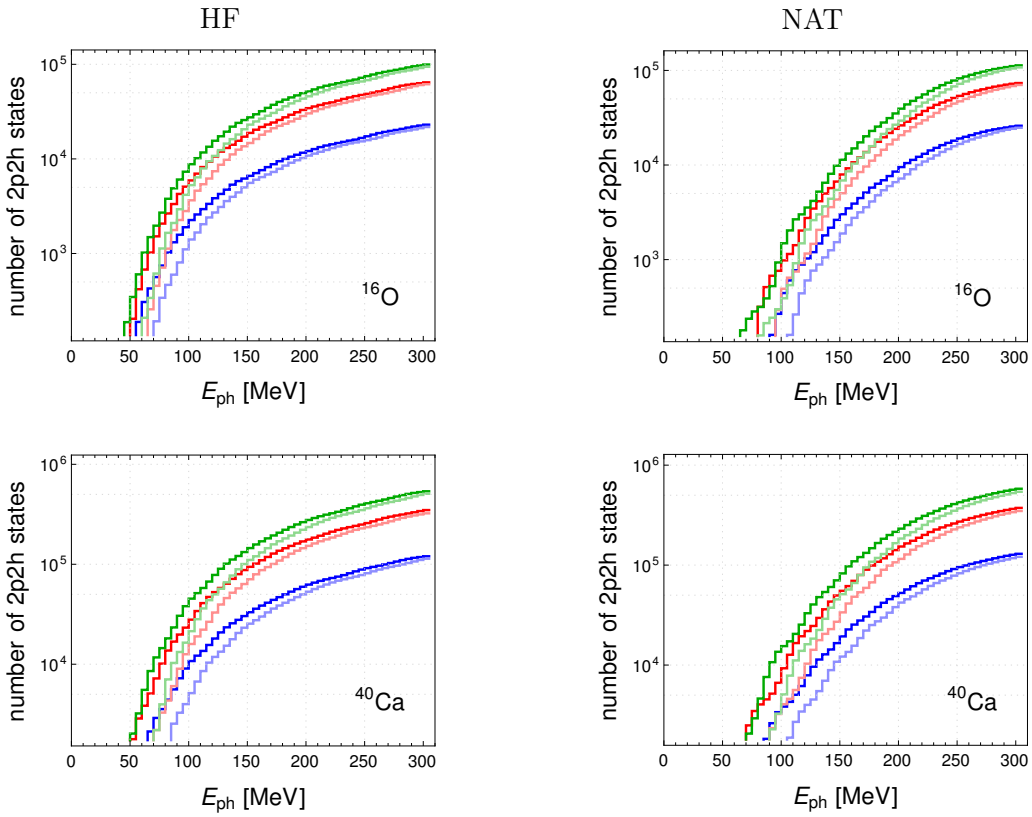

Figure 10.11: Cumulative number of 2p2h states of the ISM (——), IVD (——) and ISQ (——) strength distributions depending on the excitation energy threshold for ^{16}O (above) and ^{40}Ca (below). The left column compares the number of 2p2h excitations for HF and IM-HF matrix elements, whereas the right column shows the results obtained for NAT and IM-NAT matrix elements. The more transparent lines represent the IM results.

In order to reduce computational time of more than 24h, we choose $E_{\text{2p2hMax}} = 150$ MeV (200 MeV) for oxygen and $E_{\text{2p2hMax}} = 100$ MeV (130 MeV) for calcium isotopes within IM-HF-SRPA (IM-NAT-SRPA), if not stated otherwise.

The discussion of convergence with respect to characteristic parameters includes a variation of the oscillator frequency, the single-particle truncation and the SRG flow parameter.

Oscillator Frequency Dependence The oscillator frequency dependence of the ISM, IVD, and ISQ transition strengths is shown in Fig. 10.13. We investigate the influence of $\hbar\Omega = 16$ MeV (——), $\hbar\Omega = 20$ MeV (·····), and $\hbar\Omega = 24$ MeV (- - - -) on the response obtained with IM-HF-SRPA (above) and IM-NAT-SRPA (below). The overall structure is similar to the already discussed single-particle bases and different orders of RPA. For larger oscillator frequencies, the transition strengths are shifted higher energies. The shift is largest for the ISM response of ^{24}O and the calcium isotopes. For the IVD and ISQ response of both calcium isotopes, the difference between the transition strengths with $\hbar\Omega = 16$ MeV and $\hbar\Omega = 20$ MeV is smaller than between one of them and $\hbar\Omega = 24$ MeV. This can be observed for the results of both in-medium approaches. The ISQ response of ^{16}O is particularly remarkable. While for the results obtained with IM-HF-SRPA, the strength distributions are almost converged with respect to the oscillator frequency, the ones obtained with IM-NAT-SRPA lie exactly on top of each other. The only differences between both in-medium approaches can be found in the detailed structure of the transition strengths. Especially for the ISM response of all nuclei,

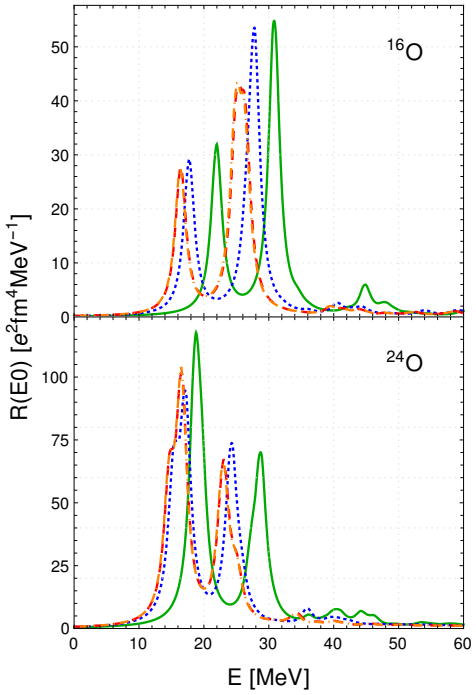

Figure 10.12: Isoscalar monopole response of oxygen isotopes, obtained with IM-NAT-SRPA, for different SRPA model-space truncations $E_{\mathrm{2p2hMax}} = \{100\ (\text{——}), 150\ (\cdots\cdots), 200\ (\text{- - -}), 250\ (\text{-·-·-})\}$.

the transition strengths obtained with IM-NAT-SRPA leads to more pronounced peaks than the HF counterpart.

Single-Particle Truncation In Fig. 10.14, the ISM, IVD, and ISQ transition strengths is illustrated for a single-particle truncation of $e_{\mathrm{max}} = 12$ (——) and $e_{\mathrm{max}} = 14$ (⋯⋯). We compare the results obtained with IM-HF-SRPA (above) with the ones from IM-NAT-SRPA (below). Note that the SRG flow parameter is $\alpha = 0.04$ fm^4. For the ISQ mode of ^{24}O obtained in IM-NAT-SRPA, we use with $E_{\mathrm{2p2hMax}} = 150$ MeV a smaller SRPA model-space size than for the other oxygen isotopes and transition types due to computational time limits. The calculation for $e_{\mathrm{max}} = 12$ is still feasible within 24h, but for the larger model space, more computational time is needed. In order to allow a comparison between both transition strengths, we compare them while applying the same SRPA model-space truncation. The smaller SRPA model space leads to a shift of the transitions strengths of a few MeV to larger energies according to Fig. 10.12. We observe a similar pattern as for the previous cases. The larger model-space size, indicated by $e_{\mathrm{max}} = 14$, shifts the transition strengths slightly to lower energies. This shift is only noticeable for the ISM response of ^{24}O and ^{48}Ca. All other transition strengths are converged with respect to the single-particle model space. This pertains to both in-medium approaches. As in the discussion of the oscillator frequency dependence mentioned, the transition strengths obtained in IM-NAT-SRPA exhibits more pronounced peaks. In particular, this is noticeable for the ISM response of both calcium isotopes, where the transition is more broadened with 3 peaks instead of one clear sharp peak for ^{40}Ca within IM-HF-SRPA. The broadening partially is an artifact of the smaller SRG flow parameter of $\alpha = 0.04$ fm^4, which is discussed in more detail in the next paragraph.

SRG Flow Parameter Dependence The convergence behavior with respect to the SRG flow parameter is shown in Fig. 10.15 for $\alpha = 0.04$ fm^4 (——) and $\alpha = 0.08$ fm^4 (⋯⋯).

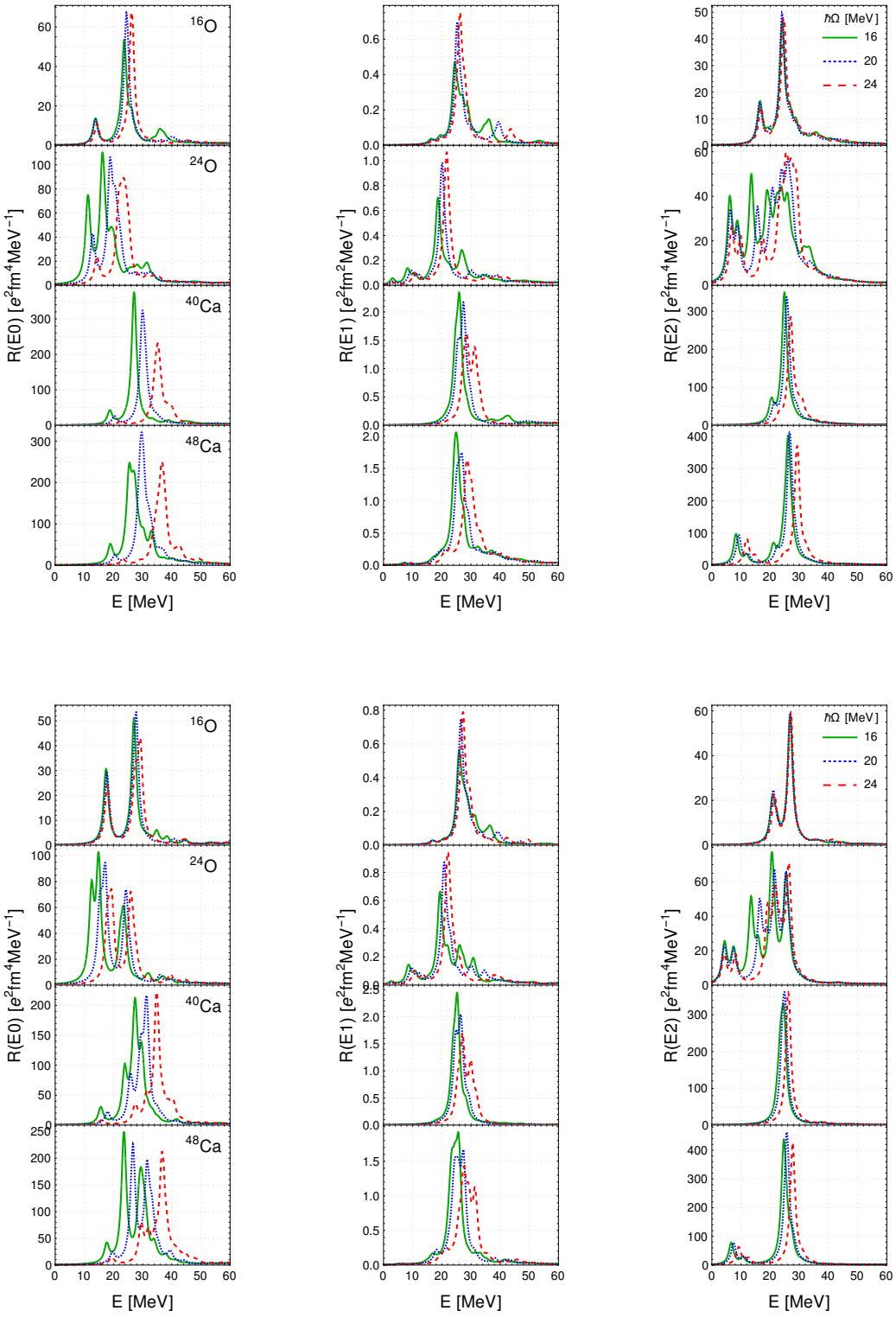

Figure 10.13: Electric ISM (left), IVD (middle) and ISQ (right) response of oxygen and calcium isotopes for different oscillator frequencies $\hbar\Omega = 16$ MeV (——), $\hbar\Omega = 20$ MeV (·····), and $\hbar\Omega = 24$ MeV (- - - -) obtained with IM-HF-SRPA (above) and IM-NAT-SRPA (below).

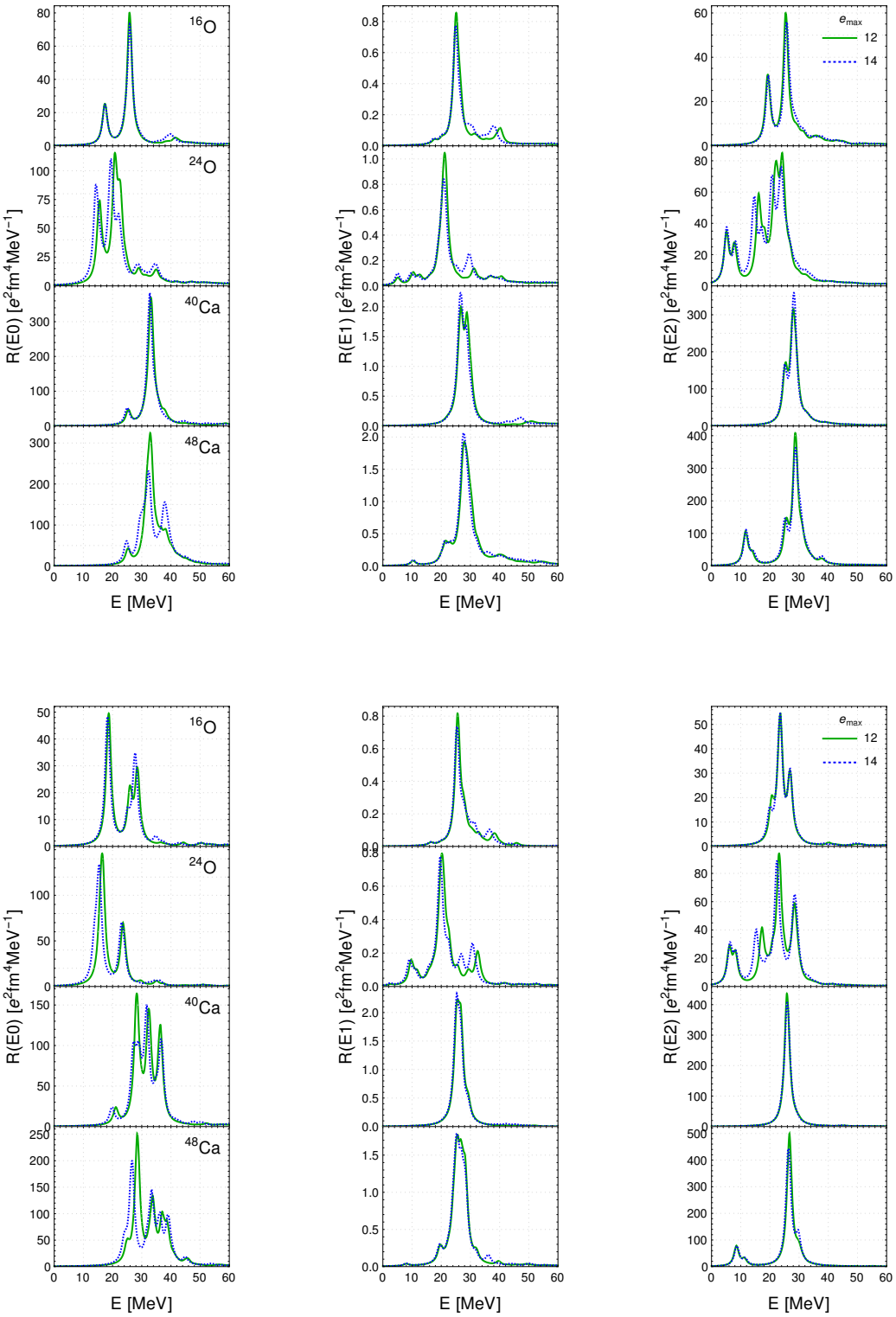

Figure 10.14: Electric ISM (left), IVD (middle) and ISQ (right) response of oxygen and calcium isotopes for different model-space truncations $e_{\max} = 12$ (——) and $e_{\max} = 14$ (·····) obtained with IM-HF-SRPA (above) and IM-NAT-SRPA (below). Here, we use an SRG flow parameter of $\alpha = 0.04$ fm^4.

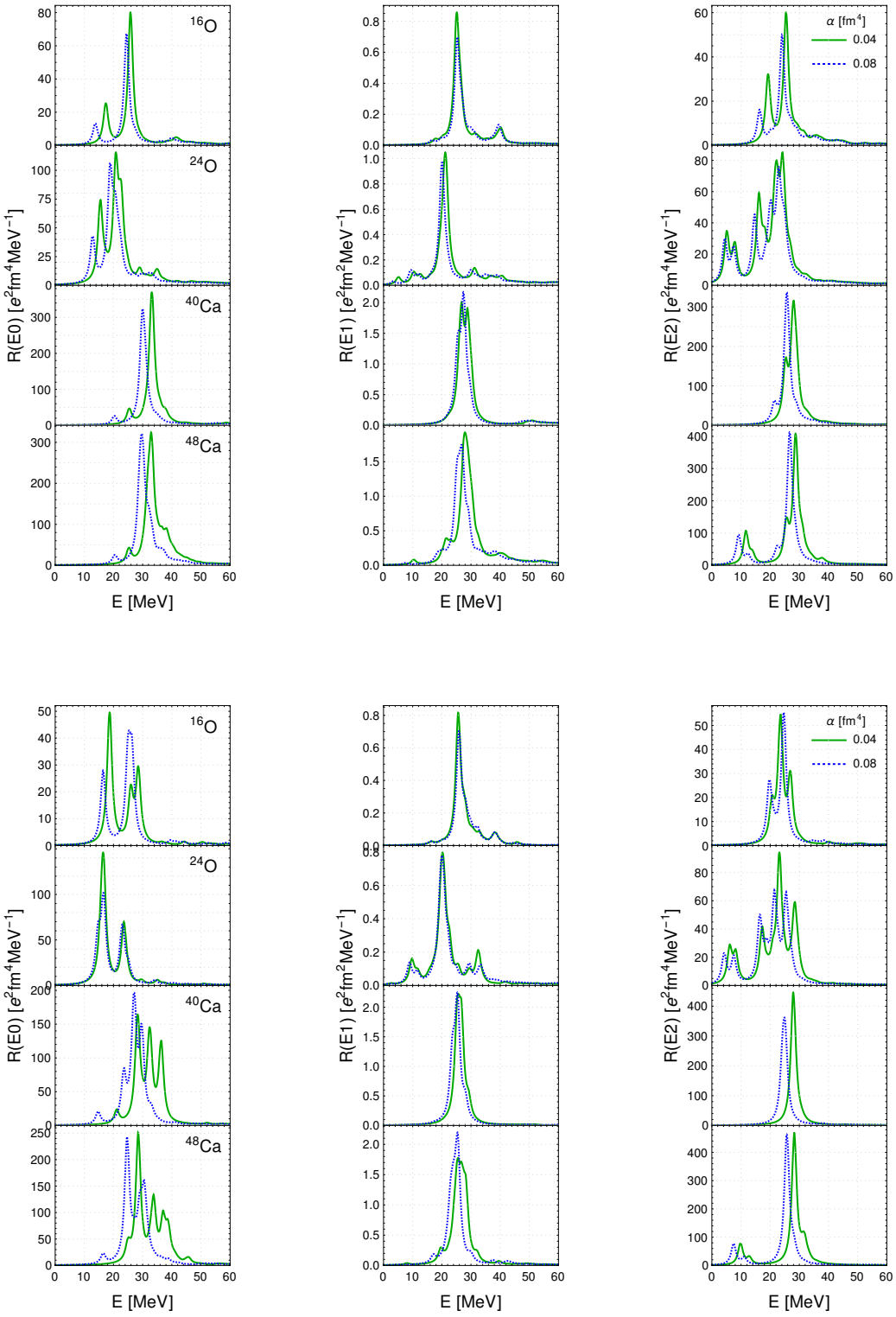

Figure 10.15: Electric ISM (left), IVD (middle) and ISQ (right) response of oxygen and calcium isotopes for different SRG flow parameters $\alpha = 0.04$ fm^4 (——) and $\alpha = 0.08$ fm^4 (·····) obtained with IM-HF-SRPA (above) and IM-NAT-SRPA (below).

The results obtained with the IM-HF-SRPA are shown above, whereas the IM-NAT-SRPA transition strengths are presented below. We choose $E_{\mathrm{2p2hMax}} = 150$ MeV for the ISQ response of ^{24}O based on IM-NAT-SRPA and $E_{\mathrm{2p2hMax}} = 130$ MeV for the ISQ response of both calcium isotopes. As observed in first-order IM-RPA, the transition strengths are shifted to lower energies for larger SRG flow parameters by a similar extent. Again, the detailed structure of the single transition strengths varies for both in-medium approaches. This is especially the case for the ISM response. For the IM-NAT-SRPA result of ^{16}O, we find two narrow peaks, which change their heights for the different SRG flow parameters, while the IM-HF-SRPA result exhibits one pronounced peak and one smaller peak at lower energies. Furthermore, the ISM response of both calcium isotopes obtained in IM-NAT-SRPA shows the aforementioned broadening for an SRG flow parameter of $\alpha = 0.04$ fm^4. For the larger flow parameter $\alpha = 0.08$ fm^4, the peaks are narrower than for $\alpha = 0.04$ fm^4, but still broadened in comparison with transition strengths from IM-HF-SRPA. In first-order IM-RPA, this phenomenon arises to a different extent. There, a second smaller peak emerges for the ISM response of ^{48}Ca, which is located close to the distinct peak.

10.4 Consistent Electromagnetic Operator

In the in-medium framework, the calculation of the strength distributions is inconsistent with respect to the electromagnetic operators, since we use an IM-SRG evolved Hamiltonian and, instead of IM-SRG evolved matrix elements of the electromagnetic operators, the corresponding HF matrix elements. In order to get rid of this inconsistency, non-scalar operators need to be IM-SRG evolved as well. This is part of current research. Furthermore, the transition strengths are calculated for a one-body operator so far. For a consistent description of IM-SRG evolved electromagnetic operators, the two-body operator (6.61) is required as well. First test calculations show a very small effect [97].

10.5 Comparison of Different Types of SRPA

Within this section, the results obtained with SRPA are compared for the different single-particle bases. Therefore, we first focus on the deviations obtained when going from first- to second-order RPA and afterwards on the difference between HF- and IM-HF-SRPA. Including second-order 2p2h excitations in the calculations leads to a pathological shift of the transition strengths to lower energies, as illustrated in Fig. 10.16. This pattern can be observed for all nuclei, transition types and different single-particle bases. Thus, the transition strengths based on NAT behave similarly to the HF results and, therefore, we do not show the results here. For the ISM response of ^{16}O, the strengths from first-order RPA are already in a good agreement with the experiment. An inclusion of second-order terms leads to a worsening compared to the experimental data. For the ISM response of the calcium isotopes, the SRPA results can describe the experimental data better than results from first-order RPA. For the ISQ mode, the RPA transition strengths tend to be at too high energies, while the SRPA predict transition strengths at too low energies compared to the experimental data.

Compared to experimental data, the RPA transition strengths tend to lie at too high energies. Thus, a shift in energy is desired in order to predict transition strengths that are comparable with the experiment. The energy shift of the transition strengths when going from RPA to SRPA is beneficial for this. However, the entire transition strengths are shifted, which includes the low-lying states as well as seen for ^{48}Ca in Fig. 10.16. Here, the low-lying states are shifted to negative excitation energies and, thus, yield nonphysical results. We are interested in the

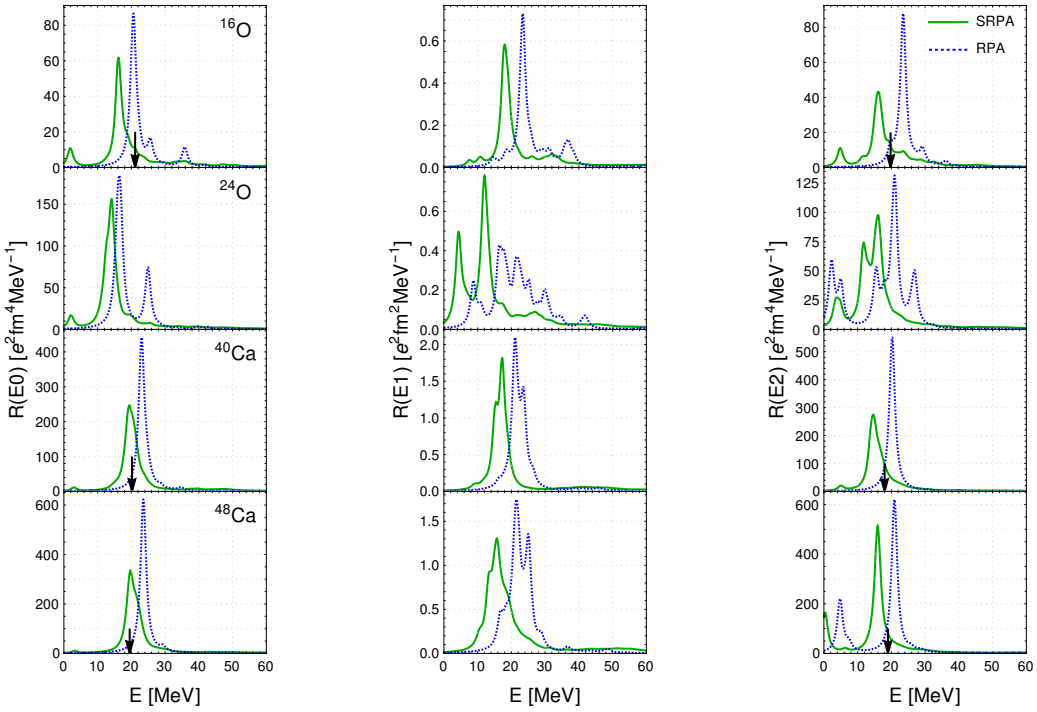

Figure 10.16: Electric ISM (left), IVD (middle) and ISQ (right) response of oxygen and calcium isotopes obtained by HF-RPA (·····) and HF-SRPA (——) calculations. The arrows indicate the experimental centroid energies.

region of the giant dipole resonance, but still, a negative connotation remains due to these instabilities [43, 45, 50, 63].

The reason for this lies in the construction of the HF ground state, which only includes 1p1h variations. However, the SRPA model space is extended to 2p2h states. Thus, the HF ground state is not stable against 2p2h variations For more information, we refer to Ref. [10].

In Fig. 10.17, the ISM, IVD, and ISQ response of oxygen and calcium isotopes, obtained by an HF-SRPA (——) and an IM-HF-SRPA (·····) calculation, is presented. For all transition types and nuclei, we observe a significant shift of the strengths towards higher transition energies. This is already known from first-order RPA (c.f. Sec. 9.4), where the reasons of the shift are discussed. Since the input of IM-SRG matrix elements is the same no matter if we perform a first- or second-order RPA calculation, the origin of the shift remains unaltered, since the appearance of 2p2h excitations shows the same pattern as for 1p1h states. Thus, we do not repeat this discussion here. Using IM-SRG matrix elements reduces the (S)RPA to an (S)TDA as discussed in Sec. 7.2. These missing correlations are an additional reason for the energy shift to higher energies. The instabilities, which occur when going from RPA to SRPA and which are given in the pathological shift of the transition strengths to lower energies, are removed when including IM-SRG matrix elements due to the decoupling of the reference state from its ph excitations within the IM-SRG.

We emphasize that the transitions strengths are not yet fully converged with respect to the SRPA model space which causes an energy shift of about 8 MeV, especially for the calcium isotopes.

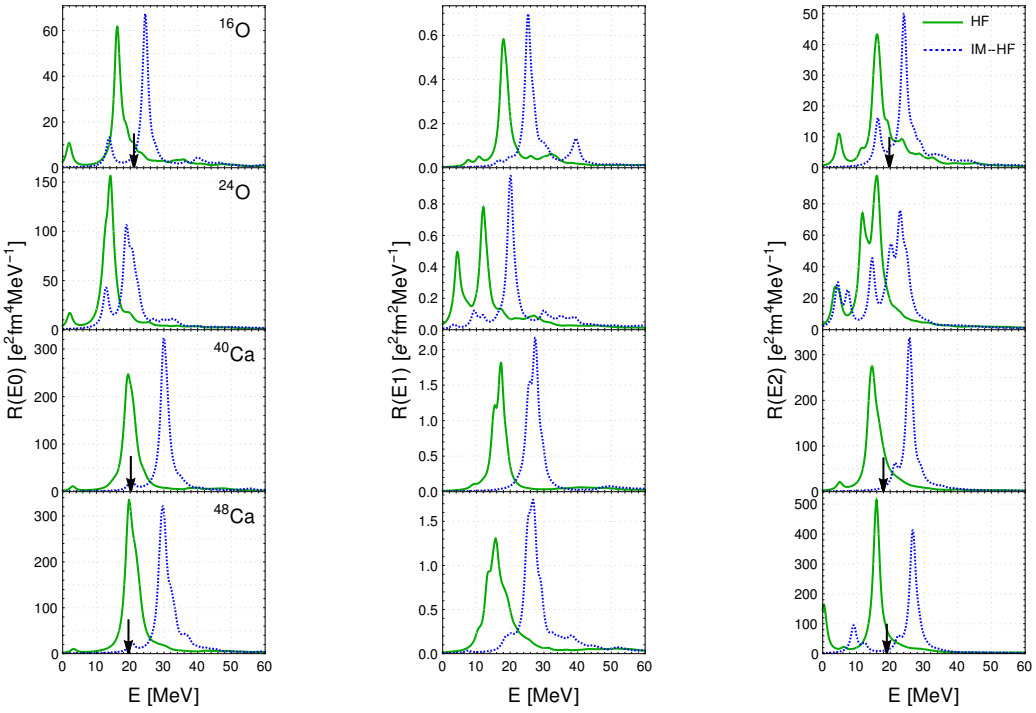

Figure 10.17: Electric ISM (left), IVD (middle) and ISQ (right) response of oxygen and calcium isotopes obtained by HF-SRPA (——) and IM-HF-SRPA (·····) calculations. The arrows indicate the experimental centroid energies.

11

Lanczos Strength Functions

Contents

In this chapter, collective excitations and their transition strengths are investigated by utilizing the Lanczos strength function method in combination with the IT-NCSM. First, the Lanczos model-space convergence is examined regarding the number of Lanczos iterations. Afterwards, we present and discuss the electric monopole and quadrupole response for different even-mass helium and oxygen isotopes and investigate the model-space convergence by considering different truncation parameters, single-particle bases and interactions.

11.1 Lanczos Iterations

First, we study the Lanczos model-space convergence of the electric isoscalar monopole strength function for ^{16}O. For this investigation, we start with a standard set of parameters: The underlying chiral interaction at N^{3}LO in the NO2B approximation is SRG-evolved with $\alpha = 0.08$ fm^4. We use natural orbitals as a single-particle basis. The model space is truncated at $e_{\max} = 12$, $l_{\max} = 8$, and the oscillator frequency is given by $\hbar\Omega = 20$ MeV. The center-of-mass control parameter is set to $\beta = 0.5$ and the 3N matrix elements are cut at $E_{3\max} = 14$. For the IT-NCSM calculation, we use the importance threshold $\kappa_{\min} = 3 \cdot 10^{-5}$ and truncate the model space at $N_{\max} = 8$ for natural-parity states. The width of the Lorentzian function is $\Gamma = 1$ MeV.

In Fig. 11.1, the dependence of the discrete ISM strength distribution of ^{16}O on the number of Lanczos iterations is shown. The strength functions are obtained in the NAT basis with the above truncation parameters. Two points are remarkable: First, the discrete strength functions converge fast with respect to the Lanczos iterations. After 500 Lanczos vectors (LV), no obvious changes are perceptible. Second, the convergence occurs step by step, starting with low-lying excited states in accordance with the Lanczos algorithm. This is beneficial, since the region of interest includes energies up to about 60 MeV. Figure 11.2 illustrates the convergence behavior of the smoothed-out ISM strength distributions of different oxygen isotopes for a set of Lanczos iterations LV = {50(——), 200(——), 400(- - - -), 1000(·····)}. Here, the discrete strength functions are convolved with a Lorentzian of width $\Gamma = 1$ MeV. For 50 Lanczos iterations, the strength functions are not yet fully converged and slightly deviate in the energy regime at about 40 MeV and higher compared to the strength distributions obtained with a larger number of Lanczos iterations. All other smoothed-out strength functions for the considered Lanczos iterations are indistinguishable. Thus, the choice of a few hundred Lanczos iterations is sufficient for a complete convergence of the strength functions.

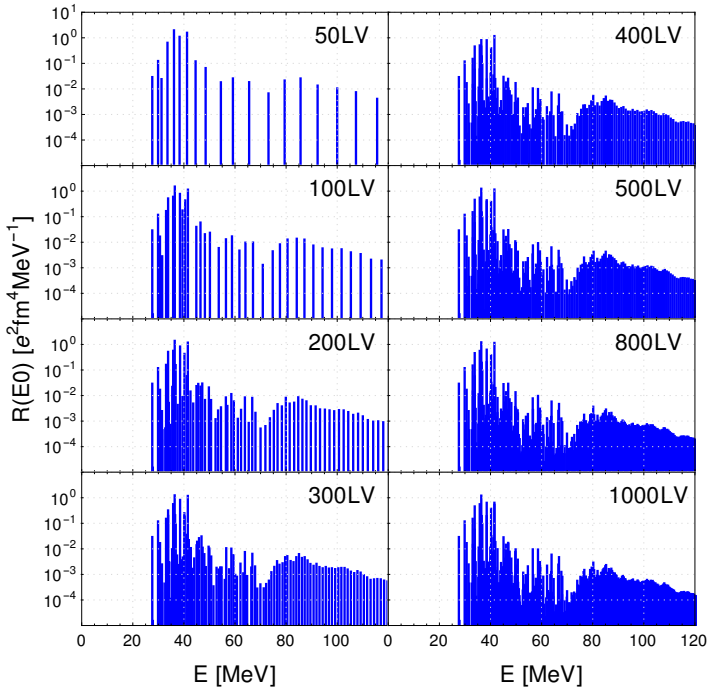

Figure 11.1: Discrete ISM strength functions of ^{16}O for different number of Lanczos vectors (LV).

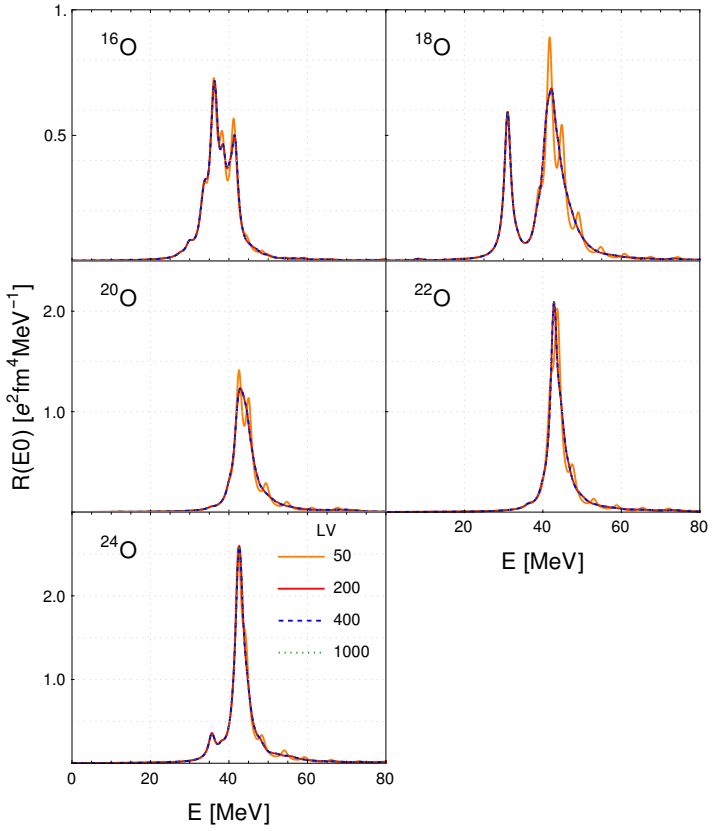

Figure 11.2: Smoothed-out ISM strength distributions of $^{16-24}$O for different number of Lanczos vectors LV = {50(——), 200(——), 400(- - - -), 1000(·····)}.

11.2 Lanczos Strength Functions for Selected Isotopes

In the following section, the electric monopole and quadrupole Lanczos strength functions of helium and oxygen isotopes are examined. First, we study the model-space convergence. This includes, besides the number of Lanczos iterations, different truncation parameters within the IT-NCSM and of the underlying single-particle bases. For the investigation, we start with a standard set of parameters: The underlying chiral interaction at N^3LO in NO2B approximation is SRG-evolved with $\alpha = 0.08$ fm^4. If not stated otherwise, the model space is truncated at $e_{\max} = 12$, $l_{\max} = 8$, and oscillator frequency $\hbar\Omega = 20$ MeV. The center-of-mass control parameter is chosen to $\beta = 0.5$ and the 3N matrix elements are cut at $E_{3\max} = 14$. For the IT-NCSM calculation, we use the importance threshold $\kappa_{\min} = 3 \cdot 10^{-5}$ and truncate the model space at $N_{\max} = 8$ for natural-parity states. We utilize natural orbitals as single-particle basis. The number of Lanczos iterations is set to 400 and the width of the Lorentzian function is $\Gamma = 1$ MeV. In the following section, we change some of these parameters systematically for the convergence discussion. Note, that we do not calculate the electric isovector dipole response since this is computationally more challenging, due to the need for unnatural-parity states.

11.2.1 Helium

First, we focus on helium isotopes. The discrete strength distributions of the helium isotopes are depicted in Fig. 11.3, where we compare two different interactions. The upper panels present the results obtained by utilizing the non-local chiral interaction by Hüther [85] (——). For the ISM response of ^{4}He, one single transition is responsible for the strong peaks. This is also the case for the low-lying states of the responses of ^{6}He and ^{8}He. Comparing the nuclei and response types, we observe more fragmentation in the giant resonance region for ^{6}He and ^{8}He. Furthermore, the dominant peak in the ISM response of ^{4}He is shifted to lower energies when increasing the number of neutrons and, thus, going to the other isotopes.

The transition strengths in the lower panels are obtained by employing the N^2LO_{sat} interaction (——). In general, both interactions leads to comparable fragmentation and fine structure. However, they slightly differ in the peak position of the low-lying discrete strengths and in some peak heights, which causes slightly shifted smeared-out strength distributions. Especially, this can be observed for the dominant peak of the ISM response of ^{8}He.

With these considerations, we now vary some parameters in order to investigate the convergence behavior.

Model-Space Truncation In Fig. 11.4, the influence of the model-space truncation $N_{\max}$ on the strength functions is shown. We compare the ISM and ISQ response for $N_{\max} = 4$ (----), $N_{\max} = 6$ (·····), and $N_{\max} = 8$ (——). We observe a systematic downward energy shift with increasing model-space size for all isotopes and transition modes, which is larger for the comparison of $N_{\max} = 4$ and $N_{\max} = 6$ than for the comparison of $N_{\max} = 6$ and $N_{\max} = 8$. For the smallest model spaces, the energy shift amounts to about 10 MeV and for the larger model spaces to about 5 MeV. The detailed structure of the strength functions between both model-space sizes is comparable. In contrast to the ISM response, the ISQ counterpart has two dominant peaks. The low-lying ISQ transition strengths represent an exception in the overall convergence behavior, since they tend to be robust against the variation of $N_{\max}$. It converges quickly, since it is a simple ph-type excitation and, thus, non-collective.

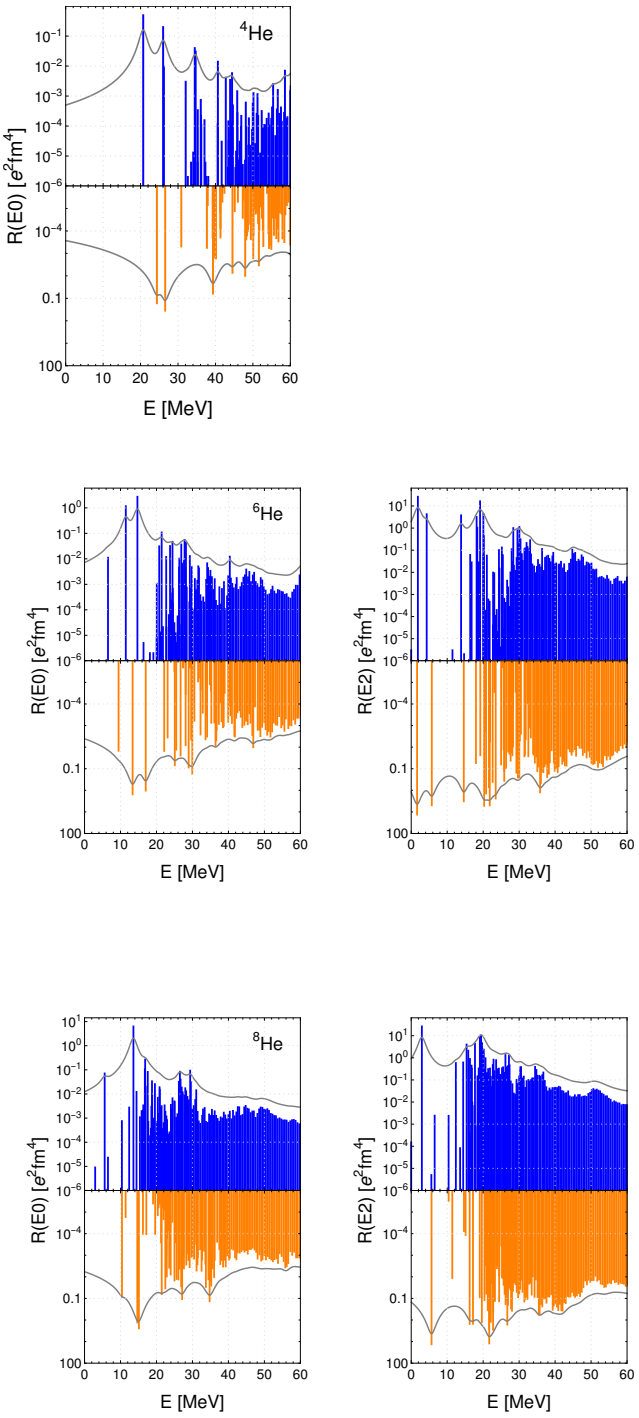

Figure 11.3: Discrete electric ISM (left) and ISQ (right) transition strengths of even-mass helium isotopes $^{4-8}$He obtained in the IT-NCSM by using the non-local chiral interaction by Hüther [85] (——) and N^{2}LO$_{\rm sat}$ interaction (——). The model-space truncation amounts to $N_{\rm max} = 6$. We employ the HF single-particle basis and a SRG flow parameter of $\alpha = 0.04$ fm^4.

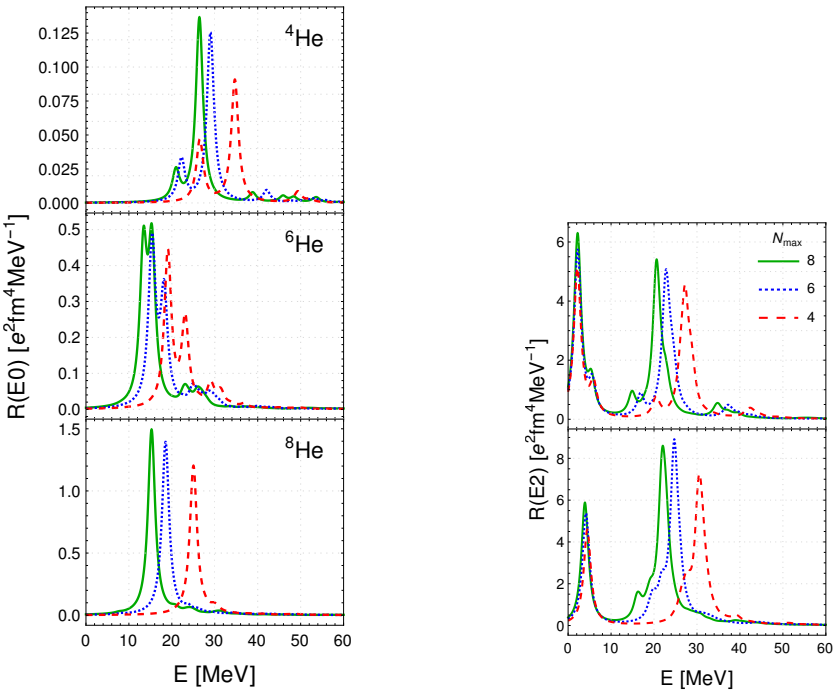

Figure 11.4: Electric ISM (left) and ISQ (right) transition strengths of even-mass helium isotopes $^{4-8}$He for different model-space truncations $N_{\max} = \{4(\text{- - -}), 6(\cdots\cdots), 8(\text{———})\}$. We employ the NAT basis.

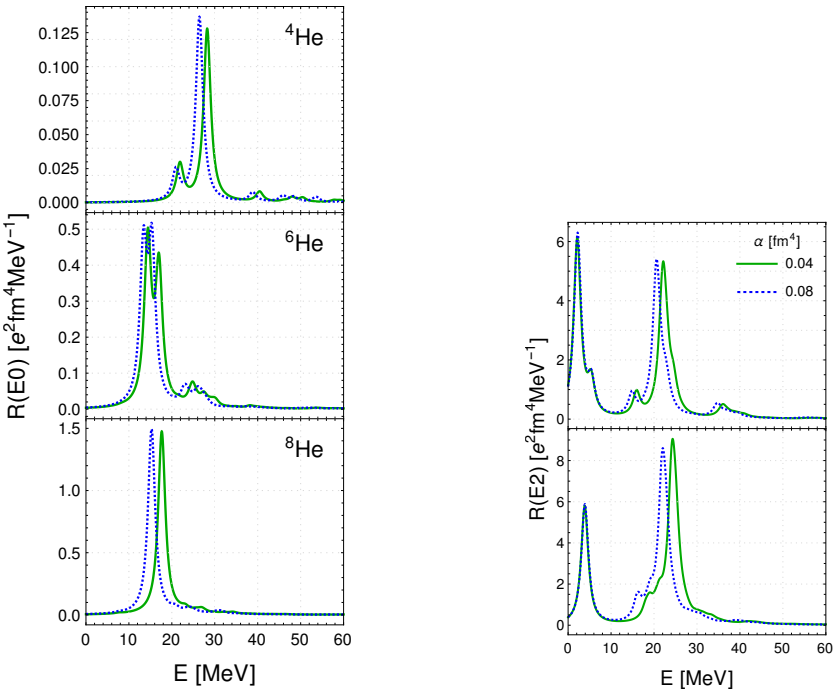

Figure 11.5: Electric ISM (left) and ISQ (right) transition strengths of even-mass helium isotopes $^{4-8}$He for different SRG flow parameters $\alpha = 0.04$ fm^4 (———) and $\alpha = 0.08$ fm^4 ($\cdots\cdots$). We employ the NAT basis.

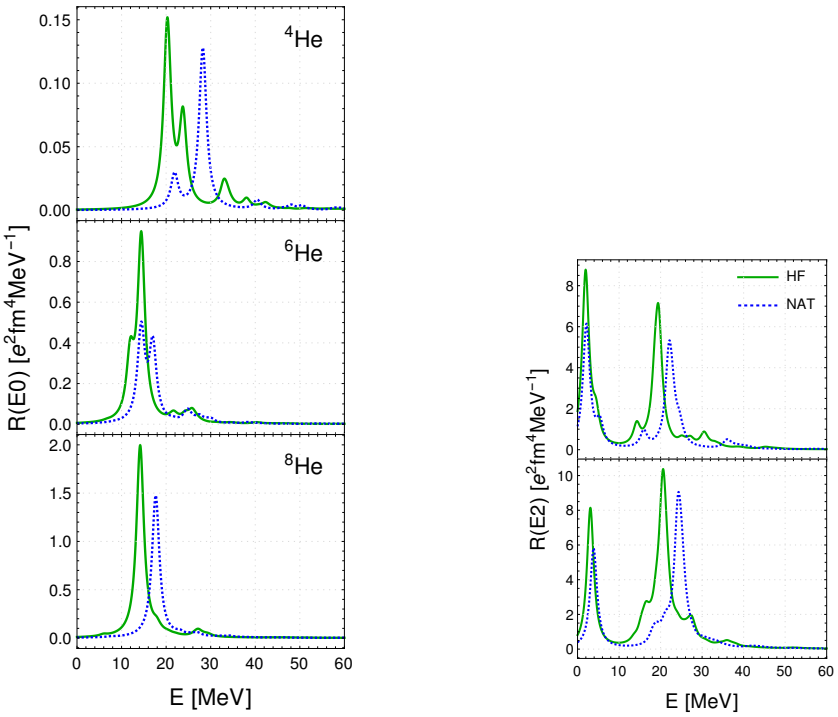

Figure 11.6: Electric ISM (left) and ISQ (right) transition strengths of even-mass helium isotopes $^{4-8}$He obtained in the IT-NCSM with HF basis (——) and natural orbitals (·····). Here, we use an SRG flow parameter of $\alpha = 0.04$ fm^4.

SRG Flow Parameter Dependence The influence of the SRG flow parameter on the ISM and ISQ response is illustrated in Fig. 11.5. For a softer Hamiltonian, which corresponds to $\alpha = 0.08$ fm^4 (·····), the transition strengths are slightly shifted to lower energies compared to the ones obtained with $\alpha = 0.04$ fm^4 (——). The detailed structure of the strength distributions remains unaltered. Again, the low-lying states of the ISQ responses tend to be robust against a variation of the flow parameter. The energy shift is smaller than for different model-space trunactions $N_{\max}$.

Single-Particle Basis As in the RPA framework, the Lanczos strength functions can be calculated based on different single-particle bases. In Fig. 11.6, the ISM and ISQ response based on HF (——) and NAT (·····) are depicted. Here, we use an SRG flow parameter of $\alpha = 0.04$ fm^4. The transition strengths based on HF are pushed to lower energies compared to the one based on NAT. The shift amounts to about 5 MeV. The low-lying states are almost unaffected by a change of the single-particle basis. The NAT excitation energies are unrealistically large.

11.2.2 Oxygen

As another interesting isotopic chain, the oxygen isotopes from ^{16}O to the neutron-rich ^{22,24}O are examined in the following section. In Fig. 11.7, the discrete ISM and ISQ strengths functions are illustrated for calculations based on the non-local chiral interaction by Hüther [85] (——) and N^{2}LO$_{\text{sat}}$ interaction (——) in the HF basis. The dominant peak of the low-lying ISM response of ^{18}O and ^{20}O is caused by one single transition. This is also the case for the low-lying ISQ response of the more neutron-rich isotopes and holds for both interactions.

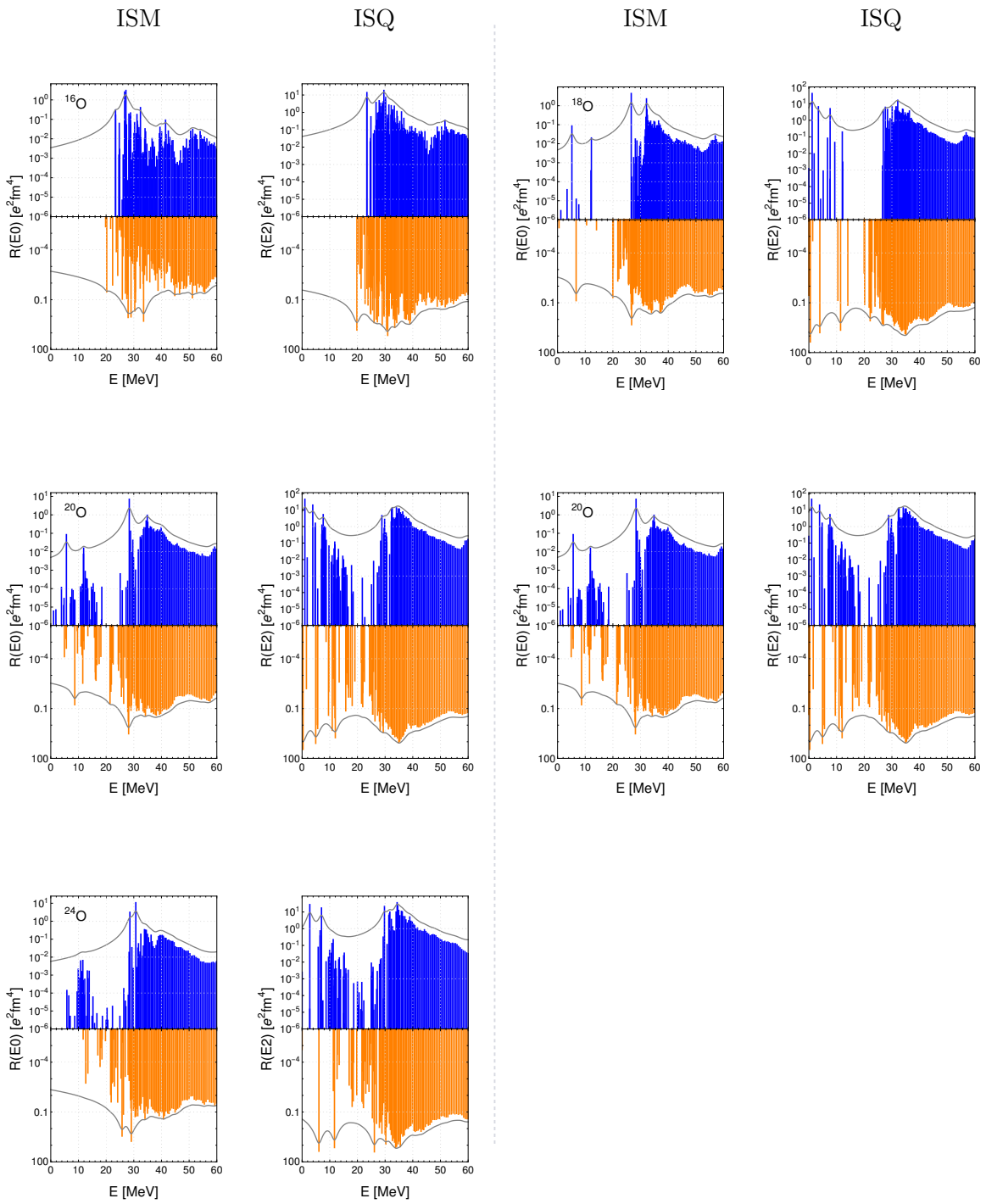

Figure 11.7: Discrete electric ISM (left) and ISQ (right) transition strengths of even-mass oxygen isotopes $^{16-24}$O obtained in the IT-NCSM by using the non-local chiral interaction by Hüther [85] (——) and N^{2}LO$_{\rm sat}$ interaction (——). The model-space truncation amounts to $N_{\rm max} = 6$. We employ the HF single-particle basis and a SRG flow parameter of $\alpha = 0.04$ fm^4.

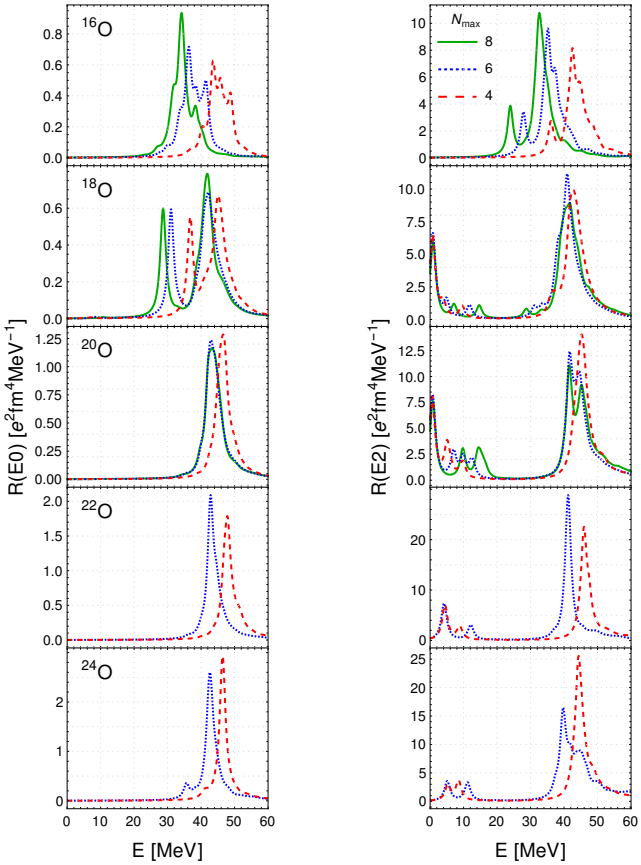

Figure 11.8: Electric ISM (left) and ISQ (right) transition strengths of even-mass oxygen isotopes $^{16-24}$O for different model-space truncations $N_{\max} = \{4(\text{- - -}), 6(\cdots\cdots), 8(\text{———})\}$. We employ the NAT basis.

Adding more neutrons leads to a result that exhibits more fragmentation and fine structure. We observe a shift in energy when comparing the N^{2}LO$_{\text{sat}}$ with the non-local interaction. This includes the discrete strengths and, thus, affects the smeared-out strengths distributions as well. Comparing with experimental data, both interactions tend to predict the centroid energies too high.

Model-Space Truncation The model-space convergence with respect to $N_{\max}$ is shown in Fig. 11.8. Up to mid-shell at ^{20}O, the ISM and ISQ response are compared for $N_{\max} = 4$ (- - -), $N_{\max} = 6$ ($\cdots\cdots$) and $N_{\max} = 8$ (———). For the more neutron-rich isotopes, only the results for smaller model-space truncations are presented due to the increased computational effort. The strength distributions are pushed to lower transition energies for larger model-space sizes. For ^{20}O, the transition strengths tend to be converged.

SRG Flow Parameter Dependence The transition strengths of an IT-NCSM for different SRG flow parameters $\alpha = 0.04$ fm^4 (———) and $\alpha = 0.08$ fm^4 ($\cdots\cdots$) are depicted in Fig. 11.9. The larger flow parameter, which corresponds to a softer Hamiltonian, shifts the ISM and ISQ response to lower energies. The low-lying states tend to be robust against the variation.

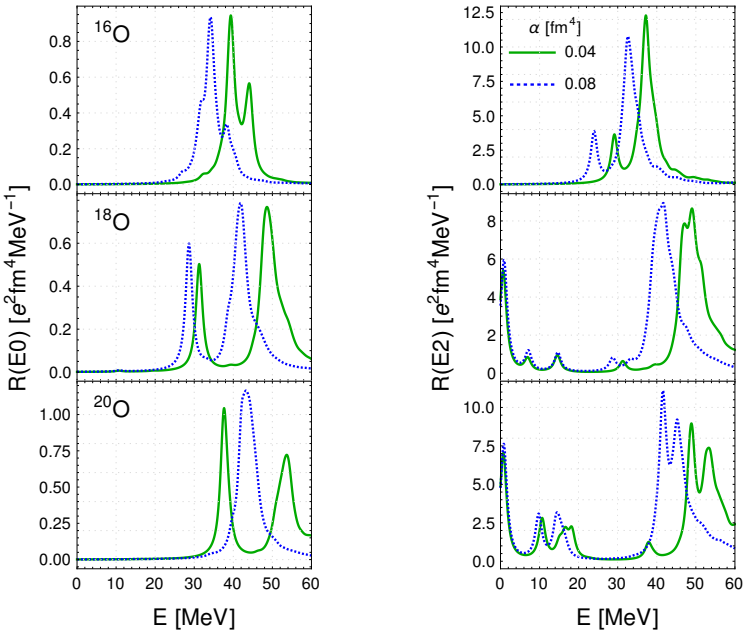

Figure 11.9: Electric ISM (left) and ISQ (right) transition strengths of even-mass oxygen isotopes $^{16-20}$O for different SRG flow parameters $\alpha = 0.04$ fm^4 (——) and $\alpha = 0.08$ fm^4 (·····). We employ the NAT basis.

The shift is more pronounced for isotopes with more neutrons. In contrast to the helium isotopes, where the transition strengths are almost converged with respect to α, the energy for the oxygen isotopes amounts to about 10 MeV.

Single-Particle Basis The comparison of Lanczos strength function calculations based on HF (——) and NAT (·····) is shown in Fig. 11.10. The transition strengths obtained with HF are located at significantly lower energies. The detailed structure varies as well. One reason for that lies in the choice of the SRG flow parameter. Here, we compare HF and NAT results for $\alpha = 0.04$ fm^4, which deviates in the convergence pattern as discussed before. The behavior of the transition strengths with respect to different single-particle bases is worse than for the helium isotopes. The results obtained with the HF single-particle basis tend to predict centroid energies that are in better agreement with experimental data.

In conclusion, the NAT basis produces transition strengths at unreasonably high energies and does not seem to perform well, i.e., converge well for highly excited states. This was observed within the RPA framework as well. As mentioned before, previous studies in Ref. [81] has shown that the natural orbitals are a good choice for ground-state properties of nuclei. The problems observed for collective excitations appear due to the inclusion of higher-lying orbitals of the NAT basis.

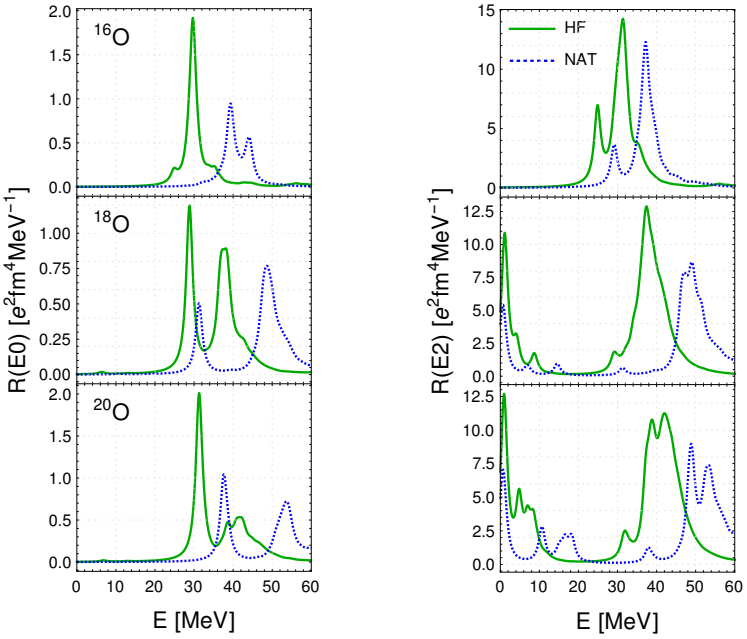

Figure 11.10: Electric ISM (left) and ISQ (right) transition strengths of even-mass oxygen isotopes $^{16-24}$O obtained in the IT-NCSM with HF basis (——) and natural orbitals (·····). Here, we use a SRG flow parameter of $\alpha = 0.04$ fm^4.

12

Uncertainty Quantification

Contents

In *ab initio* nuclear structure theory, interactions based on chiral EFT are used as a starting point for the calculation of several properties of nuclei. The systematic low-momentum expansion within chiral EFT allows for a systematic improvement of the interaction. Additionally, this can be an opportunity for a theoretical uncertainty estimation for observables. An approach for this estimation based on the chiral expansion uses Bayesian statistics to quantify a degree-of-believe interval. This Bayesian model of chiral interaction uncertainties is introduced in this chapter, following Refs. [80, 82], and the application to collective excitations is discussed.

12.1 Bayesian Model of Chiral Interaction Uncertainties

We assume that any observable X based on chiral EFT interactions can be expanded in terms of the momentum scale Q^n with the chiral order $n = 0, 2, 3, 4, ...$

$$\begin{aligned} X &= X^{(0)} + \Delta X^{(2)} + \Delta X^{(3)} + \dots \\ &= X_{\text{ref}} \left(c_0 + c_2 Q^2 + c_3 Q^3 + \dots \right) \\ &= X_{\text{ref}} \sum_{n=0}^{m} c_n \cdot Q^n \end{aligned} \tag{12.1}$$

with $\Delta X^{(2)} = X^{(2)} - X^{(0)}$ and $\Delta X^{(n)} = X^{(n)} - X^{(n-1)}$ for $n > 2$ and dimensionless coefficients c_n. The reference value

$$X_{\text{ref}} = X^{(0)} \tag{12.2}$$

is set as leading-order contribution. In this case, the zeroth coefficient yields $c_0 = 1$. The chiral expansion parameter is the ratio of the typical momentum scale and the chiral breakdown scale and is selected to be $Q \approx \frac{1}{3}$. Each correction $\Delta X^{(n)}$ is suppressed by the chiral EFT order Q^n.

We now assume that the observable values $\{X^{(0)}, X^{(2)}, ..., X^{(k)}\}$ are known up to k-th order with $k \geq 2$. The uncertainty estimation is then achieved by summing over all neglected higher-order terms

$$\delta X^{(k)} = \sum_{n>k} \Delta X^{(n)}. \tag{12.3}$$

Formally, a posterior probability distribution function (pdf) for $\delta X^{(k)}$ is calculated with the help of the known observable results $X^{(k)}$ up to k-th order.

Following Ref. [82], we assume that the unknown coefficients c_n for $n > k$ are distributed as Gaussian prior probability distribution function (pdf)

$$\text{pr}(c_n|\bar{c}) = \frac{1}{\sqrt{2\pi}\bar{c}} e^{c_n^2/(2\bar{c}^2)} \tag{12.4}$$

with hyperparameter $\bar{c}$. Furthermore, we make the assumption that the chiral orders up to h with $h > k$ are responsible for the major truncation error while higher chiral orders play a

less important role

$$\Delta_k = \sum_{m=k+1}^{\infty} c_m Q^m \simeq \sum_{m=k+1}^{k+h} c_m Q^m. \tag{12.5}$$

The general posterior pdf $\mathrm{pr}_h(\Delta|\{c_{n\leq k}\})$ is obtained by applying Bayes' theorem for $\Delta_k = \Delta$, leading to

$$\mathrm{pr}_h(\Delta|\{c_{n\leq k}\}) = \frac{\int_0^\infty d\bar{c}\, \mathrm{pr}_h(\Delta|\bar{c})\mathrm{pr}(\bar{c}) \prod_{n\in A} \mathrm{pr}(c_n|\bar{c})}{\int_0^\infty d\bar{c}\, \prod_{n\in A} \mathrm{pr}(c_n|\bar{c})} \tag{12.6}$$

with the set $A = \{m \in \mathbb{N}_0 | m \leq k \wedge m \neq 1 \wedge m \neq i\}$ and the probability distribution

$$\mathrm{pr}_h(\Delta|\bar{c}) = \left[\prod_{n=k+1}^{k+h} \int_\infty^\infty dc_n \mathrm{pr}(c_n|\bar{c})\right] \delta\left(\Delta - \sum_{j=k+1}^{k+h} c_j Q^j\right). \tag{12.7}$$

For the Gaussian prior pdf (12.4) and an assumed log-uniform probability distribution

$$\mathrm{pr}(\bar{c}) = \frac{1}{\ln(\bar{c}_>/\bar{c}_<)} \frac{1}{\bar{c}} \theta(\bar{c} - \bar{c}_<)\theta(\bar{c}_> - \bar{c}), \tag{12.8}$$

the posterior pdf (12.6) can be simplified to

$$\mathrm{pr}_h(\Delta|\{c_{n\leq k}\}) = \frac{1}{\sqrt{\pi \bar{q} c_k^2}} \left(\frac{c_k^2}{c_k^2 + \Delta^2/\bar{q}^2}\right)^{k/2} \frac{\Gamma\left[\frac{k}{2}, \frac{1}{2\bar{c}_>^2}\left(c_k^2 + \frac{\Delta^2}{\bar{q}^2}\right)\right] - \Gamma\left[\frac{k}{2}, \frac{1}{2\bar{c}_<^2}\left(c_k^2 + \frac{\Delta^2}{\bar{q}^2}\right)\right]}{\Gamma\left[\frac{k-1}{2}, \frac{c_k^2}{2\bar{c}_>^2}\right] - \Gamma\left[\frac{k-1}{2}, \frac{c_k^2}{2\bar{c}_<^2}\right]}, \tag{12.9}$$

since an analytical integration is possible. Here, the momentum scale is $\bar{q}^2 = \sum_{n=k+1}^{k+h} Q^{2n}$, the coefficients are given by $c_k^2 = \sum_{n\in A} c_n^2$, and the incomplete gamma function

$$\Gamma(s, x) = \int_x^\infty dt\, t^{s-1} e^{-t} \tag{12.10}$$

is applied. The posterior pdf can be further summarized by assuming a noninformative prior C with $\bar{c}_< = \epsilon$ and $\bar{c}_> = \frac{1}{\epsilon}$ within the limit $\epsilon \to 0$ for $c_k^2 \neq 0$, which yields

$$\mathrm{pr}_h(\Delta|\{c_{n\leq k}\}) = \frac{1}{\sqrt{\pi \bar{q} c_k^2}} \frac{\Gamma\left(\frac{k}{2}\right)}{\Gamma\left(\frac{k-1}{2}\right)} \left(\frac{c_k^2}{c_k^2 + \Delta^2/\bar{q}^2}\right)^{k/2}. \tag{12.11}$$

The numerically integration of $\mathrm{pr}_h(\Delta|\{c_{n\leq k}\})$ over deviation Δ for any degree-of-believe interval leads to the truncation uncertainty $\delta X^{(k)} = X_{\mathrm{ref}} \Delta_k$.

A first application of the uncertainty estimation is shown in Fig. 12.1 for a random sample. For higher orders, the uncertainty estimation yields a smaller result than for the lowest order.

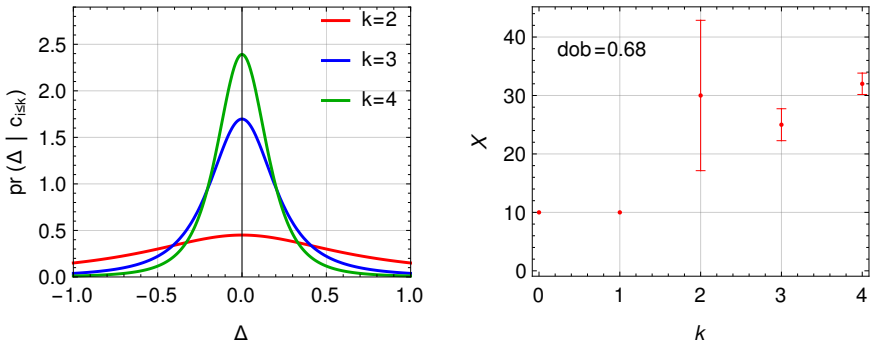

Figure 12.1: Application of the uncertainty estimation: The posterior pdf for different orders k is shown on the left. The observable X for different orders with corresponding uncertainty estimation is illustrated on the right. The data points are chosen randomly.

12.2 Uncertainty Quantification for Transition Strengths

For the application of the Bayesian model of chiral interaction uncertainties, the discrete strengths need to be transferred to well-defined continuous functions. Thus, we use the running sum, where the strengths is summed at each energy, leading to a succession of step functions as shown in Fig. 12.2. We can then apply the uncertainty model and obtain the uncertainties for each chiral order up to $\mathrm{N^3LO}$. The uncertainties depend on the lower chiral orders. For the ISM, IVD and ISQ response, the uncertainties become smaller for higher chiral orders. For the highest chiral order, the uncertainty is remarkably small. The uncertainty has not necessarily steps at the same energies as the running sum, since the discrete strengths of the lower chiral order, which is used as input for the uncertainty estimation, deviates.

The next step is now to transfer these information to the smeared-out strength distribution in order to obtain error bands. Therefore, we first smooth the step functions via a Fermi-type function

$$\frac{1}{e^{\frac{E-E_i}{w}}+1} \tag{12.12}$$

with the width w and the eigenenergy E_i. The result is illustrated in Fig. 12.3. We now have for every transition energy a strength with corresponding uncertainty.

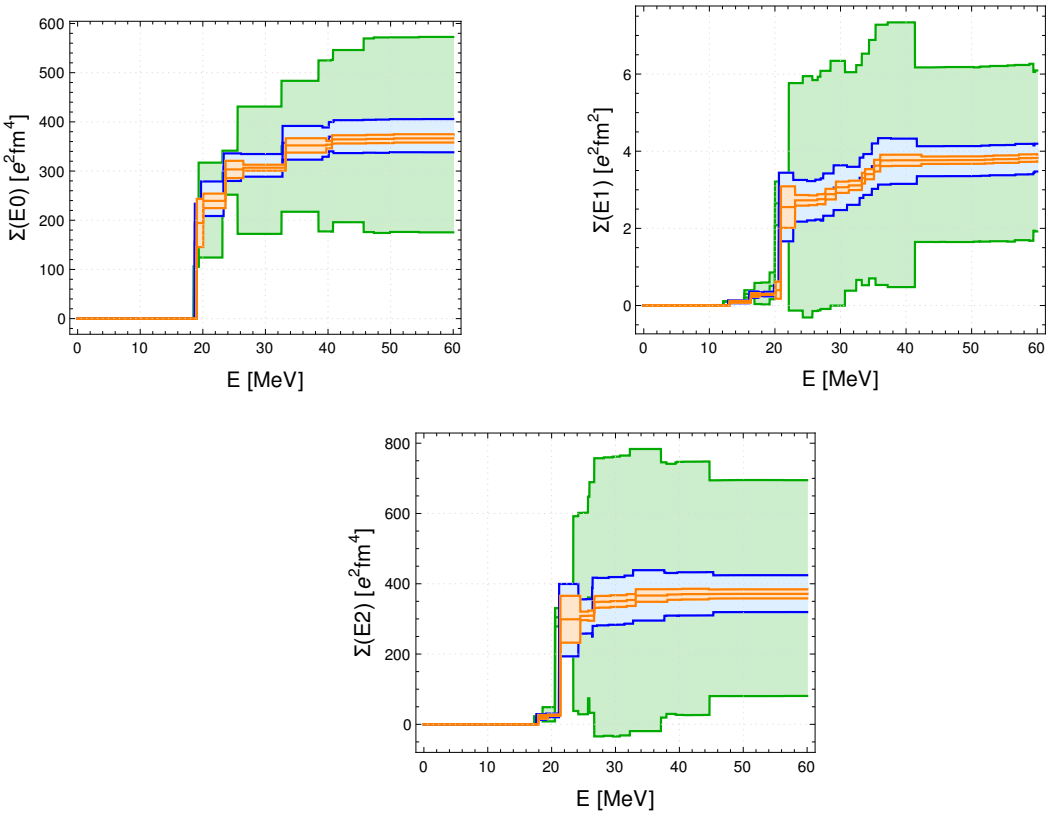

Figure 12.2: Running sum of the electric ISM, IVD and ISQ response of ^{16}O, obtained by a NAT-RPA calculation, with uncertainties for different chiral orders {NLO(——), N^{2}LO(——), N^{3}LO(——)} of the interaction.

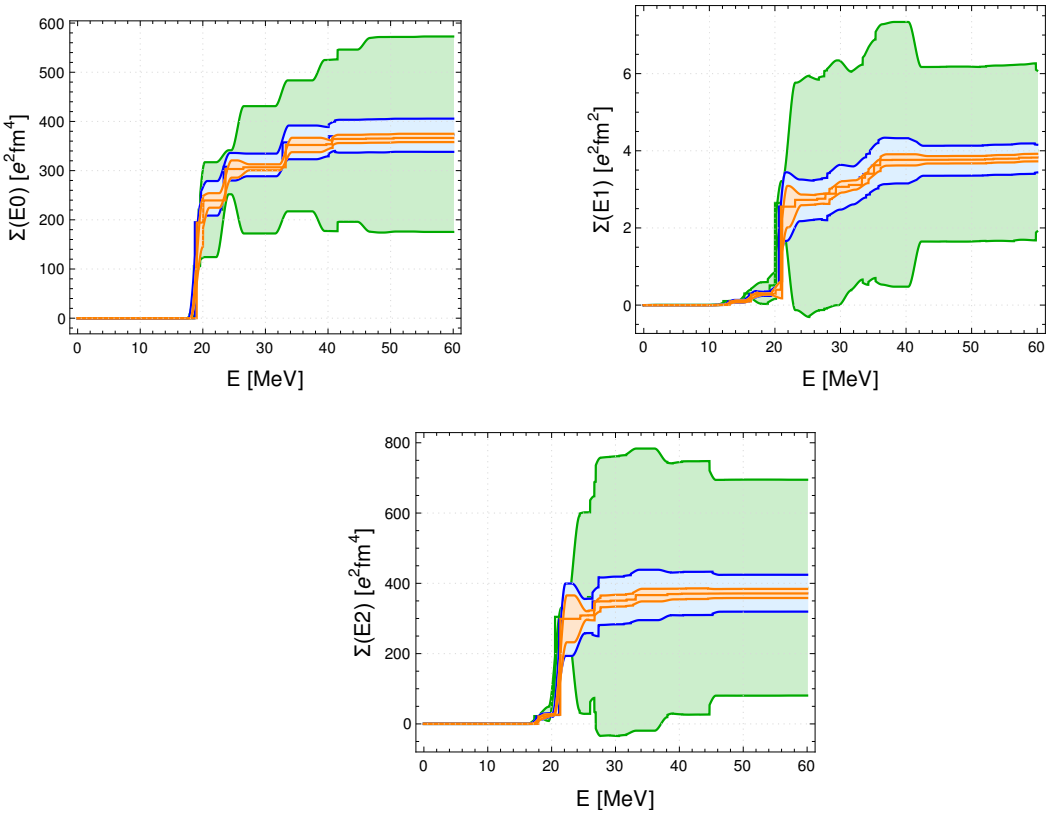

Figure 12.3: Running sum of the electric ISM, IVD and ISQ response of ^{16}O, obtained by a NAT-RPA calculation, with smoothed-out uncertainties for different chiral orders {NLO(——), N^{2}LO(——), N^{3}LO(——)} of the interaction.

13

Comparison of Lanczos vs. RPA-type methods

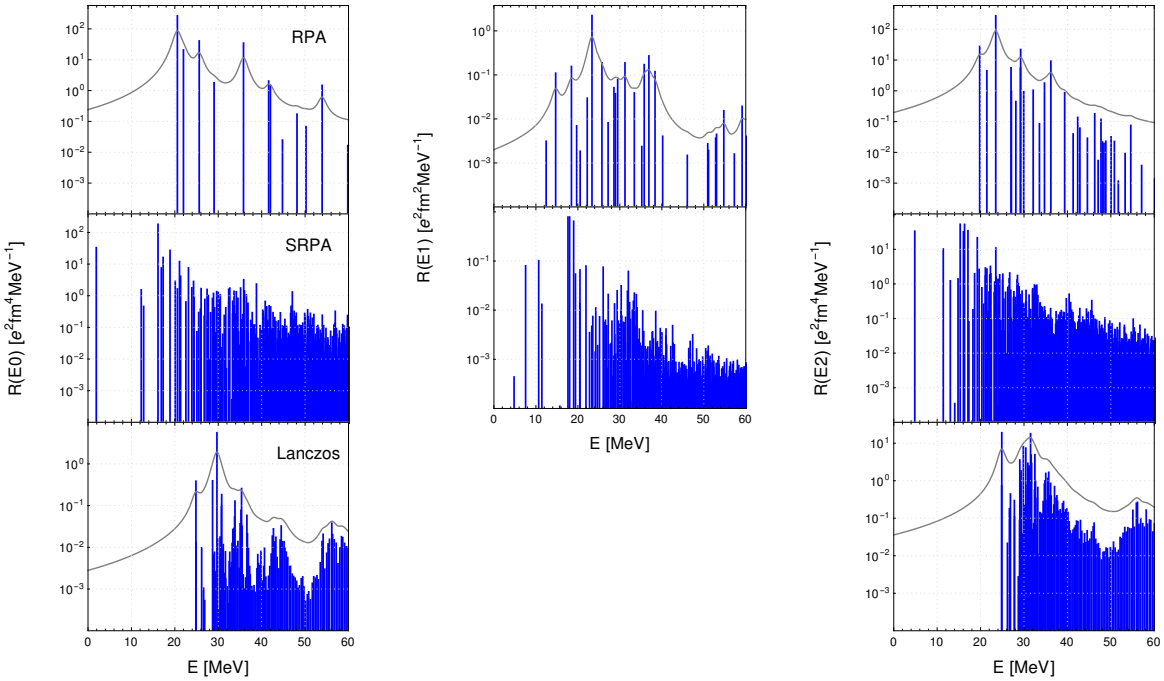

Figure 13.1: Discrete electric ISM, IVD, and ISQ response for ^{16}O obtained with the HF-RPA (above), HF-SRPA (middle), and Lanczos strength function method (below).

Figure 13.1 compares the electric ISM, IVD, and ISQ responses for ^{16}O obtained by the different methods introduced in this thesis. Here, we use $e_{\max} = 12$, $l_{\max} = 8$, an oscillator frequency of $\hbar\Omega = 20$ MeV, an SRG flow parameter of $\alpha = 0.08$ fm^4, and the HF basis. For first-order RPA calculations, fragmentation and fine structure is practically absent. Including additional second-order terms in the ECOs in SRPA leads to a more pronounced fine structure. The Lanczos strength function method predicts fine structure and fragmentation comparable to SRPA. Furthermore, the position of the main resonance peak is compatible in RPA and Lanczos calculations.

As known from previous sections, the transition strengths obtained with first-order RPA tend to lie at too high energies, whereas the inclusion of second-order terms shifts the entire strength distribution to lower transition energies. Furthermore, different single-particle bases results in shifted transition strengths.

The methods exhibit different limitations. For RPA-type methods, we are restricted to nuclei with subshell closures. The computational effort is trivial for first-order RPA and a calculation can be performed on a desktop workstation. The inclusion of second-order terms leads to a significant increase of the model-space size. Calculations are only feasible with a 2p2h model-space truncation and, still, the calculations can need several days on a cluster node. With RPA-type methods, mid-mass nuclei can be addressed. Contrarily, transition strengths obtained with the Lanczos strength function method are restricted to light nuclei. The limitations of the underlying IT-NCSM are transferred to the calculation of transition strengths. The computational cost of a calculation of the pivot state, which enters the Lanczos strength function method, within IT-NCSM increases factorially with the number of nucleons. Thus, calcium isotopes cannot be reached in contrast to RPA-type methods. Furthermore, the uncertainty estimation, which includes the calculation of transition strengths at different chiral orders is computationally more expensive for the Lanczos strength functions than for RPA-type methods, since for every chiral order, a full IT-NCSM calculation needs to be performed.

14

Conclusions and Summary

In this thesis, we investigated collective excitations of nuclei with different many-body methods. We compared transition strengths from RPA-type methods with the Lanczos strength function method based on the IT-NCSM and extended the formalism to different single-particle bases.

A family of non-local NN+3N interaction was applied for the first time in the context of collective excitations. Independent of the single-particle basis, the transition strengths are converged with respect to the chiral orders as long as 3N forces are included.

The different single-particle bases as well as the different methods themselves have an impact on the transition strengths. Comparing first- and second-order RPA, we observe a pathological energy shift to lower energies for the inclusion of second-order terms. This leads to instabilities, since the low-lying states are shifted as well and can appear at negative excitation energies. Even if we are interested in the giant resonances, a negative connotation with respect to these instabilities remains. The computational effort increases tremendously for the inclusion of second-order terms. Thus, an additional truncation of the SRPA model-space size is introduced. The transition strengths, especially for the heavier nuclei, are not yet fully converged with respect to the SRPA model space.

The IM-RPA produces transition strengths that are shifted to higher energies compared to standard RPA. The difference between both methods can be explained with the widening of the Fermi gap that corresponds to the energy shift of the transition strengths. Including additional 2p2h excitations in the IM framework leads to a similar pattern as for the comparison of standard first- and second-order RPA. The transition strengths obtained with IM-(S)RPA calculations are shifted to higher energies compared to the standard counterparts. Reason for this behavior are among others missing correlations, since the (S)RPA is reduced to an (S)TDA by using IM-SRG matrix elements. This point is important as well, since the reduction to (S)TDA could improve the convergence behavior with respect to the SRPA model space. The instabilities, which occur when going from standard RPA to SRPA, are removed due to the shift to higher energies because of the decoupling in IM-SRG. Consequently HF-based RPA and IM-SRPA yield similar centroid energies.

In the IM framework, we perform inconsistent calculations of the transition strengths, since we use HF matrix elements of the electromagnetic operators instead of IM-SRG evolved matrix elements. The IM-SRG transformation of non-scalar operators is part of current research. First tests of a consistent description show a very small effect between HF and IM-SRG evolved matrix elements of the electromagnetic operators. Nevertheless, this is an important step for consistency and needs to be investigated in more detail.

For the HF-based (S)RPA, a variation of the oscillator frequency affects the transition strengths. The responses are shifted to higher energies for larger frequencies. Since natural orbitals are independent of the oscillator frequency for ground-state properties, we extended the RPA to different single-particle bases. For collective excitations, this independence cannot be reproduced. The reason for this lies in the frequency dependence of the radial wave functions of higher-lying orbitals, that are not included for the calculation of ground-state properties, but that are crucial to describe the different transition modes of collective excitations. Thus, the frequency dependence of the radial wave functions is transferred to the transition strengths. For larger model-space sizes, the frequency dependence can be shifted towards higher-lying orbitals. In order to achieve frequency independence of the wave functions, the model-space sizes need to be increased more, which is computationally challenging. For the investigation of collective excitations, not only low-lying but also highly excited states are crucial. Thus,

collective excitations would benefit from a single-particle basis, that is optimized for more than the low-lying states.

Furthermore, the Lanczos strength function method based on natural orbitals produces transition strengths that are at unreasonable high energies and, thus, are unphysical. The reason for that is not yet clear and this peculiarity needs to be investigated in more detail. For different bases as the HF single-particle basis, the Lanczos strength function method predicts fine structure and fragmentation comparable to the SRPA results. The Lanczos method is restricted to light nuclei as the underlying IT-NCSM.

The next step in the investigation of collective excitations is a consistent description in terms of IM-SRG evolved electromagnetic operators. The extension of the SRPA to the inclusion of explicit 3N forces would be another interesting point in terms of consistency. Furthermore, the Lanczos strength function method could be extended to inputs from IM-SRG. The special behavior of the transition strengths obtained by the IT-NCSM based on natural orbitals need to be understood.

A

Appendix

Contents

A.1 Basic Commutation Relations for Creator and Annihilator

Fermion creation and annihilation operators in second quantization obey the anticommutation relations

$$\left\{\hat{a}_i, \hat{a}_j^\dagger\right\} = \delta_{ij} \tag{A.1}$$

$$\left\{\hat{a}_i^\dagger, \hat{a}_j^\dagger\right\} = \{\hat{a}_i, \hat{a}_j\} = 0\,. \tag{A.2}$$

These can be rewritten into commutation relations

$$\begin{aligned}
[\hat{a}_i, \hat{a}_j] &= 2\hat{a}_i\hat{a}_j \\
\left[\hat{a}_i^\dagger, \hat{a}_j^\dagger\right] &= 2\hat{a}_i^\dagger\hat{a}_j^\dagger \\
\left[\hat{a}_i, \hat{a}_j^\dagger\right] &= \delta_{ij} - 2\hat{a}_j^\dagger\hat{a}_i \\
\left[\hat{a}_i^\dagger, \hat{a}_j\right] &= \delta_{ij} - 2\hat{a}_j\hat{a}_i^\dagger\,.
\end{aligned} \tag{A.3}$$

For any commutator, the product rule

$$\left[\hat{A}\hat{B}, \hat{C}\hat{D}\right] = \hat{A}\left[\hat{B}, \hat{C}\right]\hat{D} + \hat{A}\hat{C}\left[\hat{B}, \hat{D}\right] + \left[\hat{A}, \hat{C}\right]\hat{D}\hat{B} + \hat{C}\left[\hat{A}, \hat{D}\right]\hat{B} \tag{A.4}$$

holds. Applying this relation in combination with the above commutation relations to a commutator consisting of a product and a single creation or annihilation operator, respectively, yields

$$\begin{aligned}
\left[\hat{a}_i^\dagger\hat{a}_j, \hat{a}_k^\dagger\right] &= \delta_{jk}\hat{a}_i^\dagger \\
\left[\hat{a}_i^\dagger\hat{a}_j, \hat{a}_k\right] &= -\delta_{ik}\hat{a}_j\,.
\end{aligned} \tag{A.5}$$

Using these definitions of the commutators and the product rule, the commutator containing products of different creation and annihilation operators as emerging in Eq. (5.30) can be determined as

$$\begin{aligned}
\left[\hat{a}_h^\dagger\hat{a}_p, \hat{a}_{p'}^\dagger\hat{a}_{h'}\right] &= \hat{a}_h^\dagger\left[\hat{a}_p, \hat{a}_{p'}^\dagger\right]\hat{a}_{h'} + \hat{a}_h^\dagger\hat{a}_{p'}^\dagger\left[\hat{a}_p, \hat{a}_{h'}\right] + \left[\hat{a}_h^\dagger, \hat{a}_{p'}^\dagger\right]\hat{a}_{h'}\hat{a}_p + \hat{a}_{p'}^\dagger\left[\hat{a}_h^\dagger, \hat{a}_{h'}\right]\hat{a}_p \\
&= \hat{a}_h^\dagger\left(\delta_{pp'} - 2\hat{a}_{p'}^\dagger\hat{a}_p\right)\hat{a}_{h'} + 2\hat{a}_h^\dagger\hat{a}_{p'}^\dagger\hat{a}_p\hat{a}_{h'} - 2\hat{a}_{p'}^\dagger\hat{a}_h^\dagger\hat{a}_{h'}\hat{a}_p \\
&\quad + \hat{a}_{p'}^\dagger\left(\delta_{hh'} - 2\hat{a}_{h'}\hat{a}_h^\dagger\right)\hat{a}_p \\
&= \delta_{pp'}\hat{a}_h^\dagger\hat{a}_{h'} - 2\hat{a}_{p'}^\dagger\hat{a}_h^\dagger\hat{a}_{h'}\hat{a}_p + \delta_{hh'}\hat{a}_{p'}^\dagger\hat{a}_p - 2\hat{a}_{p'}^\dagger\left(\delta_{hh'} - \hat{a}_h^\dagger\hat{a}_{h'}\right)\hat{a}_p \\
&= \delta_{pp'}\hat{a}_h^\dagger\hat{a}_{h'} - \delta_{hh'}\hat{a}_{p'}^\dagger\hat{a}_p\,.
\end{aligned} \tag{A.6}$$

For simplicity, Eq. (A.6) is rewritten, leading to

$$\begin{aligned}\left[\hat{a}_h^\dagger \hat{a}_p, \hat{a}_{p'}^\dagger \hat{a}_{h'}\right] &= \delta_{pp'} \hat{a}_h^\dagger \hat{a}_{h'} - \delta_{hh'} \hat{a}_{p'}^\dagger \hat{a}_p \\ &= \delta_{pp'} \left(-\hat{a}_{h'} \hat{a}_h^\dagger + \delta_{hh'}\right) - \delta_{hh'} \hat{a}_{p'}^\dagger \hat{a}_p \\ &= \delta_{pp'} \delta_{hh'} - \delta_{pp'} \hat{a}_{h'} \hat{a}_h^\dagger - \delta_{hh'} \hat{a}_{p'}^\dagger \hat{a}_p \,.\end{aligned} \tag{A.7}$$

A.2 Creation and Annihilation Operators as Spherical Tensor Operators

As mentioned in Sec. 2.2, one possibility to define spherical tensor operators is via their transformation behavior which is associated with the validity of the commutation relations given in Eq. (2.17) and Eq. (2.18), depending on the z-component of the total angular momentum operator $\hat{J}_z$ and ladder operators $\hat{J}_\pm$. In second quantization, these operators are given by

$$\begin{aligned} \hat{J}_z &= \hbar \sum_\alpha m_\alpha \hat{a}_\alpha^\dagger \hat{a}_\alpha \\ \hat{J}_\pm &= \hbar \sum_\alpha m_\alpha^\mp \hat{a}_\alpha^\dagger \hat{a}_{\alpha\mp1}. \end{aligned} \tag{A.8}$$

In order to find out if an arbitrary operator is a spherical tensor operator, this operator needs to obey the commutation relations.

Single Creation and Annihilation Operator The commutation relations of the angular momentum operators and an arbitrary creation operator $\hat{a}_\beta^\dagger$ yields

$$\begin{aligned} \left[\hat{J}_z, \hat{a}_\beta^\dagger\right] &= \hbar \sum_\alpha m_\alpha \left[\hat{a}_\alpha^\dagger \hat{a}_\alpha, \hat{a}_\beta^\dagger\right] = \hbar \sum_\alpha m_\alpha \delta_{\alpha\beta} \hat{a}_\alpha^\dagger = \hbar m_\beta \hat{a}_\beta^\dagger \\ \left[\hat{J}_\pm, \hat{a}_\beta^\dagger\right] &= \hbar \sum_\alpha m_\alpha^\mp \left[\hat{a}_\alpha^\dagger \hat{a}_{\alpha\mp1}, \hat{a}_\beta^\dagger\right] = \hbar \sum_\alpha m_\alpha^\mp \delta_{\alpha\mp1,\beta} \hat{a}_\alpha^\dagger = \hbar m_{\beta\pm1}^\mp \hat{a}_{\beta\pm1}^\dagger = \hbar m_\beta^\pm \hat{a}_{\beta\pm1}^\dagger \,, \end{aligned} \tag{A.9}$$

which corresponds to the requirements in Eq. (2.17) and Eq. (2.18). Hence, the creation operator $\hat{a}_\beta^\dagger$ is a spherical tensor operator.

Considering an arbitrary annihilation operator $\hat{a}_\beta$, we obtain for the first commutation relation

$$\left[\hat{J}_z, \hat{a}_\beta\right] = \hbar \sum_\alpha m_\alpha \left[\hat{a}_\alpha^\dagger \hat{a}_\alpha, \hat{a}_\beta\right] = -\hbar \sum_\alpha m_\alpha \delta_{\alpha\beta} \hat{a}_\alpha = -\hbar m_\beta \hat{a}_\beta \neq \hbar m_\beta \hat{a}_\beta \,, \tag{A.10}$$

which differs from the prediction in the sign. Therefore, the annihilation operator does not fulfill the commutation relations and in consequence is no spherical tensor operator. Since the annihilation operator almost satisfies the commutation relation, it can be used as basis for a modified annihilation operator which is shown to be a spherical tensor operator in the following. With the ansatz for a new annihilation operator

$$\hat{\tilde{a}}_\beta = (-1)^{j_b + m_\beta} \hat{a}_{-\beta} \,, \tag{A.11}$$

we can calculate the two commutation relations, resulting in

$$\begin{aligned}\left[\hat{J}_z, \hat{\tilde{a}}_\beta\right] &= \hbar \sum_\alpha m_\alpha \left[\hat{a}^\dagger_\alpha \hat{a}_\alpha, \hat{a}_{-\beta}\right] (-1)^{j_b+m_\beta} = -\hbar \sum_\alpha m_\alpha (-1)^{j_b+m_\beta} \delta_{\alpha,-\beta} \hat{a}_\alpha \\ &= -\hbar m_{-\beta} (-1)^{j_b+m_\beta} \hat{a}_{-\beta} = \hbar \left(-m_{-\beta}\right) \hat{\tilde{a}}_\beta \\ &= \hbar m_\beta \hat{\tilde{a}}_\beta\end{aligned} \tag{A.12}$$

and

$$\begin{aligned}\left[\hat{J}_\pm, \hat{\tilde{a}}_\beta\right] &= \hbar \sum_\alpha m^\mp_\alpha \left[\hat{a}^\dagger_\alpha \hat{a}_{\alpha\mp1}, \hat{\tilde{a}}_\beta\right] = \hbar \sum_\alpha m^\mp_\alpha (-1)^{j_b+m_\beta} \left[\hat{a}^\dagger_\alpha \hat{a}_{\alpha\mp1}, \hat{a}_{-\beta}\right] \\ &= -\hbar \sum_\alpha m^\mp_\alpha (-1)^{j_b+m_\beta} \delta_{\alpha,-\beta} \hat{a}_{\alpha\mp1} \\ &= -\hbar (-1)^{j_b+m_\beta} m^\mp_{-\beta} \hat{a}_{-\beta\mp1} = \hbar m^\mp_{-\beta} \hat{a}_{-(\beta\pm1)} (-1)^{j_b+m_{\beta\pm1}} \\ &= \hbar m^\mp_{-\beta} \hat{\tilde{a}}_{\beta\pm1} = \hbar m^\pm_\beta \hat{\tilde{a}}_{\beta\pm1}\,,\end{aligned} \tag{A.13}$$

which corresponds to the fulfillment of the commutation relations. Thus, the modified annihilation operator (A.11) is actually a spherical tensor operator.

ph Creation Operator Dealing with ph creation and annihilation operators, which correspond to pairs of fermionic operators, several considerations needs to be done in the context of spherical tensor operators.

Coupled Version In order to construct a spherical tensor operator for the description of a ph creation operator containing a pair of fermion operators, we use the tensor product of spherical tensors as defined in Eq. (2.19), which yields a spherical tensor itself. Thus, the new coupled excitation creation operator is given by

$$\hat{\mathcal{A}}^\dagger_{p\hbar}(JM) = \left[\hat{a}^\dagger_p \hat{\tilde{a}}_\hbar\right]_{JM} = \sum_{m_p, m_h} (-1)^{j_h - m_h} \cdot \begin{pmatrix} j_p & j_h & \Big| & J \\ m_p & -m_h & \Big| & M \end{pmatrix} \hat{\mathcal{A}}^\dagger_{ph} \tag{A.14}$$

with the uncoupled ph creation operator $\hat{\mathcal{A}}^\dagger_{ph}$.

For the ph annihilation operator, it is not sufficient to take the Hermitian conjugate of the ph creation operator $\hat{\mathcal{A}}_{p\hbar}(JM) = (\hat{\mathcal{A}}^\dagger_{p\hbar}(JM))^\dagger$ due to the loss of spherical properties. Therefore, we define a coupled annihilator $\hat{\tilde{\mathcal{A}}}_{p\hbar}(JM)$ as spherical tensor. The adjoint tensor operators exhibit the same modifications as for single annihilation operators, c.f. Eq. (5.17) and Eq. (A.11):

$$\begin{aligned}\hat{\tilde{\mathcal{A}}}_{p\hbar}(JM) &= (-1)^{J+M} \left(\hat{\mathcal{A}}^\dagger_{p\hbar}(J-M)\right)^\dagger \\ &= (-1)^{J+M} \hat{\mathcal{A}}_{p\hbar}(J-M)\end{aligned} \tag{A.15}$$

Inserting the Hermitian conjugate of the definition of the coupled creation operator given in Eq. (A.14) and applying the symmetry properties of Clebsch-Gordan coefficients in Eq. (2.6) leads to

$$\begin{aligned} &= \sum_{m_p,m_h} (-1)^{J+M}(-1)^{j_h-m_h} \left(\begin{matrix} j_p & j_h \\ m_p & -m_h \end{matrix}\middle| \begin{matrix} J \\ -M \end{matrix}\right) \hat{\mathcal{A}}_{ph} \\ &= \sum_{m_p,m_h} (-1)^{J+M}(-1)^{j_h-m_h}(-1)^{j_p+j_h-J} \left(\begin{matrix} j_p & j_h \\ -m_p & m_h \end{matrix}\middle| \begin{matrix} J \\ M \end{matrix}\right) \hat{\mathcal{A}}_{ph}\,. \end{aligned} \tag{A.16}$$

The phase factor can be reformulated to

$$(-1)^{J+M}(-1)^{j_h-m_h}(-1)^{j_p+j_h-J} = (-1)^{2j_h}(-1)^{j_p-m_p} = -(-1)^{j_p-m_p}\,, \tag{A.17}$$

where we exploited the additivity of the m_i quantum numbers in the Clebsch-Gordan coefficient $-m_p + m_h = M$. Since the angular momenta j_i are half-odd integer, the first phase factor results in a global minus. Thus, we find for the coupled annihilation operator

$$\begin{aligned} &= -\sum_{m_p,m_h} (-1)^{j_p-m_p} \left(\begin{matrix} j_p & j_h \\ -m_p & m_h \end{matrix}\middle| \begin{matrix} J \\ M \end{matrix}\right) \hat{a}^\dagger_{\hbar,m_h}\hat{a}_{p,m_p} \\ &= -\sum_{m_p,m_h} (-1)^{j_p+m_p} \left(\begin{matrix} j_p & j_h \\ m_p & m_h \end{matrix}\middle| \begin{matrix} J \\ M \end{matrix}\right) \hat{a}^\dagger_{\hbar,m_h}\hat{a}_{p,-m_p}. \end{aligned} \tag{A.18}$$

In the last step, we swapped the sign of m_p. Applying the anticommutation relation (A.1), which leads to a global minus sign, and inserting the definition of the modified annihilation operator (A.11) results finally in

$$\begin{aligned} &= \sum_{m_p,m_h} (-1)^{j_p+m_p} \left(\begin{matrix} j_p & j_h \\ m_p & m_h \end{matrix}\middle| \begin{matrix} J \\ M \end{matrix}\right) \hat{a}_{p,-m_p}\hat{a}^\dagger_{\hbar,m_h} \\ &= \sum_{m_p,m_h} \left(\begin{matrix} j_p & j_h \\ m_p & m_h \end{matrix}\middle| \begin{matrix} J \\ M \end{matrix}\right) \hat{\tilde{a}}_p\hat{a}^\dagger_h \\ &= \left[\hat{\tilde{a}}_p\hat{a}^\dagger_\hbar\right]_{JM}\,, \end{aligned} \tag{A.19}$$

which is the definition of a tensor product of spherical tensors yielding a new spherical tensor.

A.3 Phase Factor in Coupled RPA A Matrix

The single-particle angular momenta j_i and the corresponding projection m_i are half-integer. Thus, we can ensure that $2j_i$ is odd. There are some other considerations regarding sums of single-particle angular momenta which can guarantee that the phase factor is 1. First, we find

$$(-1)^{4i} = 1 \tag{A.20}$$

with an arbitrary half-integer quantum number i. Another helpful rule combines the angular momenta being part of a Clebsch-Gordan coefficient

$$(-1)^{2(j_1+j_2+j_3)} = 1 \tag{A.21}$$

which is also valid if the j_i are replaced by their projection m_i or with any reversed sign. Since any combination of j_i and m_i is an integer, it holds

$$(-1)^{2(j_i-m_i)} = 1 \tag{A.22}$$

This holds additionally for a reversed sign and as well for two different single-particle angular momenta. With these considerations, we can reformulate the phase factor in Eq. (5.87), which is given by

$$(-1)^{j_h+m_h}(-1)^{j_{h'}+m_{h'}}. \tag{A.23}$$

For the replacement of the $3j$ symbols by a $6j$ symbol, we need the following phase factor

$$(-1)^{j_{p'}+j_{h'}+J'-m_{p'}-m_{h'}-M'}. \tag{A.24}$$

Starting with the phase factor (A.23) and adding phase factors that have even integers as exponent, we find

$$\begin{aligned}
&(-1)^{j_h+m_h}(-1)^{j_{h'}+m_{h'}}\ (-1)^{2(j_{p'}-m_{p'})}\ (-1)^{2(j_{h'}-m_{h'})}\ (-1)^{2(J'-M')} \\
&= (-1)^{2j_{h'}+m_h-m_{p'}-M'}\ (-1)^{j_{p'}+j_{h'}+J'-m_{p'}-m_{h'}-M'}\ (-1)^{j_h+j_{p'}+J'} \\
&= (-1)^{2(j_{h'}-m_{p'})}\ (-1)^{j_{p'}+j_{h'}+J'-m_{p'}-m_{h'}-M'}\ (-1)^{j_h+j_{p'}+J'},
\end{aligned} \tag{A.25}$$

where we used the additivity of the projection quantum number $M' = m_{p'} + m_h$. The first phase factor is equal to 1, the second one is important for rewriting the $3j$ symbols into $6j$ symbols. Thus, only the last phase factor remains.

A.4 Derivation of SRPA Equations

The SRPA equations of motion are given by Eqs. (6.29)-(6.32)

$$\delta X_1^\omega: \quad \langle \mathrm{SD}| [\hat{\mathcal{A}}_{1,i}, [\hat{H}, \hat{Q}^\dagger_\omega]] |\mathrm{SD}\rangle = E^{\mathrm{SRPA}}_\omega \langle \mathrm{SD}| [\hat{\mathcal{A}}_{1,i}, \hat{Q}^\dagger_\omega] |\mathrm{SD}\rangle \ , \tag{A.26}$$

$$\delta Y_1^\omega: \quad \langle \mathrm{SD}| [\hat{\mathcal{A}}^\dagger_{1,i}, [\hat{H}, \hat{Q}^\dagger_\omega]] |\mathrm{SD}\rangle = E^{\mathrm{SRPA}}_\omega \langle \mathrm{SD}| [\hat{\mathcal{A}}^\dagger_{1,i}, \hat{Q}^\dagger_\omega] |\mathrm{SD}\rangle \ , \tag{A.27}$$

$$\delta X_2^\omega: \quad \langle \mathrm{SD}| [\hat{\mathcal{A}}_{2,i}, [\hat{H}, \hat{Q}^\dagger_\omega]] |\mathrm{SD}\rangle = E^{\mathrm{SRPA}}_\omega \langle \mathrm{SD}| [\hat{\mathcal{A}}_{2,i}, \hat{Q}^\dagger_\omega] |\mathrm{SD}\rangle \ , \tag{A.28}$$

$$\delta Y_2^\omega: \quad \langle \mathrm{SD}| [\hat{\mathcal{A}}^\dagger_{2,i}, [\hat{H}, \hat{Q}^\dagger_\omega]] |\mathrm{SD}\rangle = E^{\mathrm{SRPA}}_\omega \langle \mathrm{SD}| [\hat{\mathcal{A}}^\dagger_{2,i}, \hat{Q}^\dagger_\omega] |\mathrm{SD}\rangle \ . \tag{A.29}$$

Since the structure is more complicated for the second-order, we have a look on the right-hand side of each equation first and evaluate the left-hand side afterwards.

Right-Hand Side We start with the right-hand side of the first equation which correspond to the variation of the amplitude δX_1^ω known from standard RPA. Employing the commutation relations derived in Sec. 6.1.2, we find

$$\begin{aligned}
\langle \mathrm{SD}| [\hat{\mathcal{A}}_{1,i}, \hat{Q}^\dagger_\omega] |\mathrm{SD}\rangle &= \langle \mathrm{SD}| [\hat{\mathcal{A}}_{1,i}, \hat{Q}^\dagger_{1,\omega} + \hat{Q}^\dagger_{2,\omega}] |\mathrm{SD}\rangle \\
&= \langle \mathrm{SD}| [\hat{\mathcal{A}}_{1,i}, \hat{Q}^\dagger_{1,\omega}] |\mathrm{SD}\rangle + \langle \mathrm{SD}| [\hat{\mathcal{A}}_{1,i}, \hat{Q}^\dagger_{2,\omega}] |\mathrm{SD}\rangle \\
&= \langle \mathrm{SD}| [\hat{\mathcal{A}}_{1,i}, \hat{Q}^\dagger_{1,\omega}] |\mathrm{SD}\rangle \\
&= \sum_j X^\omega_{1,j} \langle \mathrm{SD}| [\hat{\mathcal{A}}_{1,i}, \hat{\mathcal{A}}^\dagger_{1,j}] |\mathrm{SD}\rangle \\
&= X^\omega_{1,i}.
\end{aligned} \tag{A.30}$$

The first term is evaluated to the amplitude $X^\omega_{1,i}$ according to standard RPA while the second term is zero as stated in Eq. (6.26). Analogously, the right-hand side of the second equation corresponding to the variation of the amplitude δY_1^ω reads

$$\begin{aligned}
\langle \mathrm{SD}| [\hat{\mathcal{A}}^\dagger_{1,i}, \hat{Q}^\dagger_\omega] |\mathrm{SD}\rangle &= \langle \mathrm{SD}| [\hat{\mathcal{A}}^\dagger_{1,i}, \hat{Q}^\dagger_{1,\omega}] |\mathrm{SD}\rangle + \langle \mathrm{SD}| [\hat{\mathcal{A}}^\dagger_{1,i}, \hat{Q}^\dagger_{2,\omega}] |\mathrm{SD}\rangle \\
&= \langle \mathrm{SD}| [\hat{\mathcal{A}}^\dagger_{1,i}, \hat{Q}^\dagger_{1,\omega}] |\mathrm{SD}\rangle = Y^\omega_{1,i}.
\end{aligned} \tag{A.31}$$

Again, the second term is zero according to the expectation value of a commutator concerning operators of mixed order while the first term yields $Y^\omega_{1,i}$. The expectation values corresponding to the second-order forward and backward amplitudes are evaluated in the same way. In these cases, the expectation value of the commutator between the two-particle annihilator or creator, respectively, and the first-order ECO yield zero. The remaining term of the third equation

corresponding to δX_2^ω leads to

$$\begin{aligned}
\langle \mathrm{SD}| [\hat{\mathcal{A}}_{2,i}, \hat{Q}_\omega^\dagger] |\mathrm{SD}\rangle &= \langle \mathrm{SD}| [\hat{\mathcal{A}}_{2,i}, \hat{Q}_{1,\omega}^\dagger] |\mathrm{SD}\rangle + \langle \mathrm{SD}| [\hat{\mathcal{A}}_{2,i}, \hat{Q}_{2,\omega}^\dagger] |\mathrm{SD}\rangle \\
&= \langle \mathrm{SD}| [\hat{\mathcal{A}}_{2,i}, \hat{Q}_{2,\omega}^\dagger] |\mathrm{SD}\rangle \\
&= \sum_j \langle \mathrm{SD}| [\hat{\mathcal{A}}_{2,i}, X_{2,j}^\omega \hat{\mathcal{A}}_{2,j}^\dagger - Y_{2,j}^\omega \hat{\mathcal{A}}_{2,j}] |\mathrm{SD}\rangle \\
&= \sum_j X_{2,j}^\omega \langle \mathrm{SD}| [\hat{\mathcal{A}}_{2,i}, \hat{\mathcal{A}}_{2,j}^\dagger] |\mathrm{SD}\rangle - Y_{2,j}^\omega \langle \mathrm{SD}| [\hat{\mathcal{A}}_{2,i}, \hat{\mathcal{A}}_{2,j}] |\mathrm{SD}\rangle \\
&= \sum_j X_{2,j}^\omega \langle \mathrm{SD}| [\hat{\mathcal{A}}_{2,i}, \hat{\mathcal{A}}_{2,j}^\dagger] |\mathrm{SD}\rangle \\
&= \sum_j X_{2,j}^\omega \delta_{ij} = X_{2,i}^\omega \,.
\end{aligned} \tag{A.32}$$

Here, we inserted the definition of the second-order ECO. The second term is zero as verified in the last chapter. The first term is determined to the second-order forward amplitude.

The expectation value in the last equation associated with δY_2^ω yields

$$\begin{aligned}
\langle \mathrm{SD}| [\hat{\mathcal{A}}_{2,i}^\dagger, \hat{Q}_\omega^\dagger] |\mathrm{SD}\rangle &= \langle \mathrm{SD}| [\hat{\mathcal{A}}_{2,i}^\dagger, \hat{Q}_{2,\omega}^\dagger] |\mathrm{SD}\rangle \\
&= \langle \mathrm{SD}| [\hat{\mathcal{A}}_{2,i}^\dagger, X_{2,j}^\omega \hat{\mathcal{A}}_{2,j}^\dagger - Y_{2,j}^\omega \hat{\mathcal{A}}_{2,j}] |\mathrm{SD}\rangle \\
&= \sum_j -Y_{2,j}^\omega \langle \mathrm{SD}| [\hat{\mathcal{A}}_{2,i}^\dagger, \hat{\mathcal{A}}_{2,j}] |\mathrm{SD}\rangle \\
&= \sum_j Y_{2,j}^\omega \delta_{ij} = Y_{2,i}^\omega \,.
\end{aligned} \tag{A.33}$$

As for the first-order RPA, the expectation values of the right-hand side are proportional to the forward and backward amplitudes but the structure is more complicated due to the extension of the model space by inclusion of 2p2h contributions.

Left-Hand Side The left-hand side equations are more complex due to the double commutator of the ECOs and the Hamiltonian. The Hamiltonian is the reason why the expectation values including a commutator of first- and second-order (de-)excitation creation operators does not automatically vanish. First, we start with the left-hand side of Eq. (A.26) associated with the variation of the amplitude δX_1^ω. The expectation value becomes

$$\langle \mathrm{SD}| [\hat{\mathcal{A}}_{1,i}, [\hat{H}, \hat{Q}_\omega^\dagger]] |\mathrm{SD}\rangle = \underbrace{\langle \mathrm{SD}| [\hat{\mathcal{A}}_{1,i}, [\hat{H}, \hat{Q}_{1,\omega}^\dagger]] |\mathrm{SD}\rangle}_{\text{contribution in RPA}} + \langle \mathrm{SD}| [\hat{\mathcal{A}}_{1,i}, [\hat{H}, \hat{Q}_{2,\omega}^\dagger]] |\mathrm{SD}\rangle \,. \tag{A.34}$$

Since the first term is already evaluated in first-order RPA, c.f. Eq. (5.40)

$$\langle \mathrm{SD}| [\hat{\mathcal{A}}_{1,i}, [\hat{H}, \hat{Q}_{1,\omega}^\dagger]] |\mathrm{SD}\rangle = \sum_j X_{1,j}^\omega (A_{11})_{ij} + Y_{1,j}^\omega (B_{11})_{ij} \tag{A.35}$$

we only consider the second-order term, leading to

$$\begin{aligned}
&\langle \mathrm{SD}|[\hat{\mathcal{A}}_{1,i},[\hat{H},\hat{Q}^\dagger_{2,\omega}]]\,|\mathrm{SD}\rangle \\
&\quad= \sum_j \langle \mathrm{SD}|\,[\hat{\mathcal{A}}_{1,i},[\hat{H},X^\omega_{2,j}\hat{\mathcal{A}}^\dagger_{2,j}-Y^\omega_{2,j}\hat{\mathcal{A}}_{2,j}]]\,|\mathrm{SD}\rangle \\
&\quad= \sum_j X^\omega_{2,j}\underbrace{\langle \mathrm{SD}|\,[\hat{\mathcal{A}}_{1,i},[\hat{H},\hat{\mathcal{A}}^\dagger_{2,j}]]\,|\mathrm{SD}\rangle}_{(A_{12})_{ij}} - \sum_j Y^\omega_{2,j}\underbrace{\langle \mathrm{SD}|\,[\hat{\mathcal{A}}_{1,i},[\hat{H},\hat{\mathcal{A}}_{2,j}]]\,|\mathrm{SD}\rangle}_{-(B_{12})_{ij}} \\
&\quad= \textstyle\sum_j X^\omega_{2,j}\,(A_{12})_{ij} + Y^\omega_{2,j}\,(B_{12})_{ij}
\end{aligned} \tag{A.36}$$

where the ij-th matrix element of the A_{12} matrix

$$(A_{12})_{ij} = \langle \mathrm{SD}|[\hat{\mathcal{A}}_{1,i},[\hat{H},\hat{\mathcal{A}}^\dagger_{2,j}]]|\mathrm{SD}\rangle \tag{A.37}$$

is introduced. The explicit form of the A matrix in SRPA is addressed in Sec. 6.1.3. Furthermore, the introduced ij-th matrix element of the B_{12} matrix is evaluated to zero

$$\begin{aligned}
-\,(B_{12})_{ij} &= \langle \mathrm{SD}|\,[\hat{\mathcal{A}}_{1,i},[\hat{H},\hat{\mathcal{A}}_{2,j}]]\,|\mathrm{SD}\rangle \\
&= \langle \mathrm{SD}|\,[\hat{\mathcal{A}}_{1,i},[\hat{H},\hat{\mathcal{A}}_{1,j_1}\hat{\mathcal{A}}_{1,j_2}]]\,|\mathrm{SD}\rangle \\
&= \langle \mathrm{SD}|\,[\hat{\mathcal{A}}_{1,i},\hat{\mathcal{A}}_{1,j_1}[\hat{H},\hat{\mathcal{A}}_{1,j_2}]]\,|\mathrm{SD}\rangle + \langle \mathrm{SD}|\,[\hat{\mathcal{A}}_{1,i},[\hat{H},\hat{\mathcal{A}}_{1,j_1}]\hat{\mathcal{A}}_{1,j_2}]\,|\mathrm{SD}\rangle \\
&= 0.
\end{aligned} \tag{A.38}$$

In the first term, the annihilators can be summarized as an effective 3p3h operator. Since the Hamiltonian is only on two-body level, one ph operator remains resulting in a Kronecker delta which becomes zero since particle and hole states are disjoint. The second term is zero since both terms of the commutator contain a ph annihilator acting on the Slater determinant. Thus, the entire block matrix B_{12} is zero. This is only valid for a two-body Hamiltonian. Including higher-orders of interaction could compensate the effective 3p3h operator leading to a non-vanishing block matrix.

The expectation value corresponding to the variation of the amplitude δY^ω_1 reads

$$\langle \mathrm{SD}|\,[\hat{\mathcal{A}}^\dagger_{1,i},[\hat{H},\hat{Q}^\dagger_{\omega}]]\,|\mathrm{SD}\rangle = \underbrace{\langle \mathrm{SD}|\,[\hat{\mathcal{A}}^\dagger_{1,i},[\hat{H},\hat{Q}^\dagger_{1,\omega}]]\,|\mathrm{SD}\rangle}_{\text{contribution in RPA}} + \langle \mathrm{SD}|\,[\hat{\mathcal{A}}^\dagger_{1,i},[\hat{H},\hat{Q}^\dagger_{2,\omega}]]\,|\mathrm{SD}\rangle \tag{A.39}$$

Again, the first term arises as well in first-order RPA, c.f. Eq. (5.41)

$$\langle \mathrm{SD}|\,[\hat{\mathcal{A}}^\dagger_{1,i},[\hat{H},\hat{Q}^\dagger_{1,\omega}]]\,|\mathrm{SD}\rangle = -\textstyle\sum_j X^\omega_{1,j}\,(B_{11})^*_{ij} - \sum_j Y^\omega_{1,j}\,(A_{11})^*_{ij}\,. \tag{A.40}$$

The second term is evaluated to

$$\begin{aligned}
&\langle \mathrm{SD}|[\hat{\mathcal{A}}^\dagger_{1,i},[\hat{H},\hat{Q}^\dagger_{2,\omega}]]\,|\mathrm{SD}\rangle \\
&\quad= \sum_j \langle \mathrm{SD}|\,[\hat{\mathcal{A}}^\dagger_{1,i},[\hat{H},X^\omega_{2,j}\hat{\mathcal{A}}^\dagger_{2,j}-Y^\omega_{2,j}\hat{\mathcal{A}}_{2,j}]]\,|\mathrm{SD}\rangle \\
&\quad= \sum_j X^\omega_{2,j}\,\langle \mathrm{SD}|\,[\hat{\mathcal{A}}^\dagger_{1,i},[\hat{H},\hat{\mathcal{A}}^\dagger_{2,j}]]\,|\mathrm{SD}\rangle - \sum_j Y^\omega_{2,j}\,\langle \mathrm{SD}|\,[\hat{\mathcal{A}}^\dagger_{1,i},[\hat{H},\hat{\mathcal{A}}_{2,j}]]\,|\mathrm{SD}\rangle\ .
\end{aligned} \tag{A.41}$$

Hermitian conjugation of the first term leads to an expression that can be identified with the matrix elements of the B_{12} matrix

$$\begin{aligned}
\langle \mathrm{SD}|\,[\hat{\mathcal{A}}^\dagger_{1,i},[\hat{H},\hat{\mathcal{A}}^\dagger_{2,j}]]\,|\mathrm{SD}\rangle &= \langle \mathrm{SD}|\,[\hat{\mathcal{A}}^\dagger_{1,i},[\hat{H},\hat{\mathcal{A}}^\dagger_{2,j}]]^\dagger\,|\mathrm{SD}\rangle^* \\
&= \langle \mathrm{SD}|\,[\hat{\mathcal{A}}_{1,i},[\hat{H},\hat{\mathcal{A}}_{2,j}]]\,|\mathrm{SD}\rangle^* \\
&= -\,(B_{12})^*_{ij} = 0\,.
\end{aligned} \tag{A.42}$$

The adjoint of the commutator is derived in App. A.5. Analogously, the second term is the hermitian adjoint of the A_{12} matrix

$$\begin{aligned}
\langle \mathrm{SD}|\,[\hat{\mathcal{A}}^\dagger_{1,i},[\hat{H},\hat{\mathcal{A}}_{2,j}]]\,|\mathrm{SD}\rangle &= \langle \mathrm{SD}|\,[\hat{\mathcal{A}}^\dagger_{1,i},[\hat{H},\hat{\mathcal{A}}_{2,j}]]^\dagger\,|\mathrm{SD}\rangle^* \\
&= \langle \mathrm{SD}|\,[\hat{\mathcal{A}}_{1,i},[\hat{H},\hat{\mathcal{A}}^\dagger_{2,j}]]\,|\mathrm{SD}\rangle^* \\
&= (A_{12})^*_{ij}\,.
\end{aligned} \tag{A.43}$$

Similarly to first-order RPA, this expectation value contains the already known matrices where only the amplitudes are changed

$$\langle \mathrm{SD}|\,[\hat{\mathcal{A}}^\dagger_{1,i},[\hat{H},\hat{Q}^\dagger_{2,\omega}]]\,|\mathrm{SD}\rangle = -\textstyle\sum_j X^\omega_{2,j}\,(B_{12})^*_{ij} - \sum_j Y^\omega_{2,j}\,(A_{12})^*_{ij}\,. \tag{A.44}$$

The third equation associated with δX^ω_2 yields

$$\langle \mathrm{SD}|\,[\hat{\mathcal{A}}_{2,i},[\hat{H},\hat{Q}^\dagger_{\omega}]]\,|\mathrm{SD}\rangle = \langle \mathrm{SD}|\,[\hat{\mathcal{A}}_{2,i},[\hat{H},\hat{Q}^\dagger_{1,\omega}]]\,|\mathrm{SD}\rangle + \langle \mathrm{SD}|\,[\hat{\mathcal{A}}_{2,i},[\hat{H},\hat{Q}^\dagger_{2,\omega}]]\,|\mathrm{SD}\rangle\ . \tag{A.45}$$

The non-vanishing part of the first term is identified with the A_{21} matrix which is equivalent to the transposed A_{12} matrix in Eq. (A.37)

$$(A_{21})_{ij} = \langle \mathrm{SD}|\,[\hat{\mathcal{A}}_{2,i},[\hat{H},\hat{\mathcal{A}}^\dagger_{1,j}]]\,|\mathrm{SD}\rangle = \Big(\langle \mathrm{SD}|\,[\hat{\mathcal{A}}_{1,i},[\hat{H},\hat{\mathcal{A}}^\dagger_{2,j}]]\,|\mathrm{SD}\rangle\Big)^T = (A_{12})^T_{ij} \tag{A.46}$$

The second term becomes

$$\begin{aligned}
&\langle \mathrm{SD}|[\hat{\mathcal{A}}_{2,i}, [\hat{H}, \hat{Q}^\dagger_{2,\omega}]] \,|\mathrm{SD}\rangle \\
&\quad = \sum_j X^\omega_{2,j} \,\langle \mathrm{SD}|\, [\hat{\mathcal{A}}_{2,i}, [\hat{H}, \hat{\mathcal{A}}^\dagger_{2,j}]] \,|\mathrm{SD}\rangle - \sum_j Y^\omega_{2,j} \,\langle \mathrm{SD}|\, [\hat{\mathcal{A}}_{2,i}, [\hat{H}, \hat{\mathcal{A}}_{2,j}]] \,|\mathrm{SD}\rangle \\
&\quad = \textstyle\sum_j X^\omega_{2,j} \,(A_{22})_{ij} + Y^\omega_{2,j} \,(B_{22})_{ij}
\end{aligned} \tag{A.47}$$

with the newly introduced block matrices A_{22} and B_{22} that are defined via expectation values. The explicit form of the block A_{22} matrix

$$(A_{22})_{ij} = \langle \mathrm{SD}|[\hat{\mathcal{A}}_{2,i}, [\hat{H}, \hat{\mathcal{A}}^\dagger_{2,j}]]|\mathrm{SD}\rangle \tag{A.48}$$

is evaluated in the Sec. 6.2. The B_{22} matrix becomes zero

$$(B_{22})_{ij} = \text{-}\ \langle \mathrm{SD}|[\hat{\mathcal{A}}_{2,i}, [\hat{H}, \hat{\mathcal{A}}_{2,j}]]|\mathrm{SD}\rangle{=}0 \tag{A.49}$$

since there is even one more ph annihilator as it is the case for the B_{12} matrix, leading to an effective 4p4h operator. The two-body Hamiltonian is not able to compensate this amount of ph annihilators. For the inclusion of higher-ordered interactions in the Hamiltonian, the explanation needs to be reconsidered since it would not automatically yield zero.

The last expectation value (A.29) which is associated with δY^ω_2 can be evaluated analogously to the third one, resulting in

$$\langle \mathrm{SD}|\, [\hat{\mathcal{A}}^\dagger_{2,i}, [\hat{H}, \hat{Q}^\dagger_\omega]] \,|\mathrm{SD}\rangle = \langle \mathrm{SD}|\, [\hat{\mathcal{A}}^\dagger_{2,i}, [\hat{H}, \hat{Q}^\dagger_{1,\omega}]] \,|\mathrm{SD}\rangle + \langle \mathrm{SD}|\, [\hat{\mathcal{A}}^\dagger_{2,i}, [\hat{H}, \hat{Q}^\dagger_{2,\omega}]] \,|\mathrm{SD}\rangle \ . \tag{A.50}$$

The first term is identified with the complex conjugate of the A_{21} matrix while the second term becomes

$$\begin{aligned}
&\langle \mathrm{SD}|[\hat{\mathcal{A}}^\dagger_{2,i}, [\hat{H}, \hat{Q}^\dagger_{2,\omega}]] \,|\mathrm{SD}\rangle \\
&\quad = \sum_j X^\omega_{2,j} \,\langle \mathrm{SD}|\, [\hat{\mathcal{A}}^\dagger_{2,i}, [\hat{H}, \hat{\mathcal{A}}^\dagger_{2,j}]] \,|\mathrm{SD}\rangle - \sum_j Y^\omega_{2,j} \,\langle \mathrm{SD}|\, [\hat{\mathcal{A}}^\dagger_{2,i}, [\hat{H}, \hat{\mathcal{A}}_{2,j}]] \,|\mathrm{SD}\rangle \\
&\quad = \textstyle -\sum_j X^\omega_{2,j} \,(B_{22})^*_{ij} - \sum_j Y^\omega_{2,j} \,(A_{22})^*_{ij}
\end{aligned} \tag{A.51}$$

The evaluated matrix elements yield the complex conjugate of the known matrices associated with the 2p2h space

$$\begin{aligned}
\langle \mathrm{SD}|\, [\hat{\mathcal{A}}^\dagger_{2,i}, [\hat{H}, \hat{\mathcal{A}}^\dagger_{2,j}]] \,|\mathrm{SD}\rangle &= \langle \mathrm{SD}|\, [\hat{\mathcal{A}}^\dagger_{2,i}, [\hat{H}, \hat{\mathcal{A}}^\dagger_{2,j}]]^\dagger \,|\mathrm{SD}\rangle^* \\
&= \langle \mathrm{SD}|\, [\hat{\mathcal{A}}_{2,i}, [\hat{H}, \hat{\mathcal{A}}_{2,j}]] \,|\mathrm{SD}\rangle^* \\
&= -\,(B_{22})^*_{ij}
\end{aligned} \tag{A.52}$$

and

$$\begin{aligned}\langle \mathrm{SD}|\,[\hat{\mathcal{A}}^{\dagger}_{2,i},[\hat{H},\hat{\mathcal{A}}_{2,j}]]\,|\mathrm{SD}\rangle &= \langle \mathrm{SD}|\,[\hat{\mathcal{A}}^{\dagger}_{2,i},[\hat{H},\hat{\mathcal{A}}_{2,j}]]^{\dagger}\,|\mathrm{SD}\rangle^{*}\\ &= \langle \mathrm{SD}|\,[\hat{\mathcal{A}}_{2,i},[\hat{H},\hat{\mathcal{A}}^{\dagger}_{2,j}]]\,|\mathrm{SD}\rangle^{*}\\ &= (A_{22})^{*}_{ij}\ .\end{aligned} \tag{A.53}$$

The obtained equations of motions (A.26) - (A.29) are finally summarized

$$\begin{aligned}
\delta X^{\omega}_{1}: &\quad X^{\omega}_{1,i} = \sum_{j} X^{\omega}_{1,j}\,(A_{11})_{ij} + Y^{\omega}_{1,j}\,(B_{11})_{ij} + X^{\omega}_{2,j}\,(A_{12})_{ij}\\
\delta Y^{\omega}_{1}: &\quad Y^{\omega}_{1,i} = -\sum_{j} X^{\omega}_{1,j}\,(B_{11})^{*}_{ij} - Y^{\omega}_{1,j}\,(A_{11})^{*}_{ij} - Y^{\omega}_{2,j}\,(A_{12})^{*}_{ij}\\
\delta X^{\omega}_{2}: &\quad X^{\omega}_{2,i} = \sum_{j} X^{\omega}_{1,j}\,(A_{12})_{ij} + X^{\omega}_{2,j}\,(A_{22})_{ij}\\
\delta Y^{\omega}_{2}: &\quad Y^{\omega}_{2,i} = \sum_{j} -Y^{\omega}_{1,j}\,(A_{21})^{*}_{ij} - Y^{\omega}_{2,j}\,(A_{22})^{*}_{ij}
\end{aligned} \tag{A.54}$$

A.5 Commutation Relations for Mixed Creation and Annihilation Operators

For the derivation of the SRPA equations, different applications of commutation relations are needed which are presented here for reasons of completeness.

The adjoined of the commutator of the Hamiltonian and the hp excitation creation operator yields

$$\begin{aligned}\left[\hat{H},\hat{\mathcal{A}}_{1,j}\right]^{\dagger} &= \left(\hat{H}\hat{\mathcal{A}}_{1,j}-\hat{\mathcal{A}}_{1,j}\hat{H}\right)^{\dagger}\\ &= \hat{\mathcal{A}}^{\dagger}_{1,j}\hat{H}-\hat{H}\hat{\mathcal{A}}^{\dagger}_{1,j}\\ &= -\left[\hat{H},\hat{\mathcal{A}}^{\dagger}_{1,j}\right]. \end{aligned} \tag{A.55}$$

With this, we find

$$\begin{aligned}\left[\hat{\mathcal{A}}^{\dagger}_{1,i},\left[\hat{H},\hat{\mathcal{A}}_{1,j}\right]\right]^{\dagger} &= \left(\hat{\mathcal{A}}^{\dagger}_{1,i}\left[\hat{H},\hat{\mathcal{A}}_{1,j}\right]-\left[\hat{H},\hat{\mathcal{A}}_{1,j}\right]\hat{\mathcal{A}}^{\dagger}_{1,i}\right)^{\dagger}\\ &= -\left[\hat{H},\hat{\mathcal{A}}^{\dagger}_{1,j}\right]\hat{\mathcal{A}}_{1,i}+\hat{\mathcal{A}}_{1,i}\left[\hat{H},\hat{\mathcal{A}}^{\dagger}_{1,j}\right]\\ &= \left[\hat{\mathcal{A}}_{1,i},\left[\hat{H},\hat{\mathcal{A}}^{\dagger}_{1,j}\right]\right]. \end{aligned} \tag{A.56}$$

A.6 Derivation of the A_{12} Matrix

The form of the A_{12} matrix is deduced in Eq. (6.35). It is defined via the expectation value

$$(A_{12})_{ij} = \langle \mathrm{SD} | \, [\hat{\mathcal{A}}_{1,i}, [\hat{H}, \hat{\mathcal{A}}^\dagger_{2,j}]] \, | \mathrm{SD} \rangle \tag{A.57}$$

with the creation and annihilation operators given in Tab. 5.1 and Tab. 7.1.

m-scheme Representation For the further derivation of the uncoupled A_{12} matrix we can insert the definitions of the first-order annihilator (5.23), the second-order creator (6.19) and the Hamiltonian (3.3) up to two-body contributions. This yields

$$A_{12} = \underbrace{\langle \mathrm{SD} | \, \hat{a}^\dagger_h \hat{a}_p [\hat{T}, \hat{a}^\dagger_{p_1} \hat{a}_{h_1} \hat{a}^\dagger_{p_2} \hat{a}_{h_2}] \, | \mathrm{SD} \rangle}_{A_{12,\mathrm{T}}} + \underbrace{\langle \mathrm{SD} | \, \hat{a}^\dagger_h \hat{a}_p [\hat{V}_{\mathrm{NN}}, \hat{a}^\dagger_{p_1} \hat{a}_{h_1} \hat{a}^\dagger_{p_2} \hat{a}_{h_2}] \, | \mathrm{SD} \rangle}_{A_{12,\mathrm{V}}} . \tag{A.58}$$

For reasons of lucidity, we neglect the indices representing the m-scheme for the following derivation. Therefore, we write A_{12} instead of $[A_{12}]_{ph;p_1p_2h_1h_2}$.

The commutator of the term including the kinetic energy can be summarized by application of the commutation relations obtained in Sec. A.1 and Sec. 5.2, leading to

$$\begin{aligned} A_{12,\mathrm{T}} = &\sum_{jj'} t_{jj'} \, \langle \mathrm{SD} | \, \hat{a}^\dagger_h \hat{a}_p \hat{a}^\dagger_{p_1} \hat{a}_{h_1} (\delta_{j'p_2} \hat{a}^\dagger_j \hat{a}_{h_2} - \delta_{jh_2} \hat{a}^\dagger_{p_2} \hat{a}_{j'}) \, | \mathrm{SD} \rangle \\ &+ \sum_{jj'} t_{jj'} \, \langle \mathrm{SD} | \, \hat{a}^\dagger_h \hat{a}_p (\delta_{j'p_1} \hat{a}^\dagger_j \hat{a}_{h_1} - \delta_{jh_1} \hat{a}^\dagger_{p_1} \hat{a}_{j'}) \hat{a}^\dagger_{p_2} \hat{a}_{h_2} \, | \mathrm{SD} \rangle \ . \end{aligned} \tag{A.59}$$

The four terms of interest are proportional to the following expectation values

$$\begin{aligned} &\langle \mathrm{SD} | \, \hat{a}^\dagger_h \hat{a}_p \hat{a}^\dagger_{p_1} \hat{a}_{h_1} \hat{a}^\dagger_j \hat{a}_{h_2} \, | \mathrm{SD} \rangle = \delta_{hh_1} \delta_{pp_1} \delta_{jh_2} \\ &\langle \mathrm{SD} | \, \hat{a}^\dagger_h \hat{a}_p \hat{a}^\dagger_{p_1} \hat{a}_{h_1} \hat{a}^\dagger_{p_2} \hat{a}_{j'} \, | \mathrm{SD} \rangle = 0 \\ &\langle \mathrm{SD} | \, \hat{a}^\dagger_h \hat{a}_p \hat{a}^\dagger_j \hat{a}_{h_1} \hat{a}^\dagger_{p_2} \hat{a}_{h_2} \, | \mathrm{SD} \rangle = -\delta_{hh_1} \delta_{pp_2} \delta_{jh_2} + \delta_{hh_2} \delta_{pp_2} \delta_{jh_1} \\ &\langle \mathrm{SD} | \, \hat{a}^\dagger_h \hat{a}_p \hat{a}^\dagger_{p_1} \hat{a}_{j'} \hat{a}^\dagger_{p_2} \hat{a}_{h_2} \, | \mathrm{SD} \rangle = \delta_{hh_2} \delta_{pp_1} \delta_{p_2 j'} \end{aligned} \tag{A.60}$$

These expectation values are evaluated via contractions and exploitation of the disjointness of particles and holes. Furthermore, only non-vanishing contractions of the form $\hat{a}^{\dagger\,\frown}_h \hat{a}_{h'} = \delta_{hh'}$ and $\hat{a}_p \hat{a}^\dagger_{p'} = \delta_{pp'}$ are considered. Finally, we find

$$A_{12,\mathrm{T}} = t_{h_2p_2} \delta_{hh_1} \delta_{pp_1} + t_{h_1p_1} \delta_{hh_2} \delta_{pp_2} - t_{h_2p_1} \delta_{hh_1} \delta_{pp_2} - t_{h_1p_2} \delta_{hh_2} \delta_{pp_1} \, . \tag{A.61}$$

The second term in Eq. (A.58) can be summarized with the aid of commutation relations to

$$\begin{aligned} A_{12,\mathrm{V}} = \langle \mathrm{SD}|\, \hat{a}_h^\dagger \hat{a}_p \hat{a}_{p_1}^\dagger \hat{a}_{h_1} \big(\frac{1}{2}\sum_{ijj'} \bar{v}_{ij,p_2j'} \hat{a}_i^\dagger \hat{a}_j^\dagger \hat{a}_{j'} \hat{a}_{h_2} + \frac{1}{2}\sum_{ii'j'} \bar{v}_{ih_2,i'j'} \hat{a}_{p_2}^\dagger \hat{a}_i^\dagger \hat{a}_{j'} \hat{a}_{i'}\big)\, |\mathrm{SD}\rangle \\ + \langle \mathrm{SD}|\, \hat{a}_h^\dagger \hat{a}_p \big(\frac{1}{2}\sum_{ijj'} \bar{v}_{ij,p_1j'} \hat{a}_i^\dagger \hat{a}_j^\dagger \hat{a}_{j'} \hat{a}_{h_1} + \frac{1}{2}\sum_{ii'j'} \bar{v}_{ih_1,i'j'} \hat{a}_{p_1}^\dagger \hat{a}_i^\dagger \hat{a}_{j'} \hat{a}_{i'}\big) \hat{a}_{p_1}^\dagger \hat{a}_{h_2}\, |\mathrm{SD}\rangle \ . \end{aligned} \tag{A.62}$$

Analogously to the kinetic energy part, the commutators containing the potential energy yield

$$\begin{aligned} \langle \mathrm{SD}|\, \hat{a}_h^\dagger \hat{a}_p \hat{a}_{p_1}^\dagger \hat{a}_{h_1} \hat{a}_i^\dagger \hat{a}_j^\dagger \hat{a}_{j'} \hat{a}_{h_2}\, |\mathrm{SD}\rangle &= \delta_{hh_1}\delta_{pp_1} \left(\delta_{ih_2}\delta_{jj'} - \delta_{ij'}\delta_{jh_2}\right) \\ \langle \mathrm{SD}|\, \hat{a}_h^\dagger \hat{a}_p \hat{a}_{p_1}^\dagger \hat{a}_{h_1} \hat{a}_{p_2}^\dagger \hat{a}_i^\dagger \hat{a}_{j'} \hat{a}_{i'}\, |\mathrm{SD}\rangle &= 0 \\ \langle \mathrm{SD}|\, \hat{a}_h^\dagger \hat{a}_p \hat{a}_i^\dagger \hat{a}_j^\dagger \hat{a}_{j'} \hat{a}_{h_1} \hat{a}_{p_2}^\dagger \hat{a}_{h_2}\, |\mathrm{SD}\rangle &= \delta_{hh_1}\left[\delta_{pp_2}\left(\delta_{ij'}\delta_{jh_2} - \delta_{jj'}\delta_{ih_2}\right) + \delta_{p_2j'}\left(\delta_{pi}\delta_{jh_2} - \delta_{pj}\delta_{ih_2}\right)\right] \\ &\quad + \delta_{hh_2}\left[\delta_{pp_2}\left(-\delta_{ij'}\delta_{jh_1} + \delta_{ih_1}\delta_{jj'}\right) + \delta_{p_2j'}\left(\delta_{pj}\delta_{ih_1} - \delta_{pi}\delta_{jh_1}\right)\right] \\ &\quad + \delta_{pp_2}\delta_{hj'}\left(\delta_{ih_2}\delta_{jh_1} - \delta_{ih_1}\delta_{jh_2}\right) \\ \langle \mathrm{SD}|\, \hat{a}_h^\dagger \hat{a}_p \hat{a}_{p_1}^\dagger \hat{a}_i^\dagger \hat{a}_{j'} \hat{a}_{i'} \hat{a}_{p_2}^\dagger \hat{a}_{h_2}\, |\mathrm{SD}\rangle &= \delta_{pp_1}\left[\delta_{hh_2}\left(\delta_{ij'}\delta_{i'p_2} - \delta_{ii'}\delta_{j'p_2}\right) + \delta_{ih_2}\left(\delta_{hi'}\delta_{j'p_2} - \delta_{hj'}\delta_{i'p_2}\right)\right] \end{aligned}$$

Thus, exploiting the antisymmetry of the interaction matrix elements in Eq. (3.4) and relabeling of the summation indices, we find

$$\begin{aligned} A_{12,\mathrm{V}} = \delta_{hh_1}\delta_{pp_1}\sum_j \bar{v}_{h_2j,p_2j} - \delta_{hh_1}\delta_{pp_2}\sum_j \bar{v}_{h_2j,p_1j} + \delta_{hh_1}\bar{v}_{ph_2,p_1p_2} + \delta_{hh_2}\bar{v}_{ph_1,p_2p_1} \\ + \delta_{hh_2}\delta_{pp_2}\sum_j \bar{v}_{h_1j,p_1j} + \delta_{pp_2}\bar{v}_{h_1h_2,hp_1} - \delta_{pp_1}\delta_{hh_2}\sum_j \bar{v}_{h_1j,p_2j} - \delta_{pp_1}\bar{v}_{h_1h_2,hp_2} \ . \end{aligned} \tag{A.63}$$

Together with Eq. (A.61) and the definition of the single-particle energies (5.73), the A_{12} matrix reads

$$\begin{aligned} [A_{12}]_{ph;p_1p_2h_1h_2} = \left(1 - P(h_1,h_2)\right)\delta_{hh_1}v_{ph_2,p_1p_2} - \left(1 - P(p_1,p_2)\right)\delta_{pp_1}v_{h_1h_2,hp_2} \\ + \left(1 - P(p_1,p_2)\right)\left(1 - P(h_1,h_2)\right)\delta_{hh_1}\delta_{pp_1}\epsilon_{h_2p_2} \end{aligned} \tag{A.64}$$

where the operator $P(p_1,p_2)$, which changes the indices p_1 and p_2, was introduced.

Coupled Representation The starting point for the derivation of the coupled A_{12} matrix is the same matrix element as for the m-scheme representation in Eq. (A.57) but with the coupled 1p1h annihilator

$$\hat{\mathcal{A}}_{p\bar{h}}(JM) = \sum_{m_p,m_h} (-1)^{j_h - m_h} \begin{pmatrix} j_p & j_h \\ m_p & -m_h \end{pmatrix} \begin{matrix} J \\ M \end{matrix} \hat{\mathcal{A}}_{ph} \tag{A.65}$$

and coupled 2p2h creator

$$\hat{\mathcal{A}}^{\dagger}_{(p_1p_2)J_p(\hbar_1\hbar_2)J_h} = \mathcal{N}_{p_1,p_2}\mathcal{N}_{\hbar_1,\hbar_2} \sum_{M_p,M_h} (-1)^{J_h-M_h} \begin{pmatrix} J_p & J_h \\ M_p & -M_h \end{pmatrix} \begin{pmatrix} J \\ M \end{pmatrix} \sum_{m_{p_1},m_{p_2}} \begin{pmatrix} j_{p_1} & j_{p_2} \\ m_{p_1} & m_{p_2} \end{pmatrix} \begin{pmatrix} J_p \\ M_p \end{pmatrix} \times \sum_{m_{h_1},m_{h_2}} \begin{pmatrix} j_{h_1} & j_{h_2} \\ m_{h_1} & m_{h_2} \end{pmatrix} \begin{pmatrix} J_h \\ M_h \end{pmatrix} \hat{\mathcal{A}}^{\dagger}_{p_1p_2h_1h_2} \,. \tag{A.66}$$

For the sake of brevity, we focus on the first term in Eq. (A.64). The derivation of the other terms is similar. The first part of the coupled A_{12} matrix reads

$$\begin{aligned} &A_{12,\text{part1}} \\ &= \sum_{m_p,m_h} (-1)^{j_h-m_h} \begin{pmatrix} j_p & j_h \\ m_p & -m_h \end{pmatrix} \begin{pmatrix} J \\ M \end{pmatrix} \mathcal{N}_{p_1,p_2}\mathcal{N}_{\hbar_1,\hbar_2} \sum_{M_p,M_h} (-1)^{J_h-M_h} \begin{pmatrix} J_p & J_h \\ M_p & -M_h \end{pmatrix} \begin{pmatrix} J \\ M \end{pmatrix} \\ &\times \sum_{m_{p_1},m_{p_2}} \begin{pmatrix} j_{p_1} & j_{p_2} \\ m_{p_1} & m_{p_2} \end{pmatrix} \begin{pmatrix} J_p \\ M_p \end{pmatrix} \sum_{m_{h_1},m_{h_2}} \begin{pmatrix} j_{h_1} & j_{h_2} \\ m_{h_1} & m_{h_2} \end{pmatrix} \begin{pmatrix} J_h \\ M_h \end{pmatrix} \delta_{hh_1}\, \bar{v}_{ph_2,p_1p_2} \,. \end{aligned} \tag{A.67}$$

Here, the matrix element $\bar{v}_{ph_2,p_1p_2}$ is still given with respect to the uncoupled basis and needs to be transformed into the coupled representation. Therefore, we can insert the basis transformation for normalized two-body states (2.8), apply the Wigner-Eckart theorem (2.20) and get

$$\begin{aligned} \bar{v}_{ph_2,p_1p_2} &= \langle ph_2 | \, \hat{V}_{\text{NN}} \, | p_1p_2 \rangle \\ &= \sum_{J'M'} \left(\mathcal{N}_{p,\hbar_2}\mathcal{N}_{p_1p_2}\right)^{-1} \begin{pmatrix} j_p & j_{h_2} \\ m_p & m_{h_2} \end{pmatrix} \begin{pmatrix} J' \\ M' \end{pmatrix} \begin{pmatrix} j_{p_1} & j_{p_2} \\ m_{p_1} & m_{p_2} \end{pmatrix} \begin{pmatrix} J' \\ M' \end{pmatrix} \langle p\hbar_2, J' | \, \hat{V}_{\text{NN}} \, | p_1p_2, J' \rangle \,. \end{aligned} \tag{A.68}$$

For lucidity, the sums and the Clebsch-Gordan coefficients in Eq. (A.67) and Eq. (A.68) are considered separately. With the aid of the orthogonality relation (2.4), the number of CGCs

can be reduced

$$\sum_{m_p,m_h}\sum_{M_p,M_h}\sum_{m_{p_1},m_{p_2}}\sum_{m_{h_1},m_{h_2}}\sum_{J'M'}\begin{pmatrix} j_p & j_h & J \\ m_p & -m_h & M\end{pmatrix}\begin{pmatrix} J_p & J_h & J \\ M_p & -M_h & M\end{pmatrix}\begin{pmatrix} j_{p_1} & j_{p_2} & J_p \\ m_{p_1} & m_{p_2} & M_p\end{pmatrix}$$
$$\times\begin{pmatrix} j_{h_1} & j_{h_2} & J_h \\ m_{h_1} & m_{h_2} & M_h\end{pmatrix}\begin{pmatrix} j_p & j_{h_2} & J' \\ m_p & m_{h_2} & M'\end{pmatrix}\begin{pmatrix} j_{p_1} & j_{p_2} & J' \\ m_{p_1} & m_{p_2} & M'\end{pmatrix}\delta_{hh_1}$$
$$=\sum_{m_h}\sum_{m_p}\sum_{M_p,M_h}\sum_{m_{h_1},m_{h_2}}\sum_{J'M'}\begin{pmatrix} j_p & j_h & J \\ m_p & -m_h & M\end{pmatrix}\begin{pmatrix} J_p & J_h & J \\ M_p & -M_h & M\end{pmatrix}\begin{pmatrix} j_{h_1} & j_{h_2} & J_h \\ m_{h_1} & m_{h_2} & M_h\end{pmatrix}$$
$$\times\begin{pmatrix} j_p & j_{h_2} & J' \\ m_p & m_{h_2} & M'\end{pmatrix}\delta_{J_pJ'}\delta_{M_pM'}\delta_{hh_1}$$
$$=\sum_{m_p}\sum_{M_p,M_h}\sum_{m_{h_1},m_{h_2}}\begin{pmatrix} j_p & j_{h_1} & J \\ m_p & -m_{h_1} & M\end{pmatrix}\begin{pmatrix} J_p & J_h & J \\ M_p & -M_h & M\end{pmatrix}\begin{pmatrix} j_{h_1} & j_{h_2} & J_h \\ m_{h_1} & m_{h_2} & M_h\end{pmatrix}$$
$$\times\begin{pmatrix} j_p & j_{h_2} & J_p \\ m_p & m_{h_2} & M_p\end{pmatrix}\delta_{hh_1}\,. \tag{A.69}$$

In the last step, the Kronecker deltas were evaluated. For the sake of clarity, the CGCs are considered separately for the further derivation of the coupled A_{12} matrix. Converting the CGCs into $3j$ symbols, applying their symmetry properties (2.12) - (2.13) in order to rearrange the columns and exploiting the symmetry of the sum over M_p and m_{h_2}, leads to

$$\begin{pmatrix} j_p & j_{h_1} & J \\ m_p & -m_{h_1} & M\end{pmatrix}\begin{pmatrix} J_p & J_h & J \\ M_p & -M_h & M\end{pmatrix}\begin{pmatrix} j_{h_1} & j_{h_2} & J_h \\ m_{h_1} & m_{h_2} & M_h\end{pmatrix}\begin{pmatrix} j_p & j_{h_2} & J_p \\ m_p & m_{h_2} & M_p\end{pmatrix}$$
$$=\hat{J}^2\hat{J}_p\hat{J}_h(-1)^{M+j_p-j_{h_1}}(-1)^{M+J_p-J_h}(-1)^{M_h+j_{h_1}-j_{h_2}}(-1)^{M_p+j_p-j_{h_2}}$$
$$\times\begin{pmatrix} j_p & j_{h_1} & J \\ m_p & -m_{h_1} & -M\end{pmatrix}\begin{pmatrix} J_p & J_h & J \\ M_p & -M_h & -M\end{pmatrix}\begin{pmatrix} j_{h_1} & j_{h_2} & J_h \\ m_{h_1} & m_{h_2} & -M_h\end{pmatrix}\begin{pmatrix} j_p & j_{h_2} & J_p \\ m_p & m_{h_2} & -M_p\end{pmatrix}$$
$$=\hat{J}^2\hat{J}_p\hat{J}_h(-1)^{M+j_p-j_{h_1}}(-1)^{M+J_p-J_h}(-1)^{M_h+j_{h_1}-j_{h_2}}(-1)^{M_p+j_p-j_{h_2}}(-1)^{j_{h_1}+j_p+J}$$
$$\times\begin{pmatrix} j_{h_1} & J & j_p \\ m_{h_1} & M & -m_p\end{pmatrix}\begin{pmatrix} J_p & J & J_h \\ M_p & M & M_h\end{pmatrix}(-1)^{j_{h_1}+j_{h_2}+J_h}\begin{pmatrix} j_{h_1} & j_{h_2} & J_h \\ -m_{h_1} & m_{h_2} & M_h\end{pmatrix}(-1)^{j_p+j_{h_2}+J_p}$$
$$\times\begin{pmatrix} J_p & j_{h_2} & j_p \\ M_p & -m_{h_2} & m_p\end{pmatrix}\,. \tag{A.70}$$

The arising phase factors can be summarized with the phase factors stemming from the definition of coupled 1p1h creation and 2p2h annihilation operators from Eq. (A.67). We then find

$$\begin{aligned}
&(-1)^{M+j_p-j_{h_1}}(-1)^{M+J_p-J_h}(-1)^{M_h+j_{h_1}-j_{h_2}}(-1)^{M_p+j_p-j_{h_2}}(-1)^{j_{h_1}+j_p+J} \\
&\times (-1)^{j_{h_1}+j_{h_2}+J_h}(-1)^{j_p+j_{h_2}+J_p}(-1)^{j_{h_1}-m_{h_1}}(-1)^{J_h-M_h} \\
&= (-1)^{j_{h_1}+j_{h_2}+j_p-m_{h_1}-m_{h_2}-m_p}(-1)^{j_p+j_{h_2}+J+J_h}\,,
\end{aligned} \tag{A.71}$$

where we use the additivity of the projection quantum numbers and the considerations on phase factors including single-particle angular momenta from Sec. A.3. The first factor is needed for the transformation of the $3j$ symbols to a $6j$ symbol. Furthermore, an additional sum over M is required for the conversion into a $6j$ symbol. Since the matrix element in Eq. (A.68) is independent of M due to the Wigner-Eckart theorem, the summation over M results in $2J+1$ terms. Therefore, the equation can be summed over M while dividing by $\hat{J}^2$, leading to the $6j$ symbol

$$\begin{aligned}
\begin{Bmatrix} J_p & J & J_h \\ j_{h_1} & j_{h_2} & j_p \end{Bmatrix} = \sum_{m_p,M}\sum_{M_p,M_h}\sum_{m_{h_1},m_{h_2}} (-1)^{j_{h_1}+j_{h_2}+j_p-m_{h_1}-m_{h_2}-m_p} \begin{pmatrix} j_{h_1} & J & j_p \\ m_{h_1} & M & -m_p \end{pmatrix} \\
\times \begin{pmatrix} J_p & J & J_h \\ M_p & M & M_h \end{pmatrix} \begin{pmatrix} j_{h_1} & j_{h_2} & J_h \\ -m_{h_1} & m_{h_2} & M_h \end{pmatrix} \begin{pmatrix} J_p & j_{h_2} & j_p \\ M_p & -m_{h_2} & m_p \end{pmatrix}.
\end{aligned} \tag{A.72}$$

In summary, including the prefactors obtained within the last steps together with the $6j$ symbol into Eq. (A.67) leads to

$$\begin{aligned}
A_{12,\text{part1}} =& \mathcal{N}_{p_1,p_2}\mathcal{N}_{\hbar_1,\hbar_2}\left(\mathcal{N}_{p,\hbar_2}\mathcal{N}_{p_1,p_2}\right)^{-1}\delta_{hh_1}\hat{J}^2\hat{J}_p\hat{J}_h\hat{J}^{-2}(-1)^{j_p+j_{h_2}+J+J_h} \\
&\times \begin{Bmatrix} J_p & J & J_h \\ j_{h_1} & j_{h_2} & j_p \end{Bmatrix} \langle p\hbar_2, J_p|\,\hat{V}_{\text{NN}}\,|p_1p_2, J_p\rangle \\
=& \delta_{hh_1}(-1)^{j_p+j_{h_2}+J+J_h}\,(1+\delta_{h_1h_2})^{-\frac{1}{2}}\,\hat{J}_p\hat{J}_h \begin{Bmatrix} J_p & J & J_h \\ j_{h_1} & j_{h_2} & j_p \end{Bmatrix} \langle p\hbar_2, J_p|\,\hat{V}_{\text{NN}}\,|p_1p_2, J_p\rangle\,.
\end{aligned} \tag{A.73}$$

In the last step, the normalization factors are inserted. The one with mixed ph is equal to one due to the disjointness of particles and holes. As mentioned before, the remaining terms in Eq. (A.64) can be derived similarly. The term in the A_{12} matrix with permutation operator $P(h_1,h_2)$, which changes the indices h_1 and h_2, needs an additional phase factor. Up to Eq. (A.66), the derivation is the same for the interchanged indices h_1 and h_2. But in the next step, the matrix element depends on h_1. In order to summarize the contributions into a $6j$ symbol in Eq. (A.70), the columns of the CGC describing the coupling of h_1 and h_2 to a total angular momentum of J_h, which is part of the coupled 2p2h creator, needs to be changed as well, leading to a phase factor $(-1)^{j_{h_1}+j_{h_2}-J_h}$. The term including the single-particle energies still contains sums and CGCs, without further summary. Thus, final result of the coupled A_{12} matrix is given by

$$
\begin{aligned}
[A_{12}]_{p\hbar;p_1p_2\hbar_1\hbar_2 J_p J_h} = {} & \left(1-(-1)^{j_{h_1}+j_{h_2}-J_h} P(h_1,h_2)\right) \delta_{hh_1} (-1)^{j_p+j_{h_2}+J+J_h} \left(1+\delta_{h_1h_2}\right)^{-\frac{1}{2}} \\
& \times \hat{J}_p \hat{J}_h \begin{Bmatrix} J_p & J & J_h \\ j_{h_1} & j_{h_2} & j_p \end{Bmatrix} \langle p_1 p_2, J_p | \, \hat{V}_{\mathrm{NN}} \, | p \hbar_2, J_p \rangle \\
& - \left(1-(-1)^{j_{p_1}+j_{p_2}-J_p} P(p_1,p_2)\right) \delta_{pp_1} (-1)^{j_{p_1}+j_{p_2}+J+J_h} \left(1+\delta_{p_1p_2}\right)^{-\frac{1}{2}} \\
& \times \hat{J}_p \hat{J}_h \begin{Bmatrix} J_h & J & J_p \\ j_{p_1} & j_{p_2} & j_h \end{Bmatrix} \langle \hbar p_2, J_h | \, \hat{V}_{\mathrm{NN}} \, | \hbar_1 \hbar_2, J_h \rangle \\
& + \sum_{m_p, m_h} (-1)^{j_h - m_h} \begin{pmatrix} j_p & j_h & \\ m_p & -m_h & \end{pmatrix} \begin{matrix} \\ \\ J \\ M \end{matrix} \Bigg) \mathcal{N}_{p_1,p_2} \mathcal{N}_{\hbar_1,\hbar_2} \\
& \times \sum_{M_p, M_h} (-1)^{J_h - M_h} \begin{pmatrix} J_p & J_h & \\ M_p & -M_h & \end{pmatrix} \begin{matrix} \\ \\ J \\ M \end{matrix} \Bigg) \sum_{m_{p_1}, m_{p_2}} \begin{pmatrix} j_{p_1} & j_{p_2} & \\ m_{p_1} & m_{p_2} & \end{pmatrix} \begin{matrix} \\ \\ J_p \\ M_p \end{matrix} \Bigg) \\
& \times \sum_{m_{h_1}, m_{h_2}} \begin{pmatrix} j_{h_1} & j_{h_2} & \\ m_{h_1} & m_{h_2} & \end{pmatrix} \begin{matrix} \\ \\ J_h \\ M_h \end{matrix} \Bigg) \left(1-P(p_1,p_2)\right) \left(1-P(h_1,h_2)\right) \delta_{hh_1} \delta_{pp_1} \epsilon_{h_2 p_2}
\end{aligned}
\tag{A.74}
$$

As concluding remark, we consider practical calculations. The term proportional to δ_{hh_2} includes a phase factor with several arguments. In order to minimize the number of angular momenta in the phase factor, the order of p and $\hbar_2$ can be changed. This leads to an additional phase factor, according to Eq. (2.10). All phase factors together and the overall minus sign can be summarized, which finally gives

$$
+\delta_{hh_2} \left(1+\delta_{h_1h_2}\right)^{-\frac{1}{2}} (-1)^{J_p+J+j_{h_1}+j_{h_2}} \hat{J}_p \hat{J}_h \begin{Bmatrix} J_p & J & J_h \\ j_{h_1} & j_{h_2} & j_p \end{Bmatrix} \langle p_1 p_2, J_p | \, \hat{V}_{\mathrm{NN}} \, | \hbar_2 p, J_p \rangle \ . \tag{A.75}
$$

For the last term, we choose $M = 0$, since the single-particle energies are independent of M, making some of the sums collapsing.

A.7 Derivation of the A_{22} Matrix

For the derivation of the A_{22} matrix we calculate the matrix elements

$$(A_{22})_{ij} = \langle \mathrm{SD}| \, [\hat{\mathcal{A}}_{2,i}, [\hat{H}, \hat{\mathcal{A}}^\dagger_{2,j}]] \, |\mathrm{SD}\rangle \tag{A.76}$$

with the creation and annihilation operators summarized in Tab. 5.1 and Tab. 7.1.

m-scheme Representation The derivation of the uncoupled A_{22} matrix follows the same steps as for the uncoupled A_{12} matrix in the last section. Inserting the definitions of the Hamiltonian, the second-order creator (6.19) and its adjoint, the matrix element reads

$$\begin{aligned} A_{22} = &\underbrace{\langle \mathrm{SD}| \, \hat{a}^\dagger_{h'_1} \hat{a}_{p'_1} \hat{a}^\dagger_{h'_2} \hat{a}_{p'_2} [\hat{T}, \hat{a}^\dagger_{p_1} \hat{a}_{h_1} \hat{a}^\dagger_{p_2} \hat{a}_{h_2}] \, |\mathrm{SD}\rangle}_{A_{22,\mathrm{T}}} \\ &+ \underbrace{\langle \mathrm{SD}| \, \hat{a}^\dagger_{h'_1} \hat{a}_{p'_1} \hat{a}^\dagger_{h'_2} \hat{a}_{p'_2} [\hat{V}_{\mathrm{NN}}, \hat{a}^\dagger_{p_1} \hat{a}_{h_1} \hat{a}^\dagger_{p_2} \hat{a}_{h_2}] \, |\mathrm{SD}\rangle}_{A_{22,\mathrm{V}}} . \end{aligned} \tag{A.77}$$

Here, the indices of $[A_{22}]_{p_1 p_2 h_1 h_2; p'_1 p'_2 h'_1 h'_2}$ are abbreviated as A_{22} for the sake of brevity. The first term depends on the kinetic energy. Analogously to the derivation of the A_{12} matrix, the matrix element can be written as

$$\begin{aligned} A_{22,\mathrm{T}} = &\sum_{jj'} t_{jj'} \, \langle \mathrm{SD}| \, \hat{a}^\dagger_{h'_1} \hat{a}_{p'_1} \hat{a}^\dagger_{h'_2} \hat{a}_{p'_2} \hat{a}^\dagger_{p_1} \hat{a}_{h_1} (\delta_{j'p_2} \hat{a}^\dagger_j \hat{a}_{h_2} - \delta_{jh_2} \hat{a}^\dagger_{p_2} \hat{a}_{j'}) \, |\mathrm{SD}\rangle \\ &+ \sum_{jj'} t_{jj'} \, \langle \mathrm{SD}| \, \hat{a}^\dagger_{h'_1} \hat{a}_{p'_1} \hat{a}^\dagger_{h'_2} \hat{a}_{p'_2} (\delta_{j'p_1} \hat{a}^\dagger_j \hat{a}_{h_1} - \delta_{jh_1} \hat{a}^\dagger_{p_1} \hat{a}_{j'}) \hat{a}^\dagger_{p_2} \hat{a}_{h_2} \, |\mathrm{SD}\rangle \, . \end{aligned} \tag{A.78}$$

Thus, we get 4 expectation values that are calculated via contractions. Note that particle and hole states are disjoint. Furthermore, the states are ordered, i.e. $p_1 < p_2$ and $p'_1 < p'_2$, c.f. Ref. [43]. While the Kronecker delta $\delta_{p_1 p'_2}$ may become one, the product $\delta_{p_1 p'_2} \delta_{p_2 p'_1}$ is indeed zero due to this ordering. Omitting these contributions, we find

$$\begin{aligned} \langle \mathrm{SD}| \, \hat{a}^\dagger_{h'_1} \hat{a}_{p'_1} \hat{a}^\dagger_{h'_2} \hat{a}_{p'_2} \hat{a}^\dagger_{p_1} \hat{a}_{h_1} \hat{a}^\dagger_j \hat{a}_{h_2} \, |\mathrm{SD}\rangle &= \delta_{h_1 h'_1} \delta_{h_2 h'_2} \left(\delta_{j p'_2} \delta_{p_1 p'_1} - \delta_{p_1 p'_2} \delta_{j p'_1} \right) \\ \langle \mathrm{SD}| \, \hat{a}^\dagger_{h'_1} \hat{a}_{p'_1} \hat{a}^\dagger_{h'_2} \hat{a}_{p'_2} \hat{a}^\dagger_{p_1} \hat{a}_{h_1} \hat{a}^\dagger_{p_2} \hat{a}_{j'} \, |\mathrm{SD}\rangle &= \delta_{p_2 p'_2} \delta_{p_1 p'_1} \left(-\delta_{h'_1 j'} \delta_{h_1 h'_2} + \delta_{h_1 h'_1} \delta_{h'_2 j'} \right) \\ \langle \mathrm{SD}| \, \hat{a}^\dagger_{h'_1} \hat{a}_{p'_1} \hat{a}^\dagger_{h'_2} \hat{a}_{p'_2} \hat{a}^\dagger_j \hat{a}_{h_1} \hat{a}^\dagger_{p_2} \hat{a}_{h_2} \, |\mathrm{SD}\rangle &= \delta_{h_2 h'_2} \delta_{h_1 h'_1} \left(\delta_{p'_1 j} \delta_{p_2 p'_2} - \delta_{j p'_2} \delta_{p_2 p'_1} \right) \\ \langle \mathrm{SD}| \, \hat{a}^\dagger_{h'_1} \hat{a}_{p'_1} \hat{a}^\dagger_{h'_2} \hat{a}_{p'_2} \hat{a}^\dagger_{p_1} \hat{a}_{j'} \hat{a}^\dagger_{p_2} \hat{a}_{h_2} \, |\mathrm{SD}\rangle &= \delta_{p_1 p'_1} \delta_{p_2 p'_2} \left(-\delta_{h_2 h'_2} \delta_{j' h'_1} + \delta_{h_2 h'_1} \delta_{h'_2 j'} \right) \end{aligned} \tag{A.79}$$

Contributions depending on a mixed ph configuration, as for instance $t_{p_1 h_1}$, do not exist. This becomes clear while considering the first expectation value in Eq. (A.79) which comprises two hole creators and two hole annihilators. In order to ensure a non-zero Kronecker delta, these hole operators can only be contracted in one possible way, namely $\delta_{h_1 h'_1} \delta_{h_2 h'_2}$ due to the ordering of states. The two remaining particle annihilators and the general creator $\hat{a}^\dagger_j$ can be combined in two ways. The result is given by Kronecker deltas connecting j and a particle

state. In combination with the Kronecker delta in Eq. (A.78), which comes from the evaluation of the commutator, it is obvious that mixed one-body ph configurations do not exist for the A_{22} matrix. With these considerations, the first part of the matrix then reads

$$\begin{aligned} A_{22,\mathrm{T}} = \delta_{h_2h_2'}\delta_{h_1h_1'}\left(\delta_{p_1p_1'}t_{p_2'p_2} + \delta_{p_2p_2'}t_{p_1'p_1} - \delta_{p_1p_2'}t_{p_1'p_2} - \delta_{p_1'p_2}t_{p_2'p_1}\right) \\ + \delta_{p_2p_2'}\delta_{p_1p_1'}\left(-\delta_{h_1h_1'}t_{h_2'h_2} - \delta_{h_2h_2'}t_{h_1'h_1} + \delta_{h_1'h_2}t_{h_1h_2'} + \delta_{h_1h_2'}t_{h_1'h_2}\right) . \end{aligned} \tag{A.80}$$

Applying the commutation relations from the last section, the second term in Eq. (A.77) becomes

$$\begin{aligned} A_{22,\mathrm{V}} = \langle \mathrm{SD}|\, \hat{a}^\dagger_{h_1'}\hat{a}_{p_1'}\hat{a}^\dagger_{h_2'}\hat{a}_{p_2'}\hat{a}^\dagger_{p_1}\hat{a}_{h_1}(\frac{1}{2}\sum_{ijj'}\bar{v}_{ij,p_2j'}\hat{a}^\dagger_i\hat{a}^\dagger_j\hat{a}_{j'}\hat{a}_{h_2} + \frac{1}{2}\sum_{ii'j'}\bar{v}_{ih_2,i'j'}\hat{a}^\dagger_{p_2}\hat{a}^\dagger_i\hat{a}_{j'}\hat{a}_{i'})\,|\mathrm{SD}\rangle \\ + \langle \mathrm{SD}|\, \hat{a}^\dagger_{h_1'}\hat{a}_{p_1'}\hat{a}^\dagger_{h_2'}\hat{a}_{p_2'}(\frac{1}{2}\sum_{ijj'}\bar{v}_{ij,p_1j'}\hat{a}^\dagger_i\hat{a}^\dagger_j\hat{a}_{j'}\hat{a}_{h_1} + \frac{1}{2}\sum_{ii'j'}\bar{v}_{ih_1,i'j'}\hat{a}^\dagger_{p_1}\hat{a}^\dagger_i\hat{a}_{j'}\hat{a}_{i'})\hat{a}^\dagger_{p_1}\hat{a}_{h_2}\,|\mathrm{SD}\rangle . \end{aligned} \tag{A.81}$$

The four terms of interest are

$$\begin{aligned} &\langle \mathrm{SD}|\, \hat{a}^\dagger_{h_1'}\hat{a}_{p_1'}\hat{a}^\dagger_{h_2'}\hat{a}_{p_2'}\hat{a}^\dagger_{p_1}\hat{a}_{h_1}\hat{a}^\dagger_i\hat{a}^\dagger_j\hat{a}_{j'}\hat{a}_{h_2}\,|\mathrm{SD}\rangle \\ &\langle \mathrm{SD}|\, \hat{a}^\dagger_{h_1'}\hat{a}_{p_1'}\hat{a}^\dagger_{h_2'}\hat{a}_{p_2'}\hat{a}^\dagger_{p_1}\hat{a}_{h_1}\hat{a}^\dagger_{p_2}\hat{a}^\dagger_i\hat{a}_{j'}\hat{a}_{i'}\,|\mathrm{SD}\rangle \\ &\langle \mathrm{SD}|\, \hat{a}^\dagger_{h_1'}\hat{a}_{p_1'}\hat{a}^\dagger_{h_2'}\hat{a}_{p_2'}\hat{a}^\dagger_i\hat{a}^\dagger_j\hat{a}_{j'}\hat{a}_{h_1}\hat{a}^\dagger_{p_2}\hat{a}_{h_2}\,|\mathrm{SD}\rangle \\ &\langle \mathrm{SD}|\, \hat{a}^\dagger_{h_1'}\hat{a}_{p_1'}\hat{a}^\dagger_{h_2'}\hat{a}_{p_2'}\hat{a}^\dagger_{p_1}\hat{a}^\dagger_i\hat{a}_{j'}\hat{a}_{i'}\hat{a}^\dagger_{p_2}\hat{a}_{h_2}\,|\mathrm{SD}\rangle \end{aligned} \tag{A.82}$$

The evaluation via contractions results in 52 terms that are not given in detail here. These can be further summarized into contributions, which give in combination with Eq. (A.80) the single-particle energies and additional two-body contributions. Introducing the permutation operator, the final result is

$$\begin{aligned} [A_{22}]_{p_1p_2h_1h_2;p_1'p_2'h_1'h_2'} = &\left(\epsilon_{p_1,p_1'}\delta_{p_2'p_2} + \epsilon_{p_2,p_2'}\delta_{p_1'p_1} - \epsilon_{p_1'p_2}\delta_{p_1p_2'} - \epsilon_{p_2'p_1}\delta_{p_1'p_2}\right)\delta_{h_1'h_1}\delta_{h_2'h_2} \\ &- \left(\epsilon_{h_1,h_1'}\delta_{h_2'h_2} + \epsilon_{h_2,h_2'}\delta_{h_1'h_1} - \epsilon_{h_1h_2'}\delta_{h_1'h_2} - \epsilon_{h_1'h_2}\delta_{h_1h_2'}\right)\delta_{p_1'p_1}\delta_{p_2'p_2} \\ &- \left(1 - P(p_1',p_2')\right)\left(1 - P(h_1',h_2')\right)\left(1 - P(p_1,p_2)\right)\left(1 - P(h_1,h_2)\right) \\ &\times \delta_{h_1'h_1}\delta_{p_1'p_1}\bar{v}_{h_2p_2',h_2'p_2} + \delta_{p_2'p_2}\delta_{p_1'p_1}\bar{v}_{h_1h_2,h_1'h_2'} + \delta_{h_1'h_1}\delta_{h_2'h_2}\bar{v}_{p_2'p_1',p_2p_1} \end{aligned} \tag{A.83}$$

Coupled Representation The coupled A_{22} matrix is deduced with the help of Eq. (A.76), of the 2p2h annihilation operator

$$\hat{\mathcal{A}}_{(p_1'p_2')J_{p'}(h_1'h_2')J_{h'}} = \mathcal{N}_{p_1',p_2'}\mathcal{N}_{h_1',h_2'} \sum_{M_{p'},M_{h'}} (-1)^{J_{h'}-M_{h'}} \begin{pmatrix} J_{p'} & J_{h'} & \middle| & J \\ M_{p'} & -M_{h'} & \middle| & M \end{pmatrix} \times \sum_{m_{p_1'},m_{p_2'}} \begin{pmatrix} j_{p_1'} & j_{p_2'} & \middle| & J_{p'} \\ m_{p_1'} & m_{p_2'} & \middle| & M_{p'} \end{pmatrix} \sum_{m_{h_1'},m_{h_2'}} \begin{pmatrix} j_{h_1'} & j_{h_2'} & \middle| & J_{h'} \\ m_{h_1'} & m_{h_2'} & \middle| & M_{h'} \end{pmatrix} \hat{\mathcal{A}}_{p_1'p_2'h_1'h_2'} \tag{A.84}$$

and of the 2p2h creation operator

$$\hat{\mathcal{A}}^{\dagger}_{(p_1p_2)J_p(h_1h_2)J_h} = \mathcal{N}_{p_1,p_2}\mathcal{N}_{h_1,h_2} \sum_{M_p,M_h} (-1)^{J_h-M_h} \begin{pmatrix} J_p & J_h & \middle| & J \\ M_p & -M_h & \middle| & M \end{pmatrix} \sum_{m_{p_1},m_{p_2}} \begin{pmatrix} j_{p_1} & j_{p_2} & \middle| & J_p \\ m_{p_1} & m_{p_2} & \middle| & M_p \end{pmatrix} \times \sum_{m_{h_1},m_{h_2}} \begin{pmatrix} j_{h_1} & j_{h_2} & \middle| & J_h \\ m_{h_1} & m_{h_2} & \middle| & M_h \end{pmatrix} \hat{\mathcal{A}}^{\dagger}_{p_1p_2h_1h_2} \,. \tag{A.85}$$

The same set of sums, CGCs and prefactors are taken into account but for different quantum numbers. Only the total angular momentum J remains same. As for the A_{12} matrix, only selected terms are evaluated. In this case, we focus on the third and on the last term in Eq. (A.83) for brevity. The other terms can be deduced analogously. First, we consider the last term in Eq. (A.83). Inserting the definitions of creation and annihilation operator leads to

$$\begin{aligned} A_{22,\text{part5}} = \sum_{\substack{M_pM_h \\ M_{p'}M_{h'}}} \sum_{\substack{m_{p1}m_{p2} \\ m_{p_1'}m_{p_2'}}} \sum_{\substack{m_{h_1}m_{h_2} \\ m_{h_1'}m_{h_2'}}} & \mathcal{N}_{p_1,p_2}\mathcal{N}_{h_1,h_2}\mathcal{N}_{p_1',p_2'}\mathcal{N}_{h_1',h_2'}(-1)^{J_h-M_h}(-1)^{J_{h'}-M_{h'}} \\ & \times \begin{pmatrix} J_p & J_h & \middle| & J \\ M_p & -M_h & \middle| & M \end{pmatrix} \begin{pmatrix} j_{p_1} & j_{p_2} & \middle| & J_p \\ m_{p_1} & m_{p_2} & \middle| & M_p \end{pmatrix} \begin{pmatrix} j_{h_1} & j_{h_2} & \middle| & J_h \\ m_{h_1} & m_{h_2} & \middle| & M_h \end{pmatrix} \\ & \times \begin{pmatrix} J_{p'} & J_{h'} & \middle| & J \\ M_{p'} & -M_{h'} & \middle| & M \end{pmatrix} \begin{pmatrix} j_{p_1'} & j_{p_2'} & \middle| & J_{p'} \\ m_{p_1'} & m_{p_2'} & \middle| & M_{p'} \end{pmatrix} \\ & \times \begin{pmatrix} j_{h_1'} & j_{h_2'} & \middle| & J_{h'} \\ m_{h_1'} & m_{h_2'} & \middle| & M_{h'} \end{pmatrix} \delta_{h_1'h_1}\delta_{h_2'h_2} v_{p_2'p_1',p_2p_1} \,. \end{aligned} \tag{A.86}$$

Again, the the matrix element is given with respect to the uncoupled basis. With a basis trans-

formation and a subsequent application of the Wigner-Eckart theorem, the matrix element reads

$$\begin{aligned}
\bar{v}_{p_2'p_1',p_2p_1} &= \langle p_2'p_1'| \hat{V}_{\mathrm{NN}} |p_2p_1\rangle \\
&= \sum_{J''M''} \left(\mathcal{N}_{p_1,p_2}\mathcal{N}_{p_1',p_2'}\right)^{-1} \begin{pmatrix} j_{p_2'} & j_{p_1'} \\ m_{p_2'} & m_{p_1'} \end{pmatrix} \begin{vmatrix} J'' \\ M'' \end{vmatrix} \begin{pmatrix} j_{p_2} & j_{p_1} \\ m_{p_2} & m_{p_1} \end{pmatrix} \begin{vmatrix} J'' \\ M'' \end{vmatrix} \langle p_2'p_1', J''| \hat{V}_{\mathrm{NN}} |p_2p_1, J''\rangle \\
&= \sum_{J''M''} \left(\mathcal{N}_{p_1,p_2}\mathcal{N}_{p_1',p_2'}\right)^{-1} (-1)^{j_{p_1'}+j_{p_2'}-J''} (-1)^{j_{p_1}+j_{p_2}-J''} \\
&\qquad \times \begin{pmatrix} j_{p_1'} & j_{p_2'} \\ m_{p_1'} & m_{p_2'} \end{pmatrix} \begin{vmatrix} J'' \\ M'' \end{vmatrix} \begin{pmatrix} j_{p_1} & j_{p_2} \\ m_{p_1} & m_{p_2} \end{pmatrix} \begin{vmatrix} J'' \\ M'' \end{vmatrix} \langle p_2'p_1', J''| \hat{V}_{\mathrm{NN}} |p_2p_1, J''\rangle \ . \quad \text{(A.87)}
\end{aligned}$$

Here, the columns of the Clebsch-Gordan coefficients are switched, what generates additional phase factors. The sums and the Clebsch-Gordan coefficients in Eq. (A.86) and Eq. (A.87) are separated for lucidity. Within the next steps, the orthogonality relation (2.4) is utilized multiple times. This reduces the CGCs and sums to Kronecker deltas.

$$\sum_{\substack{M_pM_h\\M_{p'}M_{h'}}} \sum_{m_{p_1},m_{p_2}} \sum_{m_{p'_1},m_{p'_2}} \sum_{\substack{m_{h_1}m_{h_2}\\m_{h'_1}m_{h'_2}}} \begin{pmatrix} J_p & J_h & J \\ M_p & -M_h & M \end{pmatrix} \begin{pmatrix} j_{p_1} & j_{p_2} & J_p \\ m_{p_1} & m_{p_2} & M_p \end{pmatrix} \begin{pmatrix} j_{h_1} & j_{h_2} & J_h \\ m_{h_1} & m_{h_2} & M_h \end{pmatrix} \begin{pmatrix} J_{p'} & J_{h'} & J' \\ M_{p'} & -M_{h'} & M' \end{pmatrix} \begin{pmatrix} j_{p'_1} & j_{p'_2} & J_{p'} \\ m_{p'_1} & m_{p'_2} & M_{p'} \end{pmatrix} \begin{pmatrix} j_{h'_1} & j_{h'_2} & J_{h'} \\ m_{h'_1} & m_{h'_2} & M_{h'} \end{pmatrix} \delta_{h'_1h_1}\delta_{h'_2h_2}$$

$$\times \sum_{J''M''} \begin{pmatrix} j_{p'_1} & j_{p'_2} & J'' \\ m_{p'_1} & m_{p'_2} & M'' \end{pmatrix} \begin{pmatrix} j_{p_1} & j_{p_2} & J'' \\ m_{p_1} & m_{p_2} & M'' \end{pmatrix}$$

$$= \sum_{M_{p'}} \sum_{\substack{M_pM_h\\M_{h'}}} \sum_{m_{h_1},m_{h_2}} \sum_{m_{h'_1},m_{h'_2}} \begin{pmatrix} J_p & J_h & J \\ M_p & -M_h & M \end{pmatrix} \begin{pmatrix} j_{h_1} & j_{h_2} & J_h \\ m_{h_1} & m_{h_2} & M_h \end{pmatrix} \begin{pmatrix} J_{p'} & J_{h'} & J' \\ M_{p'} & -M_{h'} & M' \end{pmatrix} \begin{pmatrix} j_{h'_1} & j_{h'_2} & J_{h'} \\ m_{h'_1} & m_{h'_2} & M_{h'} \end{pmatrix} \delta_{h'_1h_1}\delta_{h'_2h_2} \underbrace{\sum_{J''M''} \delta_{J_pJ''}\delta_{M_pM''}\delta_{J_{p'}J''}\delta_{M_{p'}M''}}_{\delta_{J_pJ_{p'}}\delta_{M_pM_{p'}}}$$

$$= \sum_{\substack{M_pM_h\\M_{h'}}} \sum_{m_{h_1},m_{h_2}} \begin{pmatrix} J_p & J_h & J \\ M_p & -M_h & M \end{pmatrix} \begin{pmatrix} j_{h_1} & j_{h_2} & J_h \\ m_{h_1} & m_{h_2} & M_h \end{pmatrix} \begin{pmatrix} J_p & J_{h'} & J' \\ M_p & -M_{h'} & M' \end{pmatrix} \begin{pmatrix} j_{h_1} & j_{h_2} & J_{h'} \\ m_{h_1} & m_{h_2} & M_{h'} \end{pmatrix} \delta_{h'_1h_1}\delta_{h'_2h_2}\delta_{J_pJ_{p'}}$$

$$= \sum_{\substack{M_pM_h\\M_{h'}}} \begin{pmatrix} J_p & J_h & J \\ M_p & -M_h & M \end{pmatrix} \begin{pmatrix} J_p & J_{h'} & J' \\ M_p & -M_{h'} & M' \end{pmatrix} \delta_{h'_1h_1}\delta_{h'_2h_2}\delta_{J_pJ_{p'}}\delta_{J_hJ_{h'}}\delta_{M_hM_{h'}}$$

$$= \sum_{M_p,M_h} \begin{pmatrix} J_p & J_h & J \\ M_p & -M_h & M \end{pmatrix} \begin{pmatrix} J_p & J_h & J' \\ M_p & -M_h & M' \end{pmatrix} \delta_{h'_1h_1}\delta_{h'_2h_2}\delta_{J_pJ_{p'}}\delta_{J_hJ_{h'}}$$

$$= \delta_{h'_1h_1}\delta_{h'_2h_2}\delta_{J_pJ_{p'}}\delta_{J_hJ_{h'}}\delta_{JJ'}$$

Inserting the definition of the normalization factors (6.10) and the Kronecker deltas back in Eq. (A.86), the fifth term of the A_{22} matrix reads

$$A_{22,\text{part5}} = (1+(-1)^{J_h}\delta_{h_1h_2})(1+\delta_{h_1h_2})^{-2}\left\langle p_2'p_1', J_p\right|\hat{V}_{\text{NN}}\left|p_2p_1, J_p\right\rangle \delta_{h_1'h_1}\delta_{h_2'h_2}\delta_{J_pJ_{p'}}\delta_{J_hJ_{h'}}\delta_{JJ'}\,. \tag{A.88}$$

The phase factor becomes one, since $(-1)^{2(J_h-M_h)}(-1)^{2(j_{p_1}+j_{p_2}-J_p)} = 1$ according to Sec. A.3. The second-last term can be deduced similarly.

The derivation of the third term in the A_{22} matrix (A.83) is more complex, since the Clebsch-Gordan coefficients cannot be combined to Kronecker deltas. The third term yields

$$\begin{aligned} A_{22,\text{part3}} = \sum_{\substack{M_pM_h\\M_{p'}M_{h'}}}\sum_{\substack{m_{p_1}m_{p_2}\\m_{p_1'}m_{p_2'}}}\sum_{\substack{m_{h_1}m_{h_2}\\m_{h_1'}m_{h_2'}}} &\mathcal{N}_{p_1,p_2}\mathcal{N}_{h_1,h_2}\mathcal{N}_{p_1',p_2'}\mathcal{N}_{h_1',h_2'}(-1)^{J_h-M_h}(-1)^{J_{h'}-M_{h'}}\\ &\times\begin{pmatrix}J_p & J_h & \big| & J\\ M_p & -M_h & \big| & M\end{pmatrix}\begin{pmatrix}j_{p_1} & j_{p_2} & \big| & J_p\\ m_{p_1} & m_{p_2} & \big| & M_p\end{pmatrix}\begin{pmatrix}j_{h_1} & j_{h_2} & \big| & J_h\\ m_{h_1} & m_{h_2} & \big| & M_h\end{pmatrix}\\ &\times\begin{pmatrix}J_{p'} & J_{h'} & \big| & J\\ M_{p'} & -M_{h'} & \big| & M\end{pmatrix}\begin{pmatrix}j_{p_1'} & j_{p_2'} & \big| & J_{p'}\\ m_{p_1'} & m_{p_2'} & \big| & M_{p'}\end{pmatrix}\\ &\times\begin{pmatrix}j_{h_1'} & j_{h_2'} & \big| & J_{h'}\\ m_{h_1'} & m_{h_2'} & \big| & M_{h'}\end{pmatrix}\delta_{h_1'h_1}\delta_{h_2'h_2}v_{h_2p_2',h_2'p_2}\,. \end{aligned} \tag{A.89}$$

with the uncoupled matrix element. The transformation into the coupled basis in combination with the Wigner-Eckart theorem leads to

$$\begin{aligned} v_{h_2p_2',h_2'p_2} &= \left\langle h_2p_2'\right|\hat{V}\left|h_2'p_2\right\rangle\\ &= \sum_{J''M''}\left(\mathcal{N}_{h_2,p_2'}\mathcal{N}_{h_2',p_2}\right)^{-1}\begin{pmatrix}j_{h_2} & j_{p_2'} & \big| & J''\\ m_{h_2} & m_{p_2'} & \big| & M''\end{pmatrix}\begin{pmatrix}j_{h_2'} & j_{p_2} & \big| & J''\\ m_{h_2'} & m_{p_2} & \big| & M''\end{pmatrix}\\ &\quad\times\left\langle h_2p_2', J''\right|\hat{V}_{\text{NN}}\left|h_2'p_2, J''\right\rangle\,. \end{aligned} \tag{A.90}$$

The normalization factors become equal to one, since particles and holes are disjoint. For clarity, we consider the contained sums and Clebsch-Gordan coefficients separately in the

next step. According to Eq. (2.11), we rewrite them into $3j$ symbols and get

$$\begin{aligned}
&\sum_{\substack{M_pM_h\\M_{p'}M_{h'}}}\sum_{\substack{m_{p_1}m_{p_2}\\m_{p'_1}m_{p'_2}}}\sum_{\substack{m_{h_1}m_{h_2}\\m_{h'_1}m_{h'_2}}}\sum_{J''M''}\begin{pmatrix}J_p & J_h\\ M_p & -M_h\end{vmatrix}\begin{matrix}J\\M\end{matrix}\end{pmatrix}\begin{pmatrix}j_{p_1} & j_{p_2}\\ m_{p_1} & m_{p_2}\end{vmatrix}\begin{matrix}J_p\\M_p\end{matrix}\end{pmatrix}\begin{pmatrix}j_{h_1} & j_{h_2}\\ m_{h_1} & m_{h_2}\end{vmatrix}\begin{matrix}J_h\\M_h\end{matrix}\end{pmatrix}\\
&\qquad\times\begin{pmatrix}J_{p'} & J_{h'}\\ M_{p'} & -M_{h'}\end{vmatrix}\begin{matrix}J\\M\end{matrix}\end{pmatrix}\begin{pmatrix}j_{p'_1} & j_{p'_2}\\ m_{p'_1} & m_{p'_2}\end{vmatrix}\begin{matrix}J_{p'}\\M_{p'}\end{matrix}\end{pmatrix}\begin{pmatrix}j_{h'_1} & j_{h'_2}\\ m_{h'_1} & m_{h'_2}\end{vmatrix}\begin{matrix}J_{h'}\\M_{h'}\end{matrix}\end{pmatrix}\\
&\qquad\times\begin{pmatrix}j_{h_2} & j_{p'_2}\\ m_{h_2} & m_{p'_2}\end{vmatrix}\begin{matrix}J''\\M''\end{matrix}\end{pmatrix}\begin{pmatrix}j_{h'_2} & j_{p_2}\\ m_{h'_2} & m_{p_2}\end{vmatrix}\begin{matrix}J''\\M''\end{matrix}\end{pmatrix}\delta_{h'_1h_1}\delta_{p'_1p_1}\\
=&\sum_{\substack{M_pM_h\\M_{p'}M_{h'}}}\sum_{\substack{m_{p_1}m_{p_2}\\m_{p'_2}}}\sum_{\substack{m_{h_1}m_{h_2}\\m_{h'_2}}}\sum_{J''M''}\kappa\begin{pmatrix}J_p & J_h & J\\ M_p & M_h & M\end{pmatrix}\begin{pmatrix}j_{p_2} & J_p & j_{p_1}\\ -m_{p_2} & M_p & m_{p_1}\end{pmatrix}\begin{pmatrix}J_h & j_{h_2} & j_{h_1}\\ M_h & m_{h_2} & m_{h_1}\end{pmatrix}\\
&\qquad\times\begin{pmatrix}J_{p'} & J_{h'} & J\\ M_{p'} & M_{h'} & M\end{pmatrix}\begin{pmatrix}j_{p'_2} & J_{p'} & j_{p_1}\\ -m_{p'_2} & M_{p'} & m_{p_1}\end{pmatrix}\begin{pmatrix}J_{h'} & j_{h'_2} & j_{h_1}\\ M_{h'} & m_{h'_2} & m_{h_1}\end{pmatrix}\\
&\qquad\times\begin{pmatrix}j_{h_2} & j_{p'_2} & J''\\ m_{h_2} & m_{p'_2} & M''\end{pmatrix}\begin{pmatrix}j_{h'_2} & j_{p_2} & J''\\ m_{h'_2} & m_{p_2} & M''\end{pmatrix}\delta_{h'_1h_1}\delta_{p'_1p_1}. \qquad \text{(A.91)}
\end{aligned}$$

In the second step, the $3j$ symbols are rearranged according to Eq. (2.12) and Eq. (2.13) and several sums are reordered. Here, κ represents all phase factors and multiplicities arising due to the reformulation into $3j$ symbols as well as those emerging by rearranging

$$\begin{aligned}
\kappa =&\hat{J''}^2\hat{J}\hat{J}_p\hat{J}_h\hat{J}\hat{J}_{p'}\hat{J}_{h'}(-1)^{M-J_h+J_p}(-1)^{M_p+j_{p_1}-j_{p_2}}(-1)^{M_h+j_{h_1}-j_{h_2}}(-1)^{M+J_{p'}-J_{h'}}(-1)^{M_{p'}+j_{p_1}-j_{p'_2}}\\
&\times(-1)^{M_{h'}+j_{h_1}-j_{h'_2}}(-1)^{M''+j_{h_2}-j_{p'_2}}(-1)^{M''+j_{h'_2}-j_{p_2}}\\
&\times(-1)^{J_p+J_h+J}(-1)^{J_{p'}+J_{h'}+J}(-1)^{j_{h_2}+j_{p'_2}+J''}(-1)^{j_{h'_2}+j_{p_2}+J''}.
\end{aligned} \qquad \text{(A.92)}$$

For the inclusion of all phase factors, we need to multiply Eq. (A.92) with $(-1)^{J_h-M_h}(-1)^{J_{h'}-M_{h'}}$, leading to the phase factor

$$\kappa' = \kappa(-1)^{J_h-M_h}(-1)^{J_{h'}-M_{h'}}. \qquad \text{(A.93)}$$

For the sum of eight $3j$ symbols, the so-called $12j$ symbol from Ref. [16] (page 361, Eq. (3)) can be used for summary

$$\begin{Bmatrix} a_1 & & a_2 & & a_3 & & a_4 & \\ & b_{12} & & b_{23} & & b_{34} & & b_{41} \\ c_1 & & c_2 & & c_3 & & c_4 & \end{Bmatrix}$$

$$= \sum_{\substack{m_{a_i} m_{c_i} \\ m_{b_{ik}}}} (-1)^{a_4+m_{a_4}+c_4+m_{c_4}} \begin{pmatrix} a_1 & a_2 & b_{12} \\ m_{a_1} & m_{a_2} & m_{b_{12}} \end{pmatrix} \begin{pmatrix} a_2 & a_3 & b_{23} \\ m_{a_2} & m_{a_3} & m_{b_{23}} \end{pmatrix} \begin{pmatrix} a_3 & a_4 & b_{34} \\ m_{a_3} & m_{a_4} & m_{b_{34}} \end{pmatrix}$$

$$\times \begin{pmatrix} a_4 & c_1 & b_{41} \\ -m_{a_4} & m_{c_1} & m_{b_{41}} \end{pmatrix} \begin{pmatrix} c_1 & c_2 & b_{12} \\ m_{c_1} & m_{c_2} & m_{b_{12}} \end{pmatrix} \begin{pmatrix} c_2 & c_3 & b_{23} \\ m_{c_2} & m_{c_3} & m_{b_{23}} \end{pmatrix} \tag{A.94}$$

Thus, the $3j$ symbols in Eq. (A.91) can be summarized into a $12j$ symbol. Therefore, we sum the equation over M which yields an additional prefactor $1/\hat{J}^2$, keeping in mind that this is possible because the matrix element is M-independent. With these considerations, the third term of the A_{22} matrix reads

$$A_{22,\text{part3}}$$

$$= \sum_{J''} \mathcal{N}_{p_1,p_2} \mathcal{N}_{\hbar_1,\hbar_2} \mathcal{N}_{p_1',p_2'} \mathcal{N}_{\hbar_1',\hbar_2'} \hat{J''}^2 \hat{J}_p \hat{J}_h \hat{J}_{p'} \hat{J}_{h'} \begin{Bmatrix} J_p & & J_h & & j_{h_2} & & j_{p_2'} & \\ & J & & j_{h_1} & & J'' & & j_{p_1} \\ J_{p'} & & J_{h'} & & j_{h_2'} & & j_{p_2} & \end{Bmatrix}$$

$$\times \kappa' \left\langle h_2 p_2', J'' \right| \hat{V}_{\text{NN}} \left| h_2' p_2, J'' \right\rangle . \tag{A.95}$$

Since a $12j$ symbol is not manageable in practical calculations, an additional relation connecting one $12j$ symbols to four $6j$ symbols is employed. This reformulation (see Ref. [16], page 362, Eq. (6)) is defined as

$$\begin{Bmatrix} a_1 & & a_2 & & a_3 & & a_4 & \\ & b_{12} & & b_{23} & & b_{34} & & b_{41} \\ c_1 & & c_2 & & c_3 & & c_4 & \end{Bmatrix}$$

$$= \sum_x \xi \, \hat{x} \begin{Bmatrix} a_1 & a_2 & b_{12} \\ c_2 & c_1 & x \end{Bmatrix} \begin{Bmatrix} a_2 & a_3 & b_{23} \\ c_3 & c_2 & x \end{Bmatrix} \begin{Bmatrix} a_3 & a_4 & b_{34} \\ c_4 & c_3 & x \end{Bmatrix} \begin{Bmatrix} a_4 & c_1 & b_{41} \\ a_1 & c_4 & x \end{Bmatrix} \tag{A.96}$$

with the phase factor

$$\xi = (-1)^{\sum_{i=1}^{4}(a_i+c_i)+b_{12}+b_{23}+b_{34}+b_{41}-x} . \tag{A.97}$$

Thus, we find as result for the considered part of the A_{22} matrix

$$
\begin{aligned}
A_{22,\text{part3}} =& (1+\delta_{p_1p_2})^{-\frac{1}{2}}(1+\delta_{h_1h_2})^{-\frac{1}{2}}(1+\delta_{p_1'p_2'})^{-\frac{1}{2}}(1+\delta_{h_1'h_2'})^{-\frac{1}{2}}\delta_{p_1'p_1}\delta_{h_1'h_1} \\
&\times (-1)^{1+j_{p_2}+j_{p_1}+j_{h_2}+j_{h_1}}\hat{J}_p\hat{J}_{p'}\hat{J}_h\hat{J}_{h'} \\
&\times \sum_L (-1)^{J_h-J_{h'}+J-L}\hat{L}^2 \begin{Bmatrix} J_p & J_{p'} & L \\ J_{h'} & J_h & J \end{Bmatrix} \begin{Bmatrix} J_p & J_{p'} & L \\ j_{p_2'} & j_{p_2} & j_{p_1} \end{Bmatrix} \begin{Bmatrix} J_h & J_{h'} & L \\ j_{h_2'} & j_{h_2} & j_{h_1} \end{Bmatrix} \\
&\times \sum_{J''} (-1)^{j_{h_2}+j_{p_2'}-J''}\hat{J''}^2 \begin{Bmatrix} j_{p_2} & j_{h_2'} & J'' \\ j_{h_2} & j_{p_2'} & L \end{Bmatrix} \left\langle \hbar_2 p_2', J'' \middle| \hat{V}_{\text{NN}} \middle| \hbar_2' p_2, J'' \right\rangle .
\end{aligned}
\tag{A.98}
$$

Bibliography

[1] Eugene Wigner. "Einige Folgerungen aus der Schrödingerschen Theorie für die Termstrukturen". In: *Zeitschrift für Physik* 43 (9 1927), pp. 624–652. URL: https://doi.org/10.1007/BF01397327.

[2] J. C. Slater. "The Theory of Complex Spectra". In: *Phys. Rev.* 34 (10 1929), pp. 1293–1322. URL: https://link.aps.org/doi/10.1103/PhysRev.34.1293.

[3] E. U. Condon. "The Theory of Complex Spectra". In: *Phys. Rev.* 36 (7 1930), pp. 1121–1133. URL: https://link.aps.org/doi/10.1103/PhysRev.36.1121.

[4] Carl Eckart. "The Application of Group theory to the Quantum Dynamics of Monatomic Systems". In: *Rev. Mod. Phys.* 2 (3 1930), pp. 305–380. URL: https://link.aps.org/doi/10.1103/RevModPhys.2.305.

[5] Cornelius Lanczos. "An iteration method for the solution of the eigenvalue problem of linear differential and integral operators". In: *J. Res. Natl. Bur. Stand.* 45.4 (1950), p. 255.

[6] G. C. Wick. "The Evaluation of the Collision Matrix". In: *Phys. Rev.* 80 (2 1950), pp. 268–272. URL: https://link.aps.org/doi/10.1103/PhysRev.80.268.

[7] David Bohm and David Pines. "A Collective Description of Electron Interactions. I. Magnetic Interactions". In: *Phys. Rev.* 82 (5 1951), pp. 625–634. URL: https://link.aps.org/doi/10.1103/PhysRev.82.625.

[8] David Pines and David Bohm. "A Collective Description of Electron Interactions: II. Collective vs Individual Particle Aspects of the Interactions". In: *Phys. Rev.* 85 (2 1952), pp. 338–353. URL: https://link.aps.org/doi/10.1103/PhysRev.85.338.

[9] David Bohm and David Pines. "A Collective Description of Electron Interactions: III. Coulomb Interactions in a Degenerate Electron Gas". In: *Phys. Rev.* 92 (3 1953), pp. 609–625. URL: https://link.aps.org/doi/10.1103/PhysRev.92.609.

[10] J. Da Providência. "Variational approach to the many-body problem". In: *Nuclear Physics* 61.1 (1965), pp. 87–96. URL: https://www.sciencedirect.com/science/article/pii/0029558265909375.

[11] Christopher Conway Paige. "The computation of eigenvalues and eigenvectors of very large sparse matrices". PhD thesis. University of London, 1971.

[12] J. Ahrens et al. "Total nuclear photon absorption cross sections for some light elements". In: *Nuclear Physics A* 251.3 (1975), pp. 479–492. URL: https://www.sciencedirect.com/science/article/pii/0375947475905436.

[13] Steven Weinberg. "Phenomenological Lagrangians". In: *Physica A: Statistical Mechanics and its Applications* 96.1–2 (1979), pp. 327 –340. URL: http://www.sciencedirect.com/science/article/pii/0378437179902231.

[14] P. Ring and P. Schuck. *The Nuclear Many-Body Problem*. Springer-Verlag, 1980.

[15] R. R. Whitehead. *Theory and Applications of Moment Methods in Many-Fermion Systems*. Ed. by B. J. Dalton et al. Springer New York, NY, 1980.

[16] D. A. Varshalovich. *Quantum Theory of Angular Momentum*. World Scientific, 1988.

[17] Kris L.G. Heyde. *The Nuclear Shell Model*. Springer Verlag, 1990.

[18] Steven Weinberg. "Nuclear forces from chiral lagrangians". In: *Physics Letters B* 251.2 (1990), pp. 288 –292. URL: http://www.sciencedirect.com/science/article/pii/0370269390909383.

[19] I. Talmi. *Simple Models of Complex Nuclei*. harwood academic publishers, 1993.

[20] Franz Wegner. "Flow-equations for Hamiltonians". In: *Annalen der Physik* 506.2 (1994), pp. 77–91. URL: http://dx.doi.org/10.1002/andp.19945060203.

[21] R. B. Wiringa, V. G. J. Stoks, and R. Schiavilla. "Accurate nucleon-nucleon potential with charge-independence breaking". In: *Phys. Rev. C* 51 (1 1995), pp. 38–51. URL: https://link.aps.org/doi/10.1103/PhysRevC.51.38.

[22] F. Catara et al. "Towards a self-consistent random-phase approximation for Fermi systems". In: *Phys. Rev. B* 54 (24 1996), pp. 17536–17546. URL: https://link.aps.org/doi/10.1103/PhysRevB.54.17536.

[23] Franz J. Wegner. "Flow equations for Hamiltonians". In: *Nuclear Physics B - Proceedings Supplements* 90.0 (2000), pp. 141 –146. URL: http://www.sciencedirect.com/science/article/pii/S0920563200009117.

[24] M. N. Harakeh and A. van der Woude. *Giant Resonances - Fundamental High-Frequency Modes of Nuclear Excitation*. Oxford University Press, 2001.

[25] Y.-W. Lui, H. L. Clark, and D. H. Youngblood. "Giant resonances in ^{16}O". In: *Phys. Rev. C* 64 (6 2001), p. 064308. URL: https://link.aps.org/doi/10.1103/PhysRevC.64.064308.

[26] R. Machleidt. "High-precision, charge-dependent Bonn nucleon-nucleon potential". In: *Phys. Rev. C* 63 (2 2001), p. 024001. URL: https://link.aps.org/doi/10.1103/PhysRevC.63.024001.

[27] D. H. Youngblood, Y.-W. Lui, and H. L. Clark. "Isoscalar $E0$, $E1$, and $E2$ strength in ^{40}Ca". In: *Phys. Rev. C* 63 (6 2001), p. 067301. URL: https://link.aps.org/doi/10.1103/PhysRevC.63.067301.

[28] E. Epelbaum et al. "Three-nucleon forces from chiral effective field theory". In: *Phys. Rev. C* 66 (6 2002), p. 064001. URL: https://link.aps.org/doi/10.1103/PhysRevC.66.064001.

[29] Ionel Stetcu and Calvin W. Johnson. "Tests of the random phase approximation for transition strengths". In: *Phys. Rev. C* 67 (4 2003), p. 044315. URL: https://link.aps.org/doi/10.1103/PhysRevC.67.044315.

[30] A.H. Wapstra, G. Audi, and C. Thibault. "The Ame2003 atomic mass evaluation: (I). Evaluation of input data, adjustment procedures". In: *Nuclear Physics A* 729.1 (2003), pp. 129–336. URL: https://www.sciencedirect.com/science/article/pii/S0375947403018086.

[31] R. Roth et al. "Hartree-Fock and many body perturbation theory with correlated realistic NN interactions". In: *Phys. Rev. C* 73 (4 2006), p. 044312. URL: https://link.aps.org/doi/10.1103/PhysRevC.73.044312.

[32] P. Papakonstantinou, R. Roth, and N. Paar. "Nuclear collective excitations using correlated realistic interactions: The role of explicit random-phase approximation correlations". In: *Phys. Rev. C* 75 (1 2007), p. 014310. URL: https://link.aps.org/doi/10.1103/PhysRevC.75.014310.

[33] J. Suhonen. *From Nucleons to Nucleus. Concepts of Microscopic Nuclear Theory*. Springer-Verlag, 2007.

[34] V. Bernard et al. "Subleading contributions to the chiral three-nucleon force: Long-range terms". In: *Phys. Rev. C* 77 (6 2008), p. 064004. URL: https://link.aps.org/doi/10.1103/PhysRevC.77.064004.

[35] L. E. Marcucci et al. "Quantum Monte Carlo calculations of magnetic moments and $M1$ transitions in $A \leqslant 7$ nuclei including meson-exchange currents". In: *Phys. Rev. C* 78 (6 2008), p. 065501. URL: https://link.aps.org/doi/10.1103/PhysRevC.78.065501.

[36] Sara Perez-Martin and L. M. Robledo. "Microscopic justification of the equal filling approximation". In: *Phys. Rev. C* 78 (1 2008), p. 014304. URL: https://link.aps.org/doi/10.1103/PhysRevC.78.014304.

[37] E. Epelbaum, H.-W. Hammer, and Ulf-G. Meißner. "Modern theory of nuclear forces". In: *Rev. Mod. Phys.* 81 (4 2009), pp. 1773–1825. URL: https://link.aps.org/doi/10.1103/RevModPhys.81.1773.

[38] Petr Navrátil et al. "Recent developments in no-core shell-model calculations". In: *Journal of Physics G: Nuclear and Particle Physics* 36.8 (2009), p. 083101. URL: https://dx.doi.org/10.1088/0954-3899/36/8/083101.

[39] S. Pastore et al. "Electromagnetic currents and magnetic moments in chiral effective field theory (χEFT)". In: *Phys. Rev. C* 80 (3 2009), p. 034004. URL: https://link.aps.org/doi/10.1103/PhysRevC.80.034004.

[40] Robert Roth. "Importance truncation for large-scale configuration interaction approaches". In: *Phys. Rev. C* 79 (6 2009), p. 064324. URL: http://link.aps.org/doi/10.1103/PhysRevC.79.064324.

[41] I. Shavitt and R. J. Bartlett. *Many-Body Methods in Chemistry and Physics - MBPT and Coupled-Cluster Theory*. Cambridge University Press, 2009.

[42] Evgeny Epelbaum. *Nuclear forces from chiral effective field theory: a primer*. 2010. URL: https://arxiv.org/abs/1001.3229.

[43] P. Papakonstantinou and R. Roth. "Large-scale second random-phase approximation calculations with finite-range interactions". In: *Phys. Rev. C* 81 (2 2010), p. 024317. URL: https://link.aps.org/doi/10.1103/PhysRevC.81.024317.

[44] V. Bernard et al. "Subleading contributions to the chiral three-nucleon force. II. Short-range terms and relativistic corrections". In: *Phys. Rev. C* 84 (5 2011), p. 054001. URL: https://link.aps.org/doi/10.1103/PhysRevC.84.054001.

[45] D. Gambacurta, M. Grasso, and F. Catara. "Low-lying dipole response in the stable ^{40,48}Ca nuclei with the second random-phase approximation". In: *Phys. Rev. C* 84 (3 2011), p. 034301. URL: https://link.aps.org/doi/10.1103/PhysRevC.84.034301.

[46] Y.-W. Lui et al. "Isoscalar giant resonances in ^{48}Ca". In: *Phys. Rev. C* 83 (4 2011), p. 044327. URL: https://link.aps.org/doi/10.1103/PhysRevC.83.044327.

[47] R. Machleidt and D.R. Entem. "Chiral effective field theory and nuclear forces". In: *Physics Reports* 503.1 (2011), pp. 1–75. URL: https://www.sciencedirect.com/science/article/pii/S0370157311000457.

[48] J. Beringer et al. "Review of Particle Physics". In: *Phys. Rev. D* 86 (1 2012), p. 010001. URL: https://link.aps.org/doi/10.1103/PhysRevD.86.010001.

[49] Bastian Erler. "Mean-Field Approach to Collective Excitations in Deformed sd-Shell Nuclei Using Realistic Interactions". PhD thesis. Darmstadt: Technische Universität, 2012. URL: http://tuprints.ulb.tu-darmstadt.de/3057/.

[50] D. Gambacurta et al. "Second random-phase approximation with the Gogny force: First applications". In: *Phys. Rev. C* 86 (2 2012), p. 021304. URL: https://link.aps.org/doi/10.1103/PhysRevC.86.021304.

[51] P. Papakonstantinou et al. "Low-energy dipole strength and the critical case of 48Ca". In: *Physics Letters B* 709.3 (2012), pp. 270–275. URL: https://www.sciencedirect.com/science/article/pii/S0370269312001554.

[52] Robert Roth et al. "Medium-Mass Nuclei with Normal-Ordered Chiral $NN+3N$ Interactions". In: *Phys. Rev. Lett.* 109 (5 2012), p. 052501. URL: https://link.aps.org/doi/10.1103/PhysRevLett.109.052501.

[53] Matthias R. Schindler Stefan Scherer. *A Primer for Chiral Perturbation Theory*. Springer Berlin, Heidelberg, 2012.

[54] S. Bacca et al. "First Principles Description of the Giant Dipole Resonance in ^{16}**O**". In: *Phys. Rev. Lett.* 111 (12 2013), p. 122502. URL: https://link.aps.org/doi/10.1103/PhysRevLett.111.122502.

[55] Bruce R. Barrett, Petr Navrátil, and James P. Vary. "Ab initio no core shell model". In: *Progress in Particle and Nuclear Physics* 69 (2013), pp. 131–181. URL: https://www.sciencedirect.com/science/article/pii/S0146641012001184.

[56] S. R. Beane et al. "Light nuclei and hypernuclei from quantum chromodynamics in the limit of SU(3) flavor symmetry". In: *Phys. Rev. D* 87 (3 2013), p. 034506. URL: https://link.aps.org/doi/10.1103/PhysRevD.87.034506.

[57] Michael K. G. Kruse. *Extensions to the No-Core Shell Model*. Springer Theses. Springer Cham, 2013.

[58] S. Pastore et al. "Quantum Monte Carlo calculations of electromagnetic moments and transitions in $A \leq 9$ nuclei with meson-exchange currents derived from chiral effective field theory". In: *Phys. Rev. C* 87 (3 2013), p. 035503. URL: https://link.aps.org/doi/10.1103/PhysRevC.87.035503.

[59] M. Piarulli et al. "Electromagnetic structure of $A = 2$ and 3 nuclei in chiral effective field theory". In: *Phys. Rev. C* 87 (1 2013), p. 014006. URL: http://link.aps.org/doi/10.1103/PhysRevC.87.014006.

[60] S. Bacca et al. "Giant and pigmy dipole resonances in ^{4}He, ^{16,22}O, and ^{40}Ca from chiral nucleon-nucleon interactions". In: *Phys. Rev. C* 90 (6 2014), p. 064619. URL: https://link.aps.org/doi/10.1103/PhysRevC.90.064619.

[61] S. R. Beane et al. "Magnetic Moments of Light Nuclei from Lattice Quantum Chromodynamics". In: *Phys. Rev. Lett.* 113 (25 2014), p. 252001. URL: https://link.aps.org/doi/10.1103/PhysRevLett.113.252001.

[62] A Günther, P Papakonstantinou, and R Roth. "Giant resonances based on unitarily transformed two-nucleon plus phenomenological three-nucleon interactions". In: *Journal of Physics G: Nuclear and Particle Physics* 41.11 (2014), p. 115107. URL: https://dx.doi.org/10.1088/0954-3899/41/11/115107.

[63] P. Papakonstantinou. "Second random-phase approximation, Thouless' theorem, and the stability condition reexamined and clarified". In: *Phys. Rev. C* 90 (2 2014), p. 024305. URL: https://link.aps.org/doi/10.1103/PhysRevC.90.024305.

[64] R. Roth. *Theoretische Kernphysik. Vorlesungsnotizen*. 2014.

[65] Robert Roth et al. "Evolved chiral $NN+3N$ Hamiltonians for *ab initio* nuclear structure calculations". In: *Phys. Rev. C* 90 (2 2014), p. 024325. URL: http://link.aps.org/doi/10.1103/PhysRevC.90.024325.

[66] A. Ekström et al. "Accurate nuclear radii and binding energies from a chiral interaction". In: *Phys. Rev. C* 91 (5 2015), p. 051301. URL: https://link.aps.org/doi/10.1103/PhysRevC.91.051301.

[67] Eskendr Gebrerufael, Angelo Calci, and Robert Roth. "Open-shell nuclei and excited states from multireference normal-ordered Hamiltonians". In: *Phys. Rev. C* 93 (3 2016), p. 031301. URL: https://link.aps.org/doi/10.1103/PhysRevC.93.031301.

[68] H. Hergert et al. "The In-Medium Similarity Renormalization Group: A novel ab initio method for nuclei". In: *Physics Reports* 621 (2016), pp. 165–222. URL: https://www.sciencedirect.com/science/article/pii/S0370157315005414.

[69] M. Miorelli et al. "Electric dipole polarizability from first principles calculations". In: *Phys. Rev. C* 94 (3 2016), p. 034317. URL: https://link.aps.org/doi/10.1103/PhysRevC.94.034317.

[70] Richard Trippel. "Collective Excitations with Chiral NN+3N Interactions from Coupled-Cluster and In-Medium SRG". PhD thesis. Darmstadt: Technische Universität, 2016. URL: http://tuprints.ulb.tu-darmstadt.de/5883/.

[71] Tobias Wolfgruber. "Strength Distributions from the No-Core Shell Model". In: *Bachelor Thesis* (2016).

[72] J. Birkhan et al. "Electric Dipole Polarizability of ^{48}Ca and Implications for the Neutron Skin". In: *Phys. Rev. Lett.* 118 (25 2017), p. 252501. URL: https://link.aps.org/doi/10.1103/PhysRevLett.118.252501.

[73] D. R. Entem, R. Machleidt, and Y. Nosyk. "High-quality two-nucleon potentials up to fifth order of the chiral expansion". In: *Phys. Rev. C* 96 (2 2017), p. 024004. URL: https://link.aps.org/doi/10.1103/PhysRevC.96.024004.

[74] Eskendr Gebrerufael et al. "Ab Initio Description of Open-Shell Nuclei: Merging No-Core Shell Model and In-Medium Similarity Renormalization Group". In: *Phys. Rev. Lett.* 118 (15 2017), p. 152503. URL: https://link.aps.org/doi/10.1103/PhysRevLett.118.152503.

[75] H. Krebs, E. Epelbaum, and U.-G. Meißner. "Nuclear axial current operators to fourth order in chiral effective field theory". In: *Annals of Physics* 378 (2017), pp. 317 –395. URL: http://www.sciencedirect.com/science/article/pii/S0003491617300350.

[76] Laura Mertes. "Precision Calculation of Electromagnetic Observables for Light Nuclei". In: *Master Thesis* (2017).

[77] Christina Stumpf, Tobias Wolfgruber, and Robert Roth. *Electromagnetic Strength Distributions from the Ab Initio No-Core Shell Model*. 2017. URL: https://arxiv.org/abs/1709.06840.

[78] Christina Stumpf. "Nuclear Spectra and Strength Distributions from Importance-Truncated Configuration-Interaction Methods". PhD thesis. Darmstadt: Technische Universität, 2018. URL: http://tuprints.ulb.tu-darmstadt.de/7571/.

[79] Y. Kim et al. *Daejeon16 NN Interaction*. 2019. URL: https://arxiv.org/abs/1910.04367.

[80] J. A. Melendez et al. "Quantifying correlated truncation errors in effective field theory". In: *Phys. Rev. C* 100 (4 2019), p. 044001. URL: https://link.aps.org/doi/10.1103/PhysRevC.100.044001.

[81] Alexander Tichai et al. "Natural orbitals for ab initio no-core shell model calculations". In: *Phys. Rev. C* 99 (3 2019), p. 034321. URL: https://link.aps.org/doi/10.1103/PhysRevC.99.034321.

[82] E. Epelbaum et al. "Towards high-order calculations of three-nucleon scattering in chiral effective field theory". In: *The European Physical Journal A* 56.3 (2020). URL: https://doi.org/10.1140%2Fepja%2Fs10050-020-00102-2.

[83] K. B. Howard. *Structure effects on the giant monopole resonance and determinations of the nuclear incompressibility*. 2020. URL: https://arxiv.org/abs/2004.02362.

[84] Kevin B Howard et al. "Compression-mode resonances in the calcium isotopes and implications for the asymmetry term in nuclear incompressibility". In: *Physics Letters B* 801 (2020), p. 135185.

[85] Thomas Hüther et al. "Family of chiral two- plus three-nucleon interactions for accurate nuclear structure studies". In: *Phys. Lett. B* 808 (2020), p. 135651. URL: https://doi.org/10.1016/j.physletb.2020.135651.

[86] Klaus Vobig. "Electromagnetic Observables and Open-Shell Nuclei from the In-Medium No-Core Shell Model". PhD thesis. Darmstadt: Technische Universität, 2020. URL: http://tuprints.ulb.tu-darmstadt.de/11375/.

[87] U. Friman-Gayer et al. "Role of Chiral Two-Body Currents in ^{6}Li Magnetic Properties in Light of a New Precision Measurement with the Relative Self-Absorption Technique". In: *Phys. Rev. Lett.* 126 (10 2021), p. 102501. URL: https://link.aps.org/doi/10.1103/PhysRevLett.126.102501.

[88] Thomas Hüther. "Families of Chiral Two- plus Three-Nucleon Interactions for Accurate Nuclear Structure Studies". PhD thesis. Darmstadt: Technische Universität, 2021. URL: http://tuprints.ulb.tu-darmstadt.de/18588/.

[89] A. Obertelli and H. Sagawa. *Modern Nuclear Physics - From Fundamentals to Frontiers*. Springer Singapore, 2021.

[90] Panagiota Papakonstantinou, James P Vary, and Youngman Kim. "Daejeon16 interaction with contact-term corrections for heavy nuclear systems". In: *Journal of Physics G: Nuclear and Particle Physics* 48.8 (July 2021), p. 085105. URL: http://dx.doi.org/10.1088/1361-6471/ac0b30.

[91] F. Bonaiti, S. Bacca, and G. Hagen. "Ab initio coupled-cluster calculations of ground and dipole excited states in ^{8}He". In: *Phys. Rev. C* 105 (3 2022), p. 034313. URL: https://link.aps.org/doi/10.1103/PhysRevC.105.034313.

[92] J. Carter et al. "Damping of the isovector giant dipole resonance in 40,48Ca". In: *Physics Letters B* 833 (2022), p. 137374. URL: https://www.sciencedirect.com/science/article/pii/S0370269322005081.

[93] Jan Lucas Hoppe. "The in-medium similarity renormalization group for ab initio nuclear structure: method advances and new applications". PhD thesis. Darmstadt: Technische Universität Darmstadt, 2022. URL: http://tuprints.ulb.tu-darmstadt.de/21576/.

[94] Marco Knöll et al. "Machine learning for the prediction of converged energies from ab initio nuclear structure calculations". In: *Physics Letters B* 839 (2023), p. 137781. URL: https://www.sciencedirect.com/science/article/pii/S0370269323001156.

[95] P. Maris et al. "Uncertainties in ab initio nuclear structure calculations with chiral interactions". In: *Frontiers in Physics* 11 (2023). URL: https://www.frontiersin.org/articles/10.3389/fphy.2023.1098262.

[96] Lisa Wagner. "Optimized Single-Particle Basis Sets for the Calculation of Radii in the NCSM". In: *Master Thesis* (2023).

[97] Michelle Müller and Cedric Wenz. *private communication*. 2024.

[98] Michelle Müller. "Consistent Description of Collective Excitations in the In-Medium (S)RPA". In: *Master Proposal* (2024).

Erklärungen laut Promotionsordnung

§8 Abs. 1 lit. c PromO

Ich versichere hiermit, dass die elektronische Version meiner Dissertation mit der schriftlichen Version übereinstimmt.

§8 Abs. 1 lit. d PromO

Ich versichere hiermit, dass zu einem vorherigen Zeitpunkt noch keine Promotion versucht wurde. In diesem Fall sind nähere Angaben über Zeitpunkt, Hochschule, Dissertationsthema und Ergebnis dieses Versuchs mitzuteilen.

§9 Abs. 1 PromO

Ich versichere hiermit, dass die vorliegende Dissertation selbstständig und nur unter Verwendung der angegebenen Quellen verfasst wurde.

§9 Abs. 2 PromO

Die Arbeit hat bisher noch nicht zu Prüfungszwecken gedient.

Ort, Datum	Laura Mertes